Iteratieve reconstructie in micro-SPECT/CT: geregulariseerde ijle-data-CT en absolute kwantificatie in in-vivo-multi-isotoop-micro-SPECT

Iterative Reconstruction in Micro-SPECT/CT: Regularized Sparse-View CT and Absolute In Vivo Multi-Isotope Micro-SPECT Quantification

Bert Vandeghinste

Promotoren: prof. dr. R. Van Holen, prof. dr. S. Vandenberghe, prof. dr. ir. S. Staelens
Proefschrift ingediend tot het behalen van de graad van
Doctor in de Ingenieurswetenschappen: Biomedische Ingenieurstechnieken

Vakgroep Elektronica en Informatiesystemen
Voorzitter: prof. dr. ir. J. Van Campenhout
Faculteit Ingenieurswetenschappen en Architectuur
Academiejaar 2013 - 2014

UNIVERSITEIT GENT

ISBN 978-90-8578-677-1
NUR 954, 959
Wettelijk depot: D/2014/10.500/23

Department of Electronics and Information Systems
Medical Imaging and Signal Processing
Faculty of Engineering and Architecture
Ghent University

MEDISIP
IBiTech - iMinds
Campus Heymans, Blok B
De Pintelaan 185
9000 Ghent
Belgium

Promotors
prof. dr. Roel Van Holen
prof. dr. Stefaan Vandenberghe

External Promotor
prof. dr. ir. Steven Staelens, University of Antwerp

Board of examiners
prof. dr. ir. Luc Taerwe, Ghent University, chairman
prof. dr. ir. Bart Goossens, Ghent University, secretary
dr. Nicola Belcari, Università di Pisa
prof. dr. Alain Seret, Université de Liège
prof. dr. ir. Steven Staelens, University of Antwerp
prof. dr. Stefaan Vandenberghe, Ghent University
prof. dr. Roel Van Holen, Ghent University
prof. dr. Christian Vanhove, Ghent University
dr. ir. Jeroen Verhaeghe, University of Antwerp

This work was funded by a PhD grant of the Agency for Innovation by Science and Technology (IWT).

Acknowledgements

First, a big word of gratitude goes out to my three advisors. The quest towards my PhD started at MEDISIP in 2009, after writing my masters thesis under supervision of prof. dr. ir. Patrick Segers, prof. dr. Stefaan Vandenberghe and Bram Trachet. Thanks to the research done at the newly-built Infinity preclinical lab, I was inspired to start in the field of biomedical image reconstruction. Prof. dr. ir. Steven Staelens and Stefaan left the choice up to me: work on TOF-PET or continue on with CT. I'm very grateful that I got to choose my own line of research, even though no other researchers were actually working on CT. This didn't make it any easier to supervise me. Steven later left for the University of Antwerp – I hope that wasn't because of me – still supervising my progress. At that time prof. dr. Roel Van Holen was promoted to professor, ultimately leaving me with 3 promotors.

I'm well aware that supervising my work was never really easy. The discussions on which research track to follow were always ongoing, but we always found a way out that we mutually agreed on. Steven, Roel and Stefaan, thanks for the guidance and the confidence.

During my 4.5-year stint at the lab I've also had help from a lot of other people. Not in the least there's prof. Chris Vanhove, who acted a bit like a promotor lurking in the shadows. Chris, I need to thank for the many discussions on preclinical reconstruction for CT, SPECT, the talks on road cycling, and for showing me how pragmatic approaches can also be a valid way of performing research.

From the IPI group, I need to thank primarily Bart Goossens for his help with the work on CT regularisation. It is unbelievable how much I have learned concerning image processing and image quality, and I'm even more astounded at how much I still have to learn. I hope we can continue our fruitful collaboration in the near future.

To the people of the pharmacy department (Filip, Sara, Lieselotte and

Caroline): thanks for helping me with the experimental work that involved radioactivity. Also thanks to the nuclear medicine department for providing me with the radioisotopes that I needed to run my experiments, even when I called only 10 minutes in advance. Christophe Casteleyn, thanks for helping me with the difficult brain dissections, even though that experiment ultimately failed (my bad). Bram Trachet, thanks for all the effort and work we've done together.

At MEDISIP - Tom, Karel and Enrico, thanks for those first days in the office a little over 4 years ago. It was immediately clear what this group was made of, I couldn't have had a better introduction. Jan, thanks for guiding me during the first years. The people at the Infinity lab, previously Philippe Joye and Steven Deleye, thanks for the good times at Infinity. I wish you all the best in Antwerp. Scharon and Benedicte, thanks for helping me with my experiments, some animal handling skills are clearly best left up to you.

Gregor, thanks for the lunch dates and bike trips. Nothing more relaxing at noon than discussing some cycling news, and to follow it up with some rides together. Also thanks to you and Lotte for the two kittens! Karen and Lara, thanks for the enlightening discussions on SPECT, multiplexing pinholes and sensitivity implementations. Carmen, thanks for helping Karel and me out when we couldn't figure out how atomic physics work.

Pieter and Pieter, drinking on Fridays wouldn't be the same without you guys. But also thanks for the advice and help while finishing this book! Ewout, thanks for turning me into some kind of entrepreneur. Vincent, thanks for the good discussions on *attenuaatie* and novel preclinical experiments, maybe we'll actually do some in the future. Tony, thanks for joining us however so briefly. Hope you'll finish your medicine degree without any problems. Also sincere thanks to Faruk, Hans, Kasper, Long, Nathalie, Radek, Roma, Shandra, Sinem, Victoria and Willeke for the pleasant time at MEDISIP.

This work would of course not have been possible if it weren't for Saskia, Inge, Aaike, Anne-Marie and Ayfer. Thanks for helping me with the administrative part!

Ik wil ook het agentschap voor innovatie door wetenschap en technologie (IWT) bedanken voor de financiële steun de afgelopen jaren.

Mijn ouders wil ik natuurlijk ook bedanken. Bedankt om me te steunen doorheen alle jaren waarin ik nu al studeer. Bedankt om toch telkens te vragen wat ik nu eigenlijk doe als onderzoeker, en even vol te houden

wanneer ik opnieuw afkom met een veel te ingewikkelde uitleg. Ook mijn schoonfamilie hoort daarbij, bedankt!

Tot slot moet ik ook mijn *Home De Pinte* vrienden bedanken die me de voorbije jaren gesteund hebben: een welgemeende dankjewel. En daar hoort als laatste, maar zeker niet in het minste, ook mijn vriendin Aagje bij. Bedankt voor je liefde en steun de voorbije 6 jaar, zonder jou was dit niet gelukt. Laat de volgende jaren maar komen!

Bert Vandeghinste, 14 april 2014.

"If the path before you is clear, you're probably on someone else's."
Josef Campbell

Table of Contents

List of Figures

List of Tables

List of Acronyms

A

ALARA	As Low As Reasonably Achievable
ART	Algebraic Reconstruction Technique

B

BLT	BioLuminescence Tomography
BV	Bounded Variation
BW	Body Weight

C

CCD	Charge Coupled Device
CFD	Computational Fluid Dynamics
CG	Conjugate Gradient
CM	Centre of Mass
CMOS	Complementary Metal-Oxide-Semiconductor
CNR	Contrast-to-Noise Ratio
CS	Compressed Sensing
CST	Continuous Shearlet Transformation
CT	Computed Tomography
CUDA	Compute Unified Device Architecture
CZT	Cadmium Zinc Telluride

D

DECT	Dual Energy CT
DEW	Dual Energy Window
DFT	Discrete Fourier Transform
DMSA	DiMercaptoSuccinic Acid
DQE	Detective Quantum Efficiency
DST	Discrete Shearlet Transformation

E

ECG	ElectroCardioGraphy
EM	ElectroMagnetic, Expectation Maximization
ESF	Edge Spread Function
ET	Emission Tomography

F

FBP	Filtered BackProjection
FDK	Feldkamp-Davis-Kress
FEW	Five Energy Window
FFT	Fast Fourier Transform
FMT	Fluorescence Molecular Tomography
FN	False Negative
FOV	Field Of View
FP	False Positive
FPCIT	ioflupane
FWHM	Full Width at Half Maximum

G

GLCM	Gray Level Co-occurrence Matrix
GPU	Graphics Processing Unit

H

HMPAO	HexaMethylPropyleneAmine Oxime

I

IMPACT	Iterative Maximum-likelihood Polychromatic Algorithm for CT
IP	IntraPeritoneal
ISRA	Image Space Reconstruction Algorithm

L

LSF	Line Spread Function
LUT	Look-Up Table

M

MAG3	MercaptoAcetyltriGlycine
MAP	Maximum A-Posteriori
MC	Monte Carlo
MDCT	Multi-Detector CT
MIBG	MetaIodoBenzylGuanidine
MDP	Methyl DiPhosphonate (medronic acid)
MI	Molecular Imaging
ML	Maximum Likelihood
MLEM	Maximum Likelihood Expectation Maximization
MLTR	Maximum-Likelihood for TRansmission tomography
MRI	Magnetic Resonance Imaging
MTF	Modulation Transfer Function

N

NEMA	National Electrical Manufacturers Association
NET	NeuroEndocrine tumor
NFFT	Nonequispaced Fast Fourier Transform
NIST	National Institute of Standards and Technology
NRMSE	Normalized Root Mean Squared Error

O

OS	Ordered Subset
OSEM	Ordered Subset Expectation Maximization
OSL	One Step Late

P

PET	Positron Emission Tomography
PMT	PhotoMultiplier Tube
PRRT	Peptide Receptor Radionuclide Therapy
PSF	Point Spread Function
PSPMT	Position Sensitive PMT
PVE	Partial Volume Effect
PWLS	Penalized Weighted Least Squares

Q

QCT	Quantitative Computed Tomography
q-GGMRF	q-Generalized Gaussian Markov Random Field

R

RF	RadioFrequent
ROI	Region Of Interest

S

SART	Simultaneous Algebraic Reconstruction Technique
SEE	Standard Error of the Estimate
SIRT	Simultaneous Iterative Reconstruction Technique
SH	SHearlet transformation
SLN	Sentinel Lymph Node
SNR	Signal-to-Noise Ratio
SpBR	Split-BRegman
SPECT	Single-Photon Emission Computed Tomography
SPR	Scatter-to-Primary Ratio
SSR	SomatoStatin Receptor

T

TAC	Time-Activity Curve
TFT	Thin Film Transistor
TP	True Positive
TV	Total Variation

U

US	UltraSound
UV	UltraViolet

V

VOI	Volume Of Interest

W

WSS	Wall Shear Stress

English summary

Nederlandstalige samenvatting

English summary

X-ray computed tomography (CT) and single photon emission computed tomography (SPECT) are two medical imaging techniques used to visualize anatomical information and functional processes in vivo, respectively. CT imaging is based on the absorption or attenuation of X-rays sent through a patient. The unattenuated X-rays are detected from different angles around the patient, and are used to calculate the patient's 3D attenuation distribution using tomographic reconstruction. Because X-ray attenuation depends on the elemental composition and density of the tissue, CT imaging results in anatomical information of the patient.

SPECT imaging is used to gather functional information, by visualizing the spatial distribution of a radioactive tracer. This is based on the tracer principle, which states that an atom in a molecule that takes part in metabolism can be replaced by one of its radioactive isotopes. The tracer will emit gamma photons because of radioactive decay. The pathways involved in the metabolism can be tracked by detecting these photons. The photons are measured from different angles around the patient, after which the 3D spatial distribution of the tracer can be reconstructed. Because the spatial tracer distribution depends on its use in different metabolic pathways, SPECT imaging results in functional information of the patient.

Both imaging modalities have also been miniaturized to enable their use for small animal imaging (preclinical imaging). These systems use a different geometrical design, mainly to increase the spatial resolution, e.g. by using a large magnification in micro-CT systems, or by using pinhole magnification in micro-SPECT systems.

Unfortunately, both modalities suffer from some limitations. Because CT uses a large number of X-rays to achieve low-noise measurements, the patient will receive a large radiation dose. The X-rays interact with the living tissue, and can damage cell DNA or kill cells. Damaged cells

may eventually grow into clinical cancer. It is therefore important to reduce the radiation dose to the minimal dose needed to achieve sufficient image quality for a specific imaging task. This is also relevant to preclinical imaging, where high-resolution scans necessitate relatively high-dose imaging protocols, and where it is multiple scans are commonly acquired.

One of the challenges in SPECT is absolute quantification. With absolute quantification, the activity concentration can be directly derived from the reconstructed images instead of only providing a qualitative view of the spatial tracer distribution. Such an accurate estimation of the activity is useful to enable dose calculations in targeted therapy treatment planning, to follow the longitudinal treatment of tumors, or to measure the dose-response curve of an experimental drug preclinically. Unfortunately, SPECT imaging suffers from patient-specific image degrading effects that influence the direction of the gamma rays (photon scattering), and the amount of gamma rays detected (photon attenuation). Both effects severely degrade the quantitative accuracy. Preclinically, the much smaller size of laboratory animals will lead to less attenuation and scattering than encountered in human patients, possibly improving the quantitative accuracy compared to clinical SPECT.

Both imaging modalities use tomographic reconstruction to estimate the 3D patient attenuation or 3D tracer distribution from measured data. Thus, the specific reconstruction algorithm can have a potentially big influence on the challenges of both modalities. This dissertation investigates the use of model-based iterative reconstruction in CT and micro-SPECT/CT imaging to address both the X-ray radiation dose in micro-CT, as well as absolute quantification in micro-SPECT/CT.

The X-ray dose was minimized for the specific task of murine vascular imaging and segmentation. We investigated if *in vivo* micro-CT imaging can be an accurate alternative for vascular corrosion casting, which is the current gold standard to make 3D models of the aortic arch and side branches. Therefore, a contrast-enhanced micro-CT study was done in mice, to compare the *in vivo* obtained 3D models to the *in vitro* models obtained after casting. The in vivo models showed a 33% increase in diameter compared to the in vitro models, which does not lead to significantly different computational fluid dynamics values. This relatively large vessel diameter increase was caused by shrinkage due to the casting agent. Retrospective respiratory gating does not improve the vessel delineation quality, but substantially increases the image noise and streaking artifacts due to the limited angular sampling.

In order to reach a sufficiently high image quality for segmentation purposes, a radiation dose of 196 mGy per scan was used. This is higher than the dose proven to lead to tumor growth inhibition in mice, and can thus potentially influence experimental results. This means that the radiation dose should be lowered if longitudinal studies are required.

We reduced the radiation dose by using less projection views in the acquisition protocol. While this decreases the radiation dose linearly, the angular under-sampling leads to image artifacts when the reconstruction algorithm is not adapted for it. A regularized iterative reconstruction technique is proposed, which minimizes the total variation (TV) of the reconstructed image. The TV model helps to minimize the variation between neighboring image voxels, and thus reduces the streaking artifacts and noise.

For the vascular segmentation task, an 8-fold reduction in radiation dose was achieved with this reconstruction algorithm. This also results in an 8-times faster scanning time. While the minimal radiation dose possible is only determined for this task, the same type of analysis can also be executed for other tasks (e.g. for trabecular bone analysis), in order to achieve a minimal-dose protocol based on advanced reconstruction techniques.

One issue noticed with the use of a TV model are the block-like imaging artifacts. These were caused by the assumptions underlying the TV model: TV regards the reconstructed images as approximately piecewise constant. Its use can thus be questioned for medical imaging: medical images are not approximately piecewise constant, but will exhibit texture. This information may be lost when TV minimization is used.

Therefore, we evaluated a regularized iterative reconstruction algorithm novel to CT in which different regularizers can be tested. This framework is applied to the shearlet-transformation, a multi-scale and multidirectional transformation shown to have an essentially optimal approximation error for images that contain edges. Although TV minimization outperformed the shearlet-based reconstruction algorithm on untextured phantoms, the shearlet-based reconstruction reconstructed realistic textures more similar to the reference texture in low-dose cases. The limitations of such a shearlet-based reconstruction algorithm is that it is unsuited for isotropic features. Although it is a promising technique, more work will be needed to try and solve this limitation.

The opportunity of improving absolute quantification in micro-SPECT/CT by using model-based iterative reconstruction was also eval-

uated. Different correction techniques were implemented, in order to include photon attenuation, photon scatter, resolution recovery, detector uniformity, geometrical sensitivity, and the partial volume effect. This implementation was first validated in a NEMA phantom study with the isotopes ^{99m}Tc and ^{111}In, on a multi-pinhole CZT-based micro-SPECT system. A quantification error of ±10% was achieved for both isotopes. Our study indicates that, for this system, the quantification error was primarily influenced by attenuation correction. The photon scatter was already effectively reduced by using photopeak windowing, due to the excellent energy resolution (4.22±0.23%) encountered with a CZT detector.

Finally, the quantification error was also directly determined in two typical preclinical *in vivo* studies. One study uses [^{99m}Tc]DMSA, a tracer that can be used to assess renal function and, preclinically, used to quantify the tubular functioning after ^{90}Y therapy. As a second model a murine model of human non-small cell lung carcinoma is chosen, imaged with [^{111}In]Octreotide. A quantification error of ±5% was achieved in both studies. The attenuation map can also be acquired at 1/16th the dose of the high-resolution CT data, as long as the same model-based iterative reconstruction techniques are used as for the vascular segmentation task. However, a high-resolution CT dataset still needs to be acquired to correct for the partial volume effect.

This research was performed in the Medical Image and Signal Processing (MEDISIP) research group. MEDISIP is a research group in the Electronics and Information Systems (ELIS) department of the Faculty of Engineering and Architecture (FEA) of Ghent University, Belgium. MEDISIP also encompasses the Innovative Flemish In Vivo Imaging Technology (INFINITY) preclinical imaging facility. The work presented here resulted in 10 journal publications (4 as first author), 8 papers published in the proceedings of international conferences with peer review (4 as first author), and 21 conference abstracts without peer review (7 as first author).

Nederlandstalige samenvatting

X-stralen computertomografie (CT) en single photon emission computertomografie (SPECT) zijn twee medische beeldvormingstechnieken voor respectievelijk anatomische informatie en functionele in vivo processen. CT beeldvorming is gebaseerd op de absorptie of attenuatie van X-stralen door een patiënt. De ongeattenueerde X-stralen worden gedetecteerd onder een aantal hoeken rondom de patiënt. Uit deze data wordt daarna de 3D attenuatiedistributie van de patiënt berekend met een reconstructiealgoritme. Aangezien de attenuatie van de X-stralen afhankelijk is van de elementcompositie en densiteit van weefsel, zal CT beeldvorming resulteren in anatomische informatie over de patiënt.

SPECT beeldvorming wordt gebruikt om functionele informatie te visualiseren op basis van de ruimtelijke verdeling van een radioactieve speurstof. Dit is gebaseerd op het speurstofprincipe, het inzicht dat een atoom van een molecule dat gebruikt wordt in het metabolisme vervangen kan worden door één van zijn radioactieve isotopen. De speurstof zal gammafotonen uitstralen vanwege radioactief verval. Door deze fotonen te detectoren kunnen de reactiepaden in het metabolisme gevolgd worden. De fotonen worden opgemeten uit verschillende projectiehoeken rond de patiënt, en worden daarna tot een 3D ruimtelijke distributie van de speurstof gereconstrueerd. Omdat de distributie van de speurstof afhankelijk is van het gevolgde reactiepad, resulteert SPECT beeldvorming in functionele informatie over de patiënt.

Beide beeldvormingsmodaliteiten werden eveneens geminiaturiseerd, om ze bruikbaar te maken voor het beeldvormen van kleine proefdieren (preklinische beeldvorming). Deze systemen zijn gebaseerd op een ander geometrisch ontwerp en andere componenten, voornamelijk gekozen om het ruimtelijk scheidend vermogen te verbeteren. Bij micro-CT systemen

wordt veelal vergroting gebruikt. In micro-SPECT wordt dit bekomen door een pinholecollimator te gebruiken.

Jammer genoeg zijn er ook enkele limitaties verbonden aan beide modaliteiten. Bij CT beeldvorming is een groot aantal X-stralen noodzakelijk om laag-ruizige metingen te verkrijgen van de attenuatie. Daardoor krijgen de patiënten een grote stralingsdosis. De X-stralen zullen immers reageren met het levende weefsel en kunnen daarbij het DNA van cellen beschadigen, of de cellen zelfs doden. De beschadigde cellen kunnen later uitgroeien tot kankercellen. Daarom is het van belang om de stralingsdosis te verkleinen tot het absolute minimum nodig om een bepaalde beeldvormingstaak uit te voeren. Dit is ook relevant voor preklinische beeldvorming, aangezien daar een hoog scheidend vermogen noodzakelijk is, wat enkel mogelijk is onder hoge stralingsdosis. Daarnaast zijn er ook vaak meerdere opnames nodig van hetzelfde dier om een studie op te volgen.

Eén van de uitdagingen in SPECT beeldvorming is absolute kwantificatie. Met absolute kwantificatie kan de concentratie aan radioactiviteit onmiddellijk afgelezen worden op het beeld, in plaats van beelden te bekomen met een meer kwalitatief idee over de ruimtelijke lokatie van de speurstof. Zo'n accurate bepaling van de concentratie is bruikbaar bij het berekenen van stralingsdosis bij therapeutische behandelingen, om langdurige kankerbehandelingen beter op te volgen, of om de effectiviteit van een experimenteel geneesmiddel te bepalen op proefdieren. Er bestaan echter beelddegraderende effecten die de kwantificatie beïnvloeden door het gevolgde fotonpad te veranderen (fotonverstrooiing), en door het aantal gedetecteerde fotonen te verminderen (fotonattenuatie). Beide degradaties zullen de precisie van de absolute kwantificatie ernstig verminderen. In preklinische beeldvorming zullen de veel kleinere proefdieren voor minder fotonattenuatie en fotonverstrooiing zorgen vergeleken met humane SPECT, waardoor de kwantificatie misschien preciezer werkt.

Beide modaliteiten gebruiken tomografische reconstructie om de 3D attenuatiedistributie of 3D speurstofdistributie te bekomen uit de opgemeten gegevens. Dit wil zeggen dat het specifiek gebruikte reconstructiealgoritme een grote invloed kan hebben op de uitdagingen van beide modaliteiten. In dit proefschrift wordt daarom de invloed van modelgebaseerde iteratieve reconstructie op de stralingsdosis in micro-CT en op absolute kwantificatie in micro-SPECT/CT onderzocht.

We verminderen de stralingsdosis voor een specifieke taak: de beeld-

vorming en segmentatie van de bloedvatenstructuur bij muizen. Daartoe onderzochten we of *in vivo* micro-CT beeldvorming een accuraat alternatief kan vormen voor vasculaire afgietsels, de huidige gouden standaard om 3D modellen van de aortaboog en aftakkingen te maken. Daarom werd een contrast-verhoogde micro-CT proef opgezet in muizen, waarbij de *in vivo* bekomen 3D modellen vergeleken werden met de *in vitro* bekomen 3D modellen. De in vivo modellen vertoonden een 33% grotere diameter vergeleken met de in vitro modellen, maar deze vergroting veroorzaakte geen significant verschillende resultaten in numiereke stromingsberekeningen. De verhoogde diameter werd ook mede veroorzaakt door een inkrimping veroorzaakt door het afgietselproduct zelf. Retrospectief de data corrigeren voor ademhalingsbeweging van het proefdier leverde geen betere aflijningskwaliteit op bij de bloedvaten, maar wel een sterk verhoogd ruisniveau en streepartefacten. Dit werd veroorzaakt doordat er te weinig projectiehoeken werden opgemeten.

Om voldoende beeldkwaliteit te bekomen voor segmentatie, werd een stralingsdosis van 196 mGy gebruikt per opname. Dit is een hogere dosis dan de dosis die tumorgroei kan vertragen in muizen, en kan dus ook een invloed uitoefenen op experimentele resultaten. Dit wil zeggen dat de stralingsdosis verlaagd moet worden indien longitudinale studies noodzakelijk zijn.

We ontwikkelden daarom een methode waarbij de stralingsdosis verminderd wordt door minder meethoeken te gebruiken in het opnameprotocol. Dit zal de stralingsdosis rechtevenredig doen dalen, maar zal ook streepartefacten veroorzaken in de beelden wanneer het reconstructiealgoritme niet aangepast wordt. We stellen een geregulariseerd iteratief reconstructiealgoritme voor, waarin de totale variatie (TV) geminimaliseerd wordt. Dit model zal helpen om de variatie tussen naburige beeldelementen te verminderen, om zo de streepartefacten en beeldruis te minimaliseren.

Dit algoritme liet toe om 8-maal minder stralingsdosis te bekomen bij opnames bedoeld voor bloedvatensegmentatie. Dit heeft ook tot gevolg dat de opnamesnelheid 8-maal hoger ligt. Alhoewel de mogelijke stralingsdosis enkel geoptimaliseerd werd voor de bloedvatensegmentatietaak, kan dit type analyse ook gedaan worden voor andere taken (bv. analyses op sponsachtig bot), om daar ook tot een optimaal opnameprotocol te komen.

Tijdens deze evaluatie werd wel een probleem opgemerkt veroorzaakt door het gebruik van het TV model. De beelden kunnen namelijk blokar-

tefacten bevatten. TV veronderstelt dat de gereconstrueerde beelden bij benadering stuksgewijs constant zijn. Het gebruik van TV moet dan ook in vraag gesteld worden voor het gebruik in medische beeldvorming: medische beelden zijn immers niet stuksgewijs constant, maar bevatten ook textuurinformatie. Deze informatie kan verloren gaan wanneer de TV geminimaliseerd wordt.

Daarom hebben we een ander geregulariseerd iteratief reconstructie-algoritme onderzocht, dat toelaat om verschillende modellen te evalueren. Dit raamwerk werd toegepast op de shearlet-transformatie, een meerschalig- en meerrichtingstransformatie met een optimale benaderingsfout voor beelden die randen bevatten. Alhoewel de TV minimalisatie beter presteerde dan shearlet-gebaseerde reconstructie op eenvoudige, vlakke fantomen, bleek shearlet-gebaseerde reconstructie de bovenhand te halen bij beelden met realistische texturen. Een beperking van het shearlet-gebaseerde algoritme werd experimenteel aangetoond: shearlets zijn niet geschikt voor richtingsonafhankelijke beelden. Alhoewel deze techniek zeker beloftevol is, zal er toch nog verder onderzoek nodig zijn om deze beperking op te lossen.

De mogelijkheid om met model-gebaseerde iteratieve reconstructiealgoritmes de absolute kwantificatie in micro-SPECT/CT te verbeteren werd ook onderzocht. Verschillende technieken werden geïmplementeerd om te corrigeren voor fotonattenuatie, fotonverstrooiing, detectoruniformiteit, geometrische sensitiviteit, het partieelvolume-effect, en om de resolutie te verbeteren. Deze implementatie werd eerst gevalideerd op een NEMA fantoom voor de isotopen ^{99m}Tc en ^{111}In, opgenomen op een CZT-gebaseerd micro-SPECT systeem met meerdere pinholes. Een kwantificatiefout van $\pm 10\%$ werd bekomen voor beide isotopen. De resultaten toonden ook aan dat, voor dit systeem, de kwantificatiefout voornamelijk bepaald wordt door de correctie voor fotonattenuatie. De invloed van de fotonverstrooiing wordt grotendeels verminderd door het fotopiekvenster dat optimaal gekozen kan worden dankzij de uitstekende energieresolutie ($4.22 \pm 0.23\%$) van de CZT stralingsdetector.

Tot slot werd de kwantificatiefout ook rechtstreeks bepaald in twee typische preklinische *in vivo* experimenten. Eén studie gebruikt [^{99m}Tc]DMSA, een speurstof om de nierfunctie te bepalen, en preklinisch ook gebruikt om het tubulaire functioneren te onderzoeken na therapie met ^{90}Y. Het tweede model is een muizenmodel van humaan niet-kleincellig longcarcinoom, met als speurstof [^{111}In]Octreotide. Een kwantificatiefout van $\pm 5\%$ werd bekomen voor beide studies. Daarnaast

werd ook bepaald dat het fotonattenuatiebeeld opgemeten kan worden aan 1/16de van de originele stralingsdosis dankzij het gebruik van modelgebaseerde iteratieve beeldreconstructie zoals bij de segmentatietaak. Een hoog-resolutie CT beeld zal echter nog steeds noodzakelijk zijn om te kunnen corrigeren voor het partieelvolume-effect.

Dit onderzoek werd uitgevoerd in de Medical Image and Signal Processing (MEDISIP) onderzoeksgroep. MEDISIP is een onderzoeksgroep binnen de Electronica en Informatiesystemen (ELIS) vakgroep van de Faculteit Ingenieurswetenschappen en Architectuur (FEA) van de Universiteit van Gent in België. MEDISIP omvat eveneens het Innovative Flemish In Vivo Imaging Technology (INFINITY) preklinisch beeldvormingslaboratorium. Het werk gepresenteerd in dit proefschrift leidde tot 10 tijdschriftpublicaties (4 als eerste auteur), 8 werken gepubliceerd in de proceedings van internationale wetenschappelijke conferenties met collegiale toetsing (4 als eerste auteur), en 21 conferentieabstracts zonder collegiale toetsing (7 als eerste auteur).

Chapter 1

Introduction

1.1 Problem statement

This dissertation is situated in the field of X-ray Computed Tomography (CT) and Single Photon Emission Computed Tomography (SPECT) imaging. In CT imaging, anatomical information is acquired by measuring the attenuation of X-rays sent through a patient. The attenuation is dependent on the elemental composition and density of the tissue. After measuring the unattenuated X-rays with a detector, this information can later be reconstructed into a cross-sectional view of the patient's anatomy or structure. In SPECT imaging, functional information is gathered from the spatial distribution of a radioactive compound (tracer). The patient is injected with a tracer, which will emit gamma-rays while decaying. After measuring the gamma photons with a detector that rotates around the patient, the data can be reconstructed into a cross-sectional view. Instead of containing anatomical information, in SPECT, the cross-sections will contain functional information.

Both modalities are used in clinical practice for diagnostic applications. CT images are primarily used to image structural information, such as bone traumas and structural changes to the lung parenchyma, but also for brain hemorrhaging, brain and heart infarctions, or to diagnose abdominal diseases such as abdominal aortic aneurysms, renal stones, or appendicitis. SPECT imaging is used to acquire functional information. The reconstructed images can be used for cardiac imaging to diagnose ischemic heart disease, for tumor imaging, infection imaging, thyroid imaging, and to find bone abnormalities.

Closely related are the applications in preclinical (small animal) imag-

ing. There, the same imaging modalities are used to accelerate the transfer of laboratory discoveries into clinical practice. This translation is made possible by small animal studies (primarily on mice and rats). Traditional investigative techniques use histology, microscopy and organ sampling, inevitably requiring the animals to be sacrificed. With miniaturized medical imaging devices, i.e. micro-CT or micro-SPECT systems, the required data can be measured *in vivo* and thus also longitudinally. This increases the statistical power of the experiments, as each animal can serve as its own control animal.

SPECT imaging is inevitably influenced by physical interactions such as photon attenuation and photon scattering, which lead to image degradation. Gamma photons can be involved in photoelectric interactions, resulting in an underestimation of the true uptake value. The photons may also diverge from their original path, leading to inaccurate spatial information. The combination of both effects leads to non-quantitative functional information. Dual-modality SPECT/CT imagers were later developed to enable the acquisition of anatomical and functional information at the same time. The reconstructed SPECT images can then be viewed on top of anatomical landmarks obtained from the CT images and the image degrading effects can be corrected by including the anatomical information obtained from CT into the reconstruction algorithm. This improves the quantitative accuracy of the functional information.

However, there remain some important limitations to CT and SPECT.

In CT, X-ray radiation dose will always be delivered to the patient. This is important in both clinical as well as preclinical studies, where patients are scanned a number of times to evaluate longitudinal progression. Reducing the radiation dose will lead to worse image quality, decreasing the value of the CT images unless corrected for with advanced reconstruction techniques.

In SPECT, absolute quantification is of major importance. Quantitative data enables measuring the dose-response curve for an experimental drug, or the evaluation of tumor regression or tumor recurrence after a novel treatment. As long as not all image degrading effects are corrected for, the data will only be semi-quantitative after a calibration step.

In this work, both the X-ray dose in CT and the absolute quantification of SPECT will be handled. We show how sufficient image quality can be obtained to segment the vascular tree from low-dose micro-CT, by using regularized CT reconstruction. We then extend this approach to other regularizers, to obtain a higher image quality near non-uniform

tissue. Furthermore, we model the image degrading effects which have an influence on SPECT quantification, and we obtain in vivo quantification results using our iterative reconstruction approach.

1.2 Organization of this dissertation

This dissertation starts in Chapter 2 with a discussion of medical and preclinical CT and SPECT imaging from a historical perspective. The principles of CT and SPECT imaging are explained, with special attention to the components and techniques needed in the succeeding chapters. Chapter 2 also encompasses the challenges seen in CT, SPECT, and SPECT/CT both for clinical applications as well as in preclinical usage.

In Chapter 3 *in vivo* CT imaging is used as an alternative to *ex vivo* techniques in current preclinical vascular imaging. Although this micro-CT approach is shown to deliver the same results as the *ex vivo* gold standard, X-ray radiation dose now becomes an important challenge. We will investigate a method to reduce the X-ray radiation dose in Chapter 4, by reducing the number of projection views during the acquisition. The resulting image artifacts will then be corrected for by using regularized iterative reconstruction. Although this method leads to an 8-fold decrease in radiation dose when the data is to be used only for image segmentation, the image quality still suffers from some newly introduced artifacts. Therefore, in Chapter 5, a framework will be designed in which different regularization approaches can be tested, after which shearlets will be used to improve the image quality for textured image features.

Chapter 6 details how absolute quantitative SPECT reconstruction can be implemented on the GPU. A ray-based reconstruction approach is used to model the image degrading effects directly in the forward model. These correction factors are first discussed in more detail. This is then followed by a phantom validation study on a multi-pinhole micro-SPECT system for ^{99m}Tc and ^{111}In. These results are further extended into two *in vivo* murine animal models in Chapter 7.

Finally, this thesis is concluded in Chapter 8 with a concise summary of each chapter, together with an overall conclusion of the complete dissertation.

1.3 Key contributions

The research presented in this thesis has resulted in several scientific contributions. The *key contributions* discussed in this work are:

- The application of TV-based regularized CT reconstruction for low-dose CT reconstruction in vascular segmentation. This method was chosen based on its high computational efficiency even in large micro-CT datasets. Using this algorithm, the same segmentation quality could be achieved at 1/8th of the original X-ray dose. Contributions are published in *Molecular Imaging and Biology* and *PLOS One*.

- A reconstruction framework based on a split-Bregman approach to regularize CT reconstructions. This method allows any general regularizer to be used in an efficient general optimization method, and has been used in this dissertation to compare shearlet-based regularization to total variation-based regularization. Contributions are published in *IEEE Transactions on Nuclear Science*, the *SPIE Conference Proceedings* and the *Fully 3D Conference Proceedings*.

- Combination of existing corrections for image degrading effects to accomplish absolute in-vivo micro-SPECT quantification. This method was implemented for a multi-pinhole micro-SPECT system, and was validated in two mouse models for two different isotopes. Contributions are published in *Molecular Imaging* and the *IEEE NSS/MIC Conference Proceedings*.

So far, this work resulted in 10 journal publications (of which 4 as first author), 8 papers published in the proceedings of international conferences with peer review (of which 4 as first author), and 21 papers published in conference abstracts without peer review (of which 7 as first author). A small selection of the key publications published during this research is given below:

- Vandeghinste B, Van Holen R, Vanhove C, De Vos F, Vandenberghe S, Staelens S. Use of a ray-based reconstruction algorithm to accurately quantify preclinical micro-SPECT images *Molecular Imaging* 2014; accepted.

- Vandeghinste B, Goossens B, Van Holen R, Vanhove C, Pižurica A, Vandenberghe S, Staelens S. Iterative CT reconstruction using

shearlet-based regularization *IEEE Transactions on Nuclear Science* 2013;60(5):3305-3317.

- Vandeghinste B, Vandenberghe S, Vanhove C, Staelens S, Van Holen R. Low-dose micro-CT imaging for vascular segmentation and analysis using sparse-view acquisitions *PLOS One* 2013;8(7):e68449.

- Vandeghinste B, Goossens B, Van Holen R, Vanhove C, Pižurica A, Vandenberghe S, Staelens S. Iterative CT reconstruction using shearlet-based regularization *Proc. of SPIE Medical Imaging* 2012.

- Vandeghinste B, Vanhove C, De Beenhouwer J, Van Holen R, Vandenberghe S, Staelens S. Absolute quantification in multi-pinhole micro-SPECT for different isotopes *Proc. of the 2011 Medical Imaging Conference* 2011;3720-3724.

- Vandeghinste B, Goossens B, De Beenhouwer J, Pižurica A, Philips W, Vandenberghe S, Staelens S. Split-Bregman-based sparse-view CT reconstruction *Proc. International Conference on Fully 3D Reconstruction* 2011;431-434.

- Vandeghinste B, Trachet B, Renard M, Casteleyn C, Staelens S, Loeys B, Segers P, Vandenberge S. Replacing vascular corrosion casting by in vivo μCT imaging for building 3D cardiovascular models in mice *Molecular Imaging and Biology* 2011;13(1):78-86.

The full list of publications can be found after the literature references.

Chapter 2

Background

This introductory chapter is used to explain the physical principles underlying medical imaging, principles which are going to be used throughout the remainder of this thesis. First, a broad overview of medical imaging is given, followed by a detailed description of the different physical effects encountered in planar (2D) X-ray and gamma-ray imaging. This is followed by a detailed description of how X-rays and gamma-rays can also be used for 3D imaging, in particular for X-ray computed tomography (CT) and single photon emission computed tomography (SPECT).

CT imaging is detailed first, by discussing the hardware components, reconstruction principles, image degrading effects and X-ray radiation dose. In the third section, SPECT imaging is described in a similar way as CT imaging, first discussing the general principles behind emission tomography (ET) and image reconstruction, followed by a discussion of image degrading effects encountered in SPECT. Both modalities are concluded with a discussion on their remaining challenges, together with attention to the specific issues encountered in preclinical imaging.

The last section of this chapter is dedicated to multimodal SPECT/CT imaging. Challenges specific to SPECT/CT imaging will be reviewed, both for clinical as well as preclinical SPECT/CT.

2.1 Medical Imaging

2.1.1 Introduction

Medical imaging consists of a number of methods and techniques used to aid diagnosis of disease or to plan disease treatment in patients. The different imaging modalities can be subdivided in two groups. Among one group are X-ray radiography, CT, magnetic resonance imaging (MRI), and ultrasound (US) imaging. These modalities are used mainly for anatomical imaging. The other group contains the modalities used for functional imaging, such as planar scintigraphy, SPECT and Positron Emission Tomography (PET). Each of these modalities has its own advantages but also disadvantages. Therefore, patients are often imaged using multiple modalities in order to combine the best of both worlds.

In CT imaging, X-rays are used to image the structural information inside the patient's body. An X-ray source rotates around the patient, sending X-ray radiation to a detector on the other side of the patient. Part of the X-rays will be absorbed by the patient tissues due to the photoelectric effect. Thus, less photons will arrive at the detector than originally emitted by the X-ray source. The ratio between the number of photons emitted and the number of photons detected is a measure of photon attenuation, which is related to the density of the tissue and thus contains anatomical information. The X-ray attenuation data obtained from different projection views around the patient can be reconstructed into cross-sectional images containing the attenuation coefficients of the patient at that position. The imaging principle, important hardware components, image degrading effects, reconstruction algorithms and the challenges encountered in CT imaging are further explained in Section 2.2.

In SPECT imaging, functional information is gathered from the spatial distribution of a radioactive compound or tracer. This information is carried by gamma (γ) rays. The radioactive tracer is injected intravenously into the patient and is used in metabolic pathways in the patient's body. Because of radioactive decay, γ-rays will be emitted by the tracer. By detecting the γ-rays outside the patient, the spatial tracer distribution can be mapped in 3D by a reconstruction algorithm. In SPECT, the information recorded is thus related to functional processes of the body. This will be further explored in Section 2.3.

Several other 3D medical imaging modalities are also commonly used in clinics. Positron Emission Tomography (PET) is a second molecular

imaging modality which uses an internal, injected source, like SPECT. However, the radioactive tracer will emit positrons instead of γ-photons. The positrons will annihilate with an electron (the positron antiparticle) to generate 2 back-to-back γ-rays. Here, the recorded information is also related to functional processes of the body, based on the detection of the γ-rays.

In Magnetic Resonance Imaging (MRI), a magnetic field aligns the magnetic moments of ensembles of protons with the magnetic field direction. The magnetization alignment can then be altered by a radio frequent (RF) pulse excitation. When this RF pulse is turned off, the protons will return to their original alignment. This results in a changing magnetic flux density, which induces a small current in receiver coils around the patient. The RF signals serve as the information carrier, and allow the localization of protons. Because proton density depends on the tissue, anatomic information can be imaged. However, it is also possible to record functional information with MRI, because oxygen-poor and oxygen-rich blood have a different magnetic susceptibility. These differences will induce small magnetic field distortions in the blood and the surrounding extra-vascular area, which is reflected in the decay process of water protons in these areas. This allows fMRI to also image brain activity.

Finally, a last modality is ultrasound (US) imaging. Different from the previously mentioned modalities, US does not use electromagnetic (EM) but pressure waves as its information carrier. After these pulses are generated by a transducer or probe, the ultrasound waves will be reflected mainly due to reflectivity changes at the edges in between different tissue types. US imaging thus provides anatomical information. The US transducer serves both as a source as well as the detector of these waves.

2.1.2 Preclinical arena

Apart from the use of medical imaging for clinical diagnostics and therapy, those imaging modalities can also be used to accelerate the transfer of laboratory discoveries into clinical practice. The growth of the pharmaceutical and biotechnology industries and advances in genetic engineering and molecular biology have led to an increased need for biological studies on small animals, primarily mice and rats. Animal models are now available for a wide variety of biological conditions. Transgenic animals currently account for a sizable and still growing fraction of animal models used in biological research. The most recent report from the

EU member states presents the use of around 11.5 million experimental animals in 2011, of which 60.9% mice and 13.9% rats [1].

Traditional investigative techniques include histology and organ sampling, which require the animals to be sacrificed. This precludes researchers to investigate longitudinal effects in the same animal, e.g. to measure the evolution of one parameter over time under influence of a therapeutic intervention. This means subgroups of control and experimental animals are needed, which in turn greatly increases the number of animals needed. This does not comply with the ethical conduct for animal experimentation.

To satisfy the needs for preclinical scanners, all clinically available medical imaging devices have been miniaturized into small-animal specific scanners. The main advantage of these scanners is the increased spatial resolution that can be achieved, e.g. by using large magnification in micro-CT, or by using pinhole magnification in micro-SPECT. Micro-PET, micro-MRI and micro-US systems have also been designed and commercially available. The specifics of micro-CT and micro-SPECT will be explained further in their respective Sections 2.2.7.3 and 2.3.6.

2.1.3 Physics

Although the information obtained in CT and SPECT is carried by waves, the information itself is the result from interactions of these waves with matter (in case of CT), or the origin of the waves (in case of SPECT). Because of its importance for the rest of this dissertation, this section will be used to explain the interaction mechanisms of γ-rays and X-rays with matter in more detail.

Figure 2.1 illustrates the different types of electromagnetic (EM) radiation. The various types can be uniquely distinguished by their energy, wavelength or frequency.

The energy E of a wave with wavelength λ is related to its frequency f by

$$E = hf = \frac{hc}{\lambda}, \tag{2.1}$$

with c the speed of light and Planck's constant $h = 6.62606957 \times 10^{-34}$ m^2kg/s. EM waves are thus uniquely determined by energy, most often identified as such in medical imaging. From now on, we will only refer to X-rays and γ-rays by referring to their specific energy in unit electron-

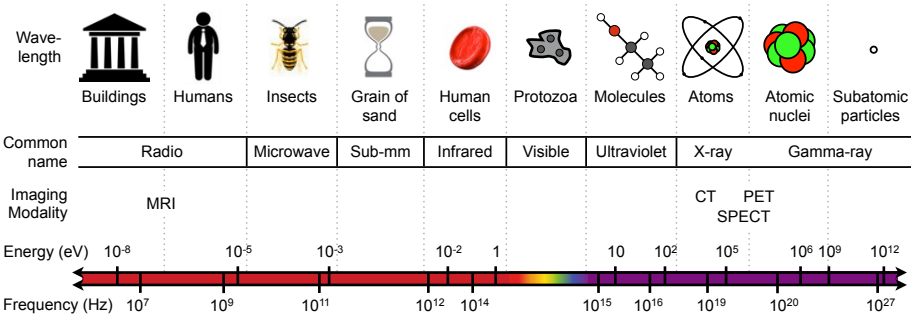

Figure 2.1: The EM spectrum with the different energy bands grouped by their commonly used names and imaging modality, a representation of their wavelength, the frequency and photon energy.

volt (eV). Although γ-rays typically have an energy above 100 keV, in the medical community they are defined as rays originating from radioactive decay. This means that there is no actual lower limit to their energy.

A property of EM waves that is very important for its use in medical imaging, is the penetration depth. Depending on the photon energy, some photons will penetrate tissue better than others. For photon energies in the band of X- and γ-rays, higher energies generally allow for deeper penetration. Photons with low energy and thus a shallow penetration depth will not be able to travel through the object under study and may be attenuated. On the other hand, highly-energetic photons may fully penetrate the patient without interacting with the patient's body. In CT imaging, the goal is to measure the attenuation of the X-rays by matter. Therefore, X-rays with an energy between 10 and 140 keV are commonly used. In SPECT, higher energy photons are generally used (up to 364 keV), so that the photons are attenuated as little as possible, but can still be detected outside the patient.

The different interaction mechanisms are illustrated on Figure 2.2. The two interaction mechanisms dominant in CT and SPECT imaging are photoelectric absorption and Compton scattering, and will be explained next. Although other photon interactions also exist (e.g. pair-production), these will not be further elaborated on because they are not relevant for the energies used in CT or SPECT imaging.

Photoelectric absorption

Photoelectric absorption, the resultant of the photoelectric effect[1], oc-

[1]First explained by Albert Einstein in 1905, for which he received the Nobel Prize

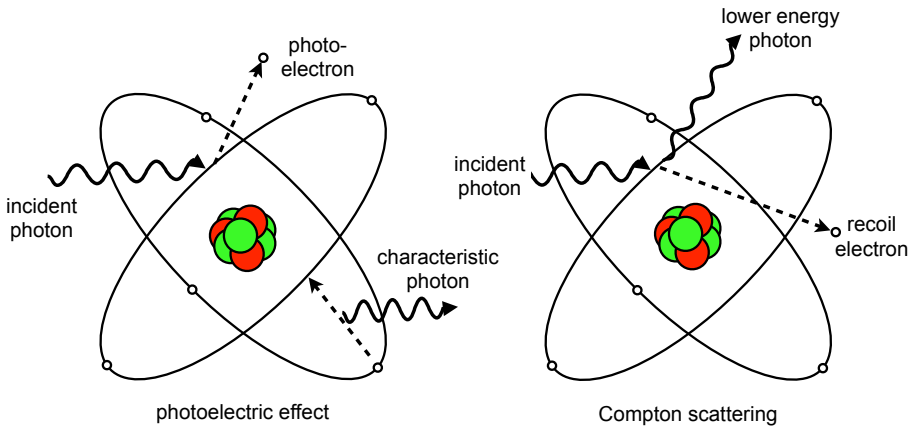

Figure 2.2: Illustration of the photoelectric effect and Compton scattering, two possible interactions of electromagnetic waves with matter.

curs when an inner shell electron bound to an atom absorbs an incident photon. The electron will absorb the photon, and if the energy of the incident photon is high enough, this electron is liberated and ejected from the atom. The photon ceases to exist, and the energy not needed for electron liberation will contribute to the ejected electron's kinetic energy. The vacancy created by the ejected electron will be filled by an outer-shell electron with higher energy (the Auger effect). This results in a release of energy either through photon emission (characteristic radiation), or through ejection of another electron (Auger electron).

The end result of photoelectric absorption is thus a positive ion (the atom with one electron removed), a photoelectron (the ejected electron), and one or more photons with characteristic energies.

The probability of the photoelectric interaction P_ϕ is roughly inversely proportional to the photon energy cubed:

$$P_\phi \propto E^{-3}. \tag{2.2}$$

Additionally, P_ϕ is also proportional to the cube of the atomic number Z:

$$P_\phi \propto Z^3. \tag{2.3}$$

in Physics in 1921.

Compton scattering

Scattering is a second way in which photons can interact with matter. Most important is the Compton effect[2]. Here, the energy of an incident photon is considerably higher than the binding energy of the electron. The photon will strike the electron and free it from the atom. However, instead of contributing all of its remaining energy to this photoelectron (as with the photoelectric effect), the photon will not cease to exist and will be deflected or scattered with partial loss of its initial energy.

The end result of the Compton effect is a positive ion (the atom with one electron removed), a recoil electron, and a scattered photon. Although the scattered photons may be deflected at any angle between 0 and 180°, low energy photons will have a larger probability of being backscattered (an angle larger than 90°) than photons of higher energy.

After deflection, the scattered photon may interact with matter again through any of the described interactions. The scattered photon retains most of its energy through Compton scattering, and loses energy depending only on the scattering angle and the original photon energy. Each step in a cascade of Compton scattering events will increase the probability of photoelectric absorption, because the photon lost some energy (Eq. 2.2).

The probability of Compton scattering (P_θ) is roughly proportional to the photon energy E [2]:

$$P_\theta \propto \frac{1+E}{E^2}\left(\frac{2(1+E)}{1+2E} - \frac{\log(1+2E)}{E}\right) + \frac{\log(1+2E)}{2E} - \frac{1+3E}{(1+2E)^2}. \tag{2.4}$$

A second form of scattering, but less important for medical imaging, is Rayleigh scattering (also known as coherent scattering or elastic scattering). Here, no energy is converted into another form, and ionization does not occur. The incident photon simply induces vibrations in the surrounding electrons, which will emit radiation at the same wavelength as the incident photon.

Figure 2.3 plots the contributions of the different physical interactions of photons with matter between 1 keV and 10^5 MeV. Only the part between 10 and 300 keV is routinely used in CT and SPECT imaging (illustrated by the gray band). The photoelectric effect contributes most to the total attenuation below 30 keV in water and below 300 keV in

[2] After Arthur Holly Compton, who received the Nobel Prize in Physics in 1927 for its discovery.

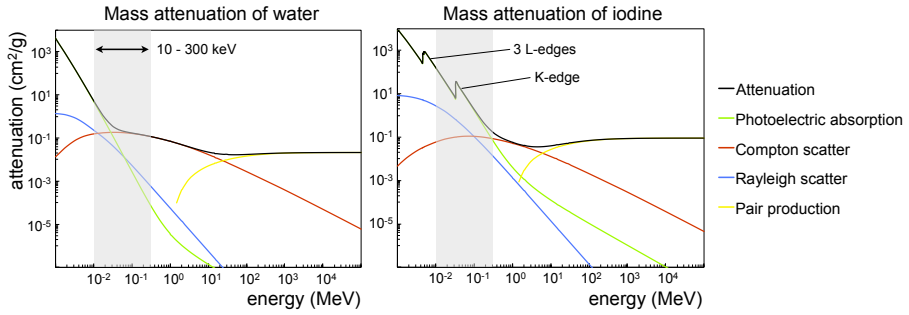

Figure 2.3: The contributions of different physical interactions with matter to the total mass attenuation coefficient for water and for iodine.

iodine. Above those energies but below 10 MeV, Compton scatter is the dominant effect.

Basics of X-ray imaging

In X-ray radiography and CT imaging, structural information is gathered with X-rays by measuring the attenuation of X-ray photons through matter. The total attenuation encountered by an X-ray beam will be primarily caused by the photoelectric effect and Compton scattering, due to the relatively low energies used in X-ray imaging (generally below 140 keV).

According to the Bouguer-Lambert-Beer Law, the intensity of a monochromatic EM wave (and thus also X-rays and γ-rays) passing through material with absorption or attenuation coefficient μ (unit cm^{-1}) and thickness d (unit cm) will fall off exponentially as

$$I = I_0 e^{-\mu d}. \tag{2.5}$$

Here, I_0 is the intensity of the photon beam before going through the material or tissue. If I_0 is known (e.g. by measuring the attenuation of air), a measured value I can be directly related to the attenuation caused by the tissue.

The photoelectric effect may seem to generate a lot of information about the atoms involved, due to the proportionality to Z (Eq. 2.2) and the emission of characteristic X-rays. However, the characteristic X-rays produced by the photoelectric effect have an energy in the order of 500 eV in tissue-like materials. These X-rays will not travel much further than the dimension of a typical human cell [3]. The characteristic X-rays pro-

duced in an object will thus be reabsorbed. The only useful information thus stems from the absorption or attenuation of the photons.

Both Eq. 2.2 and Eq. 2.3 lead to an important insight. Heterogenous tissue with small differences in atomic numbers may produce a large probability difference of photoelectric interactions. Because the photoelectric effect is also inversely proportional to the cube of the photon energy, low-energy photons will be most important for low-contrast differentiation in CT imaging.

The tissue contrast can also be enhanced by using contrast agents. X-rays with an energy just below the binding energy of a shell electron will have a much lower absorption probability than photons with an energy just above the binding energy. This effect is most prevalent with K-shell electrons of metals, which have an especially convenient binding energy because they are located close to the mean X-ray energy spectrum. Examples of useful metals for CT contrast agents are iodine (33.2 keV), barium (37.4 keV) or even gold (80.7 keV). The quoted energies are referred to as the K-edge of that material. Figure 2.3 illustrates the contribution of the K-edge of iodine to the total attenuation at an energy above 33.2 keV. The 3 L-edges at 4.56, 4.85 and 5.19 keV are not useful for CT imaging because of their very low energy.

Apart from an attenuating effect caused by photoelectric absorption and Compton scattering, the X-rays may also be scattered and still be detected outside the patient. Unfortunately, these scattered X-rays do not give us much useful information about the patient, as the photon will have changed its path and will have lost some of its energy. This means that the attenuation along the path of this ray can not be determined anymore. Scattered photons are thus unwanted in X-ray and CT imaging. Consequently, it is important to minimize the impact of Compton scattering.

CT imaging will be explored in more detail in Section 2.2.

Basics of γ-ray imaging

In contrast to X-ray imaging, the goal of γ-ray imaging is to localize the injected radioactivity that emits the γ-rays. Thus, it would be ideal to not have any interactions inside the patient before the γ-rays can leave the patient body. Attenuation will decrease the amount of photons detected outside the patient compared to the amount of photons really emitted, and will result in higher noise.

Also γ-rays will be influenced by Compton scattering. As mentioned

above, Compton scattered photons can not be used to gather useful information about the patient. This means scattered photons are equally unwanted in SPECT as in CT imaging. Therefore, also in SPECT some counter measures will be taken to limit the contribution of scattered photons to the detected data.

Emission tomography and SPECT imaging will be explored in more detail in Section 2.3.

2.2 Computed Tomography (CT)

2.2.1 Early History

The history of CT starts with the discovery of X-rays by Wilhelm Conrad Röntgen, who accidentally generated the well-known first radiographic image of his own hand in November 1895[3]. The first diagnostic X-ray examination was made 3 months later, to observe an ulna fracture in 14-year old Eddie McCarthy [4] (Fig. 2.4a). In June 1896, X-rays were already being used to locate bullets in wounded soldiers. In parallel, Nikola Tesla also investigated X-rays from 1894 onwards [5], inventing his own vacuum tube along the way. He managed to make what he called shadowgraphs of the human foot in 1896 (Fig. 2.4b). Nikola Tesla, Thomas Edison and William J. Morton each reported eye irritation from X-ray experiments, postulating a first warning of X-ray radiation damage [5].

A fundamental limitation with conventional radiography is that it can not be used to determine depth information, because it is a 2D projection of a 3D object. This effect is called the superposition principle and is visible on Fig. 2.4b, where the different mid-foot bones can not be distinguished from each other because they are all projected onto the same location onto the detector.

A recognition of this limitation lead to the use of multiple planar images, taken along different angles. Combining these different images allows us to determine some depth information. In 1940, Gabriel Frank was awarded a patent describing the ideas of tomography, where planar projection images are acquired 360° around the patient. Takahashi developed the equipment to reconstruct the set of projection views (called a sinogram) into a cross-sectional image of the patient, although they did not yet get the reconstruction technique completely right.

[3] For which he was awarded the very first Nobel Prize in Physics in 1901.

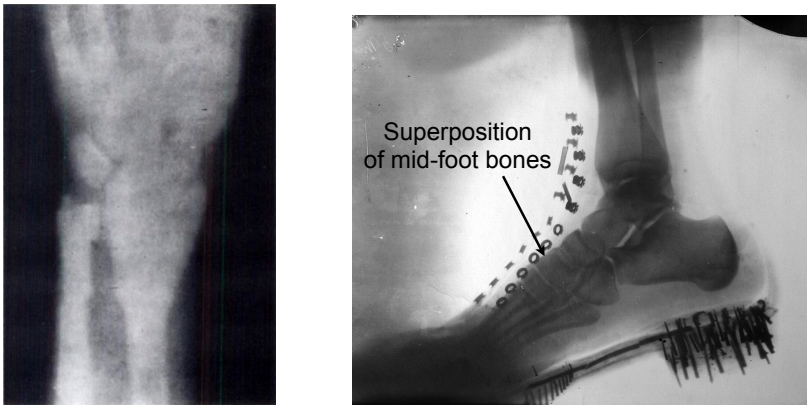

(a) (b)

Figure 2.4: First radiographs. (a) Photograph of original plate of first diagnostic X-ray examination, showing an ulnar fracture (taken from [4]). (b) Shadowgraph of a human foot in a shoe (Courtesy of the Tesla Museum, Belgrade, Serbia; document no. MNT, VI/II, 122 [5])

Experiments by Allan M. Cormack in 1963 and Godfrey N. Hounsfield in 1967 lead to the first table-top CT scanner[4] made at EMI, Ltd. in England. The first prototype clinical CT scanner was installed in 1971, and was used for the first time to image a cerebral cyst patient. In 1975, Hounsfield built the first whole-body scanner. Eventually, CT scanners evolved in geometry through different generations, with the third-generation CT still used in nearly all commercially available scanners today. In 1982, the first micro-CT devices were built to investigate the 3D distribution of mineral in bone at high resolution [6, 7], with the first *in vivo* imagers available in the early 2000's.

2.2.2 Imaging Principle

Comparable to X-ray radiography, CT imaging is used to study the patient anatomy, based on measurements of X-rays attenuation. However, instead of using only one planar image, a series of planar images is acquired from different angles around the patient, in order to later reconstruct 3D information.

This acquisition process, called tomography, is illustrated in Fig. 2.5.

[4]Cormack and Hounsfield shared the 1979 Nobel Prize in Physiology and Medicine for their pioneering work in CT.

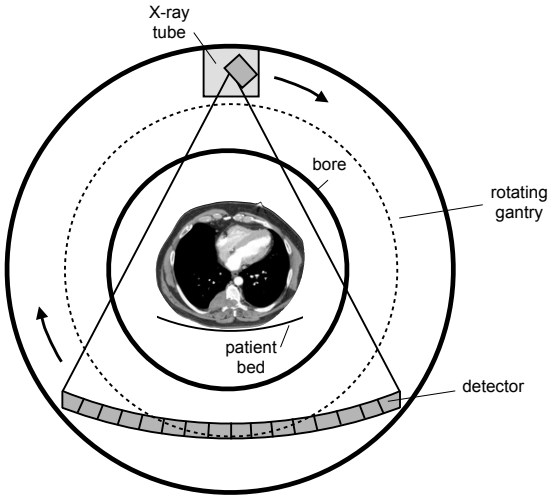

Figure 2.5: Illustration of the placing of CT scanner components.

An X-ray source – detector gantry rotates around the patient and emits X-rays in a fan-shaped fashion (fan-beam). This beam is directed towards an array of detectors, which convert the incident X-rays into electrical signals. For each rotation angle a different planar X-ray image or projection view is acquired, measuring the patient attenuation as seen from this angle. Following the acquisition of thousands of planar projections over multiple angles, the complete set of measured data can then be reconstructed into a set of 2D slices. These slices correspond to axial cross-sections through the patient. In this way, true 3D anatomical information can be obtained, useful for diagnostic purposes.

Figure 2.6 shows the reconstructed data acquired with a CT scan of the neck region after administration of a contrast agent. The reconstruction process generates transverse slices, which can then be resliced to form the sagittal or coronal slices, or even volume rendered with a color code attached to the voxel values. Bone is generally represented brighter than soft tissue to represent its higher attenuation value. There is only limited contrast between muscle and fat tissue, because both tissue types have similar attenuation values.

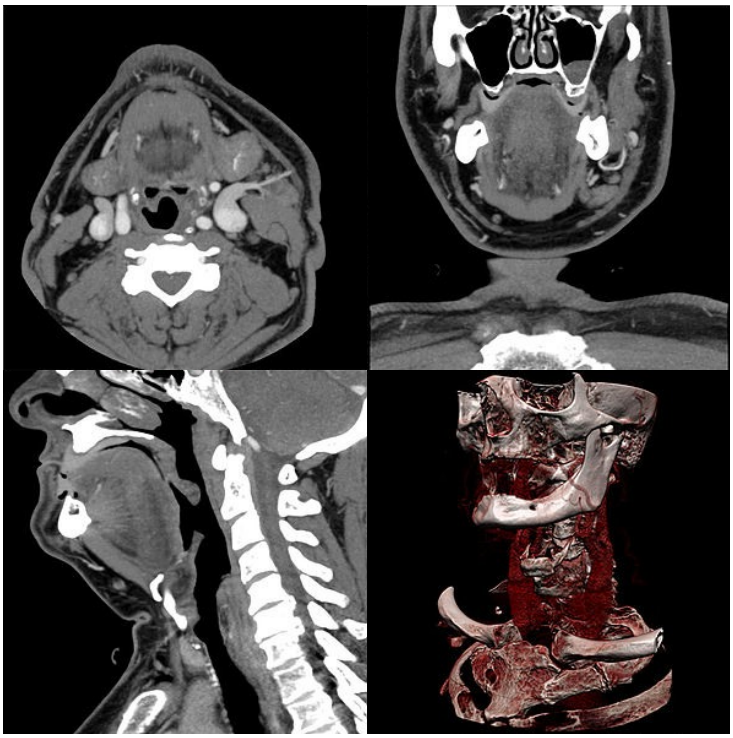

Figure 2.6: CT images obtained from the neck region. Clockwise from bottom-left: sagittal slice, transversal slice, coronal slice and volume rendering. (Image obtained from *http://commons.wikimedia.org/wiki/File:Ct-workstation-neck.jpg*, used under a Creative Commons Attribution-ShareAlike license: *http://creativecommons.org/licenses/by-sa/3.0/*)

2.2.3 Important Components

2.2.3.1 X-ray tube

Figure 2.7 depicts the X-ray tube, the source of the X-rays. The X-rays are generated by bombarding a target with high-speed electrons. These high-speed electrons are generated by heating a filament with a large electrical current (on the order of 100 μA for micro-CT, and the order of 100 mA for clinical CT). The heated filament will emit electrons due to the thermionic effect. When a large potential is applied between the filament (serving as cathode) and a dense target (the anode, usually made from tungsten or molybdenum), the electrons will be accelerated through the vacuum tube towards the target and will collide with it, generating X-rays through 2 interaction processes.

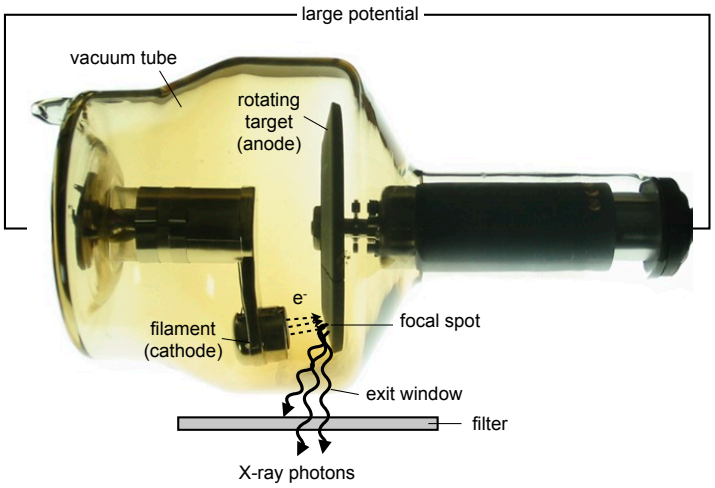

Figure 2.7: Inside workings of a Coolidge-type X-ray tube.

Unfortunately, 99% of the interactions do not actually result in X-rays but in delta rays, which are transferred as heat. In this case, the incident electron transfers its energy to electrons which are knocked out of their atom shell, ionizing the target atom.

Fig. 2.8 illustrates the 2 processes. The first and most prominent X-ray-generating interaction is bremsstrahlung. An incident electron will approach the nucleus of an atom and will be attracted by its positive charge. This attraction causes the electron to suddenly decelerate and lose a significant amount of kinetic energy. Because of the principle of energy conservation, a photon will be emitted with energy dependent on how deep into the atomic coulomb field the electron travels. This type of radiation will result in white radiation, covering the whole spectrum. When a direct collision occurs between the incident electron and the nucleus, the entire energy of the electron will appear as bremsstrahlung. Only a small portion of X-rays will be generated this way due to the low probability of a direct collision. This is the upper limit of X-ray energy that can be generated with the X-ray tube.

The second interaction process results in characteristic radiation. The electron does not pass by the nucleus, but collides with a shell electron. If its energy is larger than the binding energy of that electron, the shell electron will be ejected from its shell. Some energy will be transferred from the incident electron to the struck electron, energy which will eventually dissipate as heat. When electrons from an outer shell move into

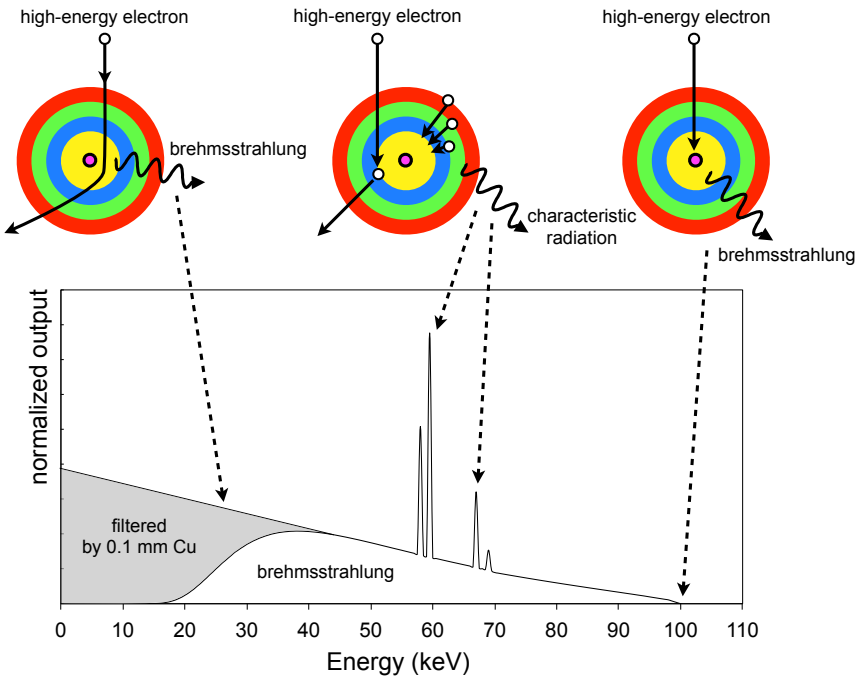

Figure 2.8: Illustration of electron interactions leading to a polyenergetic X-ray spectrum. The broad spectrum is the result of brehmsstrahlung, with low-energy X-rays which are easily filtered to pre-harden the beam. Characteristic radiation leads to peaks at specific locations in the spectrum.

the vacancy created by the ejected electron, they will emit a photon of characteristic energy. This energy is well-defined for each material, and depends on the difference in binding energy of the different shells. This type of radiation results in distinct peaks in the output spectrum.

Important to mention is the finite focal spot size of the tube. The accelerated photoelectrons will hit the target in an area of finite size, called the focal spot. This is mostly important in preclinical CT, where the focal spot size can be a limiting factor for resolution.

In a Coolidge-type tube, the heat generated by these interactions is dissipated by rotating the anode target continuously, distributing the area of electron bombardment over time. In the Straton-type tube design (developed by Siemens), the anode can be cooled directly by embedding it in oil. This creates a powerful tube with a much smaller footprint, and allowed the development of Dual-Energy CT (DECT) systems, as now two tubes could fit inside one scanner.

The latest tube research is focused on carbon nanotube (CNT) field emission tubes. An electric field is used to extract electrons right off the tip of a carbon nanotube (diameter a few nanometers), removing the need for a heated filament. This allows much faster on/off-switching of the X-ray tube than is currently possible, and may be ideal for small-animal motion-gated imaging [8].

The bottom part of Fig. 2.8 shows the theoretical spectrum obtained from a tungsten target with a potential of 100 kVp. Low-energy X-rays are filtered by the exit window of the tube (usually made from beryllium) together with additional filtration (e.g. with 0.1 mm of copper), which further hardens the beam and removes the low-energy photons. These photons would be attenuated the most by the patient, hence delivering almost no information to the detector, though still delivering a high percentage of the radiation dose. The specific choice of kVp depends on the size of the patient (e.g. 120–140 kVp for human patients, 50–70 kVp for small animals). The kVp is sometimes even modulated during the scan to minimize the radiation dose for each projection view. This will be further discussed in Section 2.2.7.1.

2.2.3.2 X-ray detector

The photons which passed through the patient are measured by an X-ray detector. The X-rays are detected by interaction mechanisms (Sec. 2.1.3) that convert the incident photon energy into a measurable quantity. Two detector types exist, either directly converting X-rays into an electrical signal, or with an additional conversion step (called indirect detection) [3]. Both methods are still in use in current state-of-the-art CT scanners, and are shortly discussed next.

Indirect conversion detectors

In indirect detectors, incident X-rays undergo photoelectric or Compton interactions with a scintillator, and release photoelectrons or recoil electrons. These electrons will move through the scintillator and will form a large number of electron-hole pairs. The positive holes migrate to activator sites and ionize them. When the moving electron encounters such an ionized activator site, it will de-excite and cause the emission of a photon with an energy of visible or UV light. Photons with these wavelengths can be detected by a sensor, which will integrate the light into an electrical signal only proportional to the deposited energy. This integration implies that energy information of single interactions is lost.

The most commonly used scintillators in CT are thallium-doped cesium-iodide (CsI:Tl), cadmium tungstate ($CdWO_4$), gadolinium oxysulfide (Gd_2O_2S, also known as GOS or Gadox), and the proprietary HiLight^{TM} [9] ($Y_{1.34}Gd_{0.60}O_3$:$(Eu,Pr)_{0.06}$) and Gemstone^{TM} [10]. These scintillators can be combined with different light sensors such as charge-coupled devices (CCD), complementary metal oxide semiconductors (CMOS) or amorphous silicon (a-Si) [11] sensors.

Direct conversion detectors

In direct conversion detectors, electron-hole pairs created from an incident X-ray photon will cause a direct change in a high-voltage electric field. Historically, the high-pressure inert gas (usually xenon) detectors have been the most popular. The gas is ionized by incident X-rays, from which the ions and electrons can be directly captured. The ionization quantity is linearly proportional to the X-ray intensity.

More common nowadays are the semiconductor or solid-state variants, usually made from cadmium telluride (CdTe), mercuric iodide (HgI), amorphous selenium (a-Se), or a-Si attached to a thin-film transistor (TFT) array.

Performance

Direct conversion detectors have the advantage over indirect detectors because there is one less step in the chain between X-rays and charge. This means that there is one less step to add noise [12], and that there is minimal spread inside the detector. This results in a high spatial resolution and high-quality images. However, the spread can be reduced in indirect conversion detectors by using columnar growth of the scintillator, common in e.g. CsI:Tl. Indirect detectors are also cheaper, as the CCDs are a more mature technology.

The choice of detector type and material depends on the performance demands for the specific CT tasks. Material choices will affect the detector stability over time, the detector blur which determines the achievable image resolution, and the detective quantum efficiency (DQE), which relates the statistical quality of the input signal to the statistical quality of the signal output [13]. A DQE of 0.5 means that the detector requires twice the irradiation dose to reach the same image quality as an ideal detector with DQE 1.

The DQE is determined by a number of factors, such as the detector material, the photon energy, and the physical thickness of the scintillator in the direction of the incident ray, but also by the dark current, photon

spread in the scintillator, decay time and afterglow. Thicker detectors generally have a higher DQE due to the increased probability for photoelectric absorption (stopping power), but may also lose resolution [14]. Detectors with a high dark current will have a lower DQE, which reduces the signal to noise ratio at low exposure.

In general, gas detectors will have inferior DQE to solid-state-sensor based systems [15], while solid-state-sensor based systems will exhibit unwanted long decay times and afterglow, and may even be susceptible to radiation damage [15]. a-Se detectors have a high DQE but are relatively unstable with regards to the exposure history of the detector, giving rise to image artifacts if not accounted for. Indirect detectors generally have a worse resolution than direct detectors, as the scintillator will introduce additional blurring. One example is using CsI:Tl instead of GOS, a change which improves the DQE by a factor of 2 without any resolution loss [13], thanks to its higher absorption efficiency and difference in conversion gain fluctuation in electron-hole pair creation (the Swank factor). It is clear that there is no perfect choice of detector and that this choice is highly task-dependent.

2.2.4 Measurement Process

In CT imaging, planar images (projection views) are recorded from different angles around the patient with the ultimate goal of reconstructing the 3D attenuation distribution in the patient. For each projection view the X-ray flux reaching the detector is recorded, after being attenuated by the object. If the object is represented by different materials of thickness d and attenuation μ (mass attenuation times density), the X-ray beam intensity measured by the detector will follow the Bouguer-Lambert-Beer law (Eq. 2.5):

$$I = I_0 e^{-\int_L \mu(x)dx}, \tag{2.6}$$

with straight line L the path followed by the X-ray.

The sinogram can be used in the reconstruction algorithm as is, or after transforming I to log-attenuation

$$\int_L \mu(x)dx = \log I_0 - \log I, \tag{2.7}$$

with I_0 the detected value from an acquisition without an object present

(called a blank scan or air scan). This is a measure of the emitted number of photons. This model is only valid for mono-energetic X-rays, which are impossible to emit by a process based on brehmsstrahlung.

A more realistic model is one with an integration over the polyenergetic spectrum E and the heterogenous object over the X-ray path:

$$I = \int_0^{E_{max}} I_0(E) e^{-\int_L \mu(x,E)dx} dE, \tag{2.8}$$

with $I_0(E) = I_s(E)\eta(E)$ the product of the emission spectrum and $\eta(E)$ the quantum efficiency of the detector at energy E.

A problem with this realistic model is that $I_0(E)$ is unknown with respect to E, as current CT detectors do not allow for energy discrimination, but are energy-integrating detectors. This means only $\int_0^{E_{max}} I_0(E)dE$ is known, so that the log-attenuation can not be accurately computed. The mismatch between the realistic model, and the model commonly used in reconstruction (based on Eq. 2.6) will lead to artifacts. These are discussed in the next section.

2.2.5 Image degrading effects

Before going into detail on how the cross-section slices are actually reconstructed from the projection views, some common image degrading effects should be explained. These effects will cause changes in the measured data, in turn leading to systematic discrepancies (commonly called artifacts) between the reconstructed CT values and the true attenuation coefficients μ of the patient [16].

2.2.5.1 Beam Hardening

Because the X-rays are produced in the X-ray tube mainly by bremsstrahlung (Sec. 2.2.3.1), the X-ray beam is poly-energetic and not mono-energetic. While the X-ray beam passes through the patient body, it will become progressively *harder*: low-energy photons have a higher probability of being attenuated than the higher-energy photons, due to the energy-dependent photoelectric effect. This means that the exit X-ray spectrum will be different from the spectrum leaving the X-ray tube, and this difference is patient-specific. Unfortunately, CT detectors can not measure in energy-discriminating mode, which means that the term

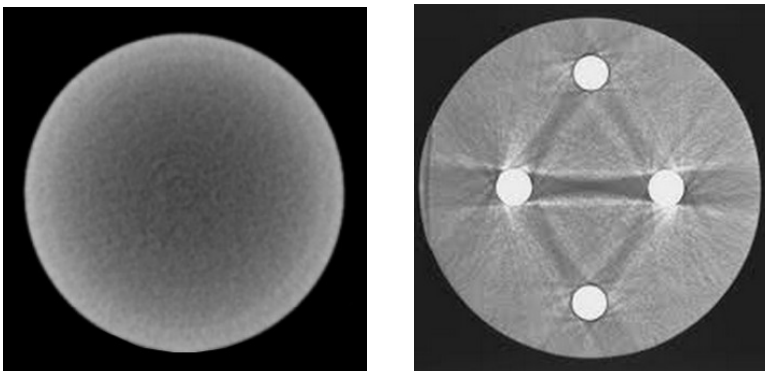

(a) (b)

Figure 2.9: The effect of beam hardening on image quality. (a) Cupping artifact in a uniform water phantom. (b) Streaks between dense objects.

$I_0(E)$ from Eq. (2.8) can not be measured in a blank scan without integrating over E.

This discrepancy between the real acquisition model and what can actually be measured gives rise to two well-known artifacts. In the cupping artifact the values in the center of the reconstructed image will have a lower value than those at the edge of a homogenous object, because rays through the center have been hardened more than rays going through an off-center part. The second artifact is the appearance of dark bands (also called streaks) between dense objects. The beam is hardened more in one direction compared to the beam measured from a different angle. This can be especially apparent in bony regions or when a contrast agent is used. An example of both artifacts is given in Fig. 2.9.

Several methods have been proposed to minimize the effect of beam hardening. One method involves using a filter between the X-ray tube and the patient to pre-harden the beam, filtering out the low-energy components before reaching the patient [17]. An added benefit is that this method also reduces the X-ray dose to the patient. A drawback is that the soft-tissue contrast will also decrease, because less low-energy photons will be present in the spectrum.

A second commonly used correction method is the application of polynomial correction on the measured data, with coefficients based on calibration scans. This is based on the correlation between the detected attenuation value of water phantoms of different thicknesses, and the X-ray path lengths these values were measured along. Values measured

from longer paths will need to be corrected to reach the correct attenuation value. Although such a technique reduces the beam hardening considerably, its accuracy depends on the resemblance between the patient and the calibration phantoms (the water phantoms of varying diameter), which is not always good [3].

2.2.5.2 Photon Starvation

Because of the very high density and the high mass attenuation of some materials (e.g. dense bone, contrast agent or metal), insufficient photons may reach the detector after passing through areas containing these materials. This greatly increases the statistical uncertainty of the measured data, and leads to significant streaking artifacts in the reconstructed images. This can be overcome by increasing the tube current, but this would also increase the radiation dose given to the patient.

2.2.5.3 Photon Scattering

Whereas beam hardening and photon starvation are manifestations of photoelectric absorption, photon scattering is a result mainly of Compton scattering in CT (Sec. 2.1.3). Because of the Compton effect, not all X-rays will travel in a straight line from the focal spot to a detector pixel, but may deviate from their path. The deflection angle of the scattered photon is random within an angular distribution determined by the photon energy (the Klein-Nishina distribution [18]). Unfortunately, CT detectors can not discriminate between energies, which means no information can be obtained from the scattered photons. When these photons are combined with the primary, unscattered photons, the composite signal will be a projection with reduced contrast due to the extra background signal. This process is illustrated in Fig. 2.10a.

The ratio of scattered photons intensity to the primary photons intensity is called the scatter-to-primary ratio (SPR). A 16 cm cylindrical phantom (representing the human head) will result in an SPR of 1 in clinical CT, increasing to 4 to 5 for a 32 cm cylindrical object (body) [19]. The SPR in cone-beam micro-CT systems is around 0.3 to 0.5 [20, 21].

In clinical CT, scattered radiation is physically stopped before reaching the detector by a collimator or anti-scatter grid with septa focused at the focal spot (Fig. 2.10b). Although the improvement of the contrast-to-noise ratio (CNR) due to use of a grid has been proven for high-scatter conditions, its usefulness is questionable for low-scatter conditions [19].

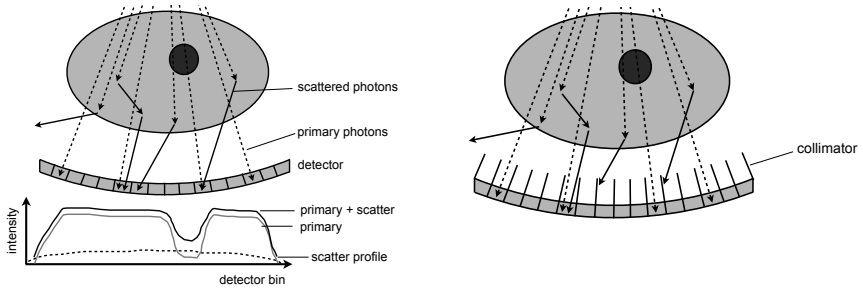

(a) The effect of photon scattering

(b) A collimator or anti-scatter grid reduces scatter detection.

Figure 2.10: The effect of photon scattering in CT.

The grid septa will stop both scattered photons as well as primary photons, possibly reducing the CNR when SPR is decreased [22]. Due to the small pixel size used in micro-CT, it is difficult to manufacture a scatter-grid for those systems.

Software correction schemes can also minimize the influence of scatter on the image quality. Because the scattered signal is typically composed of low frequencies, it can be estimated by extrapolating from only some detector cells outside the primary X-ray beam [23, 24], or from Monte Carlo simulations [25]. The scatter fraction can then be incorporated into iterative reconstruction.

2.2.5.4 Aliasing

A different image deteriorating effect is caused by using a limited number of projections or number of detector elements to sample the object. The X-ray beam intensity incident on the detector has a continuous distribution, and is sampled discretely by detector pixels and projection views. According to the Nyquist-Shannon sampling criterion, it is required that the discrete samples are collected at a rate of at least twice the highest spatial frequency contained in the continuous signal. This means that the highest resolvable spatial frequency is assumed to be limited by the physical size of the detector channel [3].

When the Nyquist-Shannon theorem is not fulfilled, aliasing streaks will appear in the reconstructed images. One approach to combat aliasing artifacts is to apply a quarter-pixel offset to the detector. Two samples taken on either side of the object (gantry rotation of 180°) will then

interleave each other, effectively doubling the sampling rate [26]. A different approach is to deliberately wobble or deflect the X-ray focal spot to not achieve two identically sampled datasets on either side of the object [27, 28]. Evidently, both techniques can also be combined to increase the effective sampling rate even further.

The same principle also applies to the number of projection views. It has been shown that a relationship exists between the sampling frequency v, the frequency contents of the object, and the size R of the aliasing-artifact-free zone. For fan-beam CT, the minimum number of projection views N_{min} over 360° needed to sample a maximum spatial frequency v_M present in a reconstructed image is [29]

$$N_{min} = \frac{4\pi R v_M}{1 - \sin\left(\frac{\Psi}{2}\right)}, \tag{2.9}$$

with Ψ the full fan-angle. For a size $R = 16$ cm and a fan-angle of 55°, a relatively low resolution of 1 line-pair per mm will already necessitate more than 3.700 projection views over 360°. Increasing the spatial resolution to 5 line-pairs per mm (or 100 μm) leads to more than 18.000 projection views. It is obvious that, in practice, the view aliasing guidelines are seldom strictly followed, and careful experiments must be conducted to establish view-sampling requirements under (pre)clinical conditions [3]. A clinical CT scanner typically acquires around 1000 views per gantry rotation of 0.3 seconds, which means 20.000 projection views can be acquired during one breath-hold of 6 seconds, with an axial FOV equal to the axial detector size.

Figure 2.11 illustrates the detrimental effect of view aliasing on image quality. The data was acquired from a contrast-enhanced murine micro-CT scan. Under-sampled data was reconstructed from 57 views taken over 180° and is shown next to quasi-noiseless data, obtained by reconstructing 1800 projection views acquired over 180°. The under-sampled data exhibits radial lines emanating from bony structures, severely degrading the image quality.

2.2.6 Reconstruction

After the interaction of the X-rays with the patient body and subsequent detection of the attenuated X-ray beam, one important step is left: the set of measurements needs to be reconstructed into cross-sectional slices representing the attenuation distribution inside the patient.

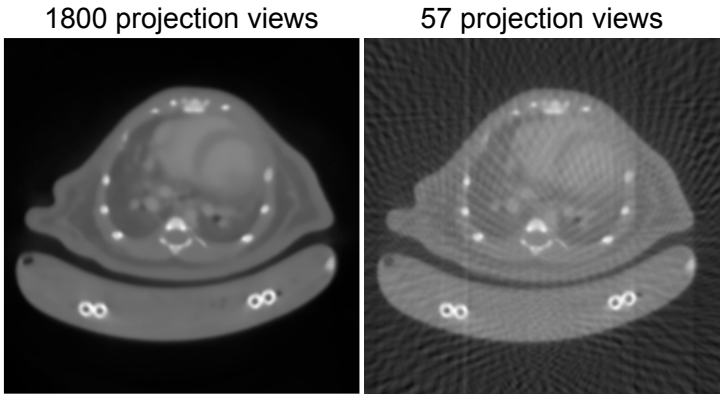

Figure 2.11: The effect of view aliasing. (Left) Reconstruction of 2048 projection views. (Right) Reconstruction of 32 projection views.

2.2.6.1 Simple Backprojection

The mathematical foundation used to reconstruct projection data into cross-sections dates back to the work of Johann Radon in 1917 [30]. Radon proved that an object can be reconstructed exactly from an infinite number of projections, when taken over 360° around the object.

In 2D, t he measurements can be mathematically represented by the Radon transform, taking line integrals along straight lines $L_{r,\theta}$ through the object (Fig. 2.12):

$$p(r,\theta) = \mathcal{R}\{f(\mathbf{x})\} = \int_{L_{r,\theta}} f(\mathbf{x})|d\mathbf{x}| \tag{2.10}$$

where $f(\mathbf{x})$ is the object under study, representing the attenuation of the object under study at spatial location $\mathbf{x}$, and each line L is parameterized over the detection location r and the angle to the origin θ.

There are several approaches to determine the unknown $f(\mathbf{x})$ from the scanner output p (reconstruction). The most simple method, although mathematically incorrect, is backprojection:

$$f(\mathbf{x}) = \mathcal{R}^*\{p\} = \int_0^\pi p(r,\theta)d\theta. \tag{2.11}$$

Each measurement $p(r,\theta)$ is redistributed over an image by uniformly adding each measurement to the locations along its corresponding line

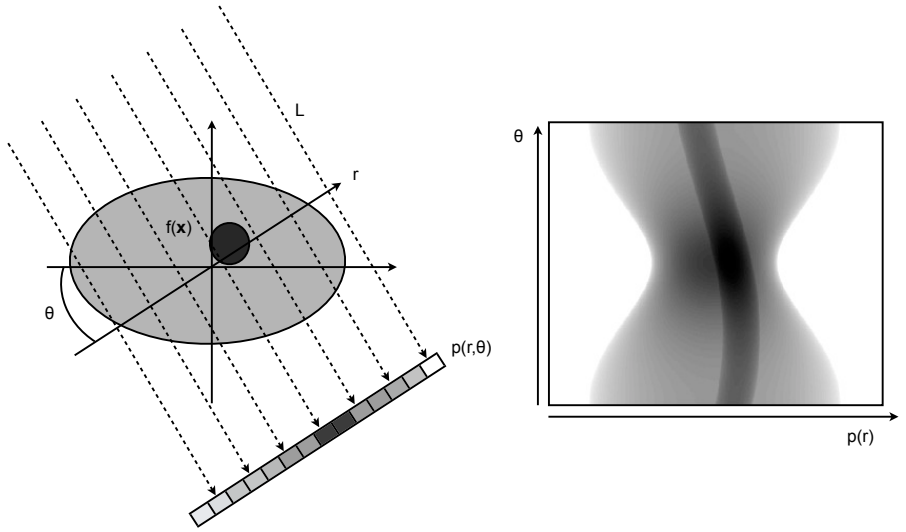

Figure 2.12: The Radon transformation and its resulting sinogram for the first 180°.

$L(r, \theta)$. As can be seen in Fig. 2.13, simple backprojection will only lead to a blurred version of the original distribution $f(\mathbf{x})$ [5]. Based on this observation, Filtered Backprojection was developed.

2.2.6.2 Filtered Backprojection

The blur can be compensated by filtering the projection data p in a preprocessing step. This is most easily done in the Fourier domain, based on the central slice theorem, which is illustrated in Fig. 2.14. This theorem states that

> The 1D Fourier transform of a parallel projection of an object $f(\mathbf{x})$ obtained at an angle θ equals one line in the 2D Fourier transform of $f(\mathbf{x})$ at the same angle θ.

In other words, when a projection is taken along different lines L_r for a projection angle θ, a 1D Fourier transform can be applied to obtain one radial line in the Fourier domain of the object. If the entire Fourier domain is filled (i.e. by collecting enough projections $\forall\theta \in]0, 2\pi]$), the object can be recovered by an inverse 2D Fourier transformation.

[5] The reason why Frank and Takahashi's reconstructions did not work correctly in 1940 (see Sec. 2.2.1)

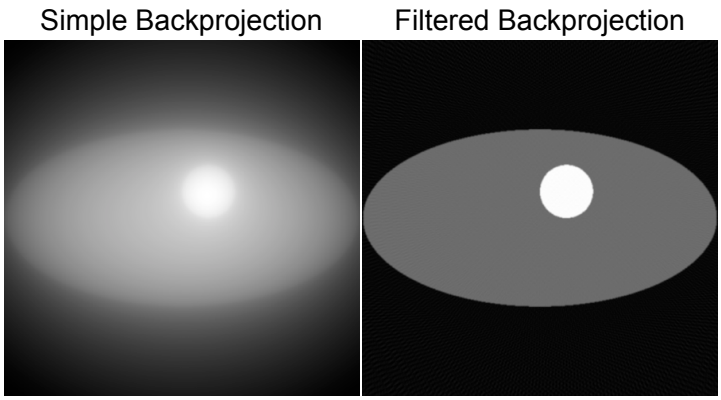

Figure 2.13: Illustration of the difference between simple backprojection and filtered backprojection.

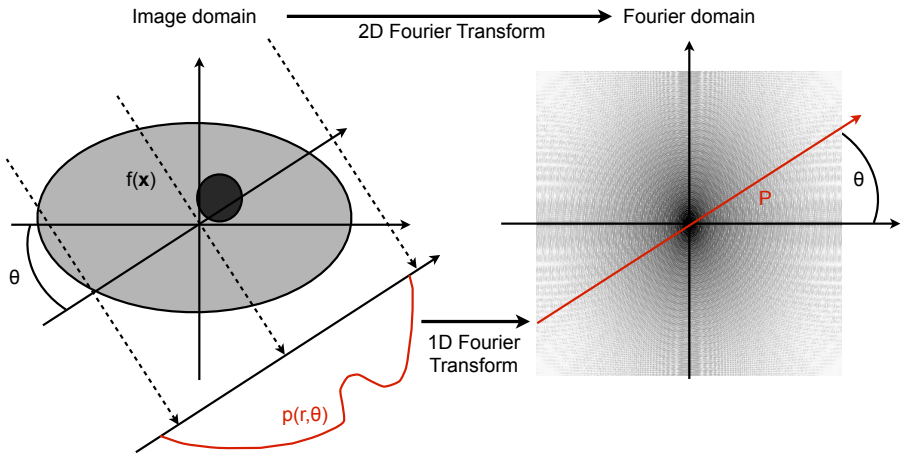

Figure 2.14: Illustration of the central slice theorem.

Fig. 2.15 illustrates the origin of the extra blur in Fourier space. As a projection is equal to a line through the origin in the 2D Fourier space, it will result in a radial sampling pattern. This means that the density of samples near the center is a factor $1/r$ higher than at the outer regions, with r the radial distance to the center.

Uniform sampling density can only be obtained if the Fourier transform of each projection is multiplied by a ramp filter proportional to this $1/r$ factor. If the radial lines are afterwards 1D inverse Fourier transformed, one can obtain data pre-corrected for the blur, which does allow for simple backprojection. This is the technique used in Filtered Backprojection (FBP). Mathematically, a filter q is used:

$$f(\mathbf{x}) = \mathcal{R}^*(q * \mathcal{R}\{f(\mathbf{x})\}), \tag{2.12}$$

whose Fourier transform is

$$\hat{q}(\omega) = \left|\frac{\omega}{2\pi}\right|, \tag{2.13}$$

and $\mathcal{R}^*$ is the back-projection operator (the adjoint of $\mathcal{R}$). The convolution of q with sinogram $\mathcal{R}\{f(\mathbf{x})\}$ is done per projection $p(r, \theta)$.

The filter q can be further modified to have improved spectral characteristics, e.g. by using a scaled version h:

$$\hat{h}(\omega) = \left|\frac{\omega}{2\pi}\right| \hat{\Omega}(\omega), \tag{2.14}$$

with $\hat{\Omega}(\omega)$ a suitable spectral window (e.g. sinc filter, Shepp-Logan filter, cosine filter, Parzen filter, a Hamming window, Hann window, ...). Different filters can change the quality of the reconstructed image in terms of noise, resolution, contrast and other measures [31].

The central slice theorem also suggest the use of more direct Fourier methods. If the full 2D frequency space is 2D inverse Fourier transformed, the object is reconstructed directly. However, the inverse 2D Fourier transform can only be applied to a Cartesian grid, necessitating resampling the implicit polar grid into a Cartesian one. The accuracy of the resulting reconstruction technique will depend heavily on the quality of the interpolation method used, and may end up less accurate than FBP.

Because FBP was originally defined for 2D objects measured by a parallel-beam geometry, several extensions have been made to make FBP

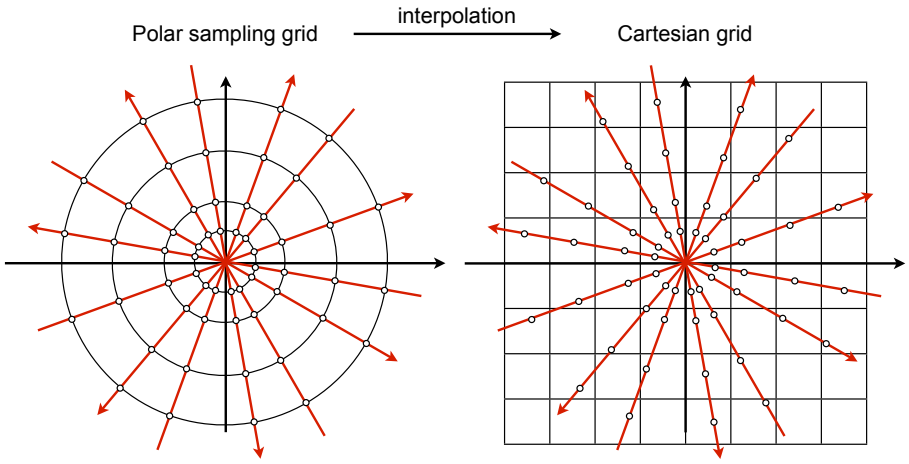

Figure 2.15: Backprojection blur is caused by polar sampling pattern in Fourier space. Inverse 2D Fourier transform requires a Cartesian grid, which can be interpolated from the original polar sampling grid.

better applicable to current systems, e.g. for cone-beam CT [32, 33] and for helical cone-beam CT [34]. For a fan-beam system, the fan-beam data can be regridded to parallel-beam data. For cone-beam systems, the Feldkamp-David-Kress (FDK) algorithm [32] is most commonly used, which is a natural extension of FBP into 3D. Although it is only an approximation, the resulting image quality is often acceptable if the cone angle is not too large.

FBP remains the most commonly used image reconstruction method in CT due to its combination of accuracy, speed of computation and simplicity of implementation. It is an exact solution to the inverse Radon transform if there is no noise, the data is complete, and the spatial resolution is uniform. Because it is a linear algorithm (two times higher attenuation will lead to two times higher image intensity) its other properties such as resolution, noise and artefacts can be easily analytically determined, and are thus well understood.

However, because FBP is an exact solution to the inverse Radon transform, it implicitly assumes that the projections are line integrals of the patient's attenuation distribution. This entails that the line integrals are not perturbed by the randomness of the Poisson counting process, and are acquired with an infinitesimal detector pixel size and focal spot size. Using a correct noise model becomes increasingly important when

the tube-current is decreased to reduce the radiation dose. Secondly, FBP reconstruction also starts with log-attenuated data, which assumes non-zero photon detection. In low-dose cases, some detector pixels may be zero, after which artificial values would need to be forced upon the data. Finally, FBP does not take into account image degrading effects such as beam hardening, photon starvation or scattering (Sec. 2.2.5), or resolution-limiting factors such as the finite detector pixel size and the finite focal spot size.

These simplifications were made with good reason (to make the mathematics more manageable). However, in the interest of image quality and accuracy in real applications iterative reconstruction techniques were later proposed, which allow more accurate modeling of the real imaging physics.

2.2.6.3 Iterative reconstruction

Iterative reconstruction offers a solution to these problems. The main advantage of iterative reconstruction methods is the ease with which models of the effects named above can be incorporated. Unfortunately this leads to computationally intensive algorithms, which are non-linear and thus difficult to predict in terms of spatial and contrast resolution performance. Most of the time extra parameters are used, which also need to be optimized.

All iterative reconstruction methods can be subdivided into two broad categories: algebraic reconstruction and statistical reconstruction, both of which are discussed next.

Algebraic Iterative Reconstruction

The algebraic iterative reconstruction methods are a class of algorithms used to solve linear systems numerically. As such, these techniques can be used for CT reconstruction, but are also applicable to any linear system of equations, e.g. 3D electron microscopy, crystallography, neural networks and parallel computing [35–37].

In algebraic reconstruction, the acquisition of the spatial attenuation distribution $\mathbf{x}$ is represented *exactly* by

$$\mathbf{y} = \mathbf{W}\mathbf{x}. \tag{2.15}$$

Matrix $\mathbf{W}$ is the so-called system matrix of elements w_{ij}, which relates the contribution of every voxel $j \in J$ in $\mathbf{x}$ to every detector element $i \in I$,

with I the product of the number of detector pixels and the number of detection angles. The sinogram as measured by the acquisition system is represented by log-attenuated data $\mathbf{y}$. While $\mathbf{y}$ is delivered by the measurement system, it is the unknown $\mathbf{x}$ that needs to be reconstructed. Instead of directly inverting $\mathbf{W}$ (which is impossible due to its size, it not always being square, noise and ill-posedness), iterative estimation is used to produce a sequence of vectors $\mathbf{x}^{(0)}$, $\mathbf{x}^{(1)}$, $\mathbf{x}^{(2)}$, ..., $\mathbf{x}^{(n)}$ such that this sequence converges to $\mathbf{x}$.

Several methods have been proposed to solve Eq. (2.15) for $\mathbf{x}$. The most basic method is the Kaczmarz method, rediscovered by R. Gordon, R. Bender and G. Herman in 1970, who aptly named it the Algebraic Reconstruction Technique (ART).

In ART, an initial estimate $\mathbf{x}^{(0)} = \mathbf{0}$ is projected onto a hyperplane defined by the line-integral equation for the first detector pixel, resulting in a new solution $\mathbf{x}^{(1)}$. This new solution is then projected onto a second hyperplane, defined by the line-integral equation for the second detector pixel, resulting in $\mathbf{x}^{(2)}$. This process is repeated until convergence.

Mathematically, this is represented in vector notation by

$$\mathbf{x}^{(k+1)} = \mathbf{x}^{(k)} + \lambda_k \frac{y_i - \mathbf{w_i}\mathbf{x}^{(k)}}{\mathbf{w_i}\mathbf{w_i}}\mathbf{w_i}, \tag{2.16}$$

with i identifying a detector pixel, $\mathbf{w_i}$ the line-integral equation $\mathbf{w_i} = (w_{i1}, w_{i2}, w_{i3}, \ldots, w_{ij})$ and λ_k a relaxation parameter, which may be dependent on iteration k. Intuitively, the current image estimate $\mathbf{x}^{(k)}$ is forward projected and compared to the measured data. The error due to mis-estimation is redistributed to the current estimate, bringing it closer to the final solution.

Although ART has been shown to be superior to FBP in some applications, there are still some drawbacks associated with ART. Indeed, in the case of noise, the equations $\mathbf{w_i}$ will not necessarily intersect in one point, which leads to the existence of many possible approximate solutions. This may result in oscillating behavior of the sequence $\mathbf{x}^{(k)}$, without converging to one solution. The contribution of noise can be decreased by applying the relaxation parameter λ_k in a range of $]0, 1]$, as long as the noise level is not too large.

In addition to ART, several other techniques have also been proposed. In the Simultaneous Algebraic Reconstruction Technique (SART), instead of working with one line-integral equation $\mathbf{w_i}$ at a time, all line-

integrals for one projection view angle are used before $\mathbf{x}^{(k)}$ is updated. This changes the convergence behavior, leading to slower convergence compared to ART, with the advantage of also leading to less noise-sensitive behavior.

Going further along the same path, also the Simultaneous Iterative Reconstruction Technique (SIRT) was proposed. The image $\mathbf{x}^{(k)}$ is then only updated after taking all line-integrals of all detector pixels and all projection view angles into account. This method has the slowest convergence, and is the least sensitive to noisy data.

All three of these methods can be grouped by the ordered subset (OS) idea [38]. Mathematically, the general formula becomes

$$x_j^{(k+1)} = x_j^{(k)} + \lambda_k \frac{\sum\limits_{i \in \mathbf{S}} \left[\frac{y_i - \sum\limits_{n=1}^{J} w_{in} \mathbf{x}_n^{(k)}}{\sum\limits_{n=1}^{J} w_{in}} \right]}{\sum\limits_{i \in \mathbf{S}} w_{ij}} w_{ij}, \tag{2.17}$$

with j identifying a specific image voxel, and the summation range $i \in \mathbf{S}$ indicating the detector element contained in a subset of projections $\mathbf{S}$. ART fits in Eq. (2.17) by using as many subsets as there are detector pixels, SART uses as many subsets as there are projection angles, while SIRT uses no subsets.

Apart from working with an additive correction scheme, multiplicative correction can also be applied, called the Multiplicative Algebraic Reconstruction Technique (MART) [35]. This method has the advantage of inherently prohibiting the images $\mathbf{x}^{(k)}$ to become negative as long as the initial estimate $\mathbf{x}^{(0)} > \mathbf{0}$. However, MART is only rarely used in practice due to its nonlinear and rather chaotic behavior [39].

Statistical Iterative Reconstruction

In the previous sections, the statistical nature of the measurements was never taken into account while solving a set of linear equations. However, the probabilistic nature of the X-ray interactions will lead to the measurements deviating from the expected values. In algebraic reconstructions, the relaxation parameter can be used to decrease the contribution of noise, as long as the noise level is not too large.

To achieve an image estimate that is more accurate, a statistical model should be incorporated into the iterative reconstruction to take the ac-

curacy of the measured data into account. Furthermore, a model of the known statistical properties of the solution can also be added (prior information). The choice of statistical iterative reconstruction algorithm depends on the specific assumptions made about the measured data, which usually leads to a compromise between accuracy of the modeled statistics and physics on one hand, and the tractability of the optimization method and computational complexity on the other hand.

Several statistical reconstruction methods applicable to CT reconstruction exist. Only the image space reconstruction algorithm (ISRA), maximum likelihood for transmission tomography (MLTR) and the iterative maximum-likelihood polychromatic algorithm for CT (IMPACT) will be detailed further in this dissertation.

Image Space Reconstruction Algorithm (ISRA)

The ISRA was originally developed as a fast alternative to another statistical iterative algorithm, the maximum likelihood for emission tomography (MLEM) algorithm [40]. Whereas MLEM determines image updates by comparing estimated data in the projection space, the ISRA finds a new image estimate by comparing images and not projections. Witherspoon and Muehllehner [40] did not provide information on how the ISRA was derived apart from the *ad hoc* explanation of simply changing the final update equation in MLEM. Numerous papers have since discussed the correspondence between MLEM and ISRA, in multiple ways. We provide a short but simple derivation of ISRA in the following section, based on [40–44]. Certain steps will be reused later, when MLTR is derived for CT (Section 2.2.6.3), or when MLEM is derived for SPECT reconstruction (Section 2.3.5.2).

If the noise on the log-attenuation measurements $\mathbf{y}$ is assumed to be white Gaussian distributed, the ordinary least squares cost function can be used to find the image estimate $\hat{\mathbf{x}}$:

$$\hat{\mathbf{x}} = \underset{\mathbf{x}\geq\mathbf{0}}{\arg\min}\, \Psi(\mathbf{x}) \quad \text{with} \quad \Psi(\mathbf{x}) = \|\mathbf{y} - \mathbf{W}\mathbf{x}\|_2^2. \tag{2.18}$$

Considering $\Psi(\mathbf{x})$ as

$$\Psi(\mathbf{x}) = \sum_{i=1}^{I} (y_i - [\mathbf{W}\mathbf{x}]_i)^2, \tag{2.19}$$

means it can be rewritten as [42]

$$\Psi(\mathbf{x}) = \sum_{i=1}^{I} h_i([\mathbf{W}\mathbf{x}]_i) \quad \text{with} \quad h_i(f) \triangleq (y_i - f)^2. \tag{2.20}$$

De Pierro [41] used a clever multiplicative trick to make the minimization of Eq. (2.20) possible. Let $\hat{y}_i^{(k)} = [\mathbf{W}\mathbf{x}^{(k)}]_i$. Then

$$[\mathbf{W}\mathbf{x}]_i = \sum_{j=1}^{J} w_{ij} x_j = \sum_{j=1}^{J} \left[\frac{w_{ij} x_j^{(k)}}{\hat{y}_i^{(k)}} \right] \left(\frac{x_j}{x_j^{(k)}} \hat{y}_i^{(k)} \right). \tag{2.21}$$

Because $h_i(f)$ is convex, we can apply Jensen's inequality:

$$\begin{aligned} h_i([\mathbf{W}\mathbf{x}]_i) &= h_i \left(\sum_{j=1}^{J} \left[\frac{w_{ij} x_j^{(k)}}{\hat{y}_i^{(k)}} \right] \left(\frac{x_j}{x_j^{(k)}} \hat{y}_i^{(k)} \right) \right) \\ &\leq \sum_{j=1}^{J} \left[\frac{w_{ij} x_j^{(k)}}{\hat{y}_i^{(k)}} \right] h_i \left(\frac{x_j}{x_j^{(k)}} \hat{y}_i^{(k)} \right). \end{aligned} \tag{2.22}$$

This means that

$$\Psi(\mathbf{x}) = \sum_{i=1}^{I} h_i([\mathbf{W}\mathbf{x}]_i) \leq \sum_{i=1}^{I} \sum_{j=1}^{J} \left[\frac{w_{ij} x_j^{(k)}}{\hat{y}_i^{(k)}} \right] h_i \left(\frac{x_j}{x_j^{(k)}} \hat{y}_i^{(k)} \right) \tag{2.23a}$$

$$\leq \sum_{j=1}^{J} \phi(x_j; \mathbf{x}^{(k)}) \tag{2.23b}$$

$$\leq \phi(\mathbf{x}; \mathbf{x}^{(k)}), \tag{2.23c}$$

with $\phi(\mathbf{x}; \mathbf{x}^{(k)})$ clearly a separable surrogate function.

Surrogate function ϕ is easy to compute, easy to minimize and has a fast convergence rate [42]. The new optimization problem is now

$$\mathbf{x}^{(k+1)} = \arg\min_{\mathbf{x} \geq \mathbf{0}} \phi(\mathbf{x}; \mathbf{x}^{(k)}). \tag{2.24}$$

The minimizer of $\phi(\mathbf{x}; \mathbf{x}^{(k)})$ can be found by minimizing each argument

separately:

$$x_j^{(k+1)} = \arg\min_{x_j>0} \phi_j(x_j; \mathbf{x}^{(k)}), \qquad j = 1, \cdots, J \tag{2.25}$$

It can be minimized by setting its derivative equal to zero

$$\frac{\partial}{\partial x_j}\phi_j(x_j; \mathbf{x}^{(k)}) = \sum_{i=1}^{I} w_{ij} \frac{\partial}{\partial x_j} h_i\left(\frac{x_j}{x_j^{(k)}}\hat{y}_i^{(k)}\right) = 0, \tag{2.26}$$

and solving:

$$\frac{\partial}{\partial f}h_i(f) = 2(f - y_i) \tag{2.27a}$$

$$\frac{\partial}{\partial x_j}\phi(x_j; \mathbf{x}^{(k)}) = 2\sum_{i=1}^{I} w_{ij}\left(\frac{x_j}{x_j^{(k)}}\hat{y}_i^{(k)} - y_i\right)\Bigg|_{x_j = x_j^{(k+1)}} = 0 \tag{2.27b}$$

From Eq. (2.27b) it follows that

$$\sum_{i=1}^{I} w_{ij} \frac{x_j^{(k+1)}}{x_j^{(k)}} \hat{y}_i^{(k)} = \sum_{i=1}^{I} w_{ij} y_i, \tag{2.28}$$

or

$$x_j^{(k+1)} = x_j^{(k)} \frac{\sum\limits_{i=1}^{I} w_{ij} y_i}{\sum\limits_{i=1}^{I} w_{ij} \hat{y}_i^{(k)}}, \tag{2.29}$$

with $\hat{y}_i^{(k)} = [\mathbf{W}\mathbf{x}^{(k)}]_i = \sum\limits_{j=1}^{J} w_{ij} x_j^{(k)}$ the forward projected estimate for detector pixel i.

Eq. (2.29) is the final update equation for the ISRA. ISRA converges to a non-negative least squares solution if the initial image estimate $\mathbf{x}^{(0)} > \mathbf{0}$ [41, 43, 44].

ISRA only requires one back projection of the data (the enumerator of Eq. 2.29) and can then iterate by continuously forward and back projecting only the image estimate. The complexity, usually dictated by the size of the projection data (projection views times detector pixels),

is now determined by the much smaller size of the image space (number of discretized voxels).

Because of its low computational complexity, we will use the ISRA as a basis for Chapter 4.

Maximum Likelihood for Transmission Tomography (MLTR)

Whereas the ISRA is based on the assumption that the log-attenuated data contains white Gaussian noise, others assume that the non-log-attenuated CT measurements are Poisson distributed because the measurements are the result of a counting process. Only in the case of large flux, this distribution can also be approximated by a Gaussian distribution [45]. This assumption leads to a cost function based on maximizing the likelihood that the reconstructed image estimate will result in the measured CT data.

For a set of non-log-attenuated measurements $\mathbf{y}$, one needs to find the attenuation distribution $\boldsymbol{\mu}$ that maximizes the conditional probability $P(\boldsymbol{\mu}|\mathbf{y})$. This can be calculated by applying the rule of Bayes:

$$P(\boldsymbol{\mu}|\mathbf{y}) = \frac{P(\mathbf{y}|\boldsymbol{\mu})P(\boldsymbol{\mu})}{P(\mathbf{y})}. \tag{2.30}$$

$P(\mathbf{y})$ can be neglected because it does not depend on $\boldsymbol{\mu}$. Additionally, $P(\boldsymbol{\mu})$ contains the prior knowledge about the object, which we will include later. So,

$$\max P(\boldsymbol{\mu}|\mathbf{y}) = \max P(\mathbf{y}|\boldsymbol{\mu}). \tag{2.31}$$

$P(\mathbf{y}|\boldsymbol{\mu})$ can be factored to

$$P(\mathbf{y}|\boldsymbol{\mu}) = \prod_{i=1}^{I} P(y_i|\boldsymbol{\mu}), \tag{2.32}$$

because individual measurements in $\mathbf{y}$ are independent of each other when there is no cross-talk between detector channels. Finding the maximum of Eq. (2.32) is equal to optimizing its logarithm

$$\log P(\mathbf{y}|\boldsymbol{\mu}) = \sum_{i=1}^{I} \log P(y_i|\boldsymbol{\mu}). \tag{2.33}$$

The Poisson distribution y with mean or expected value $\hat{y}$ is described

by

$$P(\mathbf{y}|\boldsymbol{\mu}) = \prod_{i=1}^{I} P(y_i|\boldsymbol{\mu}) = \prod_{i=1}^{I} \frac{\hat{y}_i^{y_i} e^{-\hat{y}_i}}{y_i!}. \tag{2.34}$$

Thus, a measured value y_i will only be dependent on the expected $\hat{y}_i$, which in turn only depends on the attenuation distribution $\boldsymbol{\mu}$. Eq. (2.34) must be viewed with caution, since we are free to choose any representation for $\hat{y}$. It is only when the finite object representation is an adequate representation of the data, in the sense that $\hat{y}$ is a good approximation to the true continuous-to-discrete system measurements, that $P(\mathbf{y}|\boldsymbol{\mu})$ is really the likelihood of $\boldsymbol{\mu}$ [46]. The expected non-log-attenuated $\hat{y}_i$ per detector pixel i is calculated by applying, or forward projecting, a discretized mono-energetic Bouguer-Lambert-Beer (see Eq. 2.5) forward model to $\boldsymbol{\mu}$:

$$\hat{y}_i = b_i \exp(-\sum_{j=1}^{J} w_{ij}\mu_j), \tag{2.35}$$

where b_i represents the unattenuated number of photon counts in detector pixel i (blank scan I_0) and J represents the number of discretized voxels.

Combining equations (2.33) and (2.34) reduces the problem of maximizing probability $P(\boldsymbol{\mu}|\mathbf{y})$ to maximizing the log-likelihood function $\mathcal{L}$, given by

$$\mathcal{L} = \sum_{i=1}^{I} \log\left(\frac{\hat{y}_i^{y_i} e^{-\hat{y}_i}}{y_i!}\right) \tag{2.36a}$$

$$= \sum_{i=1}^{I} \left(y_i \log(\hat{y}_i) - \hat{y}_i - \log(y_i!)\right). \tag{2.36b}$$

The last term in Eq. (2.36b) can be removed because it remains constant during optimization of $\mathcal{L}$.

For the optimization of $\mathcal{L}$, the same optimization transfer method can be used as detailed above for the ISRA, with following outcome:

$$\Psi(\boldsymbol{\mu}) = \sum_{i=1}^{I} h_i([\mathbf{W}\boldsymbol{\mu}]_i) \quad \text{with} \quad h_i(f) \triangleq y_i \log(b_i e^{-f}) - b_i e^{-f} \tag{2.37}$$

The calculation of the separable surrogate stays the same as in Eq. (2.21–2.26), and will not be repeated here. Maximizing the surrogate by taking its derivative leads to the following equations:

$$\frac{\partial}{\partial f} h_i(f) = b_i e^{-f} - y_i \tag{2.38a}$$

$$\frac{\partial}{\partial \mu_j} \phi_j(\mu_j; \boldsymbol{\mu}^{(k)}) = \sum_{i=1}^{I} w_{ij} \left(b_i e^{-\frac{\mu_j}{\mu_j^{(k)}} \hat{y}_i^{(k)}} - y_i \right) \Bigg|_{\mu_j = \mu_j^{(k+1)}} = 0 \tag{2.38b}$$

Unfortunately, Eq. (2.38b) is a transcendental equation and can not be solved exactly [47]. It can be approximated numerically by using a Newton-Raphson iteration [47]:

$$\mu_j^{(k+1)} = \mu_j^{(k)} + \frac{\frac{\partial \phi_j(\mu_j; \boldsymbol{\mu}^{(k)})}{\partial \mu_j}}{-\frac{\partial^2 \phi_j(x_j; \boldsymbol{\mu}^{(k)})}{\partial \mu_j^2}}. \tag{2.39}$$

Solving (2.39) results in the same update equation as proposed by Nuyts et al. [45]:

$$\mu_j^{(k+1)} = \mu_j^{(k)} + \frac{\sum_{i=1}^{I} w_{ij} (\hat{y}_i - y_i)}{\sum_{i=1}^{I} w_{ij} \left[\sum_{h=1}^{J} w_{ih} \right] \hat{y}_i}, \tag{2.40}$$

with

$$\hat{y}_i = b_i \exp(-\sum_{j=1}^{J} w_{ij} \mu_j^{(k)}). \tag{2.41}$$

This algorithm is known as the MLTR algorithm [45, 48]. One of the reasons why it works well for low-count measurements is because it never takes the logarithm of the transmission data [42], whereas the methods in the previous sections used log-attenuated data. MLTR has been shown to achieve a lower noise level at equal resolution compared to FBP reconstruction [49].

The MLTR algorithm can be implemented efficiently to achieve a reconstruction speed half of SIRT, although it will have a little slower convergence than SIRT and a much slower convergence than the ISRA [50].

The choice of separable surrogate $\phi(\mathbf{x}; \mathbf{x}^{(k)})$ is very important in this regard. Surrogates useful for optimization transfer should be easy to compute, easy to minimize and have a fast convergence. Unfortunately, additive separable surrogates generally lead to very high curvature surrogates, i.e. with very slow convergence rates [42]. An alternative to additive separable surrogates are the paraboloidal surrogates, such as the optimal separable paraboloidal surrogate (SPS) as derived by Erdoğan and Fessler for transmission tomography [51].

Iterative Maximum Likelihood Polychromatic Algorithm for CT (IMPACT)

One problem with MLTR is that it still uses a forward model based on the assumption that X-ray beams are mono-energetic, while in reality the beam is poly-energetic. This discrepancy results in the beam-hardening artifact and streaks near dense objects due to photon starvation.

In the derivation of IMPACT [2], the forward model used in MLTR (Eq. 2.35) is replaced by a discretized polyenergetic forward model:

$$\hat{y}_i = \sum_{k=1}^{K} b_{ik} \exp\left(- \sum_{j=1}^{J} w_{ij} \mu_{jk} \right), \tag{2.42}$$

with k the energy bin index for K energy bins, μ_{jk} the linear attenuation coefficient of voxel j at photon energy E_k, and b_{ik} the unattenuated value that would be detected at detector element i for energy k ($\sum_k b_{ik} = I_0$ from Eq. 2.6). b_{ik} depends on the source spectrum I_{ik}, the photon energy E_k and the detector quantum efficiency τ_k

$$b_{ik} = I_{ik} E_k \tau_k. \tag{2.43}$$

I_{ik} depends on knowledge of the source X-ray spectrum, which can be estimated using freely-available simulators[6] or can be calibrated by measurements [52].

As the attenuation per voxel now also depends on the energy E_k, this leads to $J \times K$ unknowns instead of J, as could be solved originally with MLTR. In De Man et al. [2], the authors proposed to approximate $\mu(E)$ by a linear combination of the energy dependence of the photoelectric effect and the energy dependence of Compton scatter (Eq. 2.2

[6] X-ray Toolbox of Siemens https://w9.siemens.com/cms/oemproducts/Home/X-rayToolbox

and 2.4). This reduces the number of unknowns to $2J$: for each voxel the contribution of the photoelectric effect and the contribution of the Compton scatter basis functions need to be known. When it is assumed that all naturally occurring elements have contributions which can be pre-determined from attenuation values of known substances at a mono-energetic energy, the number of unknowns can be reduced to just J unknowns:

$$\hat{y}_i = \sum_{k=1}^{K} b_{ik} \exp\left(- \sum_{j=1}^{J} w_{ij} \left[\phi(\mu_j)\Phi_k - \theta(\mu_j)\Theta_k \right] \right). \tag{2.44}$$

Here, μ_j represents the mono-energetic attenuation at a predefined energy (e.g. 70 keV), Φ_k and Θ_k represent the energy dependence of the photoelectric effect and Compton scatter, and ϕ and θ are known functions of μ_j. Now only μ_j needs to be estimated. For the full derivation and update equations we refer the reader to De Man et al. [2].

The polyenergetic model was specifically added to minimize the effect of beam hardening and to reduce streaks near metal objects. When De Man et al. compared results obtained with IMPACT to traditional correction approaches, they found that the same level of beam hardening reduction was obtained. However, image noise and other artifacts were also reduced, illustrating the power of model-based iterative reconstruction [2].

Additional models

Just as IMPACT was an extension of MLTR towards a polyenergetic forward model, the statistical reconstruction methods can also be further extended to even more advanced forward models, e.g. to correct for the finite focal spot diameter and photon scattering, and to include prior knowledge about the scanned object. Including a prior model into the log-likelihood leads to a different log-likelihood

$$\mathcal{L} = \sum_{i=1}^{I} (y_i \log(\hat{y}_i) - \hat{y}_i) - V(\boldsymbol{\mu}), \tag{2.45}$$

with V a potential function penalizing the log-likelihood value for some property of image $\boldsymbol{\mu}$, e.g. penalizing a large difference between neighboring voxels. A good choice for potential V is the q-generalized Gaussian

Markov random field (q-GGMRF), proposed by Thibault et al. [53]:

$$V(\boldsymbol{\mu}) = \frac{1}{p\sigma^p} \sum_{\{j,k\}\in\mathbf{C}} c_{j,k}\rho\left(\mu_j - \mu_k\right), \tag{2.46}$$

with σ a scalar which determines the prior strength relative to the data fitting term. The coefficients $c_{j,k}$ are direction weighting coefficients chosen as the inverse distance between the center voxel and all elements in neighborhood $\mathbf{C}$ (26 voxels in 3D) to normalize their contribution. The calculation of ρ depends on the difference between neighboring voxels:

$$\rho(\Delta) = \frac{|\Delta|^p}{1 + |\Delta/c|^{p-q}}. \tag{2.47}$$

By changing parameters p and q, a Gaussian prior, approximate Huber prior, generalized Gaussian MRF or q-generalized Gaussian MRF can all be achieved. Parameter c determines the approximate threshold of transition between low and high contrast regions, with a higher c pushing the edge-preserving behavior towards larger Δ.

The new forward model now becomes:

$$\hat{y}_i = \sum_{k=1}^{K}\sum_{s=1}^{S} b_{iks}\exp(-\Phi_k \sum_{j=1}^{J} w_{ijs}\phi(\mu_j) - \Theta_k \sum_{j=1}^{J} w_{ijs}\theta(\mu_j)) + C_i, \tag{2.48}$$

where the finite focal spot diameter is sub-sampled by S rays, and the scatter detected in detector element i is represented by C_i.

2.2.7 Challenges in CT imaging

2.2.7.1 Radiation dose

When X-rays interact with living tissue, part or all of their energy will be deposited in the tissue through indirect creation of ion pairs. These ion pairs cause interactions with chemical systems and have a detrimental effect on the biological tissue. X-ray *exposure* describes the ability of X-rays to ionize air and is measured in roentgen (R) or Air Kerma. This term only quantifies the amount of ionization, but not the more interesting amount of energy actually deposited in the tissue. The term *absorbed dose* takes the absorbed energy into account, and is measured in gray (Gy).

Radiation dose will affect biological tissue in two ways: through stochastic effects and through deterministic effects. The stochastic effects are the result of DNA mutations. Cells irradiated by a low dose will try to repair the radiation damage. When the repair process is also damaged, the cells can not perform their normal repair function but can still replicate. Such cells are called pre-cancer cells. Under influence of physical, chemical or viral causes, these pre-cancer cells can be differentiated into cells which show minimal cancer characteristics. In turn, these cells can grow into clinical cancer, which may spread throughout the body by metastasis.

The stochastic effects described above can only occur in cases of low-dose irradiation, with no minimum-dose requirement. On the other hand, cells irradiated with a dose higher than a threshold will become non-functional and will die, which means no further DNA replication can occur. This effect is deterministic in nature, because it only happens when the absorbed dose is higher than a certain threshold. This will become more prevalent with increasing dose, up to the limit where all cells have died.

Radiation dose influence The clinical symptoms of radiation dose have been well tabulated for humans [54]: below 0.5 Gy there is generally no clinical effect seen, while hair loss already starts at 3 Gy. The lethal dose is described by the $LD_{50/30}$, which is the absorbed dose that would kill 50% of the population within 30 days. Humans have an $LD_{50/30}$ of 2.5 to 4.5 Gy. Small animals have a higher $LD_{50/30}$: 4.5 Gy for mice, and 6 Gy for rats. Cockroaches have an $LD_{50/30}$ of 50 Gy [54], thanks to their much slower cell division cycle compared to vertebrates.

To quantify the total risk entailed by stochastic and deterministic effects combined, it is important to assess the *whole-body* exposure. In CT, the exposure is highly nonuniform and often involves partial-body irradiation. Furthermore, each organ has a different sensitivity to absorbed dose [3], largely depending on the rate of cell division. These factors are taken into account in the *effective dose*, with unit sievert (Sv). It is the sum of the absorbed dose per tissue, weighted by the radiation type and the tissue type. The tissue-type weights are based on epidemiological data in humans, and are not available for small animals. In other words, there is no way to calculate effective dose for small animals, which is why preclinical doses are still reported in Gy.

It is difficult to determine the actual influence of low-level radiation

on the cancer incidence rate, because the baseline cancer rate is already very high (42 out of 100 people will be diagnosed with cancer in their lifetime), and the risk of developing cancer heavily fluctuates depending on the individual life style and environmental effects [55]. Data gathered from a cohort of Japanese atomic bomb survivors have shown that there is a linear, dose dependent increase in excess cancers, with no minimum threshold dose [56]. Others have reported that such data is too variable to allow for a statistically significant conclusion [57], because it even supports the idea that low doses might actually reduce cancer mortality (radiation hormesis) [58].

Mathews et al. [59] have statistically analyzed the data of 10.9 million people of which 680.000 were exposed to CT scans between the ages 0 to 19 and later showed cancer incidence. After accounting for age, sex, and year of birth, an overall 24% greater cancer incidence was found in the exposed people (average dose 4.5 mSv per scan) compared to the unexposed people. This corresponds to an absolute excess incidence rate of 9.38 per 100.000 person years at risk, or, for every 1000 people followed in a 10 year period after a 4.5 mSv scan, one person will develop cancer due to the irradiation. Cardis et al. [60] determined that a small excess risk of cancer exists at an average individual cumulative dose of 19.4 mSv, measured in a cohort of nuclear workers from 16 countries.

Typical effective doses range between 7 and 43 mSv for diagnostic CT scans, and between 1.3 and 4.5 mSv for low-dose CT scans used in PET/CT and SPECT/CT [61]. To put this in perspective, the annual whole-body effective dose due to natural background radiation is 3 to 6 mSv per year depending on the geographical location. The diagnostic dose is thus higher than the 4.5 mSv per scan which already increased the cancer incidence in the study by Mathews et al. [59]

In small animals, the rate of life shortening for mice has been estimated at 7.2% Gy^{-1} for whole body exposure by Sato et al. [62]. Mole et al. [63] have shown that a mouse can neutralize doses of 0.25–0.5 Gy per day when exposed daily. Continued radiation exposure will damage this recovery process.

X-ray dose reduction Because the dose-dependent cancer incidence increase is clearly still under research, the *as low as reasonably achievable* (ALARA) principle is generally advocated for all medical modalities depending on ionizing radiation. However, reducing the dose is not easy because an inevitable relationship between image spatial resolution δ,

signal-to-noise ratio (SNR) and dose D exists:

$$D \propto \frac{\mathrm{SNR}^2}{\delta^4}. \tag{2.49}$$

A high image spatial resolution can only be achieved by using magnification together with a detector with small pixels. However, smaller pixels detect less X-ray photons in the same integration time, with worse photon statistics as a result. According to Eq. (2.49), improving the spatial resolution with factor 2 will lead to a reduction of the SNR by 4 if the radiation dose is held constant, or will lead to a 16 times increase in radiation dose if the SNR is held constant. It is impossible to lower X-ray dose without having to compromise the image quality.

Several authors and vendors have proposed methods to reduce the radiation dose in CT [64, 65]. Because the dose is dependent on the tube-current-time product (mAs), a simple but effective method is to reduce the tube current in function of patient thickness [66], instead of using a fixed current for all protocols. Although this is a harmless optimization in the case of overexposure, decreasing the intensity will lead to worse photon statistics. This will lead to excessive image noise when not properly accounted for in the reconstructions.

Likewise, also the total scanning time can be reduced by using less projection views over 360° [67]. Every projection view in itself then still receives sufficient photon statistics, but the data is undersampled in the view direction. This can lead to severe aliasing artifacts, as previously shown in Sec. 2.2.5.4. While this can not be solved by using a more correct statistical model (the statistics have not changed), regularized reconstruction can be of help here. This will be explained in more detail in Chapter 4.

A second, less-obvious method is peak-voltage optimization: lower peak voltage leads to more contrast, but tends to noisier images due to the decreased penetration depth. A tradeoff must be made between image noise and contrast enhancement, taking into account the patient size. Peak-voltage changes have an exponential effect on radiation dose, e.g. a reduction from 120 kVp to 100 kVp (-16.5%) can lead to a dose reduction of almost 40% [68]. However, reducing the number of penetrating rays by decreasing the kVp will also have a detrimental effect on image noise in larger patients.

Other techniques include the optimization of filtration (pre-hardening the beam to decrease the amount of low-energy photons), the use of bow-

tie filters to attenuate off-axis rays, and prospective motion gating (to image during prescribed cardiac or respiratory phases only).

Because all these dose-reducing measures have a negative impact on image quality, the dose reduction should be weighed against the possibly worse diagnostic value of the images. Xia et al. [61] managed to reduce the dose of CT for PET/CT from 15.9 mSv to only 2.7 mSv when a diagnostic-quality CT image was not needed, but was only used to correct for image degrading effects in PET imaging. However, they only changed the scanner parameters (e.g. tube current, X-ray source filtration) within the limits that still allowed for accurate CT FBP reconstruction.

Advances in statistical reconstruction techniques (see Section 2.2.6.3) allow us to reduce the dose even further. Excellent image quality can then be achieved at only 0.5 mSv for routine head CT scans, 0.09 mSv for chest CT, and 0.6-0.8 mSv for routine abdomen and pelvis CT scans [69].

2.2.7.2 Quantitative CT

The main objective of quantitative CT or QCT is to measure tissue or material properties in an absolute quantitative way. Due to the polychromatic X-ray spectrum, the reconstructed image values will depend on the material composition and density, but also on the system parameters, and even on materials surrounding the material of interest. The goal of QCT is then to reconstruct image values only dependent on the material properties. This means a full physical model is needed in the reconstruction step, at the very least to remove beam-hardening from the images, with additional correction methods to minimize the influence of photon scatter.

Unfortunately, photon attenuation is a function of Z (through the photoelectric effect, Eq. 2.2) as well as a function of density. This means that two fundamentally different materials may have the same attenuation coefficient at a certain photon energy E, even though their mass attenuation coefficient is different. It will be impossible to differentiate both materials with a conventional CT scan. Correct differentiation is of utmost importance when contrast agents are administered, as iodine may end up with the same image value as surrounding bone, or ureic acid may be mistaken for calcium in gout studies [70].

A possible solution is to use the energy-dependence of attenuation to our benefit, as is done by dual-energy CT (DECT), and going even further, spectral CT imaging. With DECT, two CT datasets are acquired

at 2 different peak energies, e.g. one at 80 kVp and one at 120 kVp. Two different materials with the same attenuation coefficient at one energy will have a different coefficient at another energy. The information from both scans can thus be correlated to help in differentiating between the different materials.

A standard processing method was published by Granton et al. [71]. Both datasets measured with energy spectra E_1 and E_2 are first reconstructed separately. For every voxel, a system of three equations can then be solved:

$$\mu(E_1) = f_1\mu_1(E_1) + f_2\mu_2(E_1) + f_3\mu_3(E_1) \tag{2.50a}$$
$$\mu(E_2) = f_1\mu_1(E_2) + f_2\mu_2(E_2) + f_3\mu_3(E_2) \tag{2.50b}$$
$$1 = f_1 + f_2 + f_3. \tag{2.50c}$$

These equations are based on 3 basis materials $n = 1..3$ with attenuation value μ_n. The coefficients f_n represent the fraction of base material n being represented in this voxel. With the additional assumption that each voxel can contain a maximum of 3 basis materials (Eq. 2.50c) and a non-negativity constraint on these fractions, this system of equations can be solved for f_1, f_2 and f_3. With such an approach, the basis materials are usually chosen as water, cortical bone and contrast agent [71], although other possibilities certainly exist [72].

Several system geometries exist in which multi-energy data can be acquired. The simplest method is dual-kVp, a technique for which one single-energy scanner will suffice. Two scans are simply performed consecutively with a different energy spectrum. This method is prone to motion artifacts because of patient movement in between the two acquisitions. A different method is dual-source DECT, where two source-detector pairs are attached to one gantry. Both pairs acquire their own, unique CT dataset at the same time. This method does not suffer from motion artifacts because both datasets are measured at exactly the same time. A disadvantage is the space needed to place two source-detector pairs on one gantry, leading to a smaller FOV for one source-detector pair compared to the FOV of a single-source system [73]. Dual-energy information is then only available for an inner part of larger patients. A third method is kVp-switching [10], with an X-ray source rapidly switching between the two peak energies while rotating around the patient. This has the disadvantage of not acquiring two identical projection views with a different energy, but with an interleaved pattern of data. This

means missing projection values will need to be interpolated to allow for reconstruction.

Different from the methods above is enabling DECT by using a newer detector design. With dual-layer detectors, the detector is subdivided into two parts. The top part (which receives the incident X-ray photons first) will measure the full X-ray spectrum, while also providing enough attenuation to stop low-energy photons. Only the higher-energy X-rays will reach a second detector located below the first one. In essence, the incident spectrum has been measured by two bins, each with different information about the spectrum.

A more advanced solution is by using photon-counting detectors instead of energy-integrating detectors. The measured data can then be energy-integrated into arbitrary bins of different energy intervals. These bins can be used in existing dual-energy algorithms to help realize QCT. There are also some additional advantages to using photon counting detectors: electronic noise can be effectively rejected, there is no pulse-height (Swank) noise and scattered photons can be rejected [74]. Furthermore, optimal weightings can be applied to different energy bins to increase the influence of lower-energy bins, which will increase the soft-tissue contrast. Unfortunately, it is difficult to develop the electronics needed to allow spectral measurements at the high photon flux delivered by the X-ray tube.

While DECT has been in clinical use since 2005, spectral CT is still under research and development to optimize the detector for the high X-ray flux [75] and to optimize the reconstruction for the high statistical noise per bin [76].

2.2.7.3 micro-CT

Spatial resolution

Current volumetric CT scanners have typical in-plane resolutions of 200 to 300 μm and a slice thicknesses of around 500 μm using high-dose acquisition protocols (3 mSv per scan) [77]. Unfortunately, such spatial resolution is not sufficient to investigate high-resolution structural information. One example is the imaging of small animals with CT. Imaging mice with an internal detail comparable to human CT scans requires a system able to distinguish features smaller than 100 μm [78] in size, because the volume of morphological structures and organs in mammals is proportional to their weight [79]. This means clinical CT systems can

not be used for small-animal imaging. Apart from preclinical imaging, high-resolution images are also beneficial for human extremities imaging, e.g. to scan the human wrist or human knee [80]. A final example are dedicated breast CT systems, which obtain 3D images of the breast in contrast to the conventional 2D images obtained with mammography [81].

To accommodate to the demand for high-resolution *in vivo* CT imagers, several investigators have developed high-resolution imaging systems specifically designed for small animals, called micro-CT or μCT systems [12, 82, 83]. These systems follow the same working principle as clinical CT systems. A tube-detector gantry rotates around the anesthetized animal and acquires X-ray measurements from all angles, which are later reconstructed into cross-sections of the small animal. The difference between clinical CT and micro-CT can be found in the geometry, the choice of imaging components and the speed of rotation.

Magnification

The high spatial resolution is achieved by placing the X-ray tube close to the object or animal and the detector further away, achieving magnification factors of 1 to 6:

$$\mathrm{M} = \frac{\mathrm{FDD}}{\mathrm{FOD}}, \tag{2.51}$$

with FOD the focal spot-to-object distance, and FDD the distance between focal spot and detector.

A second, related, geometrical aspect is the larger relative axial FOV. It is possible to acquire whole-body images of mice without requiring bed translations, by using cone-beam detectors and by carefully choosing the magnification. This removes the need for the special, difficult helical trajectory scans as used in clinical CT. A disadvantage of cone-beam imagers is the amount of photon scatter detected, which increases considerably when more detector rows are available. Whereas in clinical CT physical scatter grids are placed between the relatively large detector pixels to stop scattered photons, this is very challenging in micro-CT due to the much smaller pixel sizes. A sufficiently thick grid would block complete pixels, and would reduce the CNR while decreasing the SPR [22].

The SPR for micro-CT ranges between 0.3 and 0.5 [20, 21]. There is a large decrease in SPR compared to clinical systems due to the smaller object and the relatively larger air gap between the object and the detector, which means scattered photons may miss the detector entirely. On the

other hand, there is a much larger axial coverage because true cone-beam detectors are used instead of multi-row detectors, which leads to more detections of axially scattered photons compared to clinical systems.

Component choice

In terms of components, a first critical component is the X-ray tube. In order to resolve high-resolution structure in the object, the focal spot size should be kept as small as possible. A focal spot diameter Δf (mm), under influence of magnification M, will lead to a spatial resolution cutoff frequency ν_f (lp/mm) [84]:

$$\nu_f = \frac{M}{\Delta f(M-1)}. \tag{2.52}$$

A larger magnification thus comes with a lower cutoff frequency, or worse spatial resolution. A high-resolution micro-CT system can then only be achieved with a sufficiently small focal spot size. Unfortunately, because of the heating of the anode target in the X-ray tube, the maximum power P which can be used is approximately limited by [85]

$$P = 1.4(1000\Delta f)^{0.88}. \tag{2.53}$$

A focal spot of 50 μm can only be reached with an X-ray tube power no larger than 44 W. To reach a higher power, the focal spot diameter would need to be increased. As the intensity of the X-ray beam is linearly proportional to the the tube power, the focal spot size and maximum power will limit the X-ray flux that can be delivered in a reasonable time. Lower flux can be compensated for by increasing the exposure time per projection angle, effectively determining the under-limit of the total acquisition time.

In general, micro-CT X-ray tubes will run at lower peak voltages compared to those used in clinical CT. In clinical CT, beams with a peak energy of 75 to 140 keV are common. However, due to the smaller object diameter in micro-CT, these high-energy photons will pass through the animal without contributing much to the overall linear attenuation. As explained in Sec. 2.1.3, soft-tissue contrast is dependent mainly on the low-energy photons. This, together with the focal power limitation leads to a more commonly used peak energy of 50 to 80 keV in micro-CT, leading to an average energy of 20 to 40 keV, averaged over the polyenergetic spectrum. This is around the optimum energy of 25 keV for mouse

imaging and 30 keV for rat imaging [86].

A second critical component is the X-ray detector. The detector pixel size Δx will also influence the spatial resolution, as it leads to a spatial resolution cutoff frequency ν_d (lp/mm) [84]:

$$\nu_d = \frac{M}{2\Delta x}. \tag{2.54}$$

Combining Eq. (2.52) and (2.54) allows the optimal focal spot size to be determined, for a fixed detector pixel size and chosen magnification:

$$\Delta f = \frac{2\Delta x}{M-1}. \tag{2.55}$$

With a magnification of 2 and a detector pixel size of 50 μm, a 100 μm focal spot size should suffice so that nor the focal spot size nor the detector pixel size would be the determining factor for an image resolution of 20 lp/mm or 25 μm. At a magnification of 1.5, one can get away with a focal spot size up to 200 μm to reach a spatial resolution of 15 lp/mm or 33 μm.

preclinical micro-CT

Apart from the general micro-CT issues described above, two separate issues stem from the fact that live animals are used in *in vivo* preclinical micro-CT imaging. The first issue is the use of contrast agents, e.g. to visualize the cardiovascular system. Due to the fast renal clearance rate in small animals, conventional clinical iodine contrast agents will be cleared long before the slow (due to the limited tube current and thus flux) micro-CT scanner is finished acquiring all projection views. Small-animal-specific contrast agents have been designed to allow the contrast agent to follow other pathways, e.g. by encapsulating iodine in lipids [87], or by using nanoparticles stabilized by a polymer coating [88]. Both methods decrease the clearance rate by necessitating a first-pass clearance in the liver, which is much slower than the kidneys. Unfortunately, even these specific contrast agents have a high injected dose volume, and may be toxic in the rather large volumes needed [89, 90].

Secondly, animals will move during the CT acquisition. While human patients are routinely asked to do a breath-hold during the CT acquisition, the breathing pattern of small animals can not be controller easily, unless through intubation and ventilation [91]. The heart beat rhythm is also too fast (600 to 800 bpm in mice), which means every consecu-

tive projection view will be acquired with the heart in a different phase of motion. The problem of respiratory motion can be addressed with retrospective respiratory gating [92], by measuring the respiratory phase by analyzing the diaphragm position on the already-measured projection data. It is also possible to measure the motion during acquisition with pressure sensors and an electrocardiogram (ECG), before using this information as prior-information in model-based iterative reconstruction [93]. However, this does not negate the fact that a fast X-ray tube and detector are still necessary to 'freeze' the heart on each projection image in order to minimize cardiac motion [94].

2.2.8 Applications

2.2.8.1 Clinical CT

The use of CT imaging has drastically increased in the last decade, thanks to advances in resolution, image quality, and imaging speed. The peak CT procedure volume in the United States was achieved in 2011, with more than 85 million procedures per year. Especially the introduction of CT scanners with multiple axial pixel rows has been a big factor in the beginning of the 21st century [95].

The most common CT procedure is abdominal and pelvic CT (32%, numbers from [96]), used to help diagnose the cause of abdominal or pelvic pain, and diseases of the internal organs, small bowel and colon, e.g. appendicitis, abscesses, inflammatory bowel diseases, cancers of abdominal organs, kidney and bladder stones, and abdominal aorta aneurysms.

Second to abdominal and pelvic CT exams are the cranial CT scans (28%), mainly to diagnose infarctions, hemorrhaging and bone trauma. Chest CT is performed in 16% of the procedures, to evaluate injury to the chest, when a tumor is suspected, or to look for fluid collections in the lungs. Angiography and extremity imaging are only done in resp. 5% and 6% of the procedures.

These numbers acknowledge the fact that CT imaging is the workhorse of medical imaging and every emergency room [97], often used as a first step in diagnostic exams. This strengthens the need for the *ALARA* principle, as CT exams can easily be overprescribed. Apart from diagnosis, these CT scans are also performed to guide procedures, plan for surgery, to plan radiation treatment for tumors, or to monitor the response to chemotherapy.

2.2.8.2 Micro-CT

in vivo

The use of preclinical micro-CT is largely different from clinical use. Preclinical CT is predominantly used together with emission tomography modalities as an anatomical landmark, and to enhance the image quality and the interpretation of the data with complementary information about the attenuation. This will be discussed in more detail in Chapter 2.4.

As the workhorse for the medical research industry, the first advances in micro-CT technology were largely driven by imaging needs for the evaluation of bone anatomy and density [98]. Here, the primary use case is trabecular bone analysis, e.g. to evaluate bone changes *in vivo* in osteoporotic mice [99, 100].

A second application domain is vascular imaging, mainly to study angiogenesis [101] and neovascularization [102] both in healthy and in diseased conditions. One such example is comparing diabetic and healthy mice with regards to growth and regression of vasculature after hindlimb ischemia [103]. Therapeutic solutions can also be evaluated longitudinally, e.g. to evaluate the influence of lung cancer therapy on the pulmonary arteries in mice [104].

Apart from the use of micro-CT scanners for small-animal research, the same scanner design ideas are also being used to build limb-specific high-resolution CT scanners for human patients. One examples is the development of and research on cone-beam CT for orthopedic imaging of the wrist or knee [80].

ex vivo

Apart from *in vivo* imaging, micro-CT is also used for *ex vivo* imaging due to its high achievable spatial resolution when the dose is increased. With ex vivo imaging, the dose can often be increased to levels which would not be supportable in *in vivo* studies, thus increasing the image quality significantly. This has enabled the evolution of micro-CT scanners into nano-CT scanners, able to reach spatial resolutions of 400 nm [105].

Mineralized tissue can be imaged as-is, e.g. to assess fracture healing [106, 107], or to evaluate preclinical models of joint disorders [108]. Non-mineralized tissue should be fixed with a casting agent beforehand [109], after which the hardened cast can be scanned. Two examples

are mouse brain imaging [110], or the imaging of lung cancer nodules in rats [109]. After cast hardening, the remaining soft-tissue can also be corroded, e.g. to image liver angiogenesis [111], or the murine arterial system [112–114].

Apart from the more medically-oriented applications, micro-CT and nano-CT can also be used for material research because its non-destructive [115]. A good review of possible applications in geosciences is given in Cnudde et al. [115]. In manufacturing, micro-CT can be used to characterize microstructures in high-strength Al-alloys [116].

2.3 Single Photon Emission Computed Tomography (SPECT)

2.3.1 Early History

The goal of emission tomography (ET) imaging is to image functional processes in living organisms with the help of radioactive molecules. ET imaging is based on the tracer principle, described first by George Charles de Hevesy[7] in 1911, and used first in animals in 1924. The *isotope tracer principle* states that

> radioactive isotopes will participate in the physiological processes of an organism in a manner indistinguishable from the same nonradioactive isotope.

Because radioactive isotopes can be localized by detecting the ionizing radiation emitted by the unstable atoms, the detected information can be used to visualize important physiological processes in the body.

Research into radioactive isotope production systems (i.e. the cyclotron and later the synchrotron) increased in the 1930s, leading to a wide range of radioactive tracers becoming available. As with the early days of X-rays, the first planar ET images were quickly acquired. The first organ studied for medical purposes was the thyroid, already known in the early 1900s to have a high uptake of iodine, and thus also a high uptake of radioactive isotopes of iodine.

By 1934, Fermi managed to produce ^{128}I by using a Po/Be neutron source, soon after used for thyroid imaging studies. In 1937, Seaborg used a cyclotron to generate ^{131}I with an 8-day half-life, which makes it much more useful than the short-lived ^{128}I (half-life of 30 minutes), as the tracer still needs transportation to the patient before image acquisitions can start. Back then, ET imaging consisted of moving a Geiger-Müller counter manually around the neck of the patient to record the number of photons emitted from the thyroid gland.

Progress in nuclear medicine slowed during World War II. Afterwards, due to the developments for the Manhattan Project, more cyclotron and reactor sources became available. This enables the generation of larger amounts of radioisotopes at lower costs. In 1949 the first planar gamma-ray scanning device was developed using a calcium tungstate

[7] For which he received the Nobel Prize in Chemistry in 1943. He was also appointed International Franqui Professor at Ghent University in 1949-1950

($CaWO_4$) scintillating detector. Two years later a commercial thallium-doped sodium iodide (NaI(Tl))-based scanner became clinically used. Finally, in 1957 the $^{99}Mo/^{99m}Tc$ generator was developed by Powell Richards. From then on, tracers could be labeled closer to the scanners and patients, which allowed smaller hospitals to use ET imaging. This is considered the major breakthrough that made ET readily available in the clinic. In 1957, Hal Anger invented the scintillation camera. Subsequent developments led to the design of systems with rotating gamma cameras, the first single photon emission computed tomography (SPECT) systems.

The first SPECT systems emerged faster than CT imagers, because the much lower data rates in emission tomography were more suitable for the electronics available in the 1960s than the high data rate encountered from X-ray sources. The first dual-detector scanner was developed in 1963 by David E. Kuhl and Roy Q. Edwards. By 1977 they had developed a more efficient scanning geometry, which later evolved in today's SPECT.

2.3.2 Imaging Principle

SPECT imaging is an *in vivo* imaging technique used to study functional processes in patients. Based on the isotope tracer principle, a molecule labelled with a radioactive isotope (radioisotope) is intravenously injected into the patient. After a time delay, to maximize the tracer uptake, the patient is imaged by a SPECT system. Fig. 2.16 illustrates the different components of such a SPECT system. The tracer will radioactively decay by emitting γ-photons in all directions. These photons will pass through the patient body and are eventually detected outside the body by a γ-camera. Because there is no sense of directionality, the γ-rays must be physically collimated before interacting with the camera. Data are acquired step-wise over 360° around the patient. The measured data, also called the sinogram, can later be used to reconstruct a 3D distribution of the spatial location of the tracer and its reaction products inside the patient body.

Figure 2.17 shows the reconstructed result of a human SPECT brain scan. The data was acquired after injecting the patient with ^{99m}Tc-labelled hexamethylpropyleneamine oxime (HMPAO), a compound that can be used to detect altered regional cerebral perfusion after the patient suffered a stroke. The 3D dataset is commonly visualized in a transverse, sagittal and coronal plane. The image presented in Figure 2.17

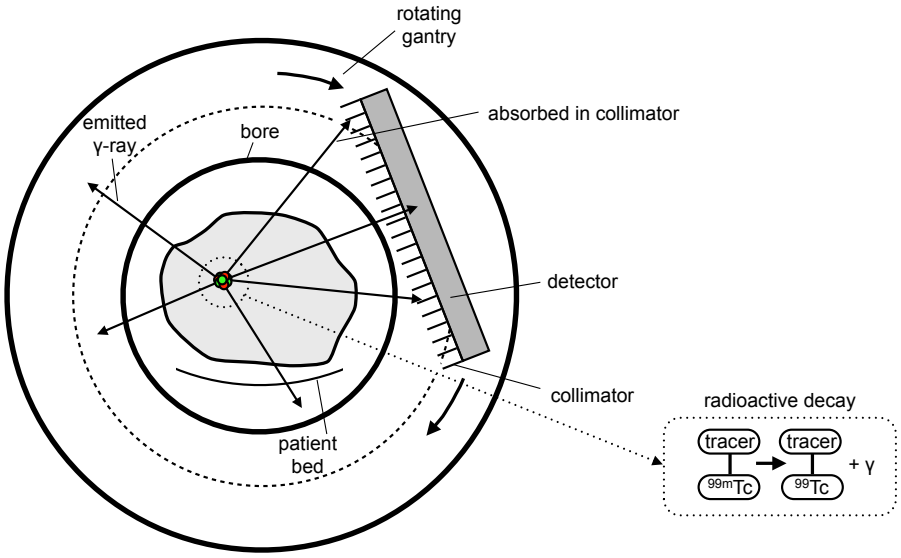

Figure 2.16: The components used in a SPECT system.

can be compared to Fig. 2.18, also the result of a brain SPECT scan. However, for Fig. 2.18 ^{123}I-labelled N-ω-fluoropropyl-2β-carbomethoxy-3β-(4-iodophenyl) nortropane (^{123}I-ioflupane or ^{123}I-FP-CIT) was used, commonly used in the diagnosis of Parkinson's disease due to its high binding affinity for presynaptic dopamine transporters (DAT). Fig. 2.18 shows clear uptake in the striatal region of the brain, the subcortical part of the brain which contains a lot of dopamine receptors. Although both figures show a human SPECT brain scan, the functional information seen clearly depends on the compound that is used.

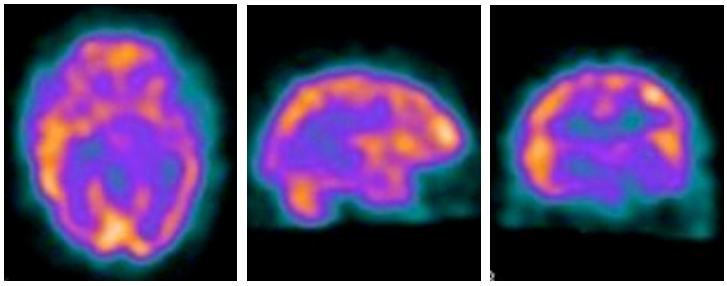

Figure 2.17: Transversal, sagittal and coronal plane of a brain SPECT study, conducted with ^{99m}Tc-HMPAO.

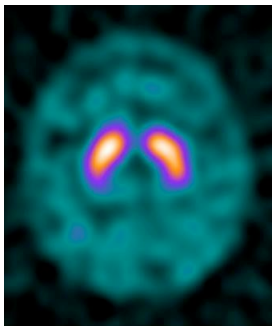

Figure 2.18: Transversal midbrain slice of a ^{123}I-FP-CIT scan, showing normal uptake in the striatal region of the human brain.

2.3.3 Important Components

2.3.3.1 Radionuclide

The specific choice of radioisotope is the divider of ET into two subdomains: SPECT and Positron Emission Tomography (PET) imaging. For SPECT imaging, the radioactive decay should be of a type that emits γ-rays, preferably with an energy between 30 to 300 keV. This allows the γ-rays to actually escape the patient body and not be attenuated too much. At higher energies, absorption collimators would be more difficult to manufacture. Several suitable radionuclides exist, of which ^{99m}Tc is used in 80% of the SPECT procedures worldwide. Some commonly used radioisotopes have been tabulated in Table 2.1. In PET imaging, the radionuclide instead emits positrons, which will undergo annihilation with an electron. The annihilation process results in the emission of two back-to-back γ-photons with energy 511 keV. These can then be detected by gamma cameras surrounding the patient.

The radioisotopes are produced by nuclear reactions, in which a stable element is bombarded with neutrons (in a nuclear reactor) or protons (in a cyclotron) to reach a higher atomic mass. This new element is an unstable isotope of the original element. The isotope will decay, typically by emitting alpha particles (two protons and two neutrons), beta particles (electrons), gamma photons, or positrons, or through the process of electron capture.

Some radionuclides (like ^{99m}Tc) are not a direct product from such an

unstable isotope, but are made indirectly:

$$^{99}\text{Mo} \rightarrow {}^{99m}\text{Tc} + e^{-} + \bar{v}_e. \tag{2.56}$$

In this case, the generator ^{99}Mo is first made from ^{98}Mo through neutron activation in a high neutron flux reactor. Because the half-life of ^{99}Mo is 66 hours, it is more practical to move the whole generator to a hospital instead of transporting an isotope with a much shorter half-life. The short-lived ^{99m}Tc can then be extracted at a site close to the patient and SPECT scanner.

The SI-derived unit of radioactivity is the becquerel (symbol Bq)[8]. One Bq is defined as the activity of a quantity of radioactive material in which one nucleus decays per second. The becquerel succeeded the curie, the older unit which was measured based on the activity of 1 gram of ^{226}Ra. It was later determined that 1 mCi is equal to 37 MBq. Typical injected doses highly depend on the expected uptake in the patient body for the tracer. The recommended injection activity for a ^{123}I-Ioflupane brain scan is 185 MBq, while the recommended activity for a ^{99m}Tc-MIBI cardiac scan ranges between 370 and 1110 MBq.

2.3.3.2 Collimator

An essential part of every SPECT imaging system is the collimator. To allow for reconstruction, knowing the position of the detector pixel which measured an incident γ-photon should suffice to determine the path it followed. Thus, to remove ambiguity about the incident ray angle it is important that each detector element can only be reached by photons from only 1 direction. This was implicitly accomplished in CT imaging, as the position of the X-ray tube is known for all projection angles. The incident ray then follows the path connecting the X-ray tube position to the detector pixel position if the X-ray was not scattered. In SPECT imaging however, the radionuclide position is what needs to be reconstructed, and is unknown.

In order to achieve directional information, a collimator is placed between the patient and the detector. It will perform mechanical collimation by absorbing all γ-rays which are not incident in the desired direction onto the gamma camera underneath. The collimator is preferably made from a dense high-Z material (e.g. Pb, W, ...) which is

[8] Named after Henri Becquerel, who shared a Nobel Prize in 1903 with Marie Curie for their discovery of radioactivity.

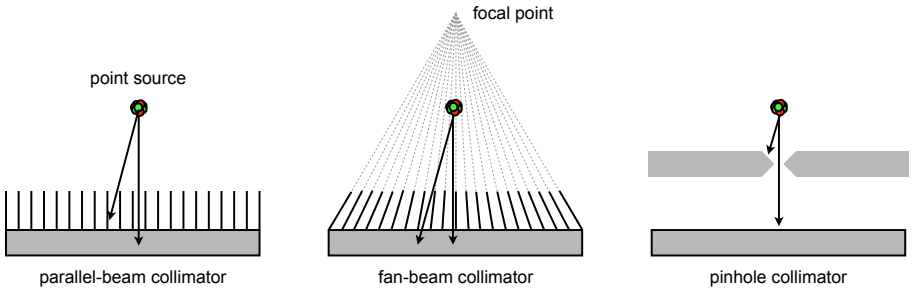

Figure 2.19: Illustration of a cross section through three types of collimators commonly used in SPECT imaging.

perforated in one or more locations. Because the collimator shape is known, all detected photons can be related to a line from detector pixel to the perforation, extending into the object space.

Several possible collimator configurations exist, of which three are presented in Fig. 2.19. In a parallel-hole collimator, all channels are arranged parallel to one another and are located perpendicular to the detector surface. Incident rays normal to the detector will be able to pass in between the septa to reach the detector. When the incident angle deviates too much from the normal on the detector, the photon will have a high chance of being absorbed by the collimator, depending on the collimator material and septa thickness. The FOV of a parallel-hole collimator is equal to the size of the detector (typically 40 $\times$ 50 cm in clinical systems), which makes this type of collimator usable for general applications.

With a fan-beam collimator, all channels are aimed at one focal line. A range of ray directions can now be detected when the rays originate from a smaller FOV than with the parallel-hole detector. The focal line can be located on the opposite side of the patient, in order to get some magnification of the projection on the detector and an increased sensitivity.

A third type of collimator is the pinhole collimator, which works just like a box camera. The pinhole collimator is commonly made of a large plate containing one or multiple holes. For each detected ray its direction is known because of the limited pinhole diameter. Other rays will be stopped by the large collimator plate. The benefit of the pinhole collimator is its magnification property (the box camera uses minification). If the object-to-pinhole distance is smaller than the pinhole-detector distance, the projection of the object will be enlarged on the detector. This

Radionuclide	energy; keV (abundance; %)	Physical half-life	Use
^{67}Ga	93 (40), 184 (20), 300 (17), 393 (5)	78 h	Lymphoma imaging, inflammation localisation
^{99m}Tc	140 (90)	6.0 h	Used in 80% of nuclear medicine procedures worldwide, primarily cardiac and brain perfusion imaging and bone scans
^{111}In	171 (90), 245 (94)	2.8 d	Brain, infection, colon transit studies, prostate cancer
^{123}I	159 (83)	13.2 h	Thyroid and adrenal carcinoma, heart function
^{125}I	35 (7)	59.4 d	Cancer brachytherapy, kidney filtration rate, deep vein thrombosis
^{131}I	284 (6), 364 (81), 637 (7)	8.0 d	Thyroid carcinoma localisation and therapy, renal blood flow
^{133}Xe	81 (38)	5.2 d	Evaluation of pulmonary function, cerebral blood flow
^{201}Tl	69-80 (89), 135 (3), 167 (10)	72.9 h	Myocardial perfusion

Table 2.1: Commonly used SPECT radionuclides, their emission peaks useful in SPECT imaging, half-life, and common usage.

forms the basis of many micro-SPECT systems, which use pinhole collimation to make high-resolution images of small animals.

A major disadvantage of the pinhole collimator is its low geometrical sensitivity at large distances, i.e. the ratio of detected photons to the number of photons emitted by the radionuclide. For a round pinhole, the geometrical sensitivity can be expressed as [117]

$$S = \frac{g^2 \cos^3 \alpha}{16 d^2}, \tag{2.57}$$

with g the pinhole diameter, d the normal distance between the point of emission and the pinhole center, and α the angle between the normal on the detector and the incident γ-ray.

2.3.3.3 Detection

The detection of γ-photons happens in a matter similar as the detection of X-rays for CT imaging (Sec. 2.2.3.2). The main difference is that SPECT detectors can measure the photon energy, which is not possible with CT detectors due to the much higher photon flux encountered in CT. The detectors can likewise be subdivided in the same two categories: indirect detectors and direct detectors.

Indirect detection

The different components of an indirect detector are illustrated in Fig. 2.20. In indirect detectors, an incident γ-photon is converted into a visible light pulse by a scintillation crystal, with a pulse intensity proportional to the photon energy. Common scintillation crystal materials in SPECT are thallium-activated sodium iodide (NaI:Tl) and thallium-activated cesium iodide (CsI:Tl). The conversion of scintillation light into an electric pulse is accomplished by a light detector (e.g. a photomultiplier tube (PMT), avalanche photodiode (APD), or silicon photomultiplier tube (SiPM)) which converts the scintillation photon into an electron, then multiplies the electrons through several dynode stages. This allows single incident photons to achieve a current high enough to measure them as an electrical signal.

In the case of PMTs, which are generally much larger than the small single scintillation crystals (which could serve as single pixels), one big crystal is attached to several PMTs. Due to the light-spread in the scintillator, multiple PMTs will receive light photons from an incident γ-ray. The location of the incident γ-ray on the scintillator can then

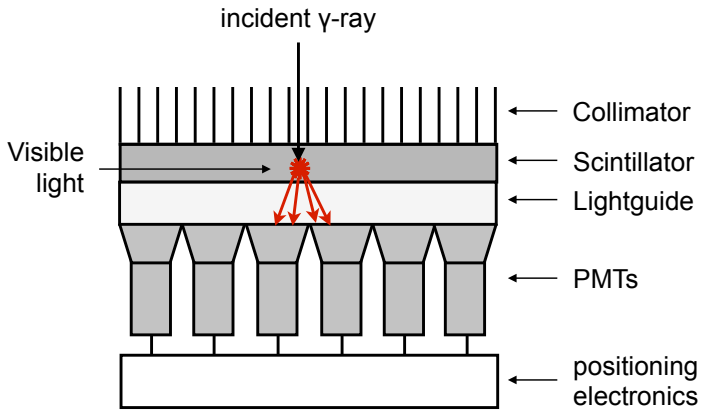

Figure 2.20: Illustration of the gamma camera components.

be determined by weighting the known position of each PMT by the strength of its signal into a mean position, a technique called Anger logic. The sum of the charges collected by all PMTs is correlated to the energy of the incident γ-photon, which means that energy can be discriminated. A light guide is often used to couple the scintillator to the PMTs to spread the light on purpose, because sufficient light spread is required for event positioning.

A major difference between the indirect SPECT and the indirect CT detectors is the respective use of PMTs and CCDs/CMOS detectors as photosensors coupled to the scintillator. This is mainly due to 3 differences. Firstly, SPECT imaging requires energy discrimination, which necessitates detectors with a good energy resolution, better than what a CCD or CMOS can offer. Secondly, due to being energy-based, the photosensor needs to be triggered per event instead of being continuously sampling (integration). PMTs will respond to single events, while CCDs or CMOSs do not. Finally, due to the geometrical sensitivity and lower radioactivity used, the number of detected photons per second will be much lower in SPECT than with CT, where a flux higher than $2{\times}10^6$ photons per mAs per second per pixel is commonly achieved. In SPECT, the data rate is in the order of 10 to 50 photons per second per pixel. Low-noise photosensors are thus necessary, which means CCDs and CMOS detectors are not a good choice.

Direct detection

Solid-state detectors differ from the indirect detectors as they directly

convert the incident γ-photon into an electrical signal, without any intermediate visible-light pulse generation. In the semi-conductor, each incident γ-ray will generate electron-hole pairs. By applying a bias voltage across the semiconductor, the holes and electrons will drift towards opposite sides, inducing a charge on those electrodes. A pixelated detector can be obtained by attaching multiple anodes, each read out individually by a different amplifier.

Direct detectors have superior energy resolution compared to indirect detectors, because there is no signal loss from the extra conversion step. Furthermore, per quantum of energy more electrons will be generated than is possible with a PMT. This leads to improved photon statistics.

Different semiconductors are in use in SPECT systems, such as those based on silicon (Si), germanium (Ge), cadmium telluride (CdTe), cadmium zinc telluride (CdZnTe) or mercury(II) iodide (HgI_2), each with its own specific properties. The most frequently used semiconductor detector is CdZnTe, because of its high stopping power and its theoretical energy resolution of 0.4% at 140 keV, which is beneficial to reduce photon scattering through windowing techniques. In practice, hole trapping and readout noise will reduce the energy resolution to 1 to 5% at 140 keV.

2.3.4 Image degrading effects

Before going into detail into how 3D distributions of the radiotracers are actually reconstructed from the measured sinogram, some common image degrading effects should be explained. These effects will distort the measured projection data, in turn leading to systematic discrepancies between the reconstructed SPECT values and the true activity concentrations in the patient.

2.3.4.1 Attenuation and scattering

The most important image degrading effects in SPECT are caused by the physical interactions of the emitted γ-rays with the patient body. In order for an emitted photon to be detected by the gamma camera, it must escape the patient body. However, photons emitted from a radionuclide may first be absorbed or scattered. This will result in

- photons that do not leave the body, due to attenuation. For the γ-ray energies used in SPECT, the attenuation will be caused mainly

by photoelectric absorption and Compton scattering (see Fig. 2.3). The attenuation factor (AF) magnitude depends on the energy E of the γ-photon and the attenuation coefficient μ (1/cm) of the traversed tissue distance d:

$$\mathrm{AF} = e^{-\int_0^d \mu(E)dx}. \tag{2.58}$$

Photon attenuation will result in a projection image with intensity lower than the expected projection image.

- photons scattered in the body, with a resultant direction which can still pass the collimator. These scattered photons will then be detected, but with a lower energy due to the energy loss from Compton scattering. This results in a projection image with intensity higher than the ideal projection image, and ultimately a reduced contrast in the reconstructed images.

Several techniques have been proposed to correct for attenuation and scatter.

SPECT attenuation can be corrected directly incorporating known attenuation values in the forward and back projector [118], or by using a method known as Chang's method [119]. Chang's method will correct post-reconstruction with a correction factor CF per voxel, which is calculated as the reciprocal of the average attenuation of this voxel over all projection paths:

$$\mathrm{CF} = \frac{1}{\frac{1}{M}\sum_{i=1}^{M} \exp(-\mu L_{\theta_i})}, \tag{2.59}$$

with L_{θ_i} the projection path for this voxel for angle θ_i, determined by the number of projection paths M used.

Regardless of how the data is corrected, the attenuation values need to be known. In stand-alone SPECT, this can be accomplished by measuring the photon attenuation with a transmission source. A common source is an encapsulated ^{153}Gd source, with a photopeak energy of 100 keV and a half-life of 270 days. This source is then placed outside the patient, after which the transmission of the emitted photons caused by the patient can be measured. These transmission measurements can then later be scaled to an attenuation map for different photopeak energies. A second method, which only takes into account the average attenuation

of the patient, is by approximating the tissue attenuation as equivalent to that of water. However, this will miss-represent the attenuation of internal but important structures such as the bones and lungs, leading to under or over corrections [120].

Correcting for photon scattering is easier. The Compton effect will always result in a decrease of the photon energy. By measuring the incident energy on the detector, and comparing this energy to the known emission spectrum of the radiotracer, scattered photons can be detected. The scattered photons can then be discarded because they will have wrong spatial information, as the direction and number of scattered events are unknown. This technique is called photopeak windowing. After windowing, the contribution of the scattered photons to the photopeak window can also be calculated. Due to the limited energy resolution of the gamma camera, some scattered photons will have an energy inside the photopeak window, and can not be discriminated from the primary γ-rays. It has been shown that the information from scatter windows around the main energy peak can deliver an estimate of the scattered photons residing in the photopeak window [121, 122], which can then be corrected for by pre-correcting the measured sinogram [121] or by including the scatter estimate in the reconstruction algorithm [123, 124].

If both attenuation and scatter are corrected for, it is important to only use the attenuation factor without the contribution of incoherent scattering to the attenuation as the scaling factor. Otherwise there would be an overlapping correction factor applied in the scatter correction step, which would overcorrect the reconstructed data.

2.3.4.2 Resolution model

Although physical collimation is already used to limit the direction of incidence on the detector, some uncertainty about the incoming ray angle still exists.

A first problem is the limited collimator resolution, illustrated in Fig. 2.21 for the parallel-hole and pinhole collimator types. Parallel-hole collimators have a certain hole-diameter and channel height, parameters which determine the uncertainty and thus resolution that can be achieved. In pinhole collimators, the pinhole has a finite diameter. In both cases, the uncertainty will increase for points located further away from the collimator.

A second issue is penetration through the collimator. The thickness

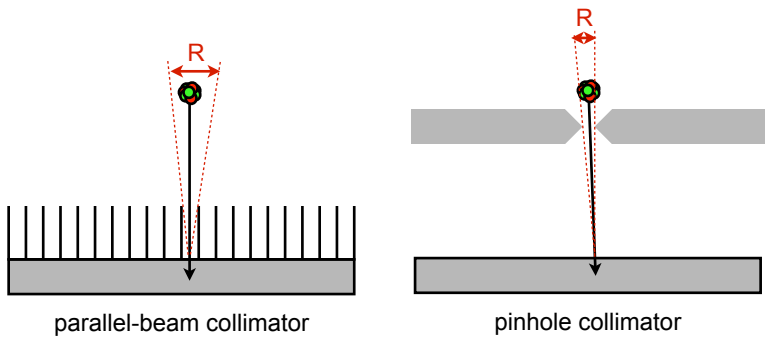

Figure 2.21: Illustration of the uncertainty of incoming rays with parallel hole and pinhole collimators.

and material of the collimator will determine its absorption properties, i.e. the attenuation of photons of some energy. Some photons may penetrate the collimator completely, a problem most apparent when a high-energy radioisotope (e.g. ^{111}In) is used together with a collimator designed for lower energy radionuclides (e.g. ^{99m}Tc). For pinhole collimators, the diameter 'seen' by the γ-photon is actually larger than the nominal pinhole diameter, because the thin knife-edge of the pinhole may be penetrated by higher-energy photons [125].

A third limitation is the detector response. The conversion of γ-rays to visible light in indirect detectors will lead to an uncertainty between the real incident γ-ray location on the detector surface and the measured detection location. The same holds with direct detectors, due to the electron-hole spread and possible charge sharing between pixels. Furthermore, pixelated detectors can not discriminate at sub-pixel resolution. The photon spread can be modeled by a low-pass filter, which is dependent on the attenuation of the detector material, the angle of incidence of the γ-ray, and the performance of the detector itself.

2.3.5 Reconstruction

2.3.5.1 Analytical Reconstruction

Iterative reconstruction is much more widespread in SPECT than in CT, because the benefits are much larger in SPECT reconstruction. Whereas iterative CT reconstruction was not considered at first due to its computational complexity, FBP was replaced with iterative reconstruction in

SPECT from 1982 onwards [126, 127] because of the smaller data sizes (due to smaller detectors with larger pixel sizes). The limits of analytical reconstruction were also reached faster in SPECT reconstruction: the FBP model is only valid in the case of a perfect parallel-beam collimator in the absence of photon scattering, attenuation, and penetration, and with a very high number of detected counts. Furthermore, also a much lower number of projection views is used (typically 60 projection views instead more than 1000 for CT), which results in aliasing artifacts with FBP. These unrealistic assumptions quickly lead to the conclusion that the use of FBP in SPECT leads to poor reconstructions [128, 129]. Thus, we will not further discuss the use of FBP for SPECT in this dissertation.

2.3.5.2 Iterative Reconstruction

Data measured in ET is Poisson distributed. However, unlike in CT imaging, it can not be approximated by a Gaussian because of the much lower detected count rate, due to the low specific activity injected in the patient, the patient attenuation, and the low geometric and detector efficiency. This means a Poisson model must be included in statistical image reconstruction to achieve accurate reconstruction.

For a set of measurements $\mathbf{y}$, the activity distribution $\mathbf{x}$ should be found which maximizes the conditional probability $P(\mathbf{x}|\mathbf{y})$. This can be calculated based on the rule of Bayes:

$$P(\mathbf{x}|\mathbf{y}) = \frac{P(\mathbf{y}|\mathbf{x})P(\mathbf{x})}{P(\mathbf{y})}. \tag{2.60}$$

As in the derivation of MLTR for CT reconstruction, $P(\mathbf{y})$ can be discarded with respect to the optimization, as it does not depend on $\mathbf{x}$. $P(\mathbf{x})$ forms the prior knowledge about the image, e.g. information determined by a transmission scan or a simultaneous CT scan (SPECT/CT).

When a flat prior distribution is used for $P(\mathbf{x})$, only $P(\mathbf{y}|\mathbf{x})$ needs to be calculated:

$$P(\mathbf{y}|\mathbf{x}) = \prod_{i=1}^{I} P(y_i|\mathbf{x}), \tag{2.61}$$

because individual measurements in $\mathbf{y}$ are independent of each other.

Finding the optimum of Eq. (2.61) involves calculating its derivative

and solving for $\mathbf{x}$. Instead, it is easier to find the optimum of its logarithm

$$\log P(\mathbf{y}|\mathbf{x}) = \sum_{i=1}^{I} \log P(y_i|\mathbf{x}), \tag{2.62}$$

because the derivative of a sum is often easier to compute: it is the sum of the derivatives of each individual log-likelihood $\log P(y_i|\mathbf{x})$. The logarithm is a monotonically increasing function and will achieve its maximum value at the same points as the original function.

The counting of γ-photons follows a Poisson distribution. The Poisson distribution y with mean or expected value $\hat{y}$ is described by

$$P(\mathbf{y}|\mathbf{x}) = \prod_{i=1}^{I} P(y_i|\mathbf{x}) = \prod_{i=1}^{I} \frac{\hat{y}_i^{y_i} e^{-\hat{y}_i}}{y_i!}. \tag{2.63}$$

Thus, a measured value y_i will only be dependent on the expected $\hat{y}_i$, which in turn only depends on the activity distribution $\mathbf{x}$. As in the derivation of MLTR for CT reconstruction, Eq. (2.63) must be viewed with caution, since we are free to choose any representation for $\hat{y}$. It is only when the finite object representation is an adequate representation of the data, in the sense that $\hat{y}$ is a good approximation to the true continuous-to-discrete system measurements, that $P(\mathbf{y}|\mathbf{x})$ is really the likelihood of $\mathbf{x}$ [46]. In SPECT, the expected value is chosen as $\hat{y}_i = [\mathbf{W}\mathbf{x}]_i$.

This means that

$$\log P(y_i|\mathbf{x}) = \log P(y_i|\hat{y}_i). \tag{2.64}$$

Maximizing probability $P(\mathbf{x}|\mathbf{y})$ can thus be reduced to maximizing the log-likelihood $\mathcal{L}$, given by

$$\mathcal{L} = \sum_{i=1}^{I} \log\left(\frac{\hat{y}_i^{y_i} e^{-\hat{y}_i}}{y_i!}\right) \tag{2.65a}$$

$$= \sum_{i=1}^{I} \left(y_i \log(\hat{y}_i) - \hat{y}_i - \log(y_i!)\right). \tag{2.65b}$$

Several methods exist to maximize Eq. (2.65b). One way is to represent the negative log-likelihood function comparable to how the ISRA was

represented in Eq. (2.20), and use the same derivation using optimization transfer:

$$\Psi(\mathbf{x}) = \sum_{i=1}^{I} h_i([\mathbf{W}\mathbf{x}]_i) \quad \text{with} \quad h_i(f) \triangleq f + \log(y_i) - y_i \log(f). \tag{2.66}$$

This means the calculation of the separable surrogate function $\phi(\mathbf{x}; \mathbf{x}^{(k)})$ stays the same (see Eq. 2.21–2.26), and will not be repeated here.

Solving the derivative of the surrogate:

$$\frac{\partial}{\partial f} h_i(f) = 1 - \frac{y_i}{f} \tag{2.67a}$$

$$\frac{\partial}{\partial x_j} \phi_j(x_j; \mathbf{x}^{(k)}) = \sum_{i=1}^{I} w_{ij} \left(1 - \frac{y_i}{\hat{y}_i^{(k)} x_j / x_j^{(k)}} \right) \Bigg|_{x_j = x_j^{(k+1)}} = 0 \tag{2.67b}$$

From which follows that

$$\sum_{i=1}^{I} w_{ij} y_i x_j^{(k)} = \hat{y}_i^{(k)} x_j^{(k+1)} \sum_{i=1}^{I} w_{ij}, \tag{2.68}$$

or

$$x_j^{(k+1)} = \frac{x_j^{(k)}}{\sum_{i=1}^{I} w_{ij}} \sum_{i=1}^{I} w_{ij} \frac{y_i}{\sum_{n=1}^{J} w_{in} x_n^{(k)}}, \tag{2.69}$$

which is the maximum-likelihood expectation-maximization (MLEM) algorithm [127]. Intuitively, the current best image estimate $\mathbf{x}^{(k)}$ is forward projected, and compared to the measured data $\mathbf{y}$ by division. This error ratio is backprojected into image-space and normalized before updating the current estimate with it.

Useful properties of MLEM are its guaranteed convergence and that the non-negativity constraint is automatically satisfied, as long as the initial image $\mathbf{x}^{(0)}$ is chosen strictly positive.

Unfortunately, the choice of additively separable surrogate functions leads to surrogates with a very high curvature, which leads to very slow convergence rates [42]. More popular than MLEM is its block-iterative extension, the ordered-subsets expectation-maximization (OSEM) algorithm [38], due to its faster convergence. The update equation is then

simply changed to

$$x_j^{(k+1)} = \frac{x_j^{(k)}}{\sum\limits_{i\in\mathbf{S}} w_{ij}} \sum_{i\in\mathbf{S}} w_{ij} \frac{y_i}{\sum\limits_{n=1}^{J} w_{in} x_n^{(k)}}, \tag{2.70}$$

with the summation range $i \in \mathbf{S}$ indicating the detector elements contained in subset $\mathbf{S}$ of the detector pixels $\mathbf{I}$. OSEM has only been proven to converge when the subset choice is balanced [130]. This is in contrast to the guaranteed convergence of MLEM. Luckily, empirical evidence shows that OSEM provides useful images more rapidly than MLEM.

A downside to MLEM, and by extension OSEM, is that, although both algorithms converge to a solution, this solution may be a very noisy solution. The reconstructed image at convergence is usually denoised by smoothing the image data, or by stopping the reconstruction early, before convergence is actually reached [131]. The image noise originates from the fact that SPECT reconstruction is an ill-posed problem when no prior knowledge is used. Some a priori knowledge about the object distribution is needed, but is not contained in the ML model from Eq. (2.65b).

A-priori knowledge can be included by using maximum a-posteriori (MAP) reconstruction [132, 133] on an extended log-likelihood. Instead of maximizing $P(\mathbf{y}|\mathbf{x})$, MAP estimates $\mathbf{x}$ by maximizing $P(\mathbf{x}|\mathbf{y})$, which is the conditional probability distribution of the image vector $\mathbf{x}$ given the measurement vector $\mathbf{y}$. The new problem becomes

$$\hat{\mathbf{x}} = \arg\max_{\mathbf{x}\geq 0} \mathcal{L}(\mathbf{x}) + \log P(\mathbf{x}). \tag{2.71}$$

A solution to Eq. (2.71) can be found using the one-step-late (OSL) approximation of Green [134]:

$$x_j^{(k+1)} = \frac{x_j^{(k)}}{\sum\limits_{i=1}^{I} w_{ij} + \beta \frac{\partial}{\partial x_j} V\left(\mathbf{x}^{(k)}\right)} \sum_{i=1}^{I} w_{ij} \frac{y_i}{\sum\limits_{n=1}^{J} w_{in} x_n^{(k)}}. \tag{2.72}$$

Parameter β can be interpreted as the relative strength of the prior knowledge compared to the data fit. For $\beta \to 0$, the OSL algorithm converges to MLEM (Eq. 2.69).

The energy function $V(\mathbf{x})$ from Eq. (2.72) is used to model the prior

knowledge $P(\mathbf{x})$. As V is a function of $\mathbf{x}$, knowledge of $\mathbf{x}$ can now be used in the reconstruction, e.g. to reduce image noise, or to reduce the partial volume effect (PVE) in micro-SPECT reconstructions [135]. Several choices have been published in literature, of which many are based on quadratic functions. A formulation depending on the image gradient (e.g. the q-generalized Gaussian Markov random field prior [53] we used in CT reconstruction, see Eq. 2.46) is not as useful in SPECT as in CT, because function edges will not be visible on the relatively low-resolution SPECT images.

2.3.6 Small Animal SPECT

The demand for longitudinal small-animal data has driven the development of miniaturized SPECT or micro-SPECT systems at the start of the 21st century. Such systems should allow for much higher spatial resolution than their clinical counterparts in order to accurately represent the small organs of laboratory animals.

First the spatial image resolution was increased by using pinhole collimators, which can project magnified data onto the detector. The magnification factor of a pinhole depends on the ratio of object-pinhole and pinhole-detector distance, which leads to system designs where the pinhole collimator is placed very close to the animal, while the detector is further away. Because the FOV of a pinhole is also limited, with increasing FOV further from the pinhole, a trade-off must be found between the FOV and the magnification one wants to achieve. As mentioned in Sec. 2.3.3.2, the use of a pinhole collimator will result in a low sensitivity, because only one small entrance window is available.

The poor sensitivity can be overcome in 2 ways, which are not mutually exclusive. The first is by applying changes to the imaging protocol, in order to improve the photon statistics. This can be achieved by increasing the injected radioactivity dose, or by increasing the acquisition time per projection view. However, an increase in radioactivity dose will unnecessarily irradiate the animal, while increasing the scan time can make the acquisitions unmanageably long.

A second proposal is to use multiple pinholes in a single collimator [136–138]. This results in a linear increase in sensitivity, when individual pinhole projections do not overlap on the detector. In the case of overlap, also called multiplexing, an even higher sensitivity can be achieved for the same detector area. However, ambiguity about the inci-

dent angle of the γ-rays in the overlapping area may lead to worse image SNR after reconstruction [139, 140]. In cases of a large amount of overlap, the image uniformity has been shown to decrease, making uniform cylinders appear smaller than their true size [141]. The multiplexing artifacts depend on the activity distribution, pinhole design, detector size and imaging distance [141]. There is no consensus yet if multiplexing—to trade image artifacts for an increase in sensitivity—is an overall benefit or not.

An additional spatial resolution increase can be achieved by decreasing the detector pixel size, especially when magnification is achieved through the use of pinholes. Some recent systems therefore use direct-conversion detectors, mostly based on CdZnTe, which can be segmented into pixels of around 320 μm [142]. Smaller pixel sizes would lead to a too large probability of charge-sharing between pixels [142]. These high-resolution detectors have excellent energy resolution, which allows for improved scatter correction and dual-isotope imaging (e.g. imaging ^{99m}Tc and ^{123}I at the same time). Other micro-SPECT systems use position-sensitive photomultiplier tubes (PSPMTs), which are PMTs with multiple anodes, essentially pixelating the PMT output.

2.3.7 Challenges in SPECT imaging

2.3.7.1 Resolution-sensitivity tradeoff

The major challenge in SPECT imaging is the trade-off relationship between spatial resolution and sensitivity. As discussed before, the use of a pinhole collimator to increase the spatial resolution through magnification will inevitably lead to less sensitivity and a smaller FOV. Furthermore, the sensitivity of pinhole collimators decreases with increasing distance between the object and the pinhole aperture. Because of this trade-off, most current SPECT scanner designs are optimized for specific applications, e.g. for cardiac imaging. Most general clinical systems still use parallel-hole collimators, and are not substantially different from those designed in the early 1980s [143]. Still, improvements in SPECT resolution are effectively only limited by technological advances [144].

2.3.7.2 Absolute quantification

A second major challenge is in obtaining absolute quantitative data. With absolute quantification, the activity concentration (in MBq/ml)

can be directly derived from the reconstructed images. Such an accurate estimation of the activity in each image voxel, and thus also each organ or a tumor, is needed to enable dose calculations in targeted therapy treatment planning, or to follow the treatment of tumors longitudinally [145].

Two criteria can be used to characterize the reconstructed estimated activity: accuracy and precision [145]. While accuracy is a measure of deviation from the true value, precision will measure the variability about its mean value. Depending on the application, low accuracy may be acceptable as long as the precision is high. A consistent bias can then be calibrated by scanning a phantom of known activity, from which the bias can be calculated.

Unfortunately, the image degrading effects described in Section 2.3.4 will lead to an inconsistent bias in SPECT [146]. The finite resolution effects can be corrected by analytical estimation based on the known system geometry, or by Monte Carlo simulation techniques. More important is the correction of attenuation and scatter, which will be patient specific. This means that one phantom acquisition can never be used to calculate the bias for all patients. Current SPECT/CT systems (see Sec. 2.4) correct for attenuation by incorporating the reconstructed patient-specific CT information inside the SPECT reconstruction [118]. Scatter can also be corrected for, e.g. by using window correction techniques [121, 122]. Absolute SPECT quantification will be possible only when a consistent bias is achieved at high precision.

2.3.7.3 Temporal resolution

The limited temporal resolution of SPECT is caused by the low sensitivity of SPECT, and is often overlooked. Biological processes will not stop redistributing the radioactive compound while scanning, and will have some influx and efflux of the tracer over time. Furthermore, in many cases it is this change in the biodistribution of the radiopharmaceuticals in the body that offers the most information about the underlying physiological processes [144]. If the change in biodistribution is imaged by a tomographic system, it is a necessity that every dynamic timespan is recorded for all projection views to get enough data sampling. This imposes a very low maximal duration in which each projection view should be acquired, because dynamic frames are commonly acquired over the order of 1 minute. Ultimately, this results in low photon statistics per view.

2.3.7.4 Small Animal SPECT imaging

Because of the importance of small-animal SPECT for pharmaceutic research, absolute quantification is more sought after in micro-SPECT compared to clinical SPECT. Multiple small-animal-specific applications require absolute quantification, such as measuring the dose-response curve for an experimental drug, monitoring tumor regression or recurrence for novel treatments, or to study changes in cerebral metabolism after sensorimotor challenges [147].

As with clinical SPECT, physical effects will still be detrimental to the quantitative accuracy. However, the much smaller size of laboratory animals will lead to less attenuation and scattering, potentially improving the accuracy compared to clinical SPECT. The overestimation errors resulting from the detection of scattered photons may even be offset by the relatively large underestimation errors caused by photon attenuation [148]. This raises the fundamental question: are attenuation and scatter correction really necessary to achieve absolute quantitative small-animal SPECT? [147]

A second issue, specific to small-animal imaging, is the much faster metabolic rate, respiration rate and heart rate of laboratory animals compared to human subjects. Tracer kinetic modeling provides the link between the distribution of radioactivity in tissue over time, and the relevant physiologic parameters associated with a particular organ or disease state. This technique requires rapid arterial blood sampling, a challenge in itself in small animals due to their small total blood volume, but also requires a fast dynamic SPECT scan to follow the rapidly changing tracer distribution. Dynamic SPECT scans will lead to low photon statistics per view. One possible solution may be to use stationary multi-pinhole SPECT systems [138, 149], which do not require camera rotations during the acquisition. However, stationary systems usually have the disadvantage of a limited FOV, which means they can not be used for fast, dynamic *whole body* scans or even for scans of entire organs.

2.3.8 Applications

2.3.8.1 Clinical SPECT

Numerous medical specialities use SPECT imaging to aid in the diagnosis of disease or to plan disease treatment in patients. In 2012, most

SPECT scans were requested in oncology (44%), cardiology (18%) and endocrinology (17%), followed by pulmonology (8%), nephrology (7%) and neurology (4%) [150]. Common uses of different radioisotopes in these domains were already tabulated earlier in Table 2.1.

A common procedure in oncology is the bone scan, usually with ^{99m}Tc-labeled methyl diphosphonate (HMDP) as a tracer. MDP will measure aspects of bone metabolism or remodeling, as it is taken up by osteoblast cells. It can therefore be used to identify osteoblastic lesions. As a competitor to fluorodeoxyglucose (FDG) PET, MDP SPECT is for example superior in detecting bone metastases in breast cancer [151]. A different example of a tracer used in oncology is ^{111}In-pentetreotide (Octreoscan®). It will concentrate in tumors containing a high density of somatostatin receptors, such as neuroendocrine tumors [152], or medullary thyroid carcinoma [153].

In cardiology, considerable value is added by SPECT imaging, by comparing the blood perfusion at rest to the perfusion during exercise. Together with cardiac PET, it is considered a safe, convenient and reliable procedure to identify and risk-stratify patients with suspected coronary artery disease [154] and to find out if a heart attack has occured, e.g. by using ^{99m}Tc-sestamibi [155], ^{99m}Tc-tetrofosmin [156] or thallium-based tracers [157].

Renal applications commonly use ^{99m}Tc-dimercaptosuccinic acid (DMSA) and ^{99m}Tc-mercaptoacetyltriglycine (MAG3), which can evaluate kidney function [158, 159]. ^{99m}Tc-DMSA is for instance an important indicator of the tubular functioning after the patient received radioimmuno-therapy with ^{90}Y to treat neuroendocrine malignant disease [160]. Damage caused by the renal excretion of the β-emitting ^{90}Y can then be detected [161].

To localize infections, the current tracer of choice is ^{99m}Tc-hexamethylpropyleneamine-oxime (HMPAO)-labelled autologous leukocytes, although using ^{111}In-oxine-labelled leukocytes is also a possibility [162].

Finally, a last example is the use of brain SPECT imaging. It can provide 3D perfusion and metabolic information about the brain tissue. Brain perfusion SPECT is for example used in the diagnosis of dementias, or for the presurgical detection of the epileptic focus in patients with complex seizures refractory to medical treatment [163]. However, PET has been shown to be more sensitive than SPECT for Alzheimer's Disease, with a greater predicting outcome as a result [164]. Although

the choice between PET and SPECT seems to favor PET for the diagnosis of dementia, few clinicians will have the choice between the two [164]. SPECT is still a credible alternative to FDG-PET, thanks to its higher availability and lower cost [165].

Quantitative SPECT has its own, specific applications or potential uses, with a typical example the personalized therapy for oncological applications. Generally, the use of quantitative SPECT will allow the monitoring of serial scans to assess disease progression or the response to treatment, e.g. with ^{67}Ga in infections [166]. It can also enable true personalized planning and treatment, by using an isotope to deliver patient-specific targeting and plan patient-specific dosimetry, before using a monoclonal anitbody, peptide, receptor or radionuclide therapy to treat the patient. One such example is to acquire SPECT images with ^{123}I to determine the patient-specific dose that will be delivered by ^{131}I when it is used to ablate differentiated thyroid carcinoma with its beta decay mode [167]. ^{131}I is not routinely used for imaging by itself because of its poor properties for imaging with gamma cameras [168].

More specific applications can be found in myocardial perfusion, where quantitative SPECT would allow the determination of regional myocardial blood flow in mL.100 g^{-1}.min^{-1} [169]. In ^{99m}Tc bone scan studies, metabolic bone disease could be quantitatively measured [170]. A comprehensive review of applications benefiting from quantitative SPECT can be found in Bailey et al. [166].

2.3.8.2 Micro-SPECT

The application of SPECT in preclinical models of diseases allows us to non-invasively and longitudinally investigate dynamic biological processes at a molecular and cellular level [171]. Unsurprisingly, micro-SPECT is predominantly used to study disease progression and the biological effects of novel drug candidates on these models. It can also assist in finding disease biomarkers, from which new pharmaceutical therapies can be designed.

A large number of applications can be found in cardiovascular imaging, e.g. to study myocardial function and the influence of several vascular disorders. ECG-gated micro-SPECT studies can yield accurate measurements of left ventricle volumes and ejection fractions in rats [172] and mice [173], or they can be used to visualize necrotic tissue during myocardial infarction, e.g. to evaluate the anti-necrotic effect for ischemic

heart disease.

Another relevant cardiovascular application is the characterization of the formation and prognosis of atherosclerotic plaques, for example by using radiolabeled Annexin which targets apoptotic macrophages [174]. Here, a high spatial resolution is needed to image the small plaques in the motile vessel.

A different application is the imaging of stem cells, to track the engraftment of transplanted cells by labeling the stem cells with e.g. ^{111}In-oxyquinoline before transplanting the stem cells in rat models of myocardial infarction [175].

For oncology, the basic biological process, tissue pharmacokinetics and pharmacodynamic responses to treatment can be investigated in preclinical models of human tumors. Here, the receptors that are overexpressed in cancer cells can be imaged, e.g. by using ^{111}In-Octreotide to image the somatostatin receptors overexpressed by some non-small lung cancer carcinomas. A different example is to find the reasons why ^{111}In-Capromab suffers from poor delivery in prostate cancer [176].

In neuroimaging, preclinical models can be used to help in understanding the pathophysiology of central nervous system disorders, such as neurodegeneration, drug abuse, and testing therapeutic strategies. SPECT has for example been applied to study Parkinson's disease, by imaging the presynaptic dopamine transporter (DAT) activity which regulates the synaptic dopamine. This can be investigated with ^{123}I-FP-CIT as a DAT radioligand in rat models [177], mice [178], or even the common marmoset monkey [179].

Lastly, preclinical imaging has a key role in drug development [180]. Here, new drugs are radiolabeled and imaged with SPECT in order to determine its distribution and pharmacokinetics, to determine drug safety [181, 182], and to validate imaging biomarkers [180].

2.4 Hybrid SPECT/CT imaging

2.4.1 Principle of multi-modality imaging

Hybrid imaging is defined as the fusion of two or more imaging technologies into a single, new form of imaging [183]. Typically, the goal is to achieve an imaging modality which is more powerful than the sum of its components. The most interesting combination is one where molecular processes can be viewed *in vivo* within a broader anatomical context.

Several multi-modal combinations have been proposed to achieve this synergy: SPECT/CT [184] and PET/CT [185] are the best known combinations. PET/MRI [186, 187] has recently become available, while SPECT/MRI is still being developed [188].

In first reports, both modalities were combined by acquiring each dataset on a completely different single-modality system. It was then necessary to co-register both reconstructed images, in order to combine the information into one image [189]. The first and simplest forms of image registration used were rigid-body translations and rotations, assuming body parts did not move relative to each other while moving the patient between both system. It was soon apparent that the situation is more complicated. The geometrical relationship between anatomical regions can be affected by the shape of the patient tables used in both systems, the orientation of the body and limbs during each acquisition procedure, as well as the respiratory state of the patient [190]. This is a problem especially for functional imaging of the thorax or abdomen, because there are no anatomical landmarks available in the FOV that can be correlated with anatomic reference points [191]. More advanced registration methods do exist, but in most cases this remains challenging [192], and these methods should be avoided.

In 1995, Blankespoor et al. merged the anatomical and the functional imaging subsystems inside one single device to improve the correlation of two image modalities, based on the work of Hasegawa et al. in the 1980s and 1990s [193–195]. In this so-called dual-modality imaging device, the patient is not removed from the scanner and both imaging modalities are acquired sequentially by automatically moving the bed from one part of the system to a second. In small-animal imaging, this technique further evolved into true dual-modality systems, where both modalities are located on the same gantry [83]. Now the animal does not need to move between both, removing the need to register between two bed positions.

It is important to note that multi-modality imaging is more than the sum of its components. Correlations between functional information and anatomical landmarks is only one benefit of multi-modality imaging [196]. Firstly, it gives more confidence in diagnostics: there is an increase in the sensitivity as well as the specificity of diagnostic findings [197]. Uptake on a functional image will give more confidence that a nodule seen on a CT image does have diagnostic value. Secondly, there is a lot of information to be gained by imaging before and after

therapy. Some nodules may still be visible post-therapy on anatomic images, though they may not be responding on a functional level, informing us that the therapy is working.

2.4.2 Challenges in SPECT/CT

A first limitation of SPECT imaging is the attenuation of γ photons. Due to photoelectric absorption and Compton scattering, the attenuation will lead to projection images with lower intensity than the expected intensity. In Section 2.3.4 it was discussed how transmission-based measurements may be used to measure the attenuation using a different γ-emitter [118] for single SPECT. In SPECT/CT the measured CT images can be used, as they form a direct representation of the tissue attenuation.

However, the CT-based attenuation values are measured by a polyenergetic X-ray spectrum, with energy different from that of the monoenergetic γ-rays of the radioisotope used during the SPECT acquisition. This means that the reconstructed attenuation values need to be rescaled to match the radioisotope energy. Different scaling schemes have been proposed [198], but these do not take into account the K-edge of contrast media often used to visualize the vascular system on the CT images. Furthermore, effects such as respiratory-induced misregistration of emission and transmission data, truncation artifacts due to FOV differences, metallic implants, beam-hardening, and X-ray scatter need to be considered, as these will considerably influence the apparent CT values. Inaccurate CT values will lead to inaccurate attenuation information, which will under- or over-correct the SPECT data.

In small-animal SPECT/CT, issues with the co-registration between SPECT and CT have been handled by placing the SPECT and CT subsystems on one single gantry, to reduce the need for bed translations, which is a major source for animal movement. This is also possible thanks to the common use of cone-beam detectors in micro-CT, which does not need bed translations due to its large axial FOV.

The major challenge for preclinical SPECT/CT is how absolute quantitative SPECT data can be obtained, and what the general accuracy will be of such methods. Not only is there the issue of attenuation and scatter, this is also complicated by the low sensitivity of high-resolution pinhole-based systems. Several correction schemes have been proposed to correct for the image degrading effects, but it is still unclear what the

achievable accuracy and precision is in vivo micro-SPECT/CT.

2.4.3 Applications

SPECT has become more and more used especially when combined with CT [197], as it allows to solve some challenges of SPECT in a more straight-forward way. Nevertheless, in 2012, SPECT/CT only accounted for 19% of the total number of nuclear medicine scans, when PET scans are not taken into account [150].

SPECT/CT lends itself to a wide variety of useful diagnostic applications. The role of SPECT/CT is continuously growing in oncology. Research has demonstrated diagnostic accuracy improvements in a ^{131}I scan of differentiated thyroid cancer, because cervical lymph node metastases can now be better distinguished from residual thyroid tissue, lung can be distinguished from mediastinal metastases and bone can be distinguished from soft tissue metastases [199, 200]. This resulted in an overall 21 to 73.9% increase in diagnostic accuracy, led to the modification of therapeutic management and avoided unnecessary treatment [167].

In neuroendocrine tumors (NETs), dual-modality imaging is undoubtedly necessary. The primary tumor is usually small and may evade detection on conventional CT imaging [201]. With functional imaging, e.g. imaging of somatostatin receptors (SSR) subtypes 2 and 5 with ^{111}In-Octreotide, a sensitivity of 80 to 100% can be achieved in localizing NETs. At the same time, it helps identify patients who may benefit from radiolabelled somatostatin analogue therapy [201]. When anatomical data is used to exclude physiological tracer uptake from the SPECT data, localization of uptake improved in five of eight patients [202] with NETs. Other NETs can be imaged using ^{123}I or ^{131}I-labelled metaiodobenzylguanidine (MIBG), with an improved identification of the physiological tracer uptake in 74% of the cases [203].

SPECT/CT also has its benefits in non-oncological disorders, such as benign bone diseases, to localize infection and inflammation, identify gastroinestinal bleeding, pulmonary embolisms, coronary artery disease, splenosis, and even neurodegenerative disorders [167].

2.5 Summary

In this introductory chapter, the background concepts of medical imaging were explained. A broad overview of medical imaging was given, followed

by a more detailed description of X-ray CT and SPECT in particular.

Both the CT and SPECT sections contained discussions on some important limitations encountered with those imaging modalities.

In CT, X-ray radiation dose is a major challenge. This is important in both clinical as well as preclinical studies, where patients are scanned a number of times to evaluate longitudinal progression. It is therefore important to reduce the radiation dose, without affecting the image quality. Chapters 3, 4 and 5 discuss how reducing the number of projection views can lead to an 8-fold decrease in radiation dose in micro-CT, by using regularized iterative CT reconstruction.

In SPECT, the major challenge is absolute quantification. Quantitative data enables measuring of dose-response curves for experimental drugs, or the evaluation of tumor regression or tumor recurrence after novel treatments. However, to achieve absolutely quantitative SPECT data, all image degrading effects should be corrected for. Quantitative SPECT reconstruction with such correction techniques is the topic of Chapter 6 and Chapter 7.

Chapter 3

Replacing vascular corrosion casting by in vivo CT imaging to build 3D cardiovascular models of mice

Before delving deeper into how the X-ray radiation dose can be decreased, we first need to define a specific task. This will allow us to quantify the influence of low-dose acquisitions on the task outcome. In this chapter we investigate if and how vascular corrosion casting, the golden-standard to build 3D cardiovascular models of mice, can be replaced by *in vivo* contrast-enhanced micro-CT imaging. This would allow the use of micro-CT imaging for longitudinal research, beneficial for the research into the progression of vascular diseases.

3.1 Introduction

Mouse models can provide valuable information about the development and progression of cardiovascular pathologies within a reasonable timeframe. Two such pathologies are the aortic aneurysms and aortic dissections. An aorta aneurysm can be described as an abnormal dilatation of the aorta. Aortic dissection is the splitting of layers of the aortic wall, giving rise to a secondary cavity, which results in very complex aortic lesions. Both diseases might lead to a mechanical failure with rupture of the aorta, most often leading to the immediate death of the patient. The

incidence of aortic aneurysm is 10.4 per 10000 patient-years [204], i.e., in a group of 60 year old people 6.2% will have developed an aneurysm.

There are still unresolved issues with respect to aortic disease at the level op pathophysiology and pathogenesis, its diagnose, and its treatment. Previously, hemodynamic factors and blood flow patterns have already been linked to the genesis and development of atherosclerotic cardiovascular disease [205, 206] and to the growth and progression of aneurysms [207]. The study of blood flow patterns inside the aorta is often done using Computational Fluid Dynamics (CFD), both in animal and in human models, in an attempt to elucidate the role of these biomechanical actors/stimuli in the early disease stages. An important parameter in this respect is the tangential shear force exerted by blood moving along the axis of flow (called wall shear stress or WSS). It would be very useful if realistic CFD simulations could be performed on (genetically modified) animal models to investigate the development of the cited cardiovascular pathologies over time. Such genetically modified mice can be used to study abdominal aortic aneurysm formation [208, 209], but also cerebral aneurysm formation [210], atherosclerosis [211–213], vascular remodeling [214], angiogenesis [215], or even specific genetic disorders such as Marfan and Loeys-Dietz syndrome [216–220].

In order to perform CFD simulations, reliable 3D computer models of the cardiovascular system are needed. Most studies that performed CFD simulations in mouse models in the past created a geometrical model by *ex vivo* micro-CT scanning of a plastic replica of the arterial system [112–114] (Fig. 3.1), obtained by vascular corrosion casting [221]. This technique certainly results in high quality models [112]. However, it requires sacrificing the animals and thus excludes follow-up studies, eliminating the possiblity to gather longitudinal information of disease progression. When the influence of the local hemodynamics on disease development are investigated, follow-up experiments are definitely required in order to compare the hemodynamic situation pre and post disease development [222]. Alternative *in vivo* imaging techniques permitting scans of the same animal at multiple time points are clearly indispensable.

In vivo imaging with micro-CT might be a good alternative to vascular corrosion casting. Unfortunately, it still suffers from the challenges discussed in Section 2.2.7.3. A first challenge is the limited soft-tissue contrast in X-ray based techniques. Iodine-based contrast agents are used in human studies to aid in the differentiation between the aorta and its surrounding tissues, thanks to the K-edge effect (see Section 2.1.3). How-

Figure 3.1: Plastic replica of the murine aortic arch with its branches (courtesy of Bram Trachet).

ever, traditional contrast agents developed for human use cannot be used preclinically. They are hydrophilic and have a low molecular weight, resulting in fast blood elimination via the kidneys [89]. Combined with the fact that micro-CT scanners typically have a total acquisition time of at least 5 to 10 minutes, these agents are not useful for preclinical imaging. Several contrast agents have been developed to combat this problem. One agent is Fenestra VC-131® (Advanced Research Technologies Inc., Saint Laurent, Canada), specifically developed for cardiovascular imaging in mice. It shows a slow uptake in the liver, enabling a sufficient time period of contrast-enhanced imaging of the blood before the contrast is cleared through the renal system.

The goal of the study presented in this chapter is to investigate whether reliable and accurate 3D geometrical models of the murine aortic arch can be constructed using *in vivo* micro-CT with such a novel contrast agent. First the contrast agent, micro-CT protocol and vascular corrosion casting technique will be explained in more depth. Then we will compare geometrical models obtained from both techniques based on the model diameters, bifurcation angles and geometrical shape of the model. We will also conduct CFD simulations to investigate the actual influence of possible changes. This will be followed by a description and discussion of the obtained results, followed by a conclusion. The specific remarks made in the discussion and conclusion will form the basis for Chapter 4.

3.2 Study design

A total of nine 5 to 27 week-old wild-type mice were used in the experiments, with body weights (BW) ranging from 14 to 35 g (Table 3.1). The animals were anesthetized and scanned in vivo after administration of the contrast agent. Subsequently they were casted via the abdominal aorta with 2 ml of Batson's No. 17 casting solution. The resulting plastic replicas of the arterial system were scanned in vitro using micro-CT. Both data sets were segmented and used to generate a 3D model, which was then compared. All animal experiments were approved by the Ghent University ethical committee (ECD 07/20).

3.3 In vivo micro-CT imaging

All mice were scanned in a trimodal FLEX Triumph-II cone beam CT scanner (TriFoil Imaging, Northridge, CA, USA) with the following acquisition parameters: 70 kVp tube voltage, 50 μm focal spot, 1184×1120 detector pixels of 100 μm pixel size (2x2 binning), 2048 projections over 360° total rotational angle and a 3.5 times magnification. The ideal tube current was determined by increasing the current until the detector response saturated during a blank scan. This current was determined at 180 μA for a 70 kVp tube voltage. The gantry was set to rotate continuously, providing faster acquisition compared to step-and-shoot mode.

This parameter selection results in a 33.81 mm transverse field of view (FOV), a theoretical spatial resolution of 46 μm and a total scanning time of 8.53 minutes. The projections were reconstructed with a proprietary implementation of the analytic FDK algorithm (Cobra EXXIM, EXXIM Computing corp., Livermore, USA) to a 512x512x512 voxel matrix with voxel pitch 50 μm.

3.3.1 In vivo: Fenestra VC-131

Fenestra VC-131 binds iodine particles (50 mg/ml) on lipids to ensure hepatobiliary instead of renal clearance, leading to 4 hours of contrast-enhanced visualization time. Previous research by Mukundan et al. [87] have shown that Fenestra VC-131 induced no significant risk on renal toxicity. However, anecdotal evidence has shown that some measures are warranted to help prevent dehydration caused by the use of Fenestra VC-131. The mice therefore received an intraperitoneal (IP) injection of

100 μL physiological fluid one hour before the start of the experiment to help the mice hydrating. Furthermore, because small animal feed can contain minerals which cause slight metal artifacts on abdominal images, all 9 animals were placed on a diet of cooked yam (sweet potato) 24 hours before the experiment.

Fifteen minutes after the administration of the contrast agent through the tail vein with a bolus injection, the animals were anesthetized with an 8 μL/g IP injection of a mixture of 1.05 ml ketamine (Ketamine 1000, CEVA Santé Animale, Brussel, Belgium), 0.3 ml xylazine (Xyl-M 2%, VMD, Arendonk, Belgium) and 3.4 ml physiological fluid. The micro-CT scans were acquired 10 minutes after inducing anesthesia, as optimal contrast is achieved approximately 25 minutes after administering this contrast agent [223]. The 25 minute total delay also reduced the probability of irregular animal motion due to spasms, which would otherwise affect imaging quality. The mice were placed on a heated bed (30°C) to prevent the body temperature decreasing during the scan.

To determine the minimal volume of contrast agent needed to obtain sufficient contrast for segmentation purposes, we measured the contrast increase for two volumes: 0.015 ml/g and 0.020 ml/g. Both concentrations were suggested by the contrast agent manufacturer [224]. The mean image noise in a non-contrast baseline image was determined at 24.7 gray values. Administering 0.015 ml/g (Figures 3.2b and 3.2d) contrast lead to an increase of 118±2 gray values in the aortic arch, compared to the baseline image (Figures 3.2a and 3.2c). With 0.020 ml/g, a contrast increase of 175±3 was achieved. According to Rose [225] and Burgess [226] a contrast increase of 5 times the background variation should be achieved to allow for segmentation. This means 0.020 ml/g leads to an unnecessary high contrast and a subsequent extra burden on the cardiovascular system. We chose to use 0.015 ml/g for the remainder of this study based on these findings. This leads to contrast-to-noise ratio (CNR) of 4.7.

3.3.2 Gating

As was discussed in Section 2.2.7.3, one of the challenges with small-animal micro-CT is animal movement during acquisition. This result in inconsistent data between projection views. Several methods exist to minimize the effect of movement, ranging from adjusting the acquisition protocol [8, 227], to retrospective data processing [228, 229], to incorporating measured motion signals into the reconstruction algo-

Mouse	Age (weeks)	Weight (g)	Contrast dose (ml/g)	Anesthetics (ml)	ΔT_s (min)	ΔT_c
1	27.6	23.0	0.015	0.10	25	23 h
2	14	21.7	0.015	0.10	25	22 h
3	14.9	27.5	0.015	0.10	25	21 h
4	14	25.5	0.015	0.10	25	19 h
5	27.6	30.7	0.015	0.10	25	20 h
6	27.6	35.0	0.015	0.10	25	19 h
7	5	16.8	0.015	0.10	25	6 d
8	5	15.8	0.015	0.12	25	5 d
9	5	14.6	0.015	0.12	25	7 h

Table 3.1: Mouse specifics for nine mice injected with Fenestra VC-131. ΔT_s denotes the time between contrast injection and scan. ΔT_c is the time between scanning and casting.

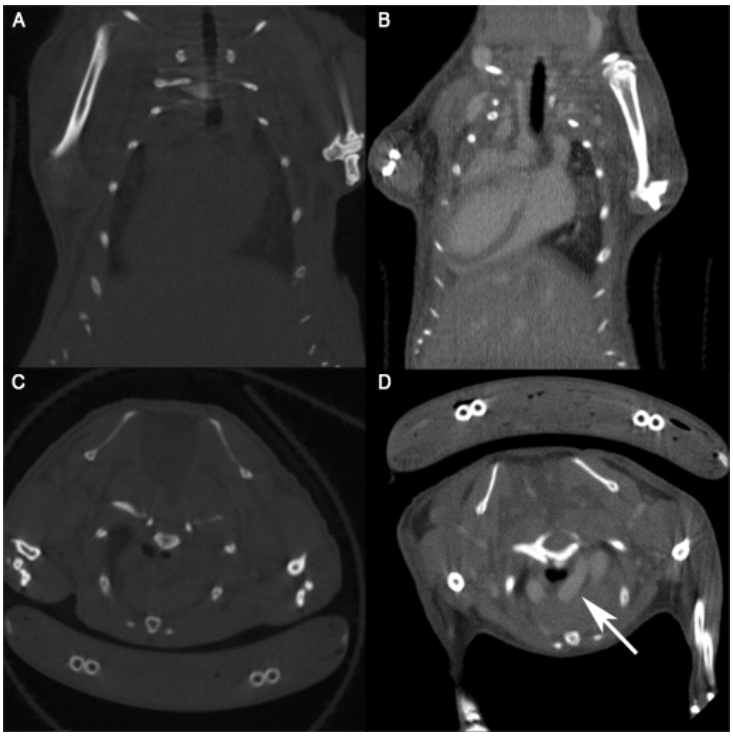

Figure 3.2: Coronal and transverse micro-CT slices showing the difference between baseline (**a** and **c**) and contrast-enhanced imaging (**b** and **d**) after administration of 0.015 ml/g Fenestra VC-131. This leads to an increase of 118±2 gray values in the aortic arch (*arrow*).

rithm [93, 230].

To investigate if gating would improve our image quality, we used a retrospective respiratory gating method proposed by Ford et al. [228, 231]. This methods requires a region of interest (ROI) selection on the projection views containing both the diaphragm and the lungs of the animal (Fig. 3.3). This allows us to compute the centre of mass (CM) in the ROI per projection. Each projection can then be classified as in end-expiration or end-inspiration phase according to the position of the CM. After classification of all projections, end-expiration was found in 820 projections. These were reconstructed and compared to the ungated reconstructions from the full 2048-view dataset. As reconstruction algorithm an FDK implementation including non-uniform weighting was used [232, 233], because the gated views are not uniformly spaced anymore over 360°.

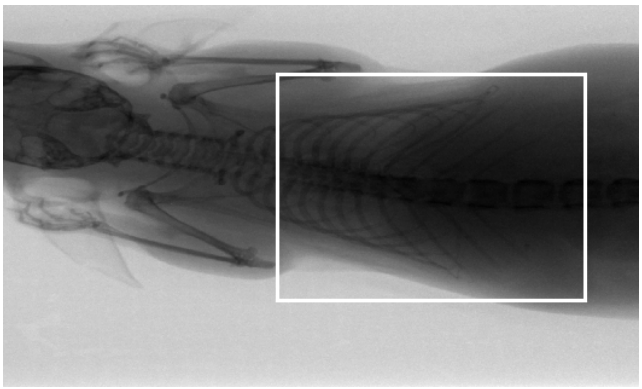

Figure 3.3: Projection view with ROI (white rectangle) in which the centre of mass can be calculated for retrospective respiratory gating.

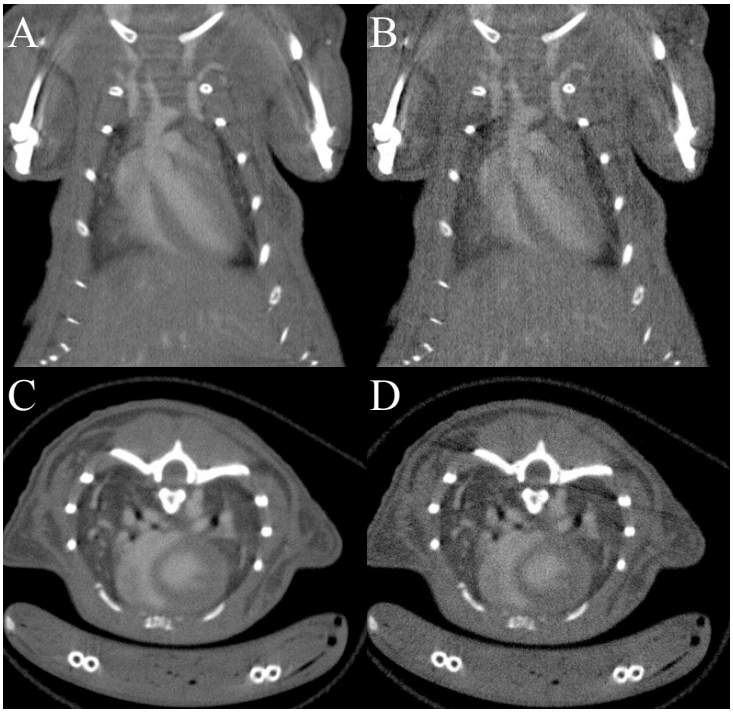

Figure 3.4: Comparison between ungated slices (**a** and **c**) and retrospective respiratory-gated slices (**b** and **d**) for mouse 5 (Table 3.1). All slices are shown in the same window level and size. The gated images show better delineation of the diaphragm and the ribs but no significant image quality increase in the cardiovascular system.

Figure 3.4 shows a comparison between ungated slices (Figures 3.4a and 3.4c) and retrospective respiratory-gated slices (Figures 3.4b and 3.4d) for mouse 5 (Table 3.1). All 4 slices are shown with the same window level and size. The gated images show no improved delineation of the cardiovascular system.

The increase in image noise and streaking artifacts due to the lower angular sampling decreases the image quality more than it is improved by improved delineation of different structures. Therefore we did not use any respiratory gating in the remainder of this study.

3.4 In vitro vascular corrosion casting

For each of the 9 animals scanned in vivo, the goal was to make a corrosion cast 1 week after the CT acquisitions, to evaluate the animal health due to the use of the contrast agent. When the health of the animal did not permit waiting one week, the animal was euthanized and casted as soon as possible to limit animal suffering. Batson's No. 17 (Polysciences, Inc., Warrington, USA) was used as casting agent [234]. This agent causes little shrinkage, can still fill the smallest vessels and delivers mechanically stable casts.

First, the mice were euthanized by an inhaled CO_2 overdose. After making an abdominal incision, the abdominal aorta was located. Special care was taken to prevent rupture to vessels or organs, as this would greatly reduce the quality of the cast. A catheter was then placed in the abdominal aorta in retrograde direction and the arterial system was perfused with a ready-made mixture of Batson's No. 17. Complete filling of the vascular system was indicated by the appearance of red intravascular polymer shining through the skin of the toes and nose [235]. After the perfusion the cadaver was placed in a cold water bath to avoid tissue damage that might occur during the exothermic curing process.

After waiting for 30 minutes, the preparation was placed in a bath containing a macerating solution of 20% KOH at room temperature. Three days later the left-over structure was removed from this bath, the cast was cleaned in distilled water and dried. An example of the result of this procedure is shown in Figure 3.5.

3D models were generated from each cast by using the same micro-CT scanner as used in the in vivo experiments, with parameters: 2x2 binning, 2048 projections, 70 kVp (180 μA) and magnification factor 3. Each cast was put in an acrylic tube to prevent the cast from moving during the

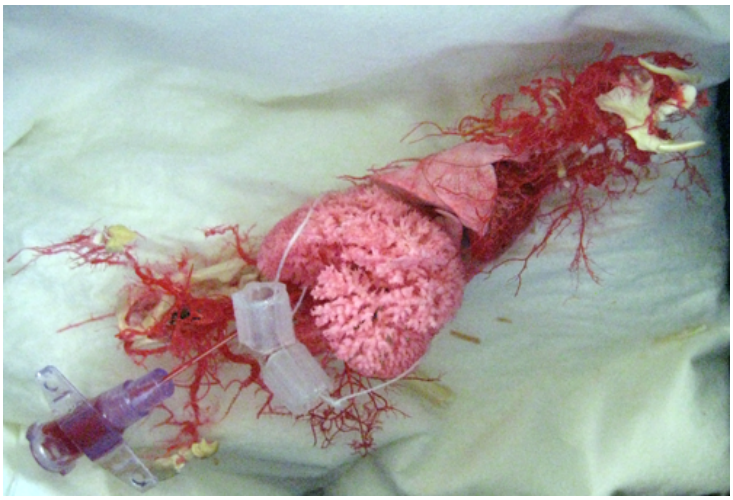

Figure 3.5: The result of the vascular corrosion casting procedure. The lungs and liver can be clearly identified, alongside the vascular system and some bones. The plastic cylinders were used as an identification tag.

scan due to airflow, which leads to a slightly lower magnification to allow the complete tube to be imaged in the FOV.

From the 9 mice, high-quality casts were obtained for only 4 animals: mice 5, 6, 7 and 8 listed in Table 3.1. Casts from the other mice were not filled completely and contained air bubbles, which made comparison impossible. Two animals died and were quickly cast before the blood would coagulate. Five out of 9 animals were sacrificed prematurely to limit animal suffering when their health was found to be declining.

While dissecting the mice in preparation of the casting procedure, some small effects were noticed: the liver was colored more white than usual, some lymph nodes were opaque white and we noticed some mice had cornea edema. We believe this to be caused by the contrast agent, which is also colored opaque white.

3.5 Segmentation

Each CT dataset (both from the in vivo and the casting procedures) was segmented manually in the Mimics (Materialise, Leuven, Belgium) software package. For the in vivo datasets, each part of the aortic arch (ascending aorta, aortic arch with its branches and the descending aorta)

	Cast (mm)	In vivo (mm)	Difference (%)	
AA	1.08±0.18	1.43±0.13	34.91±21.03	*
BT	0.55±0.12	0.78±0.10	44.13±52.46	
AoA	0.93±0.15	1.24±0.11	35.05±22.11	*
CCA	0.40±0.14	0.51±0.02	44.16±59.29	
SA	0.45±0.10	0.62±0.07	44.40±53.53	
DA	0.87±0.19	1.13±0.18	30.87±14.08	*

Table 3.2: Aortic arch diameters (mean ± SD). AA: ascending aorta. BT: brachiocephalic trunk. AoA: aortic arch. CCA: common carotid artery. SA: subclavian artery. DA: descending aorta. *: significant difference ($p < 0.05$)

was manually thresholded in a first segmentation step, using different thresholds for each part. This allows a more accurate segmentation, as every part has a distinct image value on the reconstructions. This is not necessary for the casted datasets, thanks to the high contrast between the cast and the surrounding air.

When the resulting segmentation was judged sufficiently accurate, a 3D geometric model was built according to this segmentation mask. This 3D model was smoothed in Mimics Remesher (Materialise, Leuven, Belgium), to remove unphysiological bulges and dents while care was being taken that no artificial shrinking of the model occurred. This resulted in a sufficiently smooth and simple 3D model usable for CFD simulations.

3.6 Comparison

The actual comparison between both techniques was computed in 4 different ways: by aorta diameter, bifurcation angles, a 3D distance metric, and by comparing the results of CFD simulations.

3.6.1 Aorta diameters

We determined the diameter of the 3D models on the 6 different locations illustrated in Fig. 3.6: ascending aorta, descending aorta, left subclavian artery, left common carotid artery, brachiocephalic trunk and the middle of the aortic arch between the left common carotid artery and the brachiocephalic trunk. Each diameter was calculated as the mean over a large area.

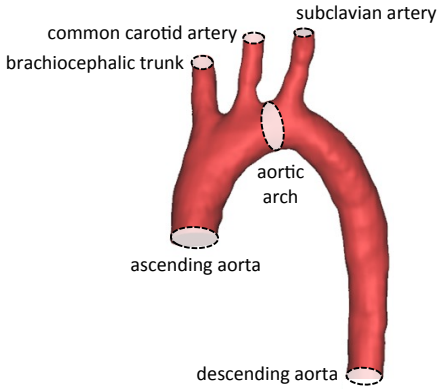

Figure 3.6: Aortic arch anatomy and the locations of diameter measurements

The aorta diameters obtained from the 3D models generated from the scanned casts and the in vivo images are listed in Table 3.2. The diameters show a significant difference (Student's t-test, $p < 0.05$) between in vivo and cast models. Using Fenestra VC-131 this difference amounts from 30% up to a 44% increase in diameter. The aortic arch diameters (AA, AoA and DA) show an overall 33.61±17.67% difference, while the three bifurcation diameters (BT, CCA and SA) exhibit a larger difference of 44.24±49.65%. The large difference and variation on the bifurcation diameters is caused by one dataset (mouse 7 in Table 3.1), where the *in vivo* segmentation was on average 118% larger than the segmentation of the cast. When the data obtained from mouse 7 is not taken into account, the difference decreases from 44.24±49.65% to 16.54±16.28%.

Figures 3.7 and 3.8 respectively depict a regression plot and a Bland-Altman plot obtained after pooling the aortic diameters. The Pearson correlation coefficient equals 0.91 for the diameters (standard error of the estimate (SEE) 0.12 mm), showing a good correlation between both measurement methods. The Bland-Altman plot shows that the variation does not depend on the diameter of the vessels. However, there is an absolute systematic bias of 0.22 mm ($p < 0.001$).

3.6.2 Bifurcation angles

As second metric the bifurcation angles were considered. These were measured in the plane of the bifurcation as the angle between the centerline of the side branch and the centerline of the aortic arch. This provides insight in the angle and resistance encountered by the blood

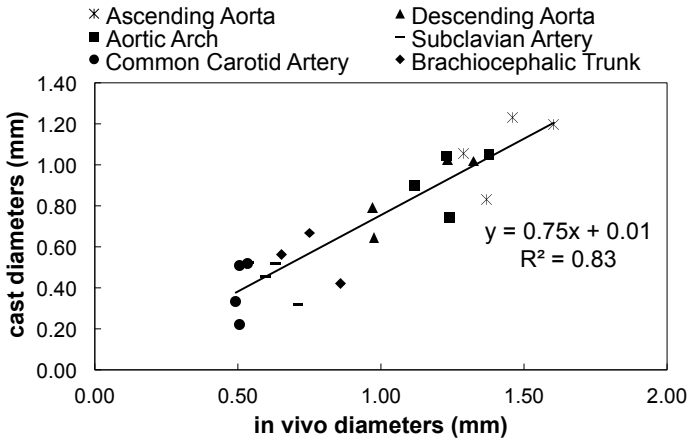

Figure 3.7: Regression plot for the pooled aortic arch diameters. Diameter SEE equals 0.125 mm.

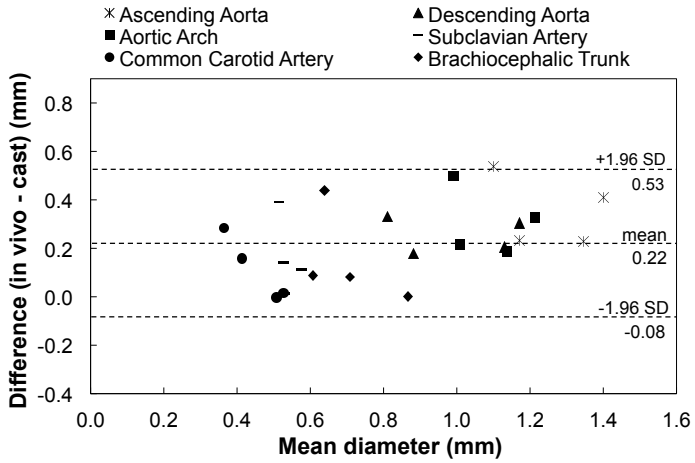

Figure 3.8: Bland-Altman plot for the aortic arch diameters. Dashed lines are the limits of agreement (mean ± 1.96 SD).

	Cast (°)	In vivo (°)	Difference (%)	
BT	136.24±6.70	127.37±5.58	-6.37±4.78	
CCA	119.56±1.64	106.76±2.47	-10.58±6.39	*
SA	103.07±5.36	87.29±2.80	-14.32±13.75	
AA–DA	27.98±4.88	34.79±2.63	31.52±28.30	

Table 3.3: Bifurcation angles (mean ± SD). BT: brachiocephalic trunk. CCA: common carotid artery. SA: subclavian artery. AA–DA: ascending aorta–descending aorta. * : significant difference ($p < 0.05$)

flow in moving from the aortic arch to a side branch.

The bifurcation angle measurements are listed in Table 3.3. The angles show a significant difference ($p < 0.05$) between the casts and the in vivo models only for the common carotid artery angle.

Figures 3.9 and 3.10 respectively show a regression plot and a Bland-Altman plot obtained after pooling the aortic angles. The Pearson correlation coefficient equals 0.97 (SEE 11.13 degrees), showing a good correlation between both methods. The Bland-Altman plot shows a significant ($p < 0.01$) absolute systematic bias of 7.66°.

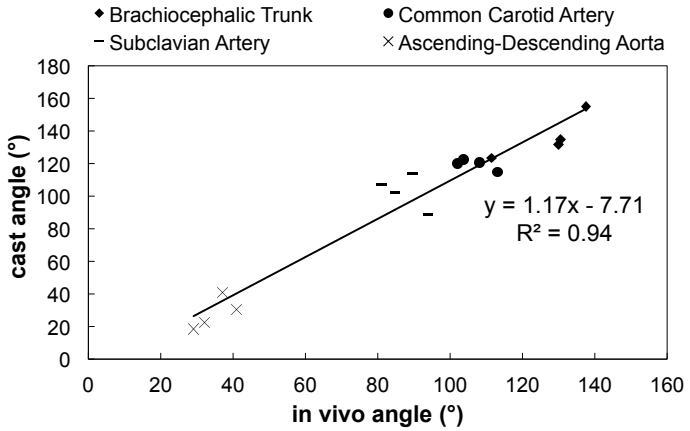

Figure 3.9: Regression plot for the aortic arch angles. Angle SEE equals 11.13°.

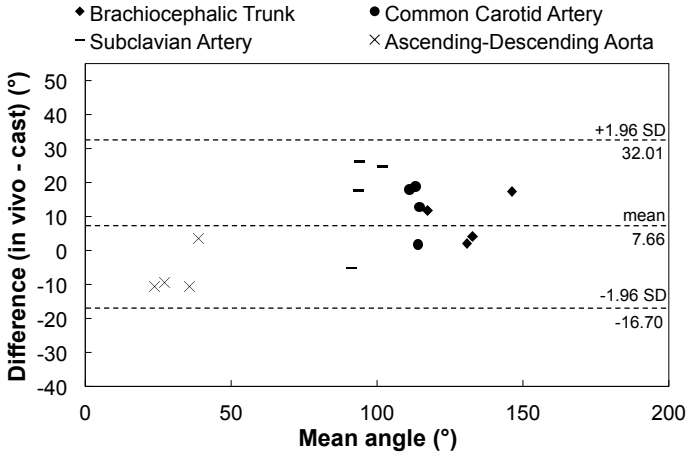

Figure 3.10: Bland-Altman plot for the aortic arch angles. Dashed lines are the limits of agreement (average ± 1.96 standard deviation of the difference).

3.6.3 3D distance metric

As a third metric a general distance metric between co-registered voxels on the models was used. First we co-registered every casting model with the in vivo data from the same animal, and then we used a color code dependent on the Euclidean distance between both 3D models.

Figure 3.11 compares the general geometry in 3 different view angles of the 3D model built from mouse 6 using both modalities. Figure 3.12 shows the co-registered models from Fenestra and the casts colored with a green-red coloring scheme. Blue was used to mark voxels with no distance difference; red was used when the distance was maximal. These colors were normalized and the different models can thus be compared. These results show that the aortic arch geometry of both the 3D cast and the 3D in vivo model are highly comparable. The descending aorta region shows the highest difference, due to the descending aorta bending away.

3.6.4 CFD simulations

Finally we performed CFD simulations on all 3D models to compare the influence of the imaging techniques on the resulting computed WSS levels. All CFD simulations were performed as described in the earlier work of Trachet et al. [112]. In order to quantify the difference in WSS

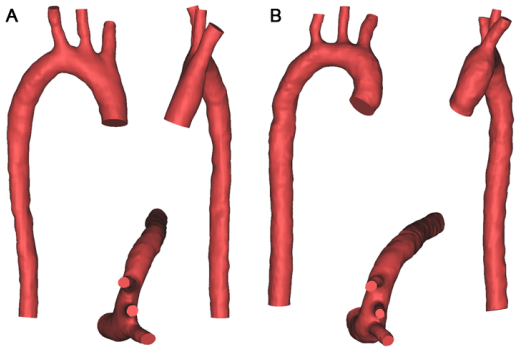

Figure 3.11: General geometry of a 3D model generated from the *in vivo* dataset for mouse 6: cast model (**a**) and *in vivo* model (**b**).

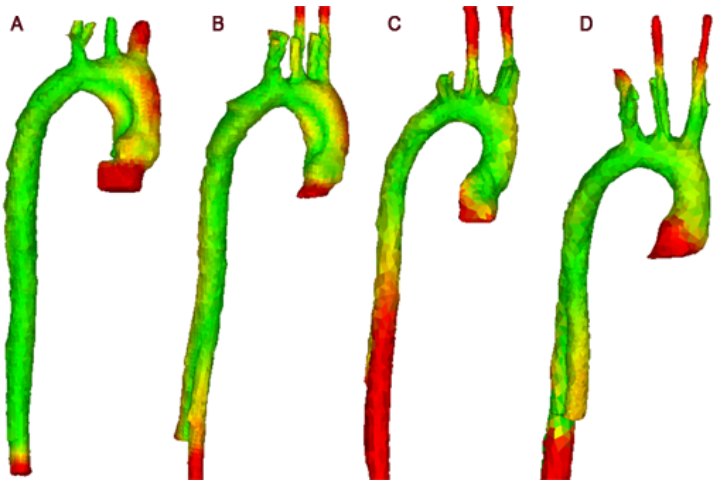

Figure 3.12: Comparison between co-registered models from Fenestra VC-131 and the casts for mice 5 (**a**), 6 (**b**), 7 (**c**), and 8 (**d**). A *green* color code was used to mark voxels with little distance; *red* was used when a large distance was measured. All colors were normalized. The descending aorta region shows the highest difference, due to the difference in AA–DA angles.

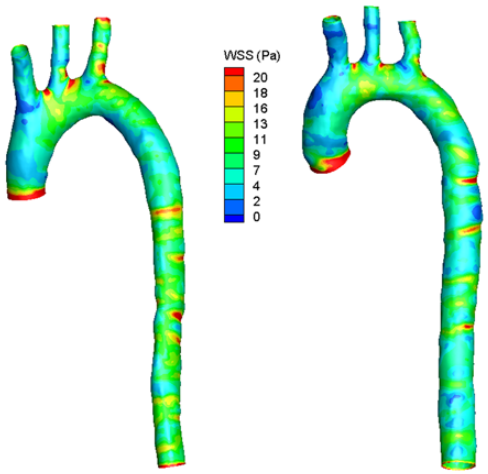

Figure 3.13: Comparison of the time-averaged WSS distribution for mouse 6 for both a casting (*left*) and an *in vivo* model (*right*).

between the models, spatially averaged WSS (WSS_{av}) was computed for each time-averaged model as well as the 95% WSS value ($WSS_{95\%}$) as an indicator of the highest WSS values.

Figure 3.13 plots the time-averaged WSS distribution for mouse 6 for both a casting and an in vivo model. The distribution of time-averaged WSS over the model surface is very similar: zones with high or low absolute values occur in the same region for both models. However, the in vivo models on average show lower absolute WSS values: the spatially- and time-averaged WSS_{av} is 8.20±0.79 Pa for in vivo models and 10.52±2.52 Pa for the cast models, which is not a statistically significant difference. The time-averaged 95% percentile $WSS_{95\%}$ was also not statistically significant different, with 16.55±1.60 Pa for the in vivo models and 19.35±3.72 Pa for the cast models.

3.7 Discussion

In this chapter, a method was proposed to visualize the aortic arch and its bifurcations using micro-CT, providing an alternative for vascular corrosion casting. The resulting 3D geometry models from in vivo scans are compared to models of vascular corrosion casts and are found to be an accurate representation: although some sections of the *in vivo*

model showed a significant difference to the casted model, no significant difference was found for the CFD analysis.

Schambach et al. [236] have already used both a blood pool contrast agent (Fenestra) and a bolus technique with a conventional contrast agent (Imeron). Their setup was different from ours, with the probe (and the animal) rotating on the anteroposterior axis. This results in a shorter acquisition time, but also introduces movement artifacts and higher radiation doses (due to the larger magnification). That study clearly shows the need to address technical challenges still involved with in vivo micro-CT imaging of the cardiovascular system in mice. Willekens et al. [223] used Fenestra and eXIA 160 to enhance liver and spleen contrast in mice, but did not study the effects on the arterial system or the difference between in vivo and ex vivo models.

The difference between in vivo and in vitro methods to obtain 3D models of murine vasculature has not been studied extensively in literature. Kratky et al. [237] have demonstrated Batson's No. 17 to induce a shrinking factor of 16–20%, but did not compare in vitro with in vivo models. Casteleyn et al. [238] showed that the morphology of 3D models of the murine aortic arch (obtained using vascular corrosion casting) is very similar to the one of the human aortic arch (obtained in vivo). An alternative method to obtain 3D models of the murine arterial geometry in vivo is MRI imaging. Moore et al. [239] compared this technique to vascular corrosion casting and also found casts to have smaller diameters and bifurcation angles. However, small animal MRI is an expensive technique that is not widely available.

Our study shows that retrospective respiratory gating is not necessary to get a high 3D model quality. The ribs and diaphragm are more clearly delineated, but the difference was not noticeable in the aorta or the aortic arch. Cardiac gating can be done prospectively, where the electrocardiogram (ECG) is used to determine if a projection should be acquired at that specific moment. This requires a very short integration time on the detector, and an X-ray tube which can be switched on and off in the order of milliseconds. Leaving the X-ray tube on for the duration of the whole gated scan would deliver a radiation overdose to the small animal. Such a fast-switching X-ray tube was unavailable to us.

In order to calculate the dose given to the mice, published data was extrapolated. Carlson et al. [240] used the same micro-CT system and measured the whole-body dose from a 80 kVp scan with 2×2 detector binning and 1.3× magnification at 1.1 $\mathrm{mGy{\cdot}mAs^{-1}}$. This dose value

should be corrected for our lower tube potential (70 kVp) and the greater magnification used (3.5×).

A complex relationship exists between the radiation dose and a reference dose at different tube potentials [3]:

$$\frac{\text{dose}(x\,\text{kVp})}{\text{dose}(80\,\text{kVp})} = \left(\frac{x}{80}\right)^{2.47}. \tag{3.1}$$

According to Eq. (3.1), the dose at 70 kVp will be reduced by 28% compared to the dose at 80 kVp.

Next, the extrapolation of the dose for a higher magnification stems from the effective area of the body irradiated by the X-ray beam. This area will grow larger by the ratio of both magnification settings (and not the square of the ratio, because a higher magnification will also decrease the area of irradiation along the axial axis). This means the dose should also be corrected by factor 2.7 due to the higher magnification.

Together, both factors lead to a dose rate of 2.13 $\text{mGy}\cdot\text{mAs}^{-1}$, or a dose of 0.196 Gy per scan, delivered only to the thorax. This dose does not take the influence of the contrast agent on absorbed dose into account. Because contrast agents cause extra absorption local in tissue, which has also been proven to cause extra damage to lymphocytes compared to irradiation when contrast media are absent [241].

It is difficult to determine the influence of this localized dose, because no conversion factors exist for small animals (see Section 2.2.7). It is already close to the upper limit of whole-body dose that can be neutralized by a mouse per day (0.25–0.5 Gy according to [63]). Laforest et al. [242] have shown that total doses of 0.180 Gy can already lead to tumor growth inhibition in mice, a dose lower than the localized dose delivered by the protocol used here.

For Fenestra VC-131 the minimal contrast dose needed to obtain sufficient contrast was determined beforehand in a small proof of concept study. A 0.015 ml/gram contrast dose induces a relatively high strain on the animals, as this accounts for 25% extra blood volume. The effects noticed in the liver, eyes and lymph nodes are with a high probability caused by the use of Fenestra and the high contrast volume, leading to the high mortality rate. We are now using a different contrast-agent: eXIA 160 XL (Binitio Biomedical, Inc., Ottawa, Canada). eXIA 160 is a blood pool contrast agent that contains 160 mg iodine/ml, a concentration 3.2 times higher than in Fenestra VC-131, which leads to a much

lower injected volume needed (7.5 μl/g). Preliminary results show that the mortality is indeed much lower than when using Fenestra VC-131, while preserving image quality.

When comparing the diameters (Table 3.2), a general difference of 30 to 44% was measured. However, the correlation plot in Figure 3.7 and the Bland-Altman plot in Figure 3.8 show that the diameters of both modalities are well correlated ($r = 0.91$). There is no bias for low or high absolute values of the diameter, only a significant absolute systematic bias (0.22 mm) is present. In literature vascular corrosion casts have been reported to shrink 16–20% [237]. One might hypothesize that our casts have shrunk more, since the Batson's solution was injected by free-hand without manometric control of the injection pressure. However, according to Hodde [243] this technique gives consistently better results than injection with an injection apparatus. We therefore hypothesize that the extra 10 to 20% difference can be attributed to the increase in arterial pressure due to overfilling the animal during the in vivo scans, given the high contrast volume administered. One should also keep in mind that no true single value for the aortic diameter exists, since the aorta is constantly expanding and relaxing. As we applied no cardiac gating, we could not determine diastolic dimensions. It makes sense to state that the diameters obtained in vivo will probably be more representative of the systolic state whereas in vitro (casting) diameters will be a better estimate for the diastolic state. The true time-averaged diameter is most probably a value in the middle between those two. Segmentation errors also have to be taken into account, as the aortic arch is influenced by cardiac motion and is thus blurred, leading to small errors in the segmentation and the resulting 3D model.

When comparing the bifurcation angles (Table 3.3) the difference between in vivo and in vitro angles is much smaller compared to the difference in diameters, and is only significant for the common carotid artery. This small difference indicates that the representation of morphological characteristics of the arterial geometry does not differ much between both imaging techniques. This can also be observed from the good color-coded agreement between in vivo and in vitro models in Figure 3.12, and from the correlation plot in Figure 3.9 and the Bland-Altman plot in Figure 3.10. The angle between the ascending and descending aorta (AA–DA in Table 3.3) is in good agreement with previously reported measurements [238].

When comparing CFD results both spatially averaged WSS_{av} and 95

percentile $WSS_{95\%}$ are insignificantly lower for in vivo models. According to Poiseuille's law theoretical WSS values (in an infinitely long straight tube) are proportional to blood velocity and inversely proportional to diameter. Since the in vivo models are larger in diameter than the cast models but the same velocity is imposed at the inlet, it makes sense that in vivo models result in lower shear stresses. This is an important aspect that should be kept in mind when performing CFD simulations of the blood flow in murine vasculature: even when exactly the same measured velocity profile is imposed at the inlet of the model, results can be different depending on the imaging technique used to build the 3D model. With the casting technique, diameters will be underestimated and WSS will be overestimated. Using in vivo micro-CT, diameters will be overestimated and WSS values will be underestimated.

Keeping these remarks in mind, our results have shown that contrast-enhanced micro-CT visualization can be used to build 3D geometrical models of the aortic arch and the aortic arch bifurcations. Because of the high mortality due to the use of Fenestra VC-131, we now use eXIA 160 XL as a contrast agent. Both agents can be used to reconstruct reliable 3D models of the cardiovascular system.

3.8 Conclusion

In this chapter we have shown that it is possible to build reliable 3D geometrical models of the cardiovascular system in mice using *in vivo* micro-CT imaging. The in vivo models have significantly larger dimensions than in vitro models based on the same geometry, though still resulting in insignificantly lower WSS values. The total morphology and bifurcation angles show only small differences, and the WSS distribution over the model surface is also very similar. In vivo micro-CT imaging thus provides a valuable alternative for vascular corrosion casting.

These results will be used as a basis for the next chapter. Although the study presented here has shown *in vivo* imaging to be possible, possibilities for longitudinal scans have only been touched upon. The white-colored liver, white lymph nodes, and cornea edema were attributed to the contrast agent. The contrast agent toxicity and high injected volume can explain why 7 out of 9 mice died prematurely or were euthanized due to severely declining health. This was already addressed by choosing novel contrast agents for more recent studies, agents which were unavailable at the time of this study. The important limiter is thus the relatively

high radiation dose in micro-CT. Decreasing this dose is the topic of the next chapter.

Chapter 4

Regularized CT reconstruction for dose reduction

In the previous chapter we have shown how *in vivo* imaging provides the same information compared to the *ex vivo* alternative. Although we obtained positive results, there is one important limitation: the radiation dose is too high when multiple scans are acquired longitudinally.

In the current chapter, we will implement a method to reduce the X-ray dose. This will be achieved by reducing the number of projection views, which will proportionally decrease the radiation dose. The undersampling of the data will lead to image degrading effects, of which the influence will be minimized by using a regularized iterative reconstruction algorithm. Because of the relevance for cardiovascular research in mice, we will validate this approach on the data presented in the previous chapter and evaluate the influence of the regularization technique on the segmentation quality.

4.1 Introduction

A major difficulty in longitudinal aneurysm studies is the total number of scans needed to fully characterize the aneurysm formation process. Because the onset of aneurysm development is not known and varies greatly per individual animal, even with animals of the same mouse model, daily CT scans need to be taken to have images just before and just after the

start of the formation. Secondly, there is a possibility of aneurysm dissection or rupture in a later stage, with the most important information available only just before the dissection occurs. This information will be lost because of the dissection, and cannot be gathered afterwards. Acquiring scans daily over the course of weeks is necessary, but this will result in a large total radiation dose.

The effects of radiation dose on human subjects were already discussed previously in Section 2.2.7.1. Unfortunately, little is known about the potential side effects of the radiation dose in small animals. The effects of animal strain, age, radiation location and the many measurement protocols available result in a large number of combinations to study [244]. Nevertheless, Laforest et al. [242] have shown that total doses of 0.180 Gy can already lead to tumor growth inhibition in mice, a dose lower than the single dose used in the previous chapter. Klinck et al. [244] showed how weekly exposure to high resolution microCT reduces the trabecular bone volume 8 to 20% in skeletally immature BALB/cByJ and C57BL/6J mice. Others have presented results to the contrary [245]. Nevertheless, using the lowest possible radiation would help remove any doubt about negatively influenced results [246], as typical X-ray whole body radiation doses from one 3D micro-CT scan ranges from 0.017 to 0.78 Gy [247], well in the range of the studies described above.

A second issue is the animal throughput. With daily scans, the throughput needs to be maximized to efficiently plan these studies amongst others in a preclinical lab. This necessitates fast acquisition protocols and fast reconstruction algorithms.

A possible solution to achieve higher throughput and lower dose at the same time is by reducing the number of projection views acquired during the scan. The acquisition system can then rotate faster, which reduces the dose-time-product proportionally. If a filtered back-projection (FBP) type algorithm is used to reconstruct these datasets, the images will show aliasing artifacts [248] (Section 2.2.5.4), because the view sampling in few-view CT simply does not comply with the Nyquist-Shannon sampling theorem. Even though iterative reconstruction algorithms allow for much more accurate modeling of the acquisition system and physics, streaking artifacts will not be completely eliminated. Angular undersampling is a data sampling problem, which is not caused by a physical effect. A different approach is needed to solve this.

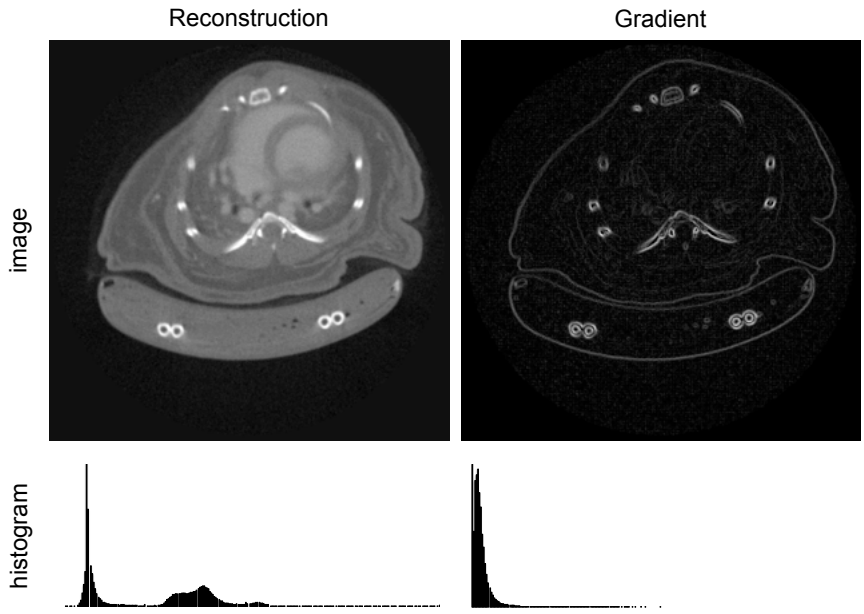

Figure 4.1: Image and image histogram, together with the gradient image and its histogram. The number of coefficients needed to represent the gradient is much smaller than the amount needed to represent the original image.

4.2 Compressed sensing

One of the techniques that have been extensively investigated to solve the problem of limited data is regularized iterative reconstruction, originating in the field of compressed sensing (CS).

In a seminal paper, Candès et al. [249] have shown that an image or signal can be recovered from far fewer samples or measurements than with traditional methods, i.e. when following the Shannon theorem. This is made possible by relying on *sparsity*, the idea that the information contained in an image may be much smaller than suggested by the image size. CS exploits the fact that many natural signals are sparse in the sense that they have a concise representation when expressed in a proper basis [250]. Though this idea was originally developed for sparse inversion of the discrete Fourier transform (DFT), Candès has also shown that this theory can actually be applied to general linear systems as well [251].

The question is which proper basis should be selected to represent medical images sparsely. A popular projection is the gradient operator,

which (in 2D) is calculated as the finite difference per direction:

$$\nabla_x(\mathbf{x})(i,j) = \mathbf{x}(i,j) - \mathbf{x}(i-1,j) \tag{4.1a}$$
$$\nabla_y(\mathbf{x})(i,j) = \mathbf{x}(i,j) - \mathbf{x}(i,j-1), \tag{4.1b}$$

with i and j pixel indices in the image represented by $\mathbf{x}$. Other possibilities will be discussed in Chapter 5.

By applying the gradient operator to an image, we can obtain an edge map representing horizontal and vertical edges. This is illustrated in Figure 4.1, where the gradient image is shown as the sum of ∇_x and ∇_y. The reconstructed image has coefficients spread out over the full width of its histogram, concentrated in two distinct areas. When the gradient operator is applied, the image is represented by only its edges. The coefficients are now concentrated much more around what we will call *significant coefficients*.

When under-sampled data is reconstructed, the system of equations will have multiple equally-possible results. No choice can be made amongst this set of images to determine which image is the best fit for the measured data: the system of equations is underdetermined. This is where the CS theory can be of help. The sparse transform can help selecting that image out of this set which is *the least complex*, i.e. which has the least number of significant coefficients.

A popular method which uses the gradient transformation inside CT reconstruction is total variation (TV) minimization. The TV-norm of a 2D image is defined by the scalar

$$\|\mathbf{x}\|_{\mathrm{TV}} = \sum_{i,j} \sqrt{|\nabla_x(\mathbf{x}(i,j))|^2 + |\nabla_y(\mathbf{x}(i,j)|^2}, \tag{4.2}$$

with ∇ as defined above. Recovering the ideal image $\mathbf{x}$ from an under-sampled set of measured data $\mathbf{y}$ can then be achieved by minimizing the TV-norm while keeping the constraint of data fitting

$$\hat{\mathbf{x}} = \min_{\mathbf{x}} \|\mathbf{x}\|_{\mathrm{TV}} \qquad \text{subject to} \qquad \|\mathbf{y} - \mathbf{W}\mathbf{x}\|_2^2. \tag{4.3}$$

TV minimization has been used before in few-view, limited angle reconstruction [67, 248, 252–258], algorithm-enabled low dose imaging [259], and CT image denoising or restoration [260, 261].

The aim of the study presented in this chapter is to investigate whether

reliable and accurate 3D geometrical models of the murine aortic arch can be reconstructed using few view in vivo micro-CT acquisitions. By reducing the number of projection views, both the acquisition time and the dose will decrease proportionally. With conventional reconstruction methods this would introduce excessive artifacts and noise in the images. We will reduce the noise and artifacts using TV minimization. The geometrical models obtained from sparse-view acquisitions will be compared to models obtained from full-view (high dose) acquisitions of the same animals.

4.3 Reconstruction methods

We re-used the data of the 4 perfectly-casted mice from Chapter 3. No additional animal experimental work was conducted. These datasets were retrospectively subsampled to simulate dose reduction. Seven distinct datasets were generated from each 2048-view dataset, by removing all but every n-th projection to obtain datasets with $2048/n$ uniformly spaced projection views. In this way, datasets were obtained with 1024, 512, 256, 128, 64 and 32 views over 360 degrees. Based on the dose extrapolation made in Chapter 3, these views correspond to nominal dose levels of 98, 49, 24.5, 12.25, 6.13 and 3.06 mGy. The dataset with all 2048 projection views (nominal dose 196 mGy) will serve as a reference dataset to these few-view datasets.

The 4×7 datasets were reconstructed using 3 different algorithms: FDK, the image space reconstruction algorithm (ISRA, first discussed in Section 2.2.6.3) and the ISRA with TV regularization (TV-ISRA).

The choice to use the ISRA is based on its fast reconstruction speed for large datasets. The ISRA algorithm reads the measured data only once from the hard drive, compared to once at every iteration for other algorithms. When measured datasets are easily larger than 10 GiB per scan, it is important to minimize the access to this data to increase the reconstruction speed.

The implementation of ISRA is easy and straightforward, and is depicted as a flow-chart in Fig. 4.2: first the measured data $\mathbf{y}$ is back-projected and stored. Next, the image $\mathbf{x}^{(k)}$ at current iteration k is forward and back-projected, and the ratio of the back-projected data and this image estimate is calculated. Finally, the error ratio is used to multiplicatively update the current image.

This type of algorithm is ideal to reconstruct large preclinical datasets,

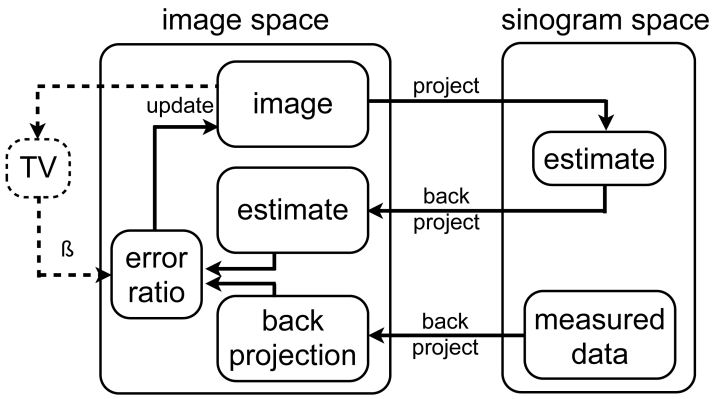

Figure 4.2: Block diagram to show how data flows through ISRA (full lines) and TV-ISRA (full + dotted)

as the large sinogram $\mathbf{y}$ is only used once to calculate the back-projection of the measured data. From then on, only forward and backward projections are needed, without comparing to the measured data again in sinogram space. This also means that one is not limited to working with the original geometry that was used to measure the data $\mathbf{y}$ [40], because the data is already backprojected into image space. A good choice for the projection geometry used in the iterations could result in a further decrease of computational time, e.g. by not using resolution recovery, or by using multiresolution approaches [262]. We did not employ this idea however, and used the exact same system matrix throughout the algorithm.

The regularized reconstruction algorithm is implemented by adapting the ISRA with a one-step-late (OSL) [132, 263, 264] modification to incorporate the TV-norm. We based our modification on Lange [263] and Defrise et al. [264], where TV-minimization was incorporated in emission and transmission tomography algorithms. In such an implementation, TV regularization acts as a penalty term, enforcing the sparse image gradient by adding a penalty to cost function (2.18) proportional to the TV norm (4.2):

$$\hat{\mathbf{x}}_\beta = \arg\min_{\mathbf{x}>\mathbf{0}} \|\mathbf{y} - \mathbf{W}\mathbf{x}\|_2^2 + \beta U(\mathbf{x}). \tag{4.4}$$

The TV-ISRA algorithm solves (4.4) with the iteration scheme

$$x_j^{(k+1)} = x_j^{(k)} \frac{\sum_{i=1}^{I} w_{ij} y_i - \beta \frac{\partial}{\partial x_j} U(\mathbf{x}^{(k)})}{\sum_{i=1}^{I} w_{ij} \sum_{j=1}^{J} w_{ij} x_j^{(k)}}, \tag{4.5}$$

with $\frac{\partial}{\partial x_j} U(\mathbf{x})$ the partial derivative of the energy function U [263, 265]:

$$\begin{aligned} \frac{\partial}{\partial x_{k,m,n}} U = {} & \frac{x_{k,m,n} - x_{k+1,m,n}}{u(k+1,m,n)} + \frac{x_{k,m,n} - x_{k,m-1,n}}{u(k,m+1,n)} \\ & + \frac{x_{k,m,n} - x_{k,m,n+1}}{u(k,m,n+1)} \\ & + \frac{3x_{k,m,n} - x_{k-1,m,n} - x_{k,m-1,n} - x_{k,m,n-1}}{u(k,m,n)} \end{aligned} \tag{4.6a}$$

$$\begin{aligned} u(k,m,n)^2 = {} & (x_{k+1,m,n} - x_{k,m,n})^2 + (x_{k,m+1,n} - x_{k,m,n})^2 \\ & + (x_{k,m,n+1} - x_{k,m,n})^2 + \epsilon^2 \end{aligned} \tag{4.6b}$$

Here, j is the linear index of the voxel located at (k, m, n) in 3D-space.

The penalty term will force the reconstructed images towards being uniform between edges, and is thus edge-preserving. Because of the penalty subtraction the error ratio may become negative. After each iteration, we set negative elements of $\mathbf{x}$ to 0. The degree of regularization can be varied with one relaxation parameter $\beta > 0$. Because the energy function U is derived before being used, a small positive number ϵ was added to resolve the discontinuity at zero in the derivative of the TV-norm.

The dashed lines in Fig. 4.2 represent the TV penalty added to the ISRA. With an OSL algorithm, the TV-norm is always calculated on the previous image iteration and is used to change the error ratio for the next image iteration, hence the one-step-late name.

The implementation of the iterative algorithms was done on the GPU in CUDA and C++. Figure 4.3 illustrates the forward and back projection calculations as implemented with CUDA kernels. The forward projector is implemented using a pixel-driven approach, by connecting a detector pixel with the spatial location of the X-ray tube and sampling the image along this ray at spacing Δx, the isotropic voxel size. The sum of these samples is added to the chosen detector element. Each 3D sample can

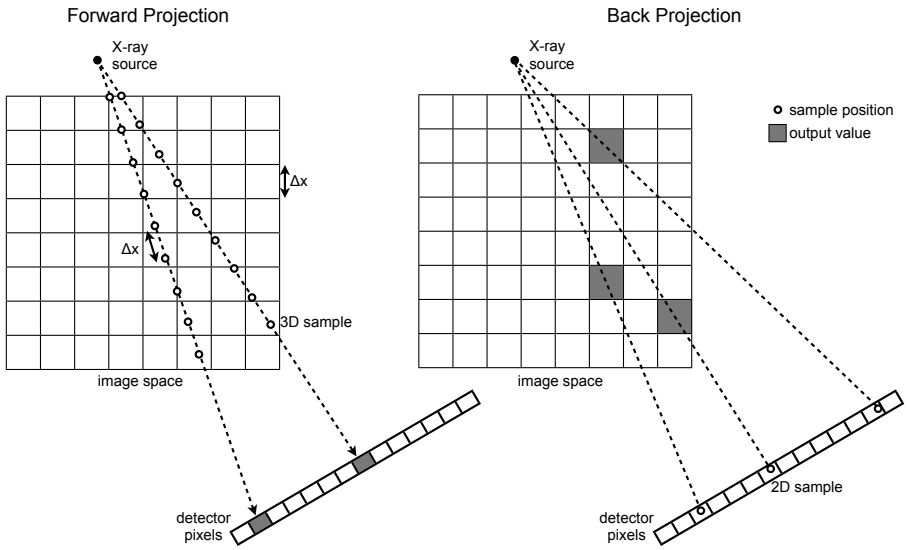

Figure 4.3: Illustration of CUDA-based ray-tracing for CT (not to scale).

be easily fetched using the 3D texture interpolation facilities available in CUDA. All detector elements are calculated in parallel.

The back projector uses a voxel-driven approach, by connecting a ray from the X-ray tube to the center of an image voxel. The intersection of this ray and the detector plane is then calculated. The value added to the image voxel is the 2D interpolated value of the intersection location on the detector. All image voxels are calculated in parallel. The 2D intersection interpolation is implemented by using the CUDA 2D texture interpolation facilities.

The finite size of the focal spot can be easily modeled with this ray-tracing approach, e.g. by sampling the focal spot size diameter with multiple starting points of the rays in an approach similar to 7-ray sub-sampling of the finite pinhole size in SPECT [266]. The ray starting points are chosen according to a Gaussian quadrature. This corresponds to calculating a weighted average of 7 forward projections, each with an X-ray emission point slightly offset from the others. Because of the increased computational complexity and relatively little benefit if low magnification is used, the finite size of the focal spot was not modeled for this study. Furthermore, no ordered subset versions of the algorithms were used, as convergence would not be guaranteed in that case [38, 267].

To compare the results obtained with ISRA and TV-ISRA with tra-

ditional results, we will also reconstruct the data with the algorithm of Feldkamp, Davis and Kress (FDK) [32] with a commercial implementation (Cobra EXXIM, EXXIM Computing corp., Livermore, USA). As mentioned before, FDK does not employ any advanced modeling to reduce artifacts induced by inadequate view sampling.

All images were reconstructed to a 100 μm voxel matrix. The image dimensions were determined per animal to always encompass the whole body. All iterative algorithms were stopped at convergence, which we defined as $\|\mathbf{x}^{(k)} - \mathbf{x}^{(k-1)}\|_2^2 < 0.14$. The value of 0.14 was empirically determined, and leads to about 200 iterations for 2048-view data. For TV-ISRA, the regularization parameter β was always set to 0.001. This was selected empirically to provide a good regularization, without overly smoothing.

4.4 Semi-Automatic 3D Segmentation

In the previous chapter, the segmentation was done manually in the Mimics software package (Materialise, Leuven, Belgium). The aortic arch was manually thresholded in a first segmentation step. When the resulting mask was judged sufficiently accurate, a 3D geometric model was built according to this mask. This 3D model was then smoothed in Mimics Remesher (Materialise, Leuven, Belgium) to remove anatomically impossible bulges and dents without shrinking the model. The result of these operations was a 3D model sufficiently smooth and simple to be useful in CFD simulations.

Since this manual thresholding approach could lead to subjective results, in this study we will use a semi-automatic method. To get an objective quantitative measure, the first steps that would be executed during manual segmentation were implemented in a semi-automatic fashion. The semi-automatic segmentation results can then be compared to each other. Although this method does not result in a perfectly segmented aortic arch with inclusion of the carotid arteries and the abdominal aorta, the segmentation result is still representative as a starting point for further manual editing.

The first step is the definition of a volume of interest (VOI) inside the aortic arch. The mean value v, standard deviation σ, minimum v_{min} and maximum voxel values v_{max} are then determined inside this VOI. Next, simple thresholding is applied to segment the image with voxel values in the interval $[\max(v_{min}, v - 3\sigma), \min(v_{max}, v + 3\sigma)]$.

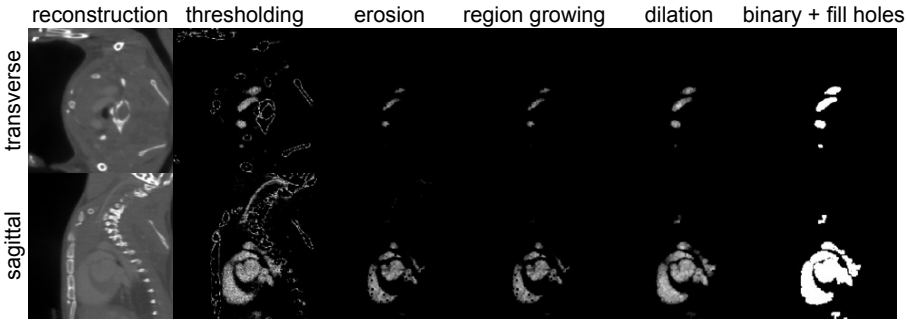

Figure 4.4: Transversal and sagittal slices of each automatic segmentation operation, going from the reconstructed dataset on the left to the final binary image on the right.

To select the arterial tree the following three steps need to be applied consecutively:

1. Because noisy voxels may wrongly associate with the arterial tree in later steps, the segmentation is eroded by 1 pixel (a voxel is replaced with the minimum value of its 26 3D neighbors).

2. Automatic region growing is started using the aortic arch VOI as seed, which removes the voxels disconnected by the previous step.

3. The resulting mask is dilated by 1 pixel (voxel value is replaced with the maximum value of the 26 3D neighbors), in order to regain the volume that was removed by the erosion operation.

As a last operation, the segmentation is converted to a binary image and the remaining holes are filled (binary OR operation of the voxel value with its 26 neighbors). The result of each operation is depicted in Fig. 4.4 for a full-view, high-dose dataset.

4.5 Analysis

4.5.1 Image Quality

Figures 4.5 and 4.6 depict the images obtained at different few-view levels, corresponding to nominal whole-body dose levels of 196 mGy (Chapter 3), 24.5 mGy, 12.25 mGy and 3.06 mGy. FDK and ISRA lead to excessive image noise for lower number of views, reducing the visibility

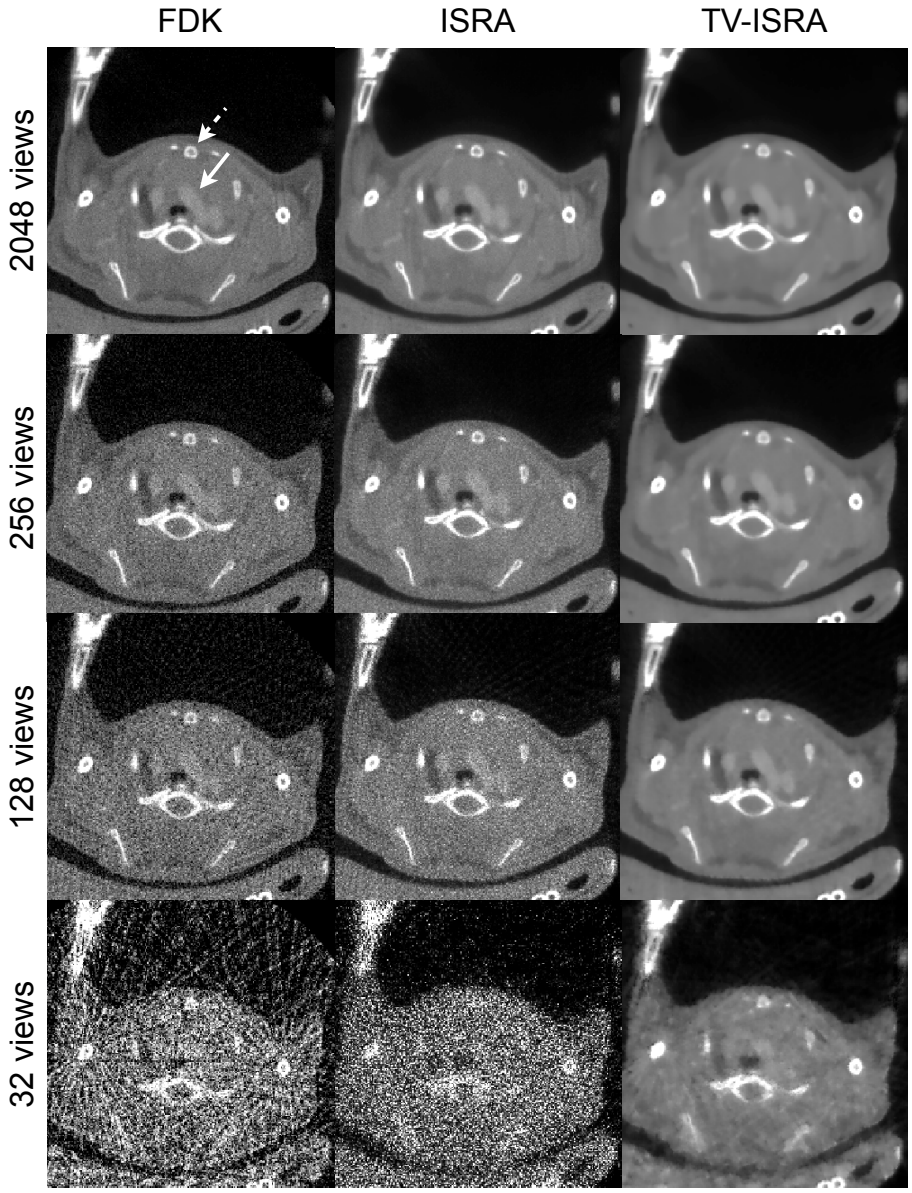

Figure 4.5: Transversal view of reconstructions for FDK (top row), ISRA (middle row) and TV-ISRA (bottom row) for different amounts of projection views. Full arrow points to the aortic arch. Dashed arrow points to the sternum.

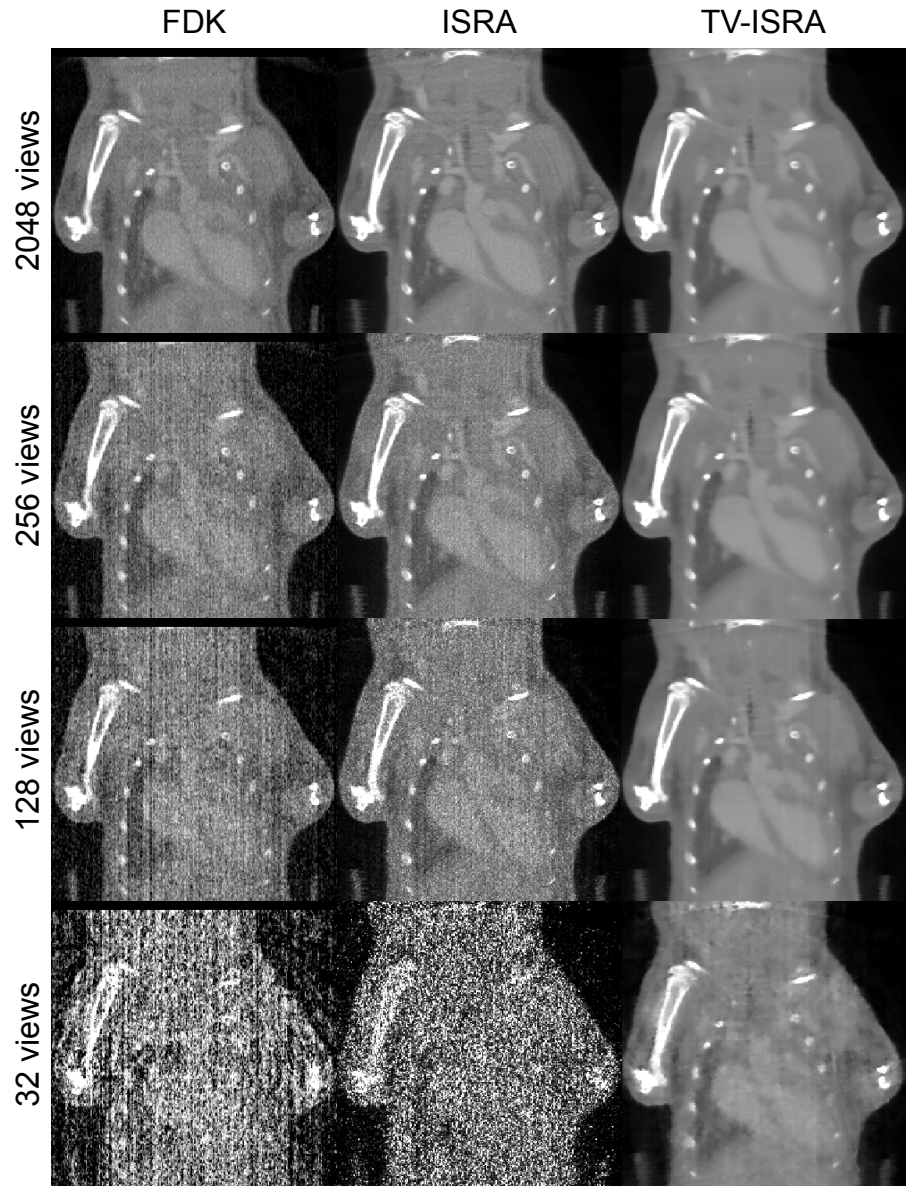

Figure 4.6: Coronal view of reconstructions for FDK (top row), ISRA (middle row) and TV-ISRA (bottom row) for different amounts of projection views.

of the aortic arch (full arrow in Fig. 4.5). While TV-ISRA reduces the streak artifacts considerably when only 256 or 128 views are used, it does not manage to sufficiently reduce the artifacts when only 32 views are used. Furthermore, a small loss of spatial resolution can be noted in all TV-ISRA reconstructions, compared to ISRA without regularization. This is especially apparent by comparing the sternum in the top right on the full-view datasets (dashed arrow in Fig. 4.5). On the other hand, the coronal view in Fig. 4.6 shows that some vessels in the lung can still be identified at 128-view TV-ISRA, while they are obscured by noise with ISRA and FDK.

4.5.2 Quantitative comparison

To compare the 3 reconstruction techniques of each few-view dataset more quantitatively, the full-view reconstruction was first automatically segmented to obtain a reference segmentation mask. This segmented model will serve as the gold standard segmentation. ISRA and TV-ISRA will be compared to the ISRA reconstruction from the 2048-view dataset. The FDK reconstructions are compared to the FDK reconstruction from the 2048-view dataset.

All sparse-view segmentations were evaluated based on 3 values: the amount of correctly classified voxels or true positives (TP), the amount of not segmented voxels or false negatives (FN) (segmented on the full-view but not on the few-view reconstruction), and the amount of additionally segmented voxels or false positives (FP) (segmented on the few-view but not on the full-view reconstruction).

Fig. 4.7 shows the classification accuracy when the amount of views is reduced. The error bars represent the standard deviation of the mean over the 4 mice. TV-ISRA manages correct classification with 2048 and 1024 view datasets, which also holds for ISRA when 1024 views are used. Starting from 512 views on, a trend of overestimation (higher FP fraction) occurs for ISRA and FDK. This trend is not seen with TV-ISRA, which remains correct as long as more than 64 views are used. A small underestimation is always present with TV-ISRA, not seen with ISRA nor FDK. The FDK reconstruction already shows some overestimation at 1024 projection views, reducing the number of correctly classified voxels.

Fig. 4.8 and 4.9 compare the reconstructions and segmentations of 2048, 1024, 256, 128 and 32 views FDK, ISRA and TV-ISRA on one transversal slice. The segmented image is color coded, showing white

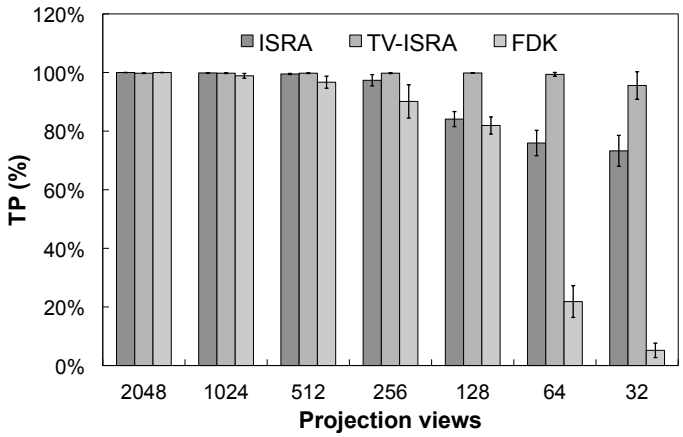

(a)

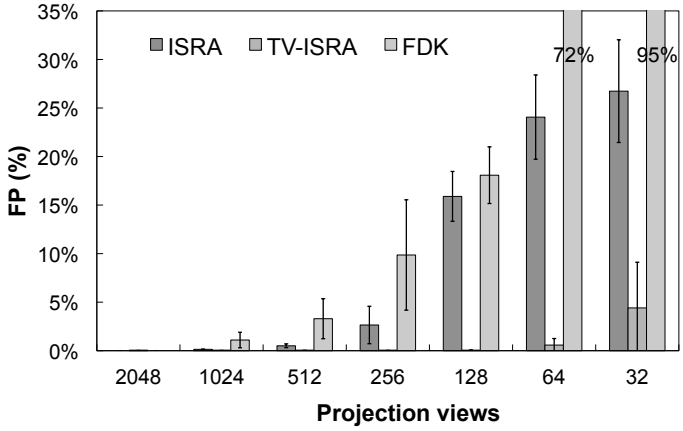

(b)

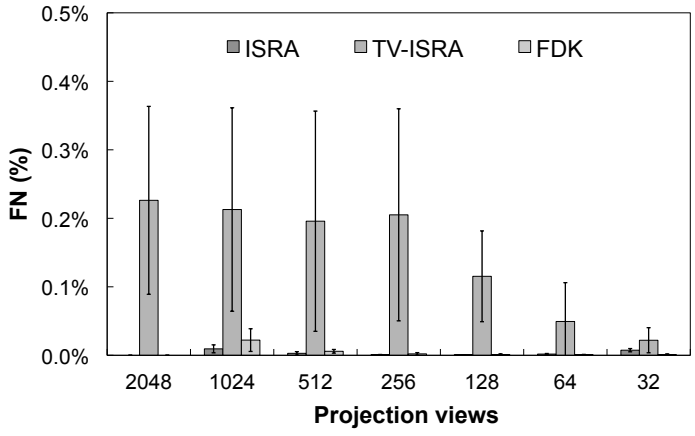

(c)

Figure 4.7: TP, FP and FN for each algorithm. Note that each plot has a different scale, which is very small in the case of FN.

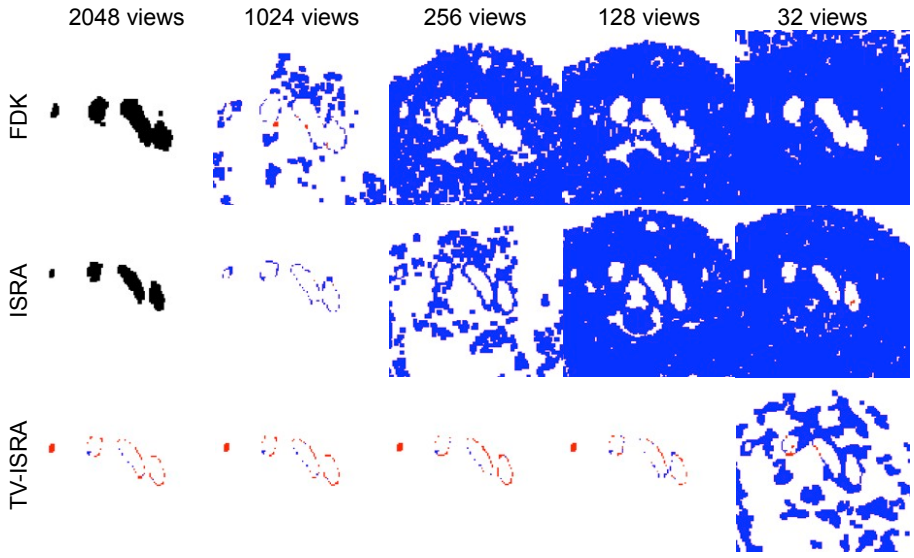

Figure 4.8: Colour coded difference images of one transversal slice through the aortic arch. Black is reference, white is TP, blue is FP, red is FN.

where there is correct classification (be it as background, or as part of the arterial tree), blue when there is overestimation and red when there is underestimation. The black segmentation mask is the reference mask obtained from the high dose FDK reconstruction for all fewer-view FDK reconstructions, or from the high dose ISRA reconstruction for all fewer-view ISRA and TV-ISRA reconstructions.

The FDK reconstructions do not lead to an accurate segmentation, even when 1024 views are available. The large shape disagreement between the 2048-view FDK and 2048-view ISRA reconstruction is due to the much higher noise in the FDK reconstruction, even though the maximum number of projection views was used.

Both iterative reconstruction methods manage to obtain an accurate segmentation on the 2048 and 1024 view datasets. There is some difference, as ISRA tends to overestimate the segmentation volume (blue), while TV-ISRA both overestimates some voxels while underestimating others at the same time. When 256 views are used, ISRA tends to overestimate considerably, increasing the segmentation volume. TV-ISRA is more accurate at 256 and 128 views, and overestimates more when the number of views is further reduced (more blue). Finally, both iterative methods fail segmentation at only 32 views.

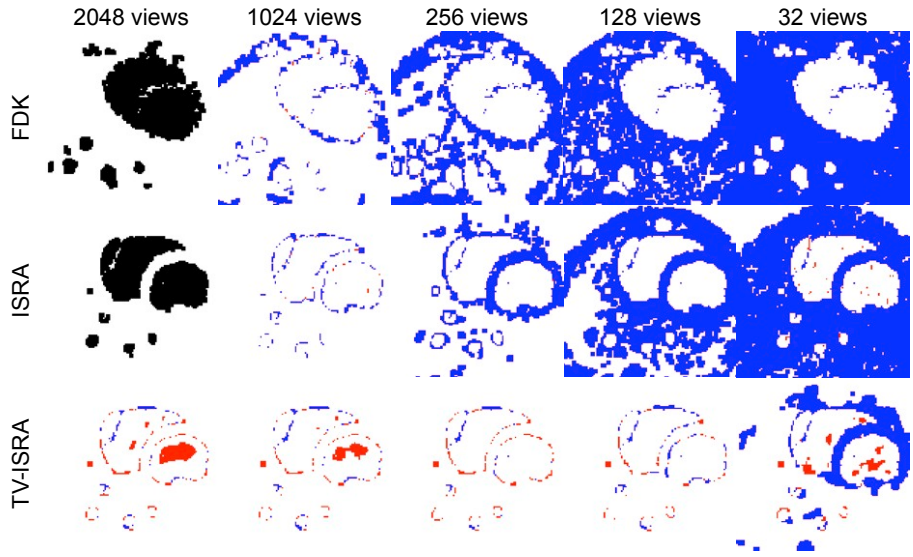

Figure 4.9: Color coded difference images of a transversal slice through the heart. Black is reference, white is TP, blue is FP, red is FN.

4.5.3 Diameter and 3D distance

To compare the segmentations in more detail, the aorta diameters and aorta positions were compared. First a centerline was fitted to the aorta segmentation mask using the MedCAD module of Mimics. Because this centerline cannot be calculated when the segmentation still includes parts of the heart, all masks had to be manually edited to only retain the aorta. This was done blinded for all datasets. The 2048-view ISRA dataset was manually edited twice: once to serve as a reference centerline and once as part of the blinded datasets. The difference between both centerlines then allows us to investigate the error due to the manual adjustments.

Figure 4.10 illustrates the shape of the resulting aorta segmentation next to its calculated centerline. No data of FDK reconstructions was included in this part of the study, as that data was reconstructed with proprietary software. Careful comparison between those proprietary FDK reconstructions and our own iteratively reconstructed data showed subvoxel differences. This led to a considerable absolute centerline offset, which does not represent changes due to sparse-viewing artifacts, but is actually due to misregistration between both software packages.

For each 3D centerline control point, the closest point (in ℓ_2-norm sense) on the reference centerline was searched. The error on the aortic

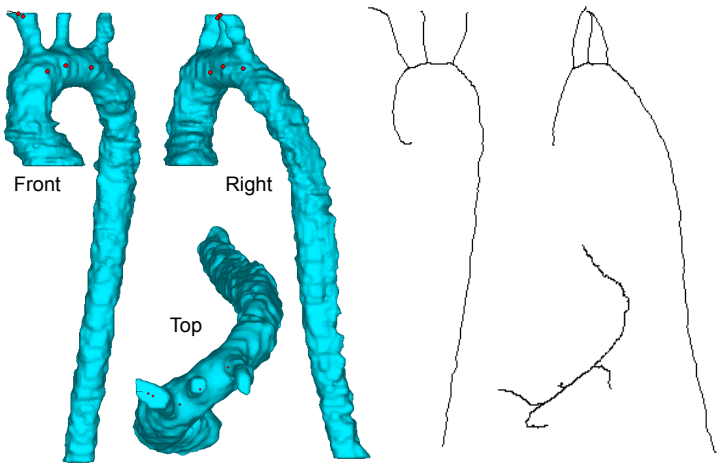

Figure 4.10: Front, right and top view of the aorta segmentation mask and the resulting centerline

diameter was then calculated by averaging the relative error between the diameter d_{ref} of the reference segmentation and the diameter d of the segmentation in question over each pair of control points, indexed by p:

$$\text{error} = \frac{1}{N} \sum_{p=1}^{N} \left| \frac{d_{\text{ref},p} - d_p}{d_{\text{ref},p}} \right| . \tag{4.7}$$

Each individual diameter was calculated as the best-fit diameter, fit on the plane orthogonal to the centerline going through the control point. The offset between both centerlines was calculated by calculating the average 3D Euclidean distance between this centerline and the reference centerline for all pairs of control points.

Student's t-test was used to test the results of different datasets for significance to the error seen with 2048-view ISRA. As the 2048-view ISRA results are segmented twice, this allows us to measure the error due to manual editing to retain the aorta. A significant ($p < 0.05$) difference with this error then signifies errors not caused by manual editing.

Table 4.1 contains the relative diameter errors compared to the reference centerline, which was calculated separately from 2048-view ISRA. The error for 2048-view ISRA is the error caused by manually adjusting the segmentation. Although the semi-automatically generated masks correctly delineated the abdominal aorta, the delineation between the

views	ISRA	TV-ISRA
2048	5.10±1.24%	7.22±1.19%
1024	6.56±2.32%	7.97±1.09%
512	13.66±3.37%*	7.59±1.94%
256	-	6.52±1.60%
128	-	-
64	-	-
32	-	-

Table 4.1: Comparison of relative aorta diameter errors (mean error ± SD, n = 4). * : Significance by comparing to 2048-view ISRA ($p < 0.05$). Manually nonadjustable data denoted with -.

heart and descending aorta was not always that clear. This means that the heart and descending aorta could not always be separated manually without a doubt. These datasets were not included in the comparison. Using 512 views with ISRA leads to a significantly larger diameter error ($p < 0.05$) than for 2048-view ISRA. The mean aorta diameter seen on the reference segmentations is 1.2 mm. The 13.7% error for 512-view ISRA is thus equal to a difference of 164 μm. When TV is used to reduce the noise and image artifacts, the diameter errors do not change significantly, even when only 256 views are used.

Table 4.2 details the centerline distance between the different methods. Again, the distance for 2048-ISRA is the distance caused by manually-

views	ISRA distance (mm)	TV-ISRA distance (mm)	
2048	0.046±0.011	0.064±0.014	
1024	0.054±0.009	0.075±0.022	
512	0.059±0.002	0.070±0.014	*
256	-	0.065±0.008	*
128	-	-	
64	-	-	
32	-	-	

Table 4.2: 3D Euclidean distance between centerlines (mean ± SD, n = 4). * : Significance by comparing to 2048-view ISRA ($p < 0.05$). Manually nonadjustable data denoted with -.

adjusting the segmentation to enable the centerline calculations. When fewer views are used with ISRA, the centerline offset does not change significantly. However, this does not hold for 512-view and 256-view TV-ISRA, where a significant ($p < 0.05$) different distance can be found compared to the distance expected from adjusting the segmentation manually. The highest error can always be found at the top of the aortic arch, where the centerline calculation is influenced by the carotid arteries.

4.5.4 Computational complexity

Fig. 4.11 plots the number of iterations needed to reach the stopping criterion and the total reconstruction time (logarithmic scale) for both iterative algorithms in function of the number of used projection views. As a reference, the total time needed for FDK is also included in Fig. 4.11b. Our implementation ran on one Intel Xeon E5620 core (2.4 Ghz) with 32 GB RAM memory, interfacing with one nVidia Tesla M2070 GPU.

The usage of TV regularization leads to a slow-down, doubling the total reconstruction time needed at 2048 views for TV-ISRA compared to ISRA. This is due to the overhead of calculating the TV per iteration. When less than 256 views are used, this slow-down will be out-weighted by the guaranteed and faster convergence of the algorithm, which means much less iterations are needed to reach the stopping criterion. For TV-ISRA, the number of iterations needed is independent of the number of projection views and remains constant around 235 ± 13 iterations. At 128 projection views or less, TV-ISRA thus leads to a faster solution compared to ISRA. At 128 views, the reconstruction time for TV-ISRA is already half the time needed by ISRA.

4.6 Discussion

In this chapter, we used the segmentation accuracy as a metric to determine if regularized CT can be used to segment the aortic arch and connected vessels in few-view datasets. Based on the results presented, we found that 256-view acquisitions can result in comparable segmentations as full-view acquisitions, as long as TV regularization is used. This results in an 8-fold reduction in X-ray dose, and an 8-fold shorter acquisition, which leads to a considerable increase in throughput when multiple studies need to be performed on the same day. Using fewer views without using regularized image reconstruction will lead to errors

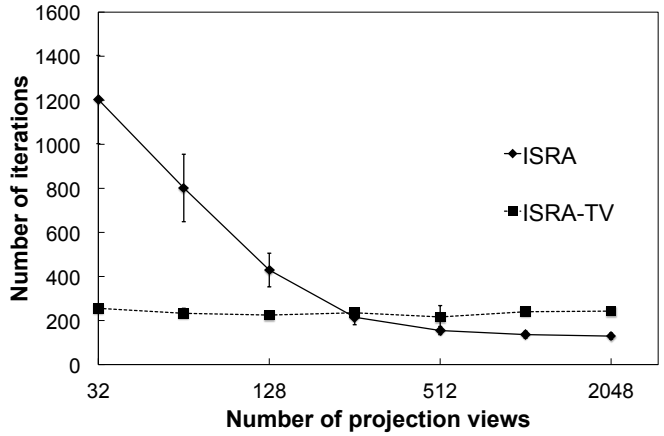

(a) Number of iterations needed to reach the stopping criterion.

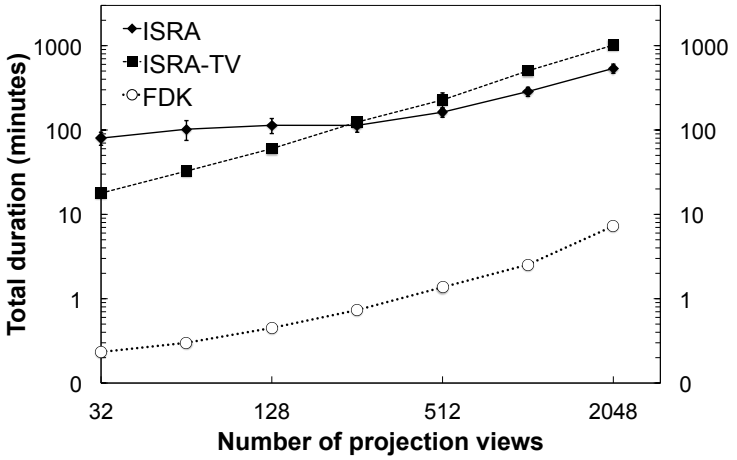

(b) Total reconstruction time needed to reach the stopping criterion (logarithmic scale).

Figure 4.11: Reconstruction iterations and total time needed to reach stopping criterion.

in the vessel diameters. Regularized reconstruction on the other hand will keep the diameters at the correct size. Although a significant geometry displacement may occur, it is generally smaller than 0.075 mm, which is smaller than the reconstructed voxel size.

FDK is currently used the most in preclinical practice due to its fast reconstruction time and because it is commonly the only option offered by the system vendor. However, this comes at a cost, as the segmentation quality is already negatively influenced even at 1024 views. In contrast, iterative reconstruction is much more robust to dose reduction. Non-regularized ISRA already shows its benefits: it can lead to a 2-fold decrease in dose compared to FDK, or even a 4-fold decrease if a small change in diameter is acceptable.

Although the accuracy of TV-ISRA is very high for high-dose data, both under and over estimation can be noticed around the aortic arch (Fig. 4.8). This agrees with the diameter loss and the sub-voxel displacement of the centerline. We hypothesize that this is due to resolution loss at the edges. However, this effect was not a limiting factor for our task.

In this study, only a reduction of projection views was employed to reduce the total image dose, as this is the only method retrospectively available. However, other dose reduction methods exist in the clinic [65]. Of these clinical methods, reducing the tube current is the only viable option in preclinical systems. The worse photon statistics will result in an increase in image noise, without inducing the streaking artifacts as encountered in sparse-viewing. We expect that using TV regularization will also result in accurate segmentations for those data sets.

TV reconstruction is expected to be useful in many of today's preclinical studies for higher throughput and dose reduction. Examples are bone imaging to assess bone density during fracture healing [106], bone resorption, remodeling and regeneration [107], bone neoplasms [268], and bone influenced by metabolic disorders such as osteoporosis [269]. Because of the piecewise constant nature of the bone and surrounding tissue, these applications are very suited for TV based reconstruction. Additionally, these studies primarily require high-resolution micro-CT imaging and thus a high X-ray dose, making them a good candidate for dose reduction. Other applications may include preclinical PET/CT and SPECT/CT studies, which utilize the CT information for attenuation correction [118], partial volume (PVE) correction [135], and as an anatomical landmark (VOI selection). Currently the same CT image is used as input for these 3 methods. Especially attenuation cor-

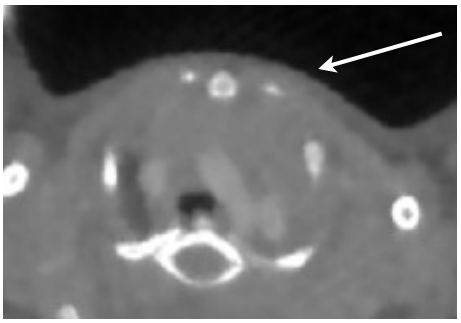

Figure 4.12: Jagged body-contour edge with TV-based reconstruction.

rection would be a good candidate for ultra-low-dose micro-CT scans. Although applying TV regularization on 32-view data leads to an inaccurate segmentation of the vessels, it does manage to obtain some visual quality (Fig. 4.5 and 4.6). Such images might still be useful for attenuation correction in small animals. These low-dose acquisitions could be co-registered with one higher dose acquisition to generate all necessary information in longitudinal studies.

4.7 Conclusion

In this chapter we determined the minimum number of projection views needed to accurately segment the aortic arch and its connected vessels. We found that the same segmentation quality can be obtained as with a high number of views when TV-ISRA is used with a minimum of 256 projection views. Because a decrease in projection views linearly decreases the X-ray dose, an 8 times decrease in X-ray dose and acquisition time can be achieved. For the system used here, this corresponds to a dose of 24.5 mGy per thorax scan, or a dose rate of 0.27 mGy·mAs^{-1}.

We have now solved one of the challenges concerning *in vivo* micro-CT imaging: the longitudinal accumulation of dose. We successfully decreased the dose as low as possible without influence for this specific task. The analysis done in this chapter can easily be repeated for other tasks as well (e.g. for trabecular bone analysis [108]) to determine the influence of a lowered dose on the specific task.

Although the reconstructed images were of sufficient image quality for the task chosen here, the image quality in itself was not that good visually. Figure 4.12 contains a zoomed image of a TV-ISRA reconstruction

for only 128 projection views. The body contour of the mouse looks aliased instead of being smoothly curved. When TV-regularization is used, we use the gradient operator to present the image in a sparse domain, where only a few significant coefficients are needed to represent the image. This is based on an assumption of what images look like (the image model): images contain uniform areas separated by edges. In other words, TV-regularization uses a piecewise-constant image model.

However, we believe this image model is suboptimal in the case of medical images. The next chapter will explore this image model in more detail, and we will try to find an improved sparsifying transformation which corresponds to more realistic image models.

Chapter 5

Improving regularized CT reconstruction

In the previous chapter we used total variation (TV)-based regularization to reduce sparse-view artifacts in low-dose CT reconstruction. For the specific task of aortic arch segmentation, we were able to reduce the total radiation dose per scan by a factor of 8 with no influence on the final 3D model. With unregularized iterative reconstruction, the dose could only be halved. Such results were deemed impossible in the past, mainly due to the artifact-ridden analytically reconstructed images.

Although a significant dose reduction was achieved, the images show block-like artifacts, which may hamper the use of TV-based regularization in other tasks. In the specific task of vascular segmentation, these artifacts only influenced the final model diameter by a small amount. However, in cases where the image quality is a more prominent factor, i.e. clinical diagnostics, these artifacts should be resolved.

In this chapter, we will further explore the image model behind TV-minimization, and how it does not fully comply with realistic medical data. We will propose regularization based on a different, improved image model. In order to accomplish reconstruction with such a different regularizer, we will develop a new framework for regularized CT reconstruction in which all kinds of regularizers fit. This framework will be validated by using the shearlet transformation as a sparsifying transform, in theory enabling us to achieve an improved image quality.

5.1 Introduction

TV minimization or regularization is not only used in CT reconstruction, but it is one of the techniques that have been extensively investigated in the context of image denoising. Pioneered by Rudin et al. in 1992 [270], it quickly became used in the image processing community in the context of image recovery or image denoising [260, 261, 271–273], segmentation [274], zooming and superresolution [275], colour enhancement [276], image fusion [277], video processing [278], inpainting [279] and image decomposition into cartoon and texture [280]. In the context of compressed sensing (CS) in CT reconstruction, TV minimization has been used for few-view, limited-angle CT reconstruction [248, 252–255], while the image denoising approaches can of course also be applied post reconstruction to CT images.

All the CS approaches take advantage of the idea that there is a natural redundancy present in images. Images can be conceptualized as being the sum of edges, uniform intensities, a repeated structure of fine-scale patterns (texture) and a noise component [280, 281]. For image denoising, it is beneficial if some representation exists that separates the noise from the other structural components.

Decomposing an image into a structural component and noise is only possible if the noise-free image can be approximated with a small number of significant coefficients in that representation. In that case the representation is called a *sparse* representation. The noise should then be non-sparse in that same representation. Let us take the gradient operator as an example of a sparsifying transformation, as illustrated in Fig. 5.1. The gradient of the noiseless reconstructed image has a very sparse histogram, with a small amount of significant coefficients. If the same image is noisy, the number of significant coefficients increases and its representation becomes less sparse.

Methods using the gradient transformation as sparsifying transform are best suited for piece-wise constant images, such as images of simple geometric shapes with flat intensity. Some authors have managed to reconstruct such a simple phantom (e.g. Shepp-Logan phantom [282], left on Fig. 5.2) exactly from only 22 projections [248, 249, 254], which is impressive and promising for dose-reduction applications in CT, if not for the unrealistically simple phantom. When the unrealistic phantom is replaced by a phantom specifically crafted for this purpose, TV minimization can not be used to reconstruct an image from 82 realistic

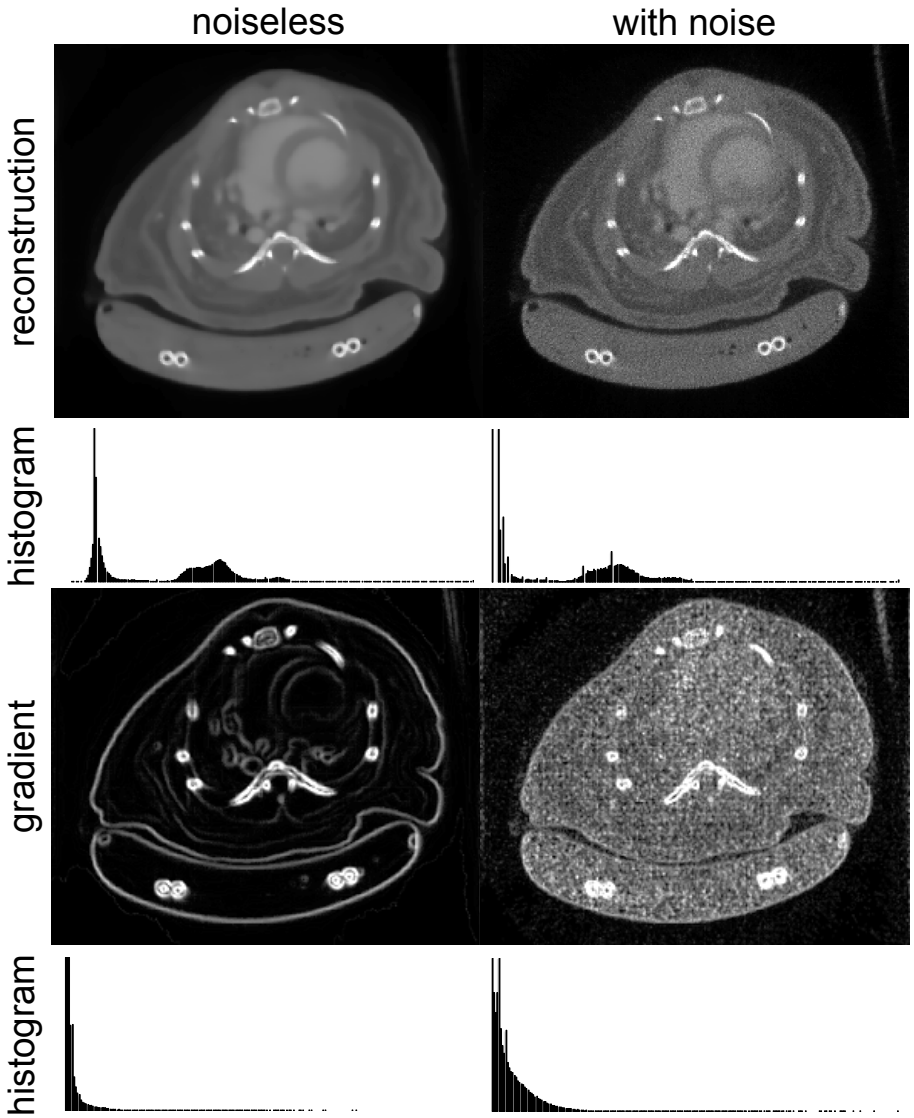

Figure 5.1: Illustration of the effect of image noise on the gradient histogram.

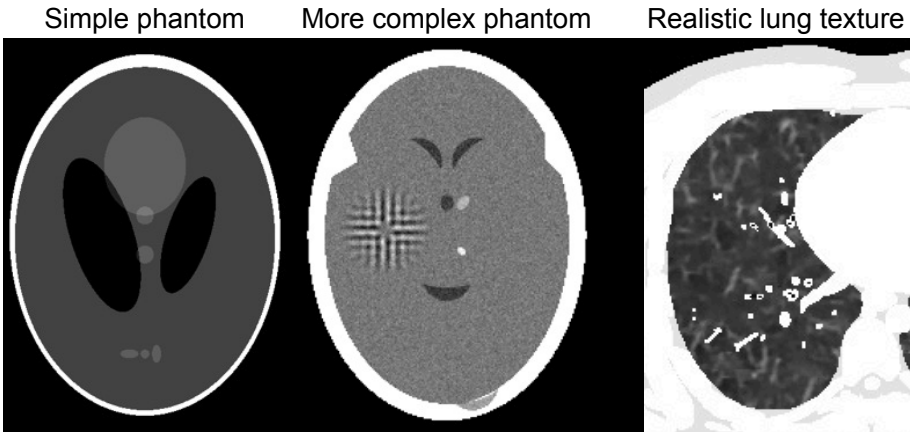

Figure 5.2: Left: Shepp-Logan phantom [282], which only requires 22 projection views to reconstruct completely. Middle: More complex phantom, as used in [252, 283]. Right: Addition of realistic lung texture to the XCAT phantom [284, 289] (Window [-900 0] HU). (Complex phantom courtesy of Gabor T. Herman, lung texture image courtesy of Jason Bond.)

projections anymore [252, 283]. This was achieved by adding a tumor into the brain which is invisible for those 82 projection views because of ghosting. Unsampled data can never be reconstructed. This means that the minimum sampling rate will depend on the object as well.

When the phantoms or images become even more complex, i.e. images that contain complex textures and gradual intensity transitions like high-resolution lung CT images (e.g. right image on Fig. 5.2, from [284]), TV based methods often produce cartoon-like approximations. Tang et al. [285] have shown that at least 100 projections views are necessary when realistic human anatomy is present. The same holds for micro-CT [286] as well as for MRI [287, 288].

The discrepancy between results obtained from simple phantoms and from realistic data reflects the fact that most natural images are actually not of bounded variation (BV) [290, 291], the search space in which TV minimization operates. Only the edge component can generally be expected to be of BV [290]. While TV minimization keeps the noise component small, the texture component is often eliminated due to the staircasing effect [271, 292–294]. Unfortunately, high-resolution medical images are not of bounded variation either [252, 290]. This makes the TV regularizer less suited for medical images from a mathematical point of view. Consequently, it would be beneficial to investigate regularizers that

offer a better sparse representation of medical images than the gradient operator.

Several alternatives have already been suggested in literature. One possibility is the use of the wavelet transformation. This transformation provides a decomposition of a signal over dilated and translated versions of a fixed waveform, called the mother wavelet. It allows the regularization to adapt to the image content at different resolution scales. While TV minimization might destroy soft edges, these would usually be reconstructed better using wavelets. The wavelet coefficients evolve across the scales at a rate that depends on the local regularity of the signal (e.g. depending on edge smoothness). Hence, even very 'weak' edges produce a significant response at a certain scale. In this way, the wavelet coefficients give valuable information about an edge, information which the discrete gradient operator lacks.

The Haar wavelet, the simplest possible wavelet, has already been investigated for regularized CT reconstruction by Garduño et al. [283]. They found that reconstructions with a sparse Haar transform are not more effective from the medical diagnostic point of view than reconstructions that have a small TV value. The authors did not explain this result. Thus, the search for an objective function that provides diagnostically efficacious reconstruction from a limited number of CT projections remains open [283].

Haar wavelets have been shown to be optimal for piecewise constant images and are very similar to TV in this regard. Steidl et al. [295] have proven that for 1-D signals, Haar wavelet shrinkage is equivalent to a single step of space-discrete TV diffusion or regularization of two pixel-pairs, when applied to one single scale only. To our knowledge the higher-dimensional case has not been proven yet, since it cannot be treated as a straightforward generalization of 1-D ideas [295]. The near equivalence of the Haar-based regularization to the TV regularization in 1-D might explain why Haar-based regularization did not outperform TV regularization.

Furthermore, it is known that the wavelet transform in general has poor directional selectivity. The discrete wavelet transform is often computed by using basis functions that are the tensor product of one-dimensional wavelets and one-dimensional scaling functions. This construction of wavelets will produce a checkerboard pattern simultaneously oriented along several directions [296], also known as *the checkerboard problem*. This approach can deal with point-wise singularities (such as

point sources), but does not allow to make a distinction between features at $+45°$ and $-45°$. As a result, many nonzero wavelet coefficients may be needed to represent a line singularity at an arbitrary orientation.

The poor orientation selectivity of the wavelet transformation led to the development of a number of multiresolution geometrical transformations with typically a very high number of analysis orientations, such as ridgelets [297, 298] and curvelets [299, 300]. The ridgelet transform is well suited for representing discontinuities along straight lines (*ridges*), in contrast to the curvelet transform, which can even represent discontinuities along *curves* with bounded curvatures.

A recent development is the shearlet transform [301]. This non-isotropic version of the wavelet transform is comparable to curvelets, as it also performs multiscale and multidirectional analysis, and both transformations can represent curve-like singularities in images. Guo et al. [302] have shown that the asymptotic decay rate of the shearlet transform, for fine scales, can be used to signal both the location and the orientation of the edges of an image and that the coefficients of large magnitude will correspond to edges. Furthermore, the decay rate across scales can be used to distinguish between noise spikes and edges [303], a property also holding for wavelet coefficients.

There are a number of advantages in using shearlets in imaging [304, 305]. The primary advantage for our use case is that shearlets allow for a lower redundant sparse tight frame representation than other related multiresolution representations (e.g. ridgelets, curvelets, dual-tree complex wavelets [306], ...), while still offering shift invariance and a directional analysis. Basically, the number of transform coefficients is not much larger than the number of pixels in the original image, and no artifacts are introduced when shearlet coefficients are adjusted. The directional analysis allows the shearlet basis functions to align with X-ray noise streaks in the reconstructed images, which allows these streaks to be approximated with less significant coefficients.

A second advantage is the multi-resolution approach: the shearlet representation can be used to decompose the image space $L^2(\mathbb{R}^2)$ into a sequence of spaces, associated to a hierarchy of scales [307, 308]. While edges are quantified in the space of bounded variation $BV(\mathbb{R}^2)$, other relevant features such as homogenous regions, texture, and other oscillatory patterns will belong to spaces in-between the smaller $BV(\mathbb{R}^2)$ and the larger $L^2(\mathbb{R}^2)$ [308]. By setting shearlet coefficients below a certain threshold to zero, image features present above a certain scale can be

extracted [307].

Both properties are useful when we will apply soft thresholding (soft shrinkage) later on in Section 5.2.4. A third property is that shearlets take edges into account in a multitude of directions, decomposed into a hierarchy of scales. This allows the detection of soft edges. Lastly, our goal is to use a transformation with the best approximation (compaction) properties. In higher dimensions, shearlets are a better candidate for this than wavelets or TV, as shearlets have an essentially optimal approximation error for images that contain edges (images that are C^2 (i.e. twice continuously differentiable) apart from discontinuities along C^2 curves) [301].

Shearlets are very similar to curvelets, as both perform a multiscale and multidirectional analysis. In fact, both transforms have optimal sparsity for images which have discontinuities (edges) along a C^2 curve [301, 309]. However, some important differences remain [305]. Shearlets are generated by applying a family of operators to a single function, contrary to curvelet basis functions. This makes the discrete implementation of curvelets very challenging. Two methods were suggested by Candès et al. [299] to make the implementation easier. In a first method, aliasing is deliberately introduced through wrapping. In a second method, the nonequispaced fast Fourier transform (NFFT) is used. The inverse NFFT should then be computed with a conjugate gradient type algorithm, utilizing one NFFT and one adjoint NFFT per iteration [310]. This makes the calculations less efficient.

A second difference with curvelets is that shearlets are associated to a multiresolution analysis, while curvelets are not. Thirdly, in the construction of the shearlet tight frame, the number of orientations doubles at every scale, while for curvelets, this number doubles every other scale. A final difference, and very important one, is that shearlets allow for a much less redundant sparse tight frame representation than curvelets, while still offering shift invariance [304]. These properties make the shearlet transform an attractive candidate for image representation [304].

In this chapter, we will investigate if shearlets can be used in regularized CT reconstruction, and if they show any of the previously mentioned benefits compared to TV regularization. This is based on the results of shearlet-based denoising in image processing [305, 307], in magnetic resonance imaging (MRI) reconstruction [311] and preliminary numerical results we published previously [312]. Previously, Colonna et al. [313] have used the shearlet representation to invert the Radon transform di-

rectly. Their approach is not directly applicable to sparse viewing. We propose to use a recently proposed efficient solver, based on an augmented Lagrangian (or split-Bregman) approach [314, 315], as an alternative method for sparse-view CT reconstruction. Split-Bregman methods have also been found to be successful in other applications, such as MRI image reconstruction [311]. This very general method allows the incorporation of extra regularization terms quite easily.

5.2 The split-Bregman based CT reconstruction method

5.2.1 Imaging model

As was discussed in Section 2.2.6.3, in a noise free case, the projection data $\mathbf{y}$ can be exactly modeled by a discrete approximation of the imaging process $\mathbf{y} = \mathbf{W}\mathbf{x}$, with $\mathbf{W}$ the system matrix modeling the X-ray transformation and $\mathbf{x}$ the reconstructed image.

In a noiseless or white Gaussian noise case, solving for the unknown image $\mathbf{x}$ can be accomplished by minimizing the least-squares cost function:

$$\Psi(\mathbf{x}) = \|\mathbf{y} - \mathbf{W}\mathbf{x}\|_2^2. \tag{5.1}$$

The optimal solution $\hat{\mathbf{x}}$ that minimizes (5.1) is given by the pseudoinverse of $\mathbf{W}$. Unfortunately, this pseudoinverse is too complicated to compute directly in practical CT imaging. Therefore, in Section 2.2.6.3, we discussed how the image space reconstruction algorithm (ISRA) can be used to minimize a least-squares cost under the assumption of white Gaussian distributed data. On the other hand, when the measured data is assumed to be noiseless, algebraic techniques such as SIRT can also be used [316, 317]. Both the statistical and the algebraic solution will lead to the same solution $\hat{\mathbf{x}}$ as would be obtained if the pseudoinverse would be calculated directly.

Others propose to model the photon noise in projection space by an additive approximation $\mathbf{y} \approx \mathbf{W}\mathbf{x} + \mathbf{n}$, with $\mathbf{n}$ given by a Gaussian Random Field [304, 318]. Because the noise is zero-mean by approximation, data fitting function (5.1) is still applicable.

In order to reduce the radiation dose, we want to reduce the number of acquired projection views (sparse-viewing), i.e. we reduce the number of

equations determined by $\mathbf{W}$ and $\mathbf{y}$. Unfortunately, minimizing (5.1) for $\mathbf{x}$ is difficult in the case of sparse-view systems. This makes the problem very ill-posed.

Therefore, we define a new cost criterium $\Psi(\mathbf{x})$ which models non-white Gaussian noise. We also add a regularization term $\Phi(\mathbf{x})$, which will provide prior information about the statistics of possible solutions:

$$\hat{\mathbf{x}} = \arg\min_{\mathbf{x}} |\Phi(\mathbf{x})|_1 \quad \text{subject to} \quad \|\mathbf{C}^{-1}(\mathbf{y} - \mathbf{W}\mathbf{x})\|_2^2 \leq \epsilon. \tag{5.2}$$

Here, ϵ acts as an upper bound on the uncertainty about the measurements $\mathbf{y}$, Φ is a linear sparsifying transformation and $\mathbf{C}$ is applied to pre-whiten non-white Gaussian distributed data. The ℓ_1-norm is crucial to the whole approach of regularization with sparsifying transforms [287]. Its use will lead to suppression of many small coefficients in favor of a few large coefficients, which is exactly what we want to achieve in order to find that one good image amongst the set of images that fit to the measured data.

Because the ℓ_1-norm has a discontinuity at the origin, it is not differentiable and more difficult to solve. Therefore, Eq. (5.2) should be converted to an unconstrained problem [315]:

$$\hat{\mathbf{x}} = \arg\min_{\mathbf{x}} |\Phi(\mathbf{x})|_1 + \lambda \|\mathbf{C}^{-1}(\mathbf{y} - \mathbf{W}\mathbf{x})\|_2^2, \tag{5.3}$$

with λ a constant. In words, among all solutions which are closest (in the weighted least-squares sense) to the acquired data, equation (5.3) finds a solution which is sparse in the ℓ_1-sense in the domain of the transform Φ.

Matrix $\mathbf{C}$ is in first instance applied to pre-whiten the data, i.e. to weight the errors corresponding to projections with high attenuation (low values of $\mathbf{y}$) [319]. These detected values will contain more noise than values projected through less dense material, and will thus have a lower signal-to-noise ratio (SNR). Therefore, the projected values should be weighted according to their variance, which is equal to the mean projection value under the assumption of poisson noise:

$$\mathbf{C} = \operatorname{diag}(c_0, c_1, \ldots, c_I) \quad \text{with} \quad c_i = e^{-\mathrm{E}[y_i]}. \tag{5.4}$$

We can use the projection value itself as an estimate for the expected value $\mathrm{E}[y_i]$.

Next to simple exponential weighing, $\mathbf{C}$ can also be used to model the detector acquisition system. Different effects can be taken into account in a diagonal matrix, such as gain per detector pixel, thermal stability, dark current drifts and linearity [3]. These effects can be modeled by multiplying c_i with appropriately measured air scans. Signal crosstalk can be modeled with off-diagonal covariance entries [320], as well as afterglow and primary speed. In that case, $\mathbf{C}$ serves as a pre-whitener for this system, de-correlating the noise.

5.2.2 Overview of the split-Bregman framework

There is a vast amount of literature available on how to solve equations such as (5.3) in general, and in particular adapted for CT reconstruction. It is a penalized weighted least squares cost function (PWLS), but in a non-quadratic form. This means no closed-form solution exists for the minimizer [42].

In the majority of cases a comparable cost function is solved through a heuristical method, alternating the optimization of the data fitting constraint with the sparsity constraint [248, 253, 255, 321, 322].

We use a different approach, by using the split-Bregman framework [315] (also known as the split-augmented Lagrangian). This is very similar to work done in iterative thresholding [323, 324], with the benefits of having a relatively low memory footprint [315], simple and fast iteration steps, and that the technique is generally easy to implement, even for complex problems.

According to Goldstein and Osher [315], the generalized constrained optimization problem

$$\arg\min_{\mathbf{x}} J(\mathbf{x}) \quad \text{s.t.} \quad \mathbf{y} = \mathbf{W}\mathbf{x} \tag{5.5}$$

with J a convex energy functional, can be solved by iterating over

$$\mathbf{x}^{(k+1)} = \arg\min_{\mathbf{x}} J(\mathbf{x}) + \frac{\lambda}{2}\|\mathbf{W}\mathbf{x} - \mathbf{b}^{(k)}\|_2^2 \tag{5.6a}$$

$$\mathbf{b}^{(k+1)} = \mathbf{b}^{(k)} + \mathbf{y} - \mathbf{W}\mathbf{x}^{(k)}. \tag{5.6b}$$

The iterates $\mathbf{x}^{(k)}$ will get arbitrarily close to a solution of the original constrained problem $\hat{\mathbf{x}}$ (5.5).

Equations (5.6a) and (5.6b) can be applied to cost function (5.3) together with variable splitting. This ultimately leads to the following three update equations [315, 325]:

$$\mathbf{x}^{(k+1)} = \arg\min_{\mathbf{x}} \frac{\lambda}{2}\|\mathbf{C}^{-1}(\mathbf{y} - \mathbf{W}\mathbf{x})\|_2^2 + \frac{\mu}{2}\|\mathbf{d}^{(k)} - \Phi(\mathbf{x}) - \mathbf{b}^{(k)}\|_2^2 \quad (5.7a)$$

$$\mathbf{d}^{(k+1)} = \arg\min_{\mathbf{d}} |\mathbf{d}|_1 + \frac{\mu}{2}\|\mathbf{d} - \Phi\left(\mathbf{x}^{(k+1)}\right) - \mathbf{b}^{(k)}\|_2^2 \quad (5.7b)$$

$$\mathbf{b}^{(k+1)} = \mathbf{b}^{(k)} + \left(\Phi\left(\mathbf{x}^{(k+1)}\right) - \mathbf{d}^{(k+1)}\right). \quad (5.7c)$$

The ℓ_1- and ℓ_2-norm from the regularized quadratic problem (5.3) are now split into different minimization problems: a sequence of unconstrained optimization problems and one Bregman update step. Eq. (5.7c) is trivial to solve. Eq. (5.7b) is easy to solve with soft-shrinking even though it is a combination of an ℓ_1- and an ℓ_2-norm, because there is no coupling between elements of $\mathbf{d}$. Finally, Eq. (5.7a) only needs to be solved for $\mathbf{x}^{(k+1)}$ approximately. Even then, the algorithm still converges [315].

We have introduced two new variables which elicit further explanation: λ and μ.

- Parameter λ was added by converting the constrained optimization problem into an unconstrained one. In this context, it can be interpreted as the contribution of the regularization to the total cost. The lower its value, the lower the importance of the data fitting term, which amounts to more regularization (denoising).
- The ratio μ/λ determines the convergence speed. If μ is set to 0 and λ to 1, no regularization is performed and a conventional weighted least-squares solution is obtained, minimizing cost function (5.1). Goldstein et al. [315] have empirically found that a ratio of 2.0 delivers a good convergence speed. We will experimentally determine good parameters for our study further on in Section 5.5.2.

5.2.3 Regularization terms

In the previous sections Φ was intentionally left unspecified, to obtain a general framework useful for different regularization terms. Indeed, no assumptions have been made apart from convexity. The purpose of this study is to investigate if using the discrete shearlet transformation as a

regularization term is superior to isotropic TV minimization. Isotropic TV was chosen as this is what is most widely used in medical imaging.

5.2.3.1 Isotropic Total Variation

For TV minimization the discrete gradient operator ∇ is used as Φ. In 2D, $J(\mathbf{x})$ becomes:

$$J(\mathbf{x}) = \sum \sqrt{\left(\nabla_x(\mathbf{x})\right)^2 + \left(\nabla_y(\mathbf{x})\right)^2}. \tag{5.8}$$

The minimization problem can then be solved by setting $\mathbf{d}_x = \nabla_x(\mathbf{x})$ and $\mathbf{d}_y = \nabla_y(\mathbf{x})$ [315]. Despite the fact that $\mathbf{d}_x$ and $\mathbf{d}_y$ can not be decoupled, the problem can still be solved using a generalized shrinkage formula [315, 326].

Equations (5.7a–5.7c) become:

$$\begin{aligned}
\mathbf{x}^{(k+1)} &= \arg\min_{\mathbf{x}} \frac{\lambda}{2}\|\mathbf{C}^{-1}(\mathbf{y}-\mathbf{W}\mathbf{x})\|_2^2 && \text{(5.9a)}\\
&\quad + \frac{\mu}{2}\|\mathbf{d}_x^{(k)} - \nabla_x(\mathbf{x}) - \mathbf{b}_x^{(k)}\|_2^2 \\
&\quad + \frac{\mu}{2}\|\mathbf{d}_y^{(k)} - \nabla_y(\mathbf{x}) - \mathbf{b}_y^{(k)}\|_2^2 \\
\mathbf{s}^{(k+1)} &= \sqrt{|\nabla_x\left(\mathbf{x}^{(k+1)}\right) + \mathbf{b}_x^{(k)}|^2 + |\nabla_y\left(\mathbf{x}^{(k+1)}\right) + \mathbf{b}_y^{(k)}|^2} && \text{(5.9b)}\\
\mathbf{d}_{\{x,y\}}^{(k+1)} &= \max\left(\mathbf{s}^{(k+1)} - 1/\mu, 0\right) \frac{\nabla_{\{x,y\}}\left(\mathbf{x}^{(k+1)}\right) + \mathbf{b}_{\{x,y\}}^{(k)}}{\mathbf{s}^{(k+1)}} && \text{(5.9c)}\\
\mathbf{b}_{\{x,y\}}^{(k+1)} &= \mathbf{b}_{\{x,y\}}^{(k)} + \left(\nabla_{\{x,y\}}\left(\mathbf{x}^{(k+1)}\right) - \mathbf{d}_{\{x,y\}}^{(k+1)}\right). && \text{(5.9d)}
\end{aligned}$$

The discrete gradient operator $\nabla_{\{x,y\}}(\mathbf{x})$ is defined as:

$$\begin{aligned}
\nabla_x(\mathbf{x})(i,j) &= \mathbf{x}(i,j) - \mathbf{x}(i-1,j) && \text{(5.10a)}\\
\nabla_y(\mathbf{x})(i,j) &= \mathbf{x}(i,j) - \mathbf{x}(i,j-1), && \text{(5.10b)}
\end{aligned}$$

with wrapping of the values at the edges of the image volume.

5.2.3.2 Discrete shearlet transformation

The main mathematical ideas of the discrete shearlet transformation (DST) are reiterated here for completeness. For more detail, the reader

is referred to the literature [301, 305, 327, 328].

Let $\psi_{j,k,\mathbf{l}}(\mathbf{x})$ denote the shearlet basis functions (or in the remainder simply called shearlets), then the continuous shearlet transformation (CST) of an image $f(\mathbf{x}) \in L_2(\mathbb{R}^2)$ is defined by [302, 329]:

$$[\mathcal{SH}_\psi f](j,k,\mathbf{l}) = \int_{\mathbb{R}^2} f(\mathbf{x})\psi_{j,k,\mathbf{l}}(\mathbf{l}-\mathbf{x})dx = \langle f, \psi_{j,k,\mathbf{l}}\rangle \tag{5.11}$$

where $j \in \mathbb{R}$, $k \in \mathbb{R}$ and $\mathbf{l} \in \mathbb{R}^2$ denote the scale, orientation and the spatial location, respectively. Shearlets are formed by dilating, shearing and translating a mother shearlet function $\psi \in L_2(\mathbb{R}^2)$, as follows:

$$\psi_{j,k,\mathbf{l}}(\mathbf{x}) = |\det \mathbf{A}|^{j/2}\psi\left(\mathbf{B}^k\mathbf{A}^j\mathbf{x} - \mathbf{l}\right) \tag{5.12}$$

where $\mathbf{A}$ and $\mathbf{B}$ are invertible 2×2 matrices, with $\det \mathbf{B} = 1$.

For shearlet analysis, the transformation matrices $\mathbf{A} = \begin{pmatrix} a & 0 \\ 0 & \sqrt{a} \end{pmatrix}$ and $\mathbf{B} = \begin{pmatrix} 1 & s \\ 0 & 1 \end{pmatrix}$ are used. $\mathbf{A}$ is an anisotropic scaling matrix with scaling factor $a > 0$ and $\mathbf{B}$ is a geometric shear matrix with parameter $s \in \mathbb{R}$.

The shearlet mother function ψ is a composite wavelet that satisfies appropriate admissibility conditions [302]. It is defined in the Fourier transform domain by $\Psi(\omega) = \Psi_1(\omega_x)\,\Psi_2\left(\frac{\omega_y}{\omega_x}\right)$, with $\omega = [\omega_x \omega_y]$, $\Psi_1(\omega_x)$ the Fourier transform of a wavelet function and $\Psi_2(\omega_y)$ a compactly supported bump function $\Psi_2(\omega_y) = 0 \Leftrightarrow \omega_y \notin [-1, 1]$.

Any $f \in L_2(\mathbb{R}^2)$ can be recovered via the reproducing formula:

$$f = \sum_{j,k,\mathbf{l}} \langle f, \psi_{j,k,\mathbf{l}}\rangle \psi_{j,k,\mathbf{l}}. \tag{5.13}$$

The DST was implemented as proposed by Goossens et al. [330–332], which leads to a very low redundancy factor and a relatively short computation time compared to other implementations. We implement Φ as the forward shearlet transformation (Eq. 5.11) and its adjoint $\Phi^\dagger$ as the inverse shearlet transformation (Eq. 5.13).

The Meyer wavelet is used as mother wavelet $\Psi_1(\omega_x)$ for the shearlet transformation. This mother wavelet is an appealing choice due to its

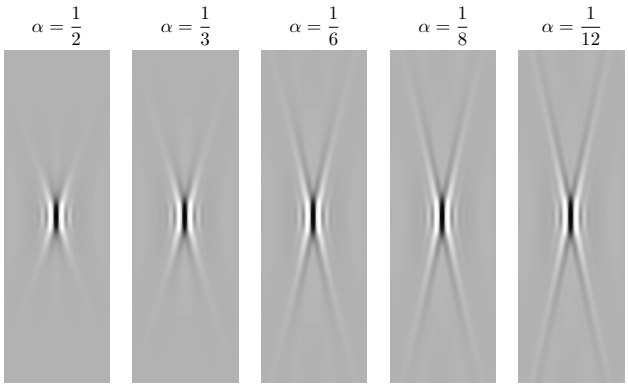

Figure 5.3: Plot showing shearlets for different values of the parameter α. The shearlets become more elongated with decreasing α values.

excellent localization properties in both time and frequency and also because the filters are defined directly in the frequency domain [330, 333]. The angular filter used is given by:

$$\Psi_2(\omega) = \begin{cases} 0 & \omega < -\frac{1+\alpha}{2} \\ \sin\left(\frac{\pi}{2} v\left(\frac{\alpha+2\omega+1}{2\alpha}\right)\right) & \left|\omega + \frac{1}{2}\right| \leq \frac{\alpha}{2} \\ 1 & |\omega| < \frac{1-\alpha}{2} \\ \cos\left(\frac{\pi}{2} v\left(\frac{\alpha+2\omega-1}{2\alpha}\right)\right) & \left|\omega - \frac{1}{2}\right| \leq \frac{\alpha}{2} \\ 0 & \text{else} \end{cases} \tag{5.14}$$

The choice of $\alpha \in \left[0, \frac{1}{2}\right]$ here is important, it is a constant parameter that determines the bandwidth of the angular filters (see Fig. 5.3). The choice of α also has an influence on the redundancy factor of the DST.

Figure 5.4 shows all subbands of the shearlet transformation using 3 scales with 4 directions per scale, applied to measured plastimouse data (see Section 5.3.2). For an input image of 512×512 voxels, this leads to subbands with respective sizes 16×16, 64×64, 256×256 and 512×512 coefficients.

5.2.4 CT reconstruction algorithm

The performance of the split-Bregman method is largely dependent on the subproblem solvers for Eq. (5.7a) and Eq. (5.7b), because Eq. (5.7c) is trivial to solve. To find a solution to Eq. (5.7a), we need to find the

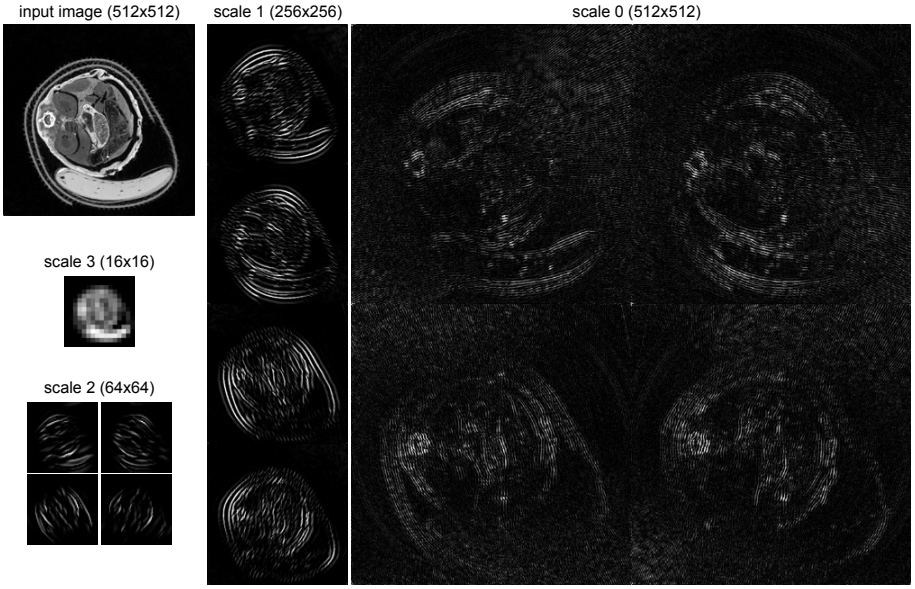

Figure 5.4: Example of shearlet transformation coefficients, using 3 subbands with 4 directions per subband and $\alpha = 1/2$, applied to measured plastimouse data. All coefficient images show the magnitude of the coefficients (white equals a high magnitude, black equals zero. Magnitude normalized per subband). Images are for illustrative purposes and not to scale.

roots of its derivative:

$$\mathbf{W}^\intercal \mathbf{C}^{-1}(\mathbf{y} - \mathbf{W}\mathbf{x}) + \frac{\mu}{\lambda}\Phi^\intercal \left(\mathbf{d}^{(k)} - \Phi(\mathbf{x}) - \mathbf{b}^{(k)}\right) = 0. \tag{5.15}$$

Eq. (5.15) can be rewritten as

$$\left(\mathbf{W}^\intercal \mathbf{C}^{-1}\mathbf{W} + \frac{\mu}{\lambda}\Phi^\intercal\Phi\right)\mathbf{x} = \mathbf{W}^\intercal \mathbf{C}^{-1}\mathbf{y} + \frac{\mu}{\lambda}\Phi^\intercal \left(\mathbf{d}^{(k)} - \mathbf{b}^{(k)}\right) \tag{5.16}$$

Remember that $\mathbf{W}$ is the forward projector and Φ is the forward sparsifying operator. We now also need $\mathbf{W}^\intercal$, the back projector, and $\Phi^\intercal$, the backward sparsifying operator.

When shearlets are used, $\Phi^\intercal\Phi = \mathbf{I}$, because of the property that shearlets form a tight frame [305, 331]. However, in CT reconstructions $\mathbf{W}^\intercal\mathbf{C}^{-1}\mathbf{W}$ will usually not be equal to $\mathbf{I}$. $\mathbf{C}$ may have off-diagonal elements due to modeling of e.g. detector element crosstalk or afterglow, and $\mathbf{W}$ is not always square. Furthermore, applying $\mathbf{W}^\intercal$ (direct back-

projection) after $\mathbf{W}$ will result in a blur proportional to $1/r$ with r the distance from the source, as seen in Section 2.2.6.1. Thus for shearlets, Eq. (5.16) can not be easily solved through inversion.

The same property holds when TV is used. For isotropic TV, Eq. (5.16) becomes:

$$\begin{aligned}\left(\mathbf{W}^\intercal\mathbf{C}^{-1}\mathbf{W}+\frac{\mu}{\lambda}\left(\nabla_x^\intercal\nabla_x+\nabla_y^\intercal\nabla_y\right)\right)\mathbf{x}=\mathbf{W}^\intercal\mathbf{C}^{-1}\mathbf{y}\\ +\frac{\mu}{\lambda}\left(\nabla_x^\intercal\left(\mathbf{d}_x^{(k)}-\mathbf{b}_x^{(k)}\right)+\nabla_y^\intercal\left(\mathbf{d}_y^{(k)}-\mathbf{b}_y^{(k)}\right)\right),\end{aligned} \tag{5.17}$$

and $\nabla_x^\intercal\nabla_x+\nabla_y^\intercal\nabla_y\neq\mathbf{I}$. Because of these issues for both shearlets and TV, we select the conjugate gradient (CG) method [334] to find a general solution for Eq. (5.16).

In Eq. (5.7b), there is no coupling between elements of $\mathbf{d}$. The optimal value of $\mathbf{d}$ can then be computed using the point-wise soft shrinkage operator:

$$\mathbf{d}_i^{(k+1)}=\text{softshrink}\left(\left[\Phi\left(\mathbf{x}\right)\right]_i+\mathbf{b}_i^{(k)},\frac{1}{\mu}\right), \tag{5.18}$$

with

$$\text{softshrink}(x,\gamma)=\frac{x}{|x|}\max\left(|x|-\gamma,0\right). \tag{5.19}$$

Here x is one coefficient and γ is the shrinkage threshold. Shrinkage is an extremely fast operation because it requires only a few operations per element of $\mathbf{d}$ and can easily be parallelized.

When shearlets are used as the sparsifying operator, all calculations involving element-wise operations (such as soft-shrinkage or the Bregman update step) need to be executed per element per scale per direction, because it is a multi-resolution transformation. It was empirically found that the soft-shrinkage is best applied using an energy dependent threshold, by multiplying the threshold value μ^{-1} by the energy of the subband filter where the threshold is being applied. This energy is calculated by applying the radial filters of the shearlet transformation to a Dirac delta function and calculating the squared ℓ_2-norm of the resulting shearlet coefficients per scale. This energy will be the highest for the highest resolution scales, and lowest for the low-resolution scale.

The pseudocode of the split-Bregman algorithm for CT reconstruction

can be found in Appendix A. Lines 1-9 correspond to the pre-calculation of the energy dependent thresholding in the case of shearlet-based regularization, and are not needed for the isotropic TV implementation.

5.3 Data acquisition

5.3.1 Data simulation

We will use 2 different phantoms, both depicted on Figure 5.5, to measure the performance and properties of the proposed algorithms. The first phantom consists of a 4 cm diameter phantom, containing two gradients. Both gradients are 1 cm wide, ranging from contrast -85% to 0%. This allows us to evaluate the difference of using TV regularization to that of SH regularization for a smooth, non-piecewise constant object.

The second phantom is the clock phantom used by Evans et al. [335], scaled down to small-animal size. It consists of a 4 cm diameter water background, modeled after the attenuation of water at an energy of 60 keV. The phantom contains 8 inserts, each with a different contrast. Each insert is located 1.1 cm from the phantom center, with a diameter of 0.4 cm. This phantom will be used to determine the optimal choice of $\frac{\mu}{\lambda}$ and the effect of contrast magnitude on the noise-resolution tradeoff.

All phantom data is simulated by forward projecting an oversampled phantom using the geometry of the micro-CT scanner used for the real measurements (Sec. 5.3.2). This allows us to use the same reconstruction settings for all datasets. We simulate fan-beam data over 512 uniformly spaced angles over 2π. The detector consists of 592 elements with a pixel pitch of 0.2 mm. The distance between tube and detector is set to 300.33 mm and the radius of rotation 113.39 mm, resulting in a zoom factor of 3. The detector is offset by 9.69 pixels. After forward projecting the phantom, photon noise is introduced corresponding to 2×10^5 photons per pixel. To investigate the influence of angular undersampling (fewer-view reconstruction), this sinogram is reduced to only 128 projection views, by uniformly selecting every 4th projection view. This would reduce the total X-ray dose by a factor of 4.

5.3.2 Measured data

To evaluate the performance on real data and for realistically textured objects, one realistic preclinical phantom is also imaged. The plastimouse

phantom (Frank Verhaegen[1], Maastro Clinic, the Netherlands) is made by plastinating a mouse [336]. A high-dose reconstructed image is shown in Figure 5.5. This ensures that no movement will occur while scanning over long time periods. Although the image contrast obtained with this technique is not realistic because all bodily fluids have been replaced by equally-dense plastic, the textures remain intact. This allows for in depth evaluation of the proposed reconstruction methods.

A Triumph-II CT scanner (TriFoil Imaging, Northridge, CA, USA) is used to acquire all data. It consists of a 2368×2240 pixel detector with pixel pitch 0.050 mm. A zoom of 3× leads to a field of view (FOV) of 42 mm. The tube voltage is set to 75 kVp, with a tube current of 240 μA, a detector exposure time of 700 ms and a focal spot size of 50 μm. The plastimouse is scanned 33 times in the same position, each time using 1024 angles over 2π. This corresponds to a total radiation dose of 12.3 Gy. As the reconstruction algorithms were only implemented for fan-beam data, only the central detector row is retained from the measured cone-beam data to give fan-beam data without the need for rebinning. This fan-beam dataset is then subsampled to 592 detector pixels (pitch 0.2 mm), and 512 angles by uniformly selecting every 2nd projection view.

Three datasets are generated from the acquisition data. The first is a reference and quasi-noiseless sinogram, generated by averaging all 33 fan-beam sinograms. The second is a noisy sinogram, made by selecting only one sinogram of the 33 measured ones. The last dataset is fewer-view data, generated by reducing the reference sinogram to 128 views, keeping every 4th sinogram row. Both the reconstructions of the noisy sinogram and the fewer-view sinogram can then be compared to the reference reconstruction obtained from the quasi-noiseless sinogram.

5.4 Data reconstruction and analysis

All datasets are reconstructed using SIRT, split-Bregman using isotropic TV (SpBR-TV) and split-Bregman using shearlets (SpBR-SH). A reconstruction pixel grid of 512^2 with pixel pitch of 0.080 mm is chosen, to include the full phantom in the FOV.

The pseudocode to SpBR found in the Appendix was implemented in C++, using the 2D distance driven algorithm [337] as forward and back

[1] Frank.Verhaegen@maastro.nl

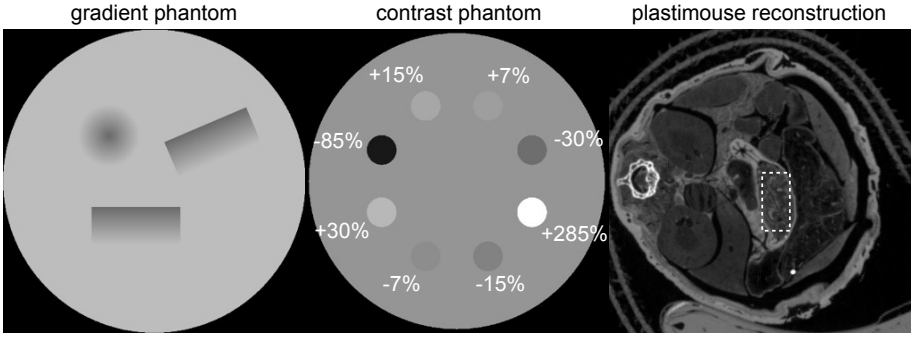

Figure 5.5: Reference image of the three datasets used. Left: gradient phantom. Middle: contrast phantom. Right: measured plastimouse reconstruction. Dashed square: ROI used for texture analysis (Section 5.5.4).

projector. The number of CG iterations used in the inner loop was always set to 30. We use $\mathbf{C} = \text{diag}\{c_i\}$ with $c_i = e^{-y_i}$, using y_i as an estimator for the mean number of photons detected in detector pixel i [319], even when the ground-truth is available from the simulations. In the case of shearlet-based regularization, four subbands are used with 8 analysis directions each. Parameter α is always set to $\frac{1}{2}$. The energy dependent thresholding was implemented by multiplying $\frac{1}{\mu}$ (γ in Eq. 5.19) with the energy of the subband where the threshold is being applied (see the last paragraph of Section 5.2.3.2).

5.5 Performance analysis

5.5.1 Gradient phantom

Figure 5.6 shows a zoomed in part of the the reconstructions of the gradient phantom using SIRT, SpBR-TV and SpBR-SH, compared to the reference phantom. Both SpBR-TV and SpBR-SH are shown at matched noise (1.5%), while SIRT is shown at convergence (800 iterations). Both methods correctly reconstruct both the spherical gradient as well as the wedge gradient. On the wedge gradient (bottom rows), it can be noticed that TV-based reconstruction does not follow a smooth line along the gradient, and follows the straight edge too fast. This is a sign of slightly lower resolution for the chosen parameter settings. The shearlet-based reconstruction follows the gradient more smoothly, but exhibits oscillating effects around sudden intensity changes. This is also visible in the

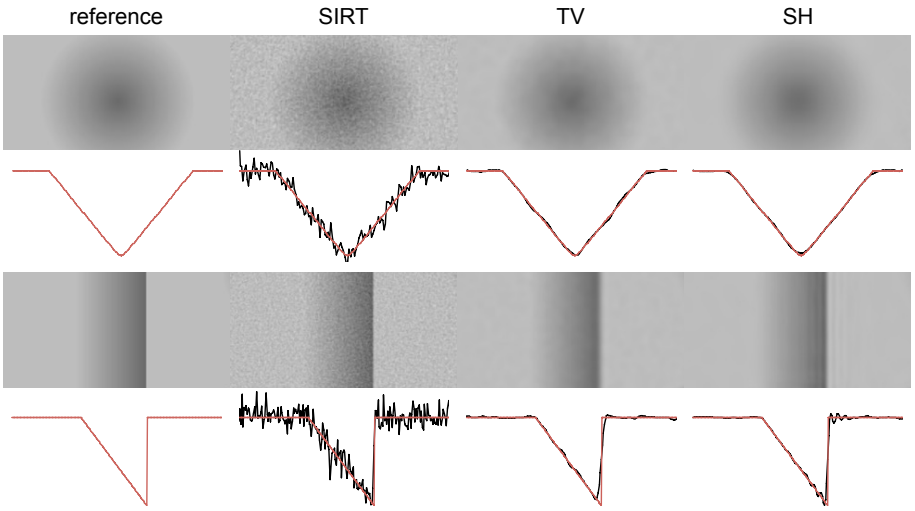

Figure 5.6: Reconstructions of gradient phantom. TV and SH are matched by noise, SIRT shown at convergence. Top rows: zoomed in on spherical gradient. Middle row: profiles through wedge gradient. Red line is the reference phantom.

image itself, where vertical lines are present around the hard edge.

5.5.2 Convergence analysis

The optimal convergence parameters are determined by holding the cost function constant (i.e. constant λ), after which the iteration at convergence is determined for different values of convergence rate $\frac{\mu}{\lambda}$. In a second step, the convergence rate is held constant, while determining the iteration at convergence for different cost functions, determined by varying λ. We define convergence as $\left\|\mathbf{x}^{(\infty)} - \mathbf{x}^{(k)}\right\|_2^2 < 10^{-4}$. $\mathbf{x}^{(\infty)}$ is approximated by the reconstructed image at iteration 80.

The convergence of SpBR-TV and SpBR-SH is plotted in Fig. 5.7a. For SpBR-TV, a convergence rate of 3 is optimal, resulting in convergence in only 10 iterations. The convergence becomes worse with a rate lower or higher than this optimum. For SpBR-SH, the optimum is a lower bound on μ/λ. All values larger than $\mu/\lambda = 9$ lead to convergence in 10 iterations.

Based on these results, the optimal μ/λ of 3 was chosen for SpBR-TV reconstruction, and $\mu/\lambda = 10$ for SpBR-SH. We can now investigate the number of iterations needed for different cost functions. Fig. 5.7b shows

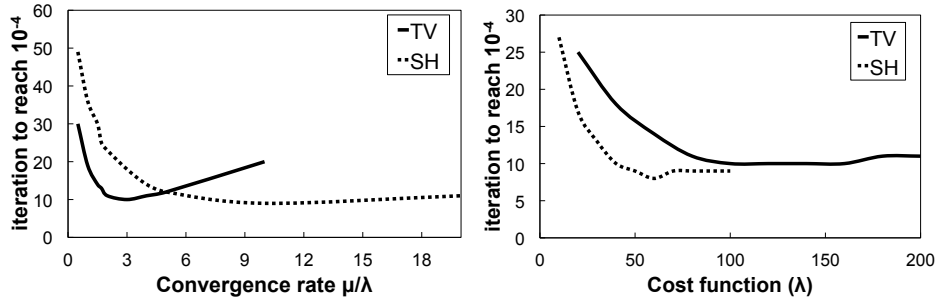

Figure 5.7: Convergence analysis for (a) fixed cost function and (b) fixed convergence rate.

that the number of iterations needed can be estimated, as long as the regularization is not too greatly enforced (large λ). For λ values smaller than 100 in the case of SpBR-TV, and smaller than 60 in the case of SpBR-SH, more and more iterations are needed to reach the level of convergence needed. Although the optimal parameters can be selected to ensure convergence in less than 10 iterations, in any case we will reconstruct all datasets in the next subsections with 30 SpBR iterations. This will ensure convergence regardless of the λ parameter selected. The convergence rate for the following experiments was set to the optimal $\mu/\lambda = 3$ for SpBR-TV and $\mu/\lambda = 10$ for SpBR-SH.

5.5.3 Noise-resolution tradeoff

The effect of contrast magnitude on the noise-resolution tradeoff for SIRT, SpBRTV and SpBRSH are determined by using a method proposed by Evans et al. [335]. Because the proposed algorithms are nonlinear, both noise and resolution need to be evaluated locally. For each contrast value, noise is determined by a circular region around the contrast insert. The resolution is determined by the Edge Spread Function (ESF) of the insert edge. A parameterized ESF model is then fitted to this profile [338], after which this analytical model can be differentiated to generate a Line Spread Function (LSF). By using an analytical model for the ESF, the influence of limited sampling and noise on the LSF calculation is reduced. The LSF is then Fourier transformed to generate the Modulation Transfer Function (MTF). Because the MTF is a function and not a single metric, Evans et al. [335] represent the MTF by the

value A_{10}:

$$A_{10} = \frac{1}{10} \int_0^{10\,\mathrm{lp/mm}} \mathrm{MTF}\,(f)\,\mathrm{d}f. \tag{5.20}$$

A_{10} is normalized to 10, as this is the area under an ideal MTF curve that has amplitude 1.0 for all spatial frequencies. The higher A_{10}, the higher the resolution.

Figures 5.8 and 5.9 plot the noise-resolution tradeoff, for different contrast magnitudes. Each data point was gathered by reconstructing with varying λ, with lower λ leading to less noise. The full-view dataset is the contrast phantom with all 512 views, while the fewer-view dataset is the contrast phantom with just 128 views. For higher-noise data points the ESF model fitting becomes difficult, leading to the erratic behavior. However, the general trend of each curve is still visible.

Three observations can be made. First, generally all SpBR-SH curves are positioned above and left of the SpBR-TV curves reconstructed from the same dataset. Thus, the noise is higher for equal resolution when shearlets are used instead of TV. For some noise level, the lowest resolution is always reached by the SpBR-SH reconstruction method on few-view data (Fig. 5.9). Both methods outperform SIRT reconstruction, especially on fewer-view data. A little better resolution can be found with SpBR-SH compared to SpBR-TV for fewer-view data for the ±7% contrast inserts. A zoom on the −7% insert reconstructed from fewer-view data is provided in Fig. 5.10. At matched resolution of $A_{10} = 0.6$, little noise is seen for TV, while some patchy structures are visible on the insert edge. For SH, some wavy lines are present that will lead to higher noise measurements, though the insert is visually rounder. At maximum resolution (SIRT $A_{10} = 0.91$, SpBR-TV $A_{10} = 0.88$, SpBR-SH $A_{10} = 0.96$) the insert is still visibly rounder for SH, though the wavy lines are even more visible now.

A second observation is the difference between both SpBR methods, which becomes more and more clear for lower contrast magnitudes. At low contrast (±7%) more noise is measured at equal resolution for SpBR-SH compared to SpBR-TV. This effect is less visible for ±30% contrast, where at lower resolution both methods obtain the same noise level. Only at higher resolution a separation between the two methods occurs.

The third and final observation can be made after comparing the results of the full-view dataset (Fig. 5.8) to the results obtained from the fewer-view dataset (Fig. 5.9). These make it clear that a higher resolu-

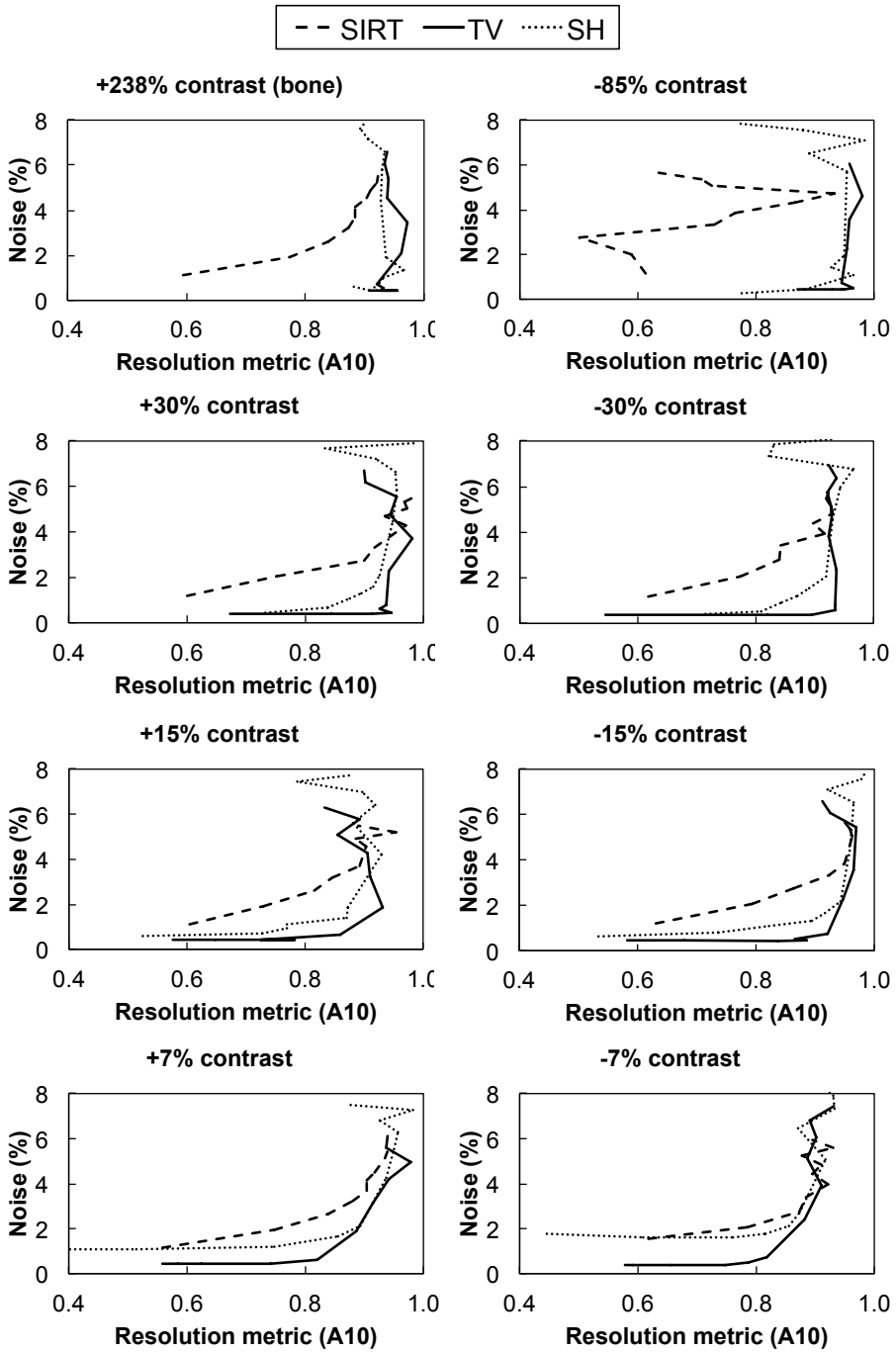

Figure 5.8: Influence of contrast magnitude on noise-resolution tradeoff for the full-view, noisy dataset. Dashed line: SIRT. Full line: SpBR-TV. Dotted line: SpBR-SH. At equal resolution, noise is higher with SpBR-SH than with SpBR-TV, especially for the $\pm 7\%$ contrast insert.

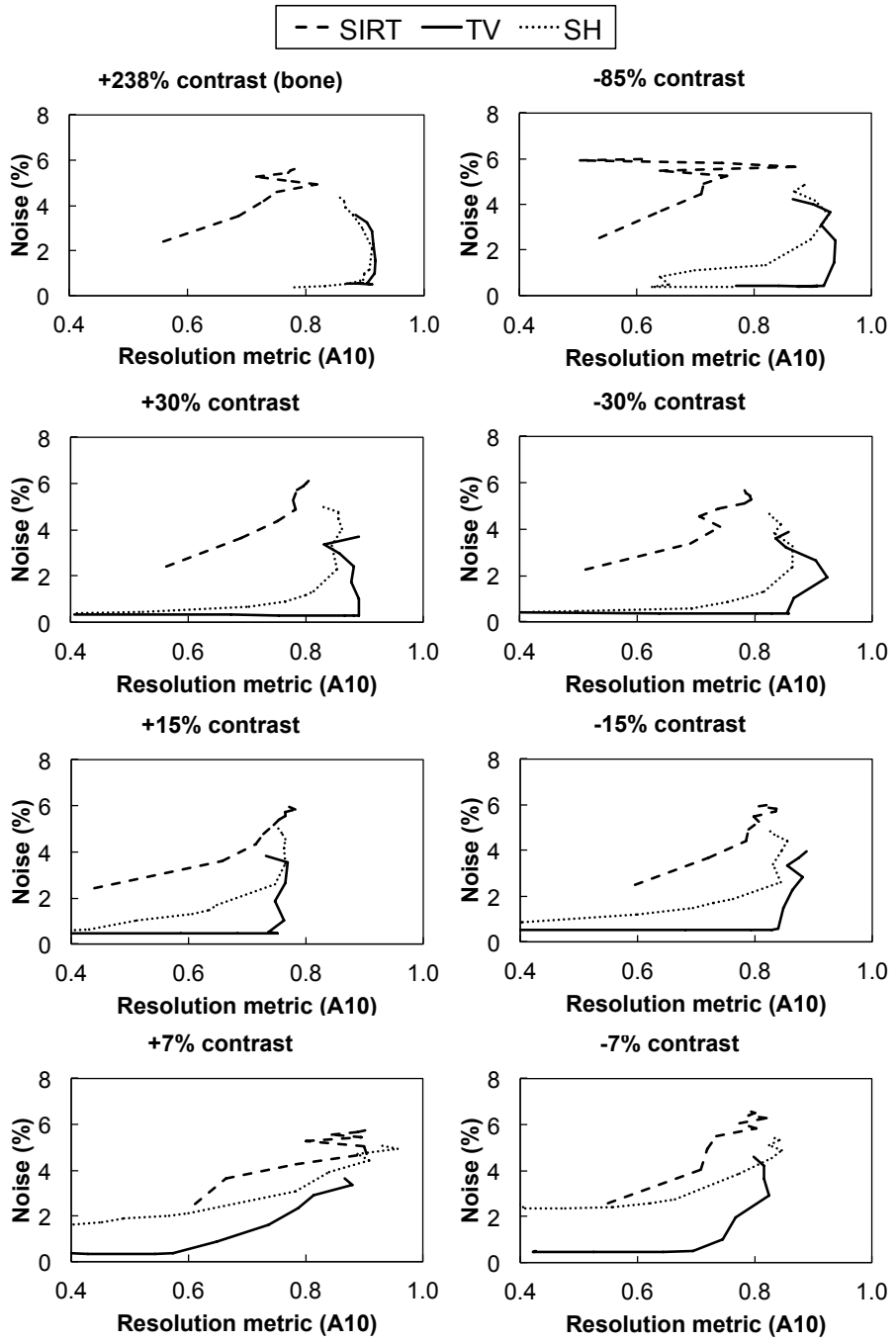

Figure 5.9: Influence of contrast magnitude on noise-resolution tradeoff for the fewer-view, noiseless dataset. Dashed line: SIRT. Full line: SpBR-TV. Dotted line: SpBR-SH. At equal resolution, noise is higher with SpBR-SH than with SpBR-TV, especially for the $\pm 7\%$ contrast insert.

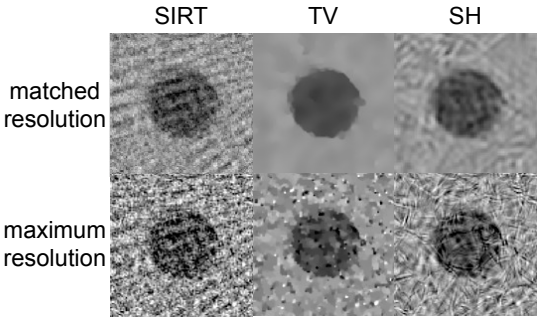

Figure 5.10: −7% contrast insert from the few-view dataset reconstructed with SIRT, SpBR-TV and SpBR-SH at matched resolution ($A_{10} = 0.6$) and at maximum resolution. Window [0.18 0.23] cm^{-1}.

tion can be achieved at the same noise level for full-view datasets. When fewer-view data are used, the resolution drops. This is true for all three the methods.

5.5.4 Texture analysis

The influence of SpBR-TV and SpBR-SH on textures is measured on the measured plastimouse data using the gray level co-occurrence matrix (GLCM) [339], which is defined by:

$$C_{\Delta x,\Delta y}(i,j) = \sum_{p=1}^{n}\sum_{q=1}^{m}\begin{cases}1, & \text{if } I(p,q)=i \text{ and } I(p+\Delta x, q+\Delta y)=j\\ 0, & \text{otherwise}\end{cases} \tag{5.21}$$

with i and j image intensity values, p and q voxel indices in image $\mathbf{I}$ and $(\Delta x, \Delta y)$ an offset determined by the directional analysis (e.g. (1, 1) for 45°).

The GLCM is calculated on a region of interest (ROI) encompassing the stomach contents (dashed square in Fig. 5.5). It allows us to extract second order statistical texture features.

For this evaluation study, we compare 4 metrics which can be measured on the GLCM: contrast, correlation, energy and homogeneity.

- Contrast is a measure of the intensity contrast between a pixel and its neighbor over the whole image, with 0 the contrast value of a

constant image.

$$\text{contrast} = \sum_{i,j} |i-j|^2 C(i,j) \tag{5.22}$$

- Correlation is a measure of how correlated a pixel is to its neighbor over the whole image.

$$\text{correlation} = \sum_{i,j} \frac{(i-\mu i)(j-\mu j)C(i,j)}{\sigma_i \sigma_j} \tag{5.23}$$

- The energy returns the sum of squared elements in the GLCM. A GLCM with a low number of high-value elements will have a higher energy than a GLCM with a high number of low-value elements. A constant image will have an energy of 1.

$$\text{energy} = \sum_{i,j} C(i,j)^2 \tag{5.24}$$

- Finally, the homogeneity represents the closeness of the distribution of elements in the GLCM to the GLCM diagonal.

$$\text{homogeneity} = \sum_{i,j} \frac{C(i,j)}{1+|i-j|} \tag{5.25}$$

For each reconstructed image, the stomach ROI is cropped and quantized to 32 levels. The GLCM is then calculated for the 0°, 45°, 90° and 135° neighbors using the functionality provided by MATLAB (MATLAB 7.11.0, The Mathworks Inc., Natick, MA). As a final aggregate texture metric, the 4 texture properties are combined to calculate the Euclidean distance to the texture metric calculated on the reference texture. All 4 properties are normalized so to give equal weight to each property inside the distance function.

Figure 5.11 plots the 4 texture metrics which were determined from the GLCM. Each plot represents one texture metric, and contains the results for SpBR-TV (full line) and SpBR-SH (dotted line) for both the noisy dataset (black) as well as the fewer-view dataset (gray) (Section 5.3.2). The value obtained for the averaged plastimouse dataset with all views is pictured by the dashed line, which serves as a reference property value. The bottom row contains two plots that represent the Euclidean distance

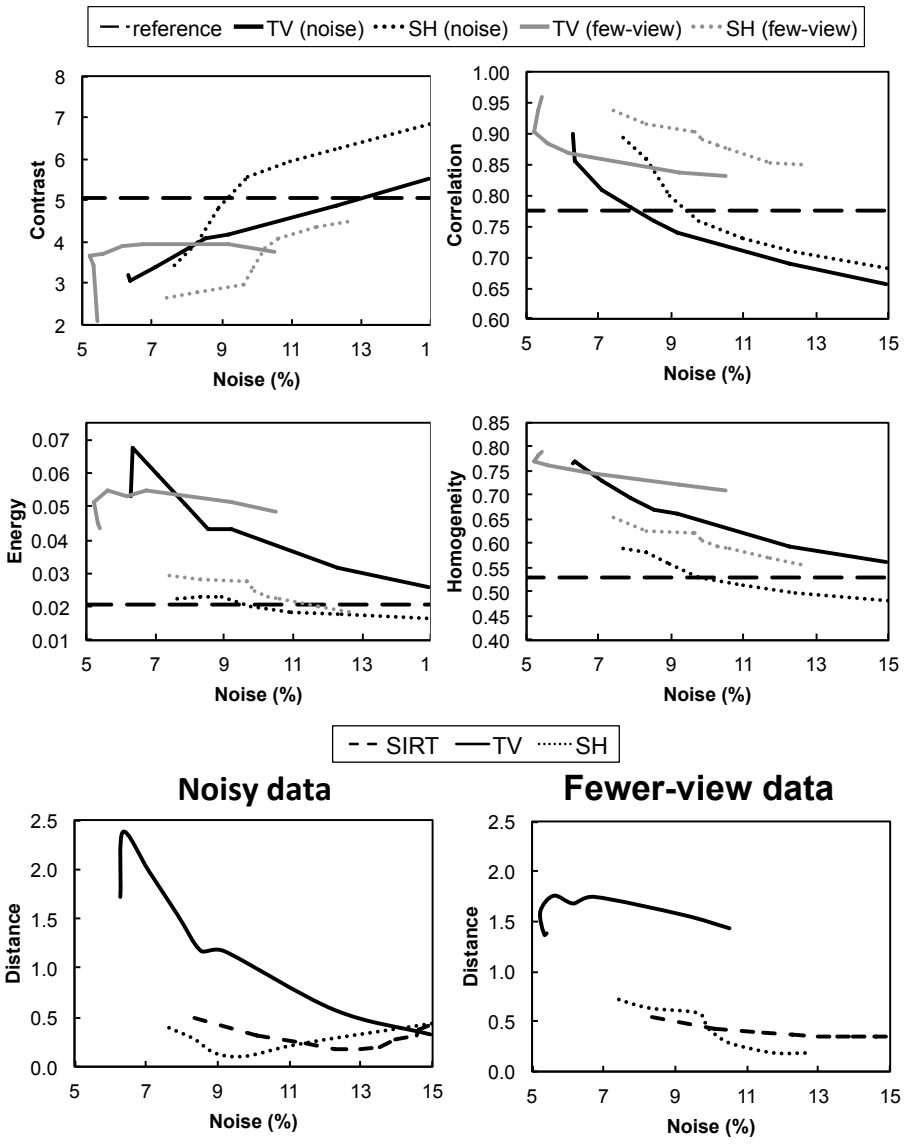

Figure 5.11: Contrast, correlation, energy and homogeneity as measured from the GLCM. Full line: SpBR-TV. Dotted line: SpBR-SH. Dashed line: reference value obtained from full-view noiseless SIRT reconstruction. Black: noisy dataset. Gray: fewer-view dataset.

of the 4 selected properties to the reference reconstruction. Different data point were gathered by reconstructing with varying λ in the case of SpBR-methods, where for SIRT this is done by varying the number of iterations. The noise is measured in the ROI depicted by the dashed ellipse in Fig. 5.12.

Here, shearlet-regularized reconstruction outperforms TV-based reconstruction, for both the noisy as well as the fewer-view dataset. TV is always closer to the reference than SH on the contrast metric. Based on correlation, both methods perform similarly independent of the dataset, though the same correlation value is reached at higher noise for SpBR-SH compared to SpBR-TV. A large difference can be found for the energy property. Here, while SH estimates the energy correctly, TV regularization removes the structure completely and replaces it by homogeneous patches. This results in a very high energy, which results in a high distance to the reference texture. The same is visible to a lesser extent on the homogeneity property.

Comparing both distance plots in the lowest row of Fig. 5.11, the distance for the noisy dataset has a clear optimum for the shearlet reconstruction. For noisy data, the texture obtained with shearlet-based reconstruction is closer to the reference than obtained with conventional SIRT reconstruction, at lower noise. With fewer-view data, SpBR-SH outperforms SIRT. When more regularization is applied, the distance to the reference reconstruction increases, and this leads to a worse texture than when normal SIRT is used. However, these low-noise SIRT reconstructions are generated with only a few iterations, which means the corresponding resolution will be far worse than the converged SpBR-SH reconstructions.

Figure 5.12 shows reconstructions of the plastimouse for the noisy dataset, comparing to the reference SIRT reconstruction generated from the 33× averaged sinogram. The SIRT, SpBR-TV and SpBR-SH reconstructions were selected with an equal noise level (12%) by experimentally selecting the correct λ value which gives this noise level at convergence for SpBR-methods, and the early-stopping of SIRT when this noise level was reached. Only SpBR-SH can accurately reconstruct the small diagonal stripes seen in the left kidney (full arrow). SpBR-TV exhibits patchiness which is especially visible on object edges, and in the darker region on the right of the image (dashed arrow). Edges are more smoothly reconstructed when SpBR-SH is used. However, the darker region shows some wavy artifacts when shearlets are used, compared to

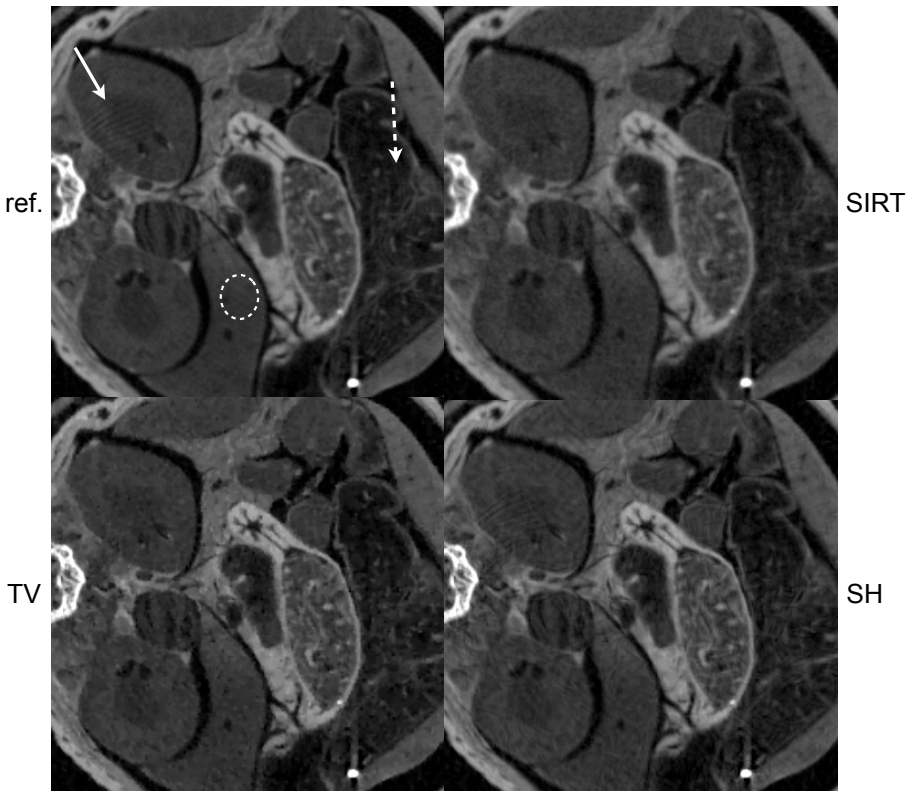

Figure 5.12: Reconstructions for the noisy dataset. Reconstruction images matched on noise, measured in a ROI (dashed ellipse) on the liver.

the blocky structures encountered in the TV-based reconstruction.

The fewer-view dataset reconstructions are shown in Figure 5.13, matched to 10% noise in the liver ROI. Both SpBR-TV and SpBR-SH have problems with reducing the noise in this dataset while keeping the texture of the stomach intact. Both methods still show a lot of aliasing artifacts, caused by the 4-fold undersampling of the data. For SpBR-SH, the aliasing streaks have been sharpened in some places, while they have been minimized in others. Small spots (full arrow) are better visible on the TV-regularized reconstruction than with SpBR-SH, where it has been smoothed away. Figure 5.14 zooms in on the upper part of the stomach. SpBR-TV optimized the air cavity above the stomach (arrow) into a square shaped cavity. The SpBR-SH image shows an improved reconstruction of the radial lines (arrow).

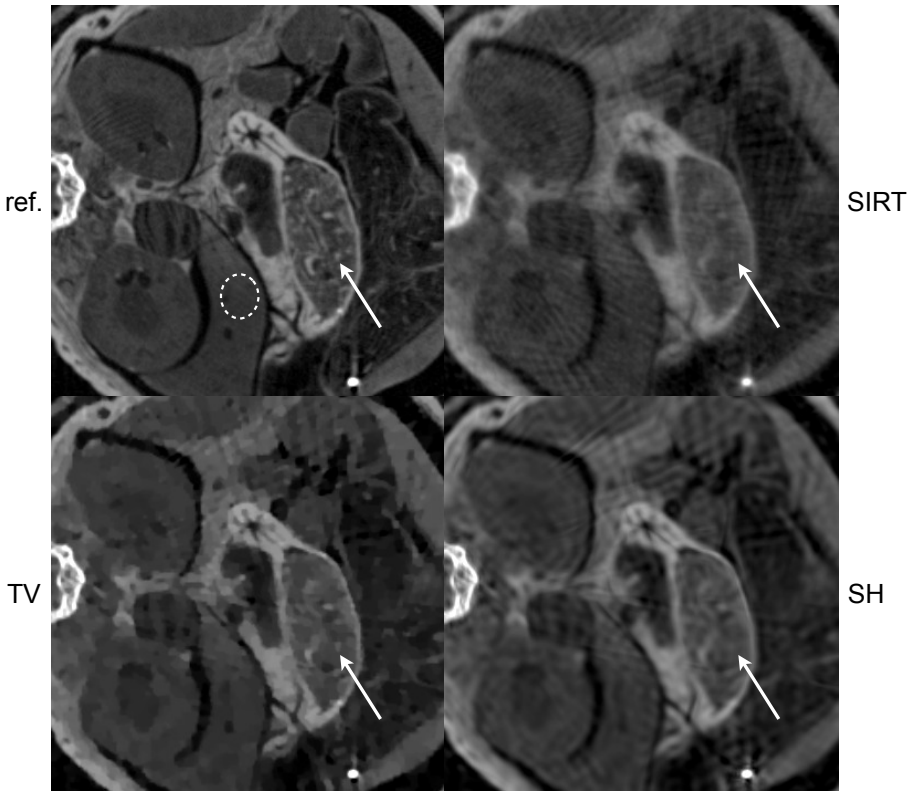

Figure 5.13: Reconstructions for the fewer-view dataset. Reconstruction images matched on noise, measured in a ROI (dashed ellipse) on the liver.

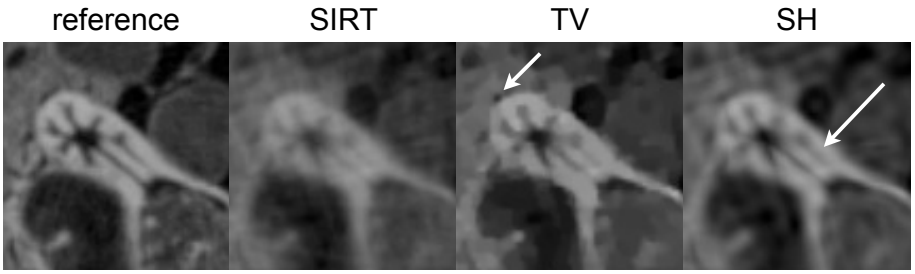

Figure 5.14: Zoom of reconstructions from Fig. 5.13.

5.6 Discussion

Replacing TV by shearlets for regularized reconstruction is promising for iterative CT imaging in theory. We have shown that shearlets do not lead to the piecewise-constant behavior as seen with TV, but instead may lead to wavy artifacts, which can be equally unwanted in medical diagnostics.

The noise-resolution tradeoff shows that SpBR-SH leads to higher noise at the same resolution as obtained with SpBR-TV. However, this could be due to the Gibbs effect also noticed in Fig. 5.6. These wavy oscillations will be included in the noise measurements, leading to a bias in the tradeoff curves. These wavy lines are also visible on Fig. 5.10 and on the real data presented in Fig. 5.12 and Fig. 5.13. They replace the patchy artefacts of TV regularization.

Unfortunately, it is very difficult to quantitatively evaluate the added usefulness from the medical diagnostic point of view, as a ground-truth reference image will always be needed. The most-used phantom in CT reconstruction evaluation is the Shepp-Logan phantom, defined by adding 10 uniformly-filled ellipses [282]. This makes it inherently piecewise constant. More realistic simulators and phantoms exist, but will always exhibit piecewise constant behavior due to the segmentation needed to transform measured patient data into phantom data. This biasses the results towards TV. Promising is the work done by Bond et al. [284], who have developed a version of the XCAT phantom [289] with realistic lung texture. However, it still needs to be expanded into 3D texture. In our study presented here, we used a high-resolution, realistically textured, plastinated mouse, so that the dataset would not be biased towards TV.

Although the texture analysis on preclinical images improved the outlook for shearlet-based regularization, it is clear that there are still some issues. Although the shearlet transform, like the curvelet transform, is suited for structures representing sharp and elongated structures, e.g. edges, it is unsuited for spherical-like sources (the point in the stomach on Fig. 5.13 has been reconstructed less accurately in SpBR-SH, while the radial lines in Fig. 5.14 are reconstructed more accurately with SpBR-SH). This is a common issue with a lot of multi-resolution techniques, as when they represent isotropic features well, they are far from optimal for analyzing anisotropic objects [340]. This was the main idea behind the development of other constructions, such as the curvelet transform [341]. It could thus be beneficial to combine the shearlet transformation with

an isotropic wavelet transform. The sensitivity of each transform to a particular shape would possibly make it a very strong discriminating tool. However, the weights of the transformations in this combination will depend on the specific study.

Although the methods presented here have been applied to fan-beam data, the techniques can certainly be carried over to 3D cone-beam data with no further adjustments. Indeed, no assumptions have been made about the scanner geometry in the derivation of the algorithms, and the optimization algorithms used can be applied irrespectively from dimensionality. Although the shearlet methodology can be extended to 3D directly [342], it will suffer from large computational complexity due to the use of multiple 3D FFTs and subsequent frequency domain filtering (which has to be repeated for every iteration of the split-Bregman algorithm). A possible alternative is a special 3D shearlet design based on separable filters in the spatial domain. This is a topic of ongoing research. Even then, there is still room to improve the existing algorithm, by using preconditioned CG [343]. This would improve the reconstruction time by reducing the number of CG iterations needed.

Future work could include the application of these developed techniques to different datasets together with numerical observer studies, e.g. the channelized Hotelling observer [344, 345], to compare different regularization strategies from the medical diagnostic point of view.

5.7 Conclusion

In this chapter we have presented a framework to perform regularized iterative CT reconstruction based on the split-Bregman technique. The split-Bregman approach allows us to combine using shearlet regularization as an alternative for TV minimization. The use of shearlets for regularization leads to different artifacts than in the case of TV, because shearlets model the structures contained in the image using a different (non-piecewise constant) image model. Based on a noise-resolution tradeoff study, TV minimization outperforms shearlet-based reconstruction. However, on acquired data with realistic textures, shearlets reconstruct textures more similar to the reference texture than when TV is used. The piecewise constant artifacts are gone, but are replaced by wave-like structures.

Chapter 6

Quantitative reconstruction of multiple isotopes for micro-SPECT/CT

6.1 Introduction

Single Photon Emission Computed Tomography (SPECT) is an *in vivo* imaging technique used to visualize functional information with radioactive tracers. In Section 2.3, a detailed description of SPECT was already given, first discussing the general principles behind emission tomography and tomographic reconstruction, followed by a discussion of the image degrading effects and the remaining challenges. Section 2.3.6 contains a discussion on the use of SPECT for small animal imaging. Preclinical or micro-SPECT is especially useful to gain information about drug biodistribution in animals, important for early phase development of drugs [346]. Historically, the pharmacokinetic information was usually obtained with *ex vivo* approaches on cohorts, e.g. by measuring the radiolabel biodistribution in organs in a well counter, or by measuring the accumulation of the radiolabel in tissue with an ex vivo autoradiograph on brain slices. When follow-up studies are required, e.g. to investigate the longitudinal effect of a new drug, a large number of animals are needed to minimize the variability in such an experimental ex vivo design.

One of the remaining challenges in SPECT imaging (see also Section 2.3.7) is absolute quantification. The goal of absolutely quanti-

tative SPECT is to provide reconstructed images in which each voxel value in the image represents the absolute activity concentration in the corresponding region in the patient or animal [347]. In preclinical research, animals could then serve as their own control during longitudinal studies [346], thereby decreasing the experimental variability. The quantitative results can be used to estimate radioligand-specific binding kinetics, receptor density or other relevant biochemical parameters [348], ultimately leading to faster drug development [349]. In clinical SPECT, absolute quantitative data can increase the accuracy of organ dosimetry, useful for targeted radionuclide therapy [350].

To achieve absolute quantification in SPECT, the effect of several image degrading factors need to be minimized (Section 2.3.4). These effects are caused by attenuation, scattering and system imperfections [146], which can all be compensated for within an iterative reconstruction framework [351]. One approach is to measure the system response (each element w_{ij} from Eq. 2.69) on a grid of discrete locations in the field of view (FOV) [352]. Such system response measurements combine geometric response together with more complex effects such as detector variability and collimator imperfections. Although they are easy to measure in completely stationary systems, it is more difficult in rotating systems due to imperfect mechanical motion [353]. Furthermore, photon scatter can not be taken into account. A different approach is to directly incorporate the physical processes leading to these effects (e.g. detector response, limited pinhole diameter, sensitivity) into ray-driven reconstruction [354–356].

Table 6.1 gives an overview of the current status of absolute quantification in preclinical SPECT. Seven recent papers [135, 346, 357–361] compare ground-truth measurements to micro-SPECT results. Wu et al. [358, 359] achieved a quantification error of 2% to 4.8% for ^{99m}Tc, and 3.7% to 9% for ^{111}In using system matrix measurements in their reconstruction. With direct modeling, an error of less than 10% was calculated regardless of the radioisotope used [135, 357, 360, 361]. Lee et al. [361] studied the errors obtained from a parallel-hole setup and achieved low errors for ^{99m}Tc ($< 2\%$). However, uncorrected FBP was used to reconstruct their emission data.

Only three studies compared in vivo to ex vivo data [346, 357, 360]. Unfortunately, the data reported in those publications also lacks in some aspects. In Vanhove et al. [357], a clinical dual-head system was used, retrofitted with a pinhole collimator. Direct modeling of attenuation and

scatter reduced the quantitative error to -7.9±10.4%. No PVE correction was applied, and no data are available for other isotopes. In Cheng et al. [346], the iterative reconstruction method was stopped well before convergence at only 24 MLEM iterations, and no results were shown for ^{99m}Tc. Lastly, Finucane et al. [360] have used uncorrected reconstructions.

The aim of the current chapter as well as Chapter 7 is to demonstrate the feasibility of *in vivo* absolute quantitative micro-SPECT, using direct ray-based corrections for ^{99m}Tc and ^{111}In. Such an approach alleviates the need to measure the system matrix for each isotope. Both isotopes encompass a range of photopeaks that serve as a good testing ground (140.5, 171.3 and 245.4 keV). We will report quantification errors from a standard, commercially-available micro-SPECT/CT system with a multi-pinhole collimator. In the current chapter we validate the iterative reconstruction against a phantom study. Chapter 7 then contains the *in vivo* validation.

6.2 Correction Methods

6.2.1 System calibrations

All data were acquired on the trimodal FLEX Triumph-II system (TriFoil Imaging, Northridge, CA, USA). The SPECT subsystem (also sold separately as the X-SPECT) consists of one 80-by-80-pixel CdZnTe (CZT) detector head and can be equipped with a multi-pinhole collimator. The detector is 5 mm thick and consists of 25 CZT modules of 16×16 pixels, with each pixel having a pitch of 1.6 mm (2.25 mm^2 active area). A 5-pinhole collimator with 1.0 mm diameters was positioned 75 mm from the detector, and 55 mm from the axis of rotation, leading to a FOV of 68 mm per pinhole. Fig. 6.1b depicts the amount of overlap on the detector caused by each pinhole. The color codes represent the amount of multiplexing, ranging from no multiplexing (blue) to a central area seen by all 5 pinholes (red).

To have full flexibility after each acquisition, we acquired all data in the list-mode file format. This allows us to use our own software, without having to use software included with the commercial system. In the list-mode file format, each detected photon is stored sequentially, with meta-data representing the detected pixel location, current acquisition time, and a detection channel number (quantized photon energy). The

Isotope	System	Type of Study	Error	Ref.
Phantom experiments				
^{99m}Tc	X-SPECT (parallel hole)	Rat-sized uniform phantom	±1.9%	[361]
	X-SPECT (parallel hole)	4-quarter phantom	2.2±3.4%	[361]
	X-SPECT (parallel hole)	Concentric phantom	±2.0%, ±35.0%	[361]
	U-SPECT-II	Homogeneous phantom	-1.7%	[358]
	U-SPECT-II	Homogeneous phantom	4.8%	[359]
	U-SPECT-II	Point sources in ex vivo rat	-6.2 to 4.8%	[358]
	U-SPECT-II	Point sources in ex vivo rat	4.8%	[359]
	NanoSPECT/CT	3 vial phantom	$< 10\%$	[360]
	Dual-head clinical camera, single pinhole	9 vial phantom	-5.1 to 1.2%	[357]
	Dual-head clinical camera, multi-pinhole	9 vial phantom	-0.3 to 4.1%	[357]
^{111}In	U-SPECT-II	Homogeneous NEMA	9.1%	[359]
	U-SPECT-II	Point sources in ex vivo rat	3.7%	[359]
	NanoSPECT/CT	3 vial phantom	8-11%	[360]
	NanoSPECT/CT	Corning tubes with 2 inserts	±5%	[346]
^{125}I	U-SPECT-II	Homogeneous NEMA	-4.0%	[359]
	U-SPECT-II	Point sources in ex vivo rat	2.1%	[359]
^{201}Tl	U-SPECT-II	Homogeneous NEMA	7.3%	[359]
	U-SPECT-II	Point sources in ex vivo rat	3.3%	[359]
In vivo experiments				
^{99m}Tc	Dual-head clinical camera, multi-pinhole	in vivo mouse liver	-9.5 to -7.9%	[357]
^{111}In	NanoSPECT/CT	in vivo rat kidney and liver	-9 and 9%	[346]

Table 6.1: Review of recent preclinical absolute quantification errors reported in literature

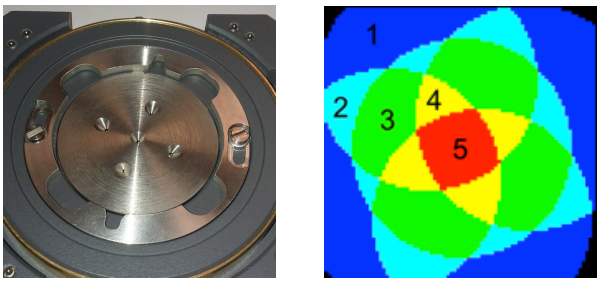

(a) (b)

Figure 6.1: (a) The bottom of the multi-pinhole collimator (b) Illustration of the overlap of individual pinhole projections on the detector, color coded and annotated with the number of overlapping pinholes in each region.

list-mode output was converted into a sinogram by counting the detected events per pixel. Each detected event was decay corrected to the start of the SPECT acquisition.

Energy calibration Each detected channel number was converted to photon energy by applying a quadratic calibration equation to correct for gain and offset. The gain and offset were determined per detector module (16×16 pixels) by least squares fitting channel numbers to the known photopeak energies of the radioisotopes ^{125}I (27.472 keV), ^{99m}Tc (140.511 keV), ^{123}I (158.97 keV) and ^{111}In (171.30 and 245.39 keV). The required raw data was acquired from low-count point sources placed one meter away from the uncollimated detector.

The final calibration equations are plotted in Figure 6.2 for all 25 modules present in 1 CZT detector. There is a clear non-linear gain on the channel number (especially for channel numbers above 1500), together with a baseline offset for the number of dark counts. We also note a substantially different gain depending on the submodule. The non-linear gain models the charge loss per pixel caused by charge sharing. Charge sharing is proportional to the photon energy, as the electron cloud diameter in each CZT pixel will quadratically increase for higher photon energies [362]. This means that the current pulse may be spread over multiple adjacent pixels, which results in a lower charge measurement for the current pixel. This leads to a lower recorded energy.

Representing each calibrated value with its mean and standard deviation over the 25 modules, the average calibration equation is equal

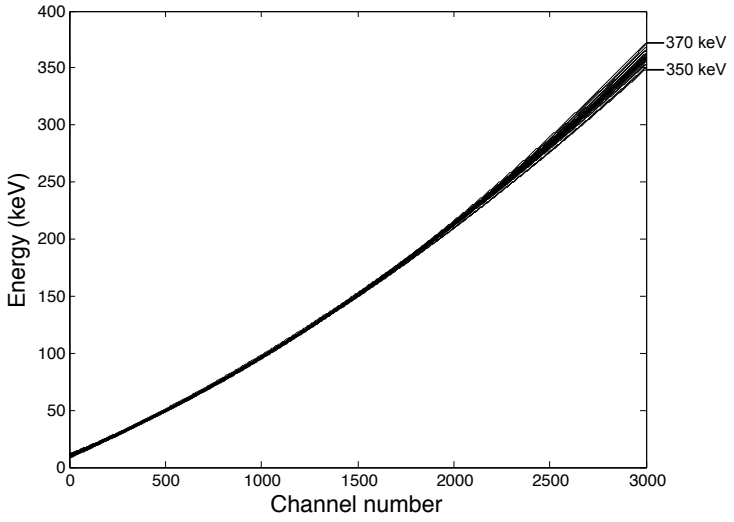

Figure 6.2: Quadratic calibration relationship between detector channel number and photon energy for each module. The non-linear gain is needed to compensate losses due to charge sharing. The baseline offset is caused by the number of dark counts. Each line represents the calibration equation for one module.

to

$$E = (1.51 \pm 0.14) \times 10^{-5} \times C^2 + (0.07 \pm 0.003) \times C + (9.69 \pm 1.00), \quad (6.1)$$

with E the photon energy in keV and C the measured channel number. Each module is corrected with its own individual calibration equation.

After applying the calibration equation to each detected event, the energy resolution can be measured. The energy resolution is measured per submodule, by fitting a Gaussian to the photopeaks acquired from the point sources. To calculate the resolution of the 171 keV peak from ^{111}In, the down scatter from the 245 keV peak is subtracted first. The down scatter was estimated by measuring the average number of photons between 187 and 215 keV.

Figure 6.3 plots the energy resolution per submodule. For the high-energy peak of ^{111}In, one submodule has a much worse resolution than the other submodules. The final energy resolutions are tabulated in Table 6.2. The resolution for ^{99m}Tc of $4.3 \pm 0.26\%$ is significantly better (one-sample t-test, $p < 0.01$) than what was reported by Wagenaar et al. [363], who reached a 4.6% resolution at 140.5 keV for this type of

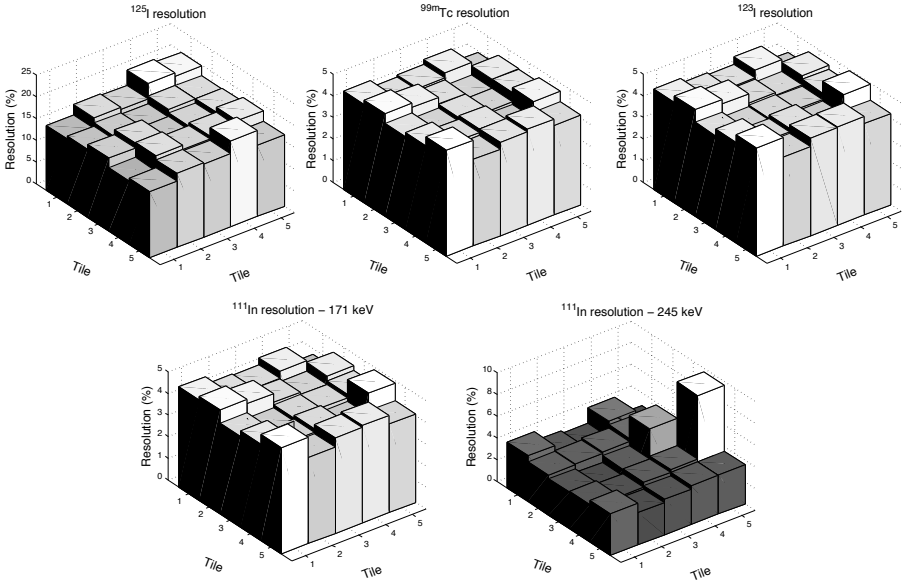

Figure 6.3: Plot of energy resolution per submodule for ^{125}I, ^{99m}Tc, ^{123}I, and both peaks of ^{111}In.

detector. Finally, Fig. 6.4 plots the spectra averaged over all detector pixels of all modules after applying the correct calibration equations per module.

Geometric calibration The SPECT system geometry is further characterized by a multi-pinhole calibration method using three point sources [364–366]. This method is based on an analytical model of the projection of a point source through a pinhole collimator onto a detector.

	Peak energy (keV)	Resolution (%) (mean±stdev)
^{125}I	27.5	17.15±1.51
^{99m}Tc	140.5	4.30±0.26
^{123}I	159.0	4.40±0.30
^{111}In	171.3	4.28±0.31
	245.4	3.90±1.38

Table 6.2: Measured CZT energy resolution.

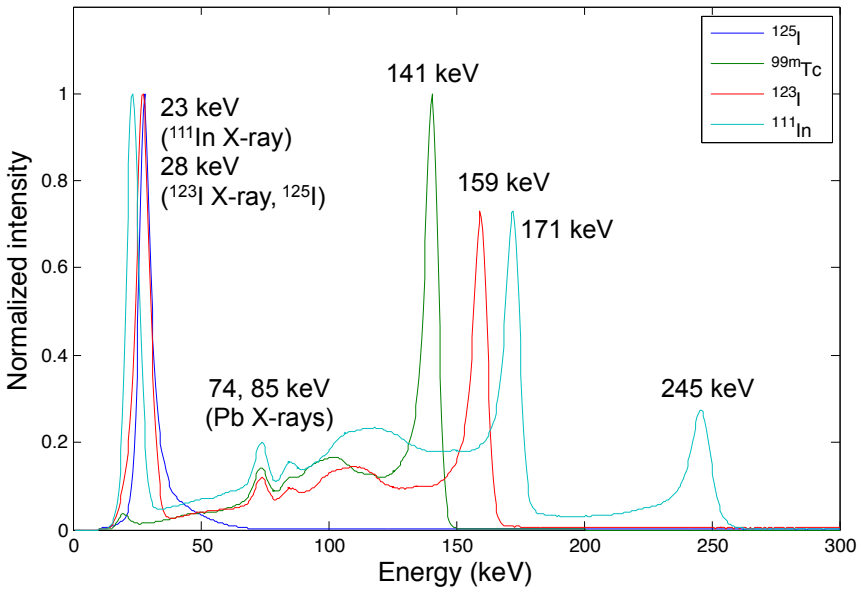

Figure 6.4: Measured spectra of ^{99m}Tc and ^{111}In with the CZT detector after per-pixel offset and gain calibration.

By parameterizing the analytical model with 5 geometrical parameters and 2 offset parameters per pinhole, the pinhole geometry can be estimated as long as three point sources are used, with a known distance between the point sources. The geometric parameters can be further refined by modeling the non-circular orbit of the detector [367].

6.2.2 Iterative SPECT reconstruction including corrections

6.2.2.1 Reconstruction algorithm

The one step late – ordered subset expectation maximization (OSL–OSEM) algorithm first discussed in Section 2.3.5.2 was implemented in C++ and CUDA. The OSL modification as proposed by Green [132] is used to incorporate image denoising into the OSEM reconstruction. The image denoising is weighted depending on each voxel belonging to edges or not [135], such that volumes are not smoothed across anatomical boundaries.

All reconstructions ran for 50 iterations with 8 subsets [368] per iteration, reconstructing 120^3 0.5 mm x 0.5 mm x 0.5 mm voxels. For

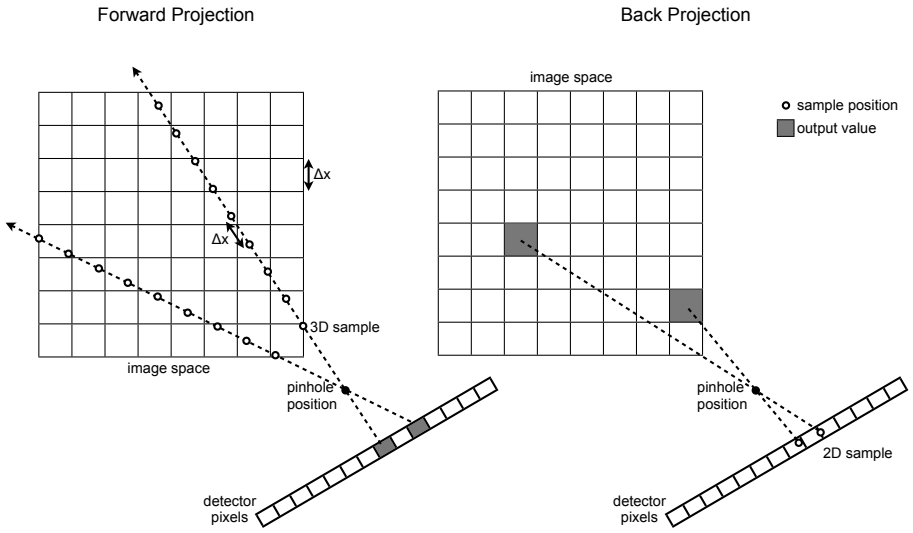

Figure 6.5: Illustration of CUDA-based ray-tracing for pinhole SPECT (not to scale).

radioisotopes that emit photons in multiple photopeaks (e.g. ^{111}In), each photopeak was reconstructed separately after which the reconstructions were summed.

Figure 6.5 illustrates the forward and back projection calculations as implemented in CUDA, similar to how this was implemented in the CT reconstruction in Section 4.3. In the forward projector, the center of each detector element is connected with a ray to the pinhole position. This ray is then traced through the image space, calculating 3D interpolated sample values at spacing Δx, the isotropic voxel size. The sum of these samples is added to the chosen detector element. All detector elements are calculated in parallel, and the 3D interpolation is implemented by using the CUDA 3D texture interpolation facilities. The forward projector is thus written as

$$\hat{y}_i^{(k)} = \sum_{s \in R(\theta)} x_s^{(k)}, \tag{6.2}$$

with s a 3D-interpolated sample along the ray R with its direction θ determined by the position of the pinhole and the detector pixel i.

The back projection is implemented by selecting the center of each image space voxel, and connecting it with a ray to the pinhole position.

The intersection of this ray and the detector plane is then calculated. The value added to the image voxel is the 2D interpolated value of the intersection location on the detector. All image voxels are calculated in parallel. The 2D intersection interpolation is implemented by using the CUDA 2D texture interpolation facilities.

6.2.2.2 Resolution recovery

Because the pinhole would be represented by an infinitesimal point using these techniques, we use a 7-ray technique to model the finite pinhole diameter by a Gaussian quadrature [266, 355]. This corresponds to calculating a weighted average of 7 forward or back projections, each with a pinhole location slightly offset from the others. The 7 rays intersect the circular pinhole opening in a polar point grid, defined on concentric circles. The weight of each ray is chosen proportional to the fraction of the total pinhole area subsampled by that ray.

A similar technique can also be used to model the finite detector pixel size, in order to decrease the spacing between rays going to neighboring detector pixels. With NaI detectors a two-dimensional Gaussian filter is commonly used to model the intrinsic detector resolution caused by the photon spread in the scintillator. Here, the contribution of each detector pixel is calculated as the average value over 3×3 subsamples per pixel.

Combining both models results in a recovery of resolution during reconstruction. In this way, the contribution to one detector pixel is sampled by 63 rays to achieve a higher resolution in the forward and back projectors. The forward projection estimate is written as

$$\hat{y}_i^{(k)} = \frac{1}{9} \sum_{d=1}^{9} \sum_{p=1}^{7} r_p \sum_{s \in R_{p,d}(\theta)} x_s^{(k)}, \tag{6.3}$$

with d the detector subsample and r_p the weight for pinhole subsample p. The ray R is now also parameterized by the specific position of the pinhole and detector subsamples. More subsamples can also be used to further increase the resolution (e.g. 21 [369] or even 2280 pinhole rays [266]), at the expense of computational speed.

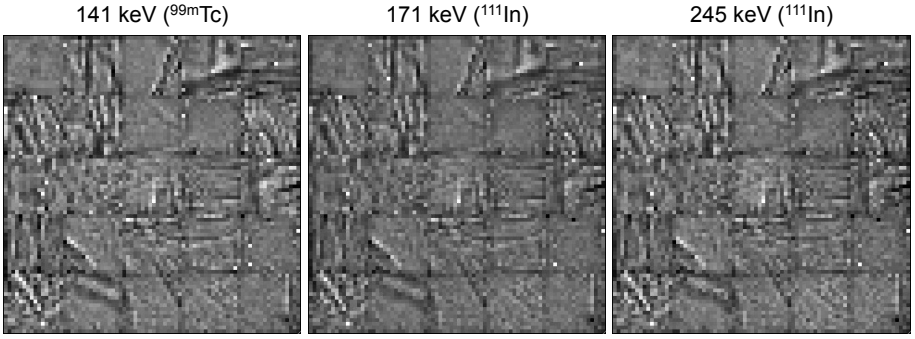

Figure 6.6: Illustration of CZT detector uniformity for three different photopeak energies.

6.2.2.3 Detector uniformity

One of the disadvantages of CZT detectors is its non-uniform response. This is caused by the techniques used to grow CdZnTe crystals [370, 371].

To correct for detector non-uniformities, the response is first measured with a low-count point source placed before an uncollimated detector. The response at 141, 171 and 245 keV is shown in Fig. 6.6. All three uniformity maps show the same general uniformity defects: the pixels on edges of CZT modules have a response different from the pixels located more centrally. The response at 141 keV and 171 keV is similar, while some very small differences can be seen at 245 keV. These maps clearly show that detector uniformity is not energy dependent and is thus caused by structural inhomogeneities.

The detector uniformity maps are incorporated in the forward projection algorithm as a correction factor. The forward projector then becomes

$$\hat{y}_i^{(k)} = U_i \frac{1}{9} \sum_{d=1}^{9} \sum_{p=1}^{7} r_p \sum_{s \in R_{p,d}(\theta)} x_s^{(k)}, \tag{6.4}$$

with U_i the uniformity response for pixel i. It is also applied before back projecting, by multiplying the estimation error with U_i before back projecting.

6.2.2.4 Scatter correction

The first step in scatter correction is scatter estimation: estimating the amount of photon scatter measured by each detector pixel. This is traditionally accomplished by using windowing techniques [121, 372, 373], where the scatter level included in a photopeak is estimated from one or more windows adjacent to the photopeak. A different method is based on scatter estimations from Monte Carlo (MC) techniques [374, 375]. Unfortunately, MC methods are computationally intensive and require the patient's attenuation map to be segmented in biological tissues.

After obtaining a scatter estimate, it can be used to minimize the influence of the photon scatter. A good review of published correction techniques has been published by Hutton et al. [376]. The scatter correction schemes can generally be grouped in 2 subgroups. The first subgroup is scatter subtraction, where the estimated scatter level is subtracted from the measured data before reconstructing. The disadvantage to this is noise amplification, due to the noisy nature of the scatter estimate. This can be reduced by filtering the scatter estimate map. If wider scatter windows are selected to reduce the noise, the bias will increase. Subtracting the scatter from the measured data also negates the assumption that measured photon counts are Poisson distributed, which is the assumption on which the reconstruction algorithm is based (see Section 2.3.5.2). Therefore, we use a correction method belonging to the second subgroup.

The second subgroup includes the scatter estimate directly into the reconstruction. This can be accomplished by adding the scatter in the forward projection step [124]:

$$\hat{y}_i^{(k)} = U_i \frac{1}{9} \sum_{d=1}^{9} \sum_{p=1}^{7} r_p \sum_{s \in R_{p,d}(\theta)} x_s^{(k)} + \alpha C_i, \tag{6.5}$$

where C_i is the scatter estimate in detector pixel i and α is a scaling factor.

For the CZT-based system used in this Chapter, we chose to use a window-based estimation technique together with adding the scatter estimate into the reconstruction. Window-based estimation was used because of the excellent energy resolution obtained with the CZT detector.

The asymmetric photopeaks of the CZT detector need to be taken into account when defining the windows for the scatter estimation. The

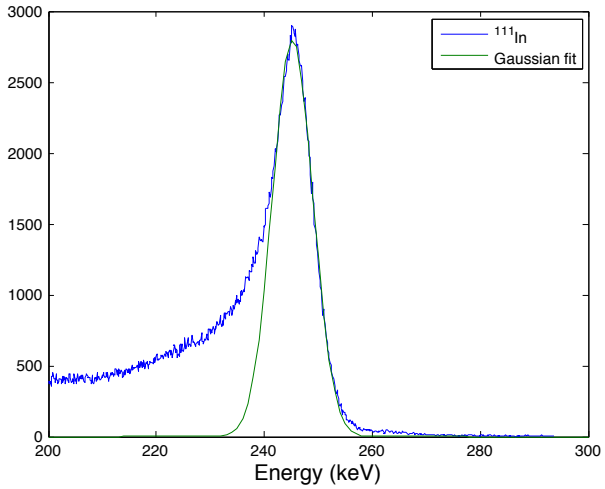

Figure 6.7: Illustration of CZT photopeak asymmetry because of low-energy tailing.

asymmetric peaks are caused by three properties characteristic for pixelated CZT [377]. Firstly, the detector pixels have boundaries where the signal collection is weaker than at the pixel center. Secondly, there is a dependence of the generated signal on the depth-of-interaction, due to hole trapping. Finally, the finite size of the signal contact results in an induced signal that depends more on the relatively slow hole drift for signals generated by events closer to the anode than for events further away. Combined, these effects create a tail of low-energy events [377]. More photons will be pushed into lower energy channels or even outside of the photopeak window, than will be pulled into higher energy channels or inside the photopeak window [378]. Figure 6.7 shows the photopeak asymmetry by comparing the measured photopeak data of the 245 keV photopeak of ^{111}In to a Gaussian fit.

Because of this asymmetry, the scatter estimation windows were selected based on the calibrated spectra (Fig. 6.4). The photon scatter was measured during list mode conversion, using the Dual Energy Window (DEW) [372] and the Five Energy Window (FEW) method [373] for ^{99m}Tc and ^{111}In, respectively. The final window selection is tabulated in Table 6.3 for the radioisotopes used in our validation study.

The resulting scatter map is very noisy. Therefore, a filter (e.g. a Butterworth filter) is usually applied to smooth the low-frequency nature of the scatter fraction [379]. Instead, we used a median filter with a 2-

	Peak window(s) (keV)	Scatter window(s) (keV)	Technique
^{99m}Tc	128–150	126–129	DEW [372]
^{111}In	164–182; 238–256	160–168; 180–200; 236–239	FEW [373]

Table 6.3: Specific technique and scatter windows used for ^{99m}Tc and ^{111}In.

pixel radius to reduce the noise [357]. This filter is edge-preserving and will not move data across pinhole boundaries in multiplexing systems.

6.2.2.5 Sensitivity correction

Each value sampled on a ray through the image space should be corrected for a distance and angle dependent factor. Furthermore, the pinhole collimator is not a perfect absorber. Because of its shape, the pinhole will have a very thin edge (knife edge), where some penetration may occur. Therefore it is important to take an enlarged pinhole diameter into account, in function of the angle of incidence and the photon energy [125, 355].

The effective pinhole diameter is equal to [125]:

$$d_s = \sqrt{d\left(d + \frac{2}{\mu_{pin}} \tan\frac{\alpha}{2}\right) + \frac{2}{\mu_{pin}^2} \tan^2\frac{\alpha}{2}}, \tag{6.6}$$

with d the nominal pinhole diameter, α the full acceptance angle of the pinhole and μ_{pin} the linear attenuation coefficient of the pinhole material for the radioisotope under consideration.

Conventionally, the effective pinhole diameter is used in an analytical sensitivity formula:

$$S_{pin,1}(\theta) = \frac{d_s^2 \cos^3\theta}{16h^2}, \tag{6.7}$$

with h the perpendicular distance of the collimator to the point source and θ the incidence angle measured from the plane of the pinhole (θ_{pin} in Fig. 6.8) [117, 355, 380].

However, this formula is not correct in the case of a ray-driven forward projector. The number of rays drawn through a voxel at distance h from the pinhole will be inversely proportional to the square of this distance.

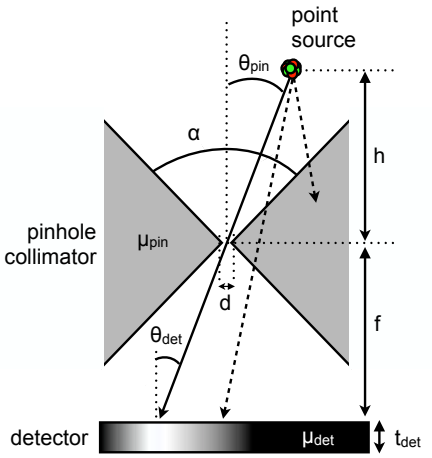

Figure 6.8: Cross section of a pinhole collimator for a point source above the pinhole aperture (not to scale). f is the perpendicular collimator-detector distance, h is the perpendicular collimator-point source distance. θ_{pin} is the incidence angle measured from the plane of the pinhole. α is the full acceptance angle. μ is the linear attenuation coefficient of the pinhole material for the photon energy of the point source.

This means that there is an already inherent correction for the $1/h^2$ factor by using ray-tracing. Additionally, if the number of rays should be constant through the pinhole at different focal lengths f, then the sensitivity should be inversely proportional to the square of f. These two properties lead to a slightly different sensitivity formula:

$$S_{pin,2}(\theta) = \frac{d_s^2 \cos^3 \theta}{16 f^2}. \tag{6.8}$$

A basic model of detector efficiency or sensitivity is implemented by attenuating the incoming ray with a factor dependent on the incidence angle and the attenuation of CZT for the isotope used [381]:

$$S_{det}(\theta) = 1 - \exp\left(-\mu_{det} \frac{t_{det}}{\cos\theta}\right), \tag{6.9}$$

with μ_{det} the linear attenuation coefficient of the detector and t_{det} the detector thickness.

For each ray sample measured in the image by the forward projector, its value is multiplied by $S_{pin,2}(\theta_{\text{pin}}) \times S_{det}(\theta_{\text{det}})$. In the back projector

we need the original sensitivity formula $S_{pin,1}(\theta_{\text{pin}})$, as the back projector has no inherent weighting for $1/h^2$ included.

6.2.2.6 Attenuation correction

Photon attenuation is calculated based on the CT data, acquired beforehand with the micro-CT subsystem of the FLEX Triumph-II scanner. The CT subsystem is mounted in the same gantry as the SPECT subsystem, leading to optimal co-registration between both modalities. All CT images were acquired on a 2368×2240 pixel detector (pitch 50 μm) using 512 projection views acquired over 2π. A peak voltage of 75 kVp, exposure time of 345 ms and tube current of 510 μA were chosen, with a 2-fold magnification, leading to a FOV of 59.2 x 56 mm. The total acquisition time was 13 minutes per CT scan. The dose is approximately 130 mGy per scan.

All CT datasets were reconstructed using the Maximum Likelihood for Transmission Tomography (MLTR) [45] algorithm (see Section 2.2.6.3) in a voxel matrix with isotropic voxel pitch 100 μm, leading to an image with $592 \times 592 \times 560$ voxels. MLTR was implemented in CUDA, with the same ray-driven core as the SPECT reconstruction.

After reconstruction, all voxel values are bilinearly scaled [198] to linear attenuation values. When scatter correction is also applied, we use narrow-beam attenuation values, which is the attenuation determined in the ideal situation (no scatter present). This is different from broad-beam attenuation, which takes into account that scattered photons will also contribute to the total measured counts per pixel. In case of non-ideal situations, this means that there will be less loss of photons than predicted from the idealized narrow-beam values [376]. For water, an attenuation of 0.15 cm^{-1} at 140 keV is thus used instead of of broad-beam value 0.12 cm^{-1} [382]. If photon scatter is not corrected for separately, the broad-beam attenuation value should be used.

To use the attenuation values as a correction factor for SPECT reconstruction, the high-resolution attenuation map is first loaded as a 3D CUDA texture. During SPECT ray-tracing, each ray is sampled starting nearest to the pinhole. The projection value $\hat{y}_i$ for detector pixel i can

thus be approximated by

$$\hat{y}_i = U_i \frac{1}{9} \sum_{d=1}^{9} \sum_{p=1}^{7} r_p S_{pin,2}(\theta) S_{det}(\theta) \sum_{s \in R_{p,d}(\theta)} x_s^{(k)} \exp\left(-\Delta x \sum_{k=1}^{s} \mu_k \right) + \alpha C_i, \tag{6.10}$$

from current emission estimate $\mathbf{x}^{(k)}$, for all samples s in the set of samples spaced Δx along the ray $R_{p,d}(\theta)$, and k representing all the samples between the pinhole and current sample position s.

6.2.2.7 Partial volume effect correction

The partial volume effect (PVE) is a displacement of the signal from small structures under influence of discretization and the limited spatial resolution of the imaging system [383]. Any structure smaller than 2.5 times the system resolution will be PV affected. For a point source, the reconstructed voxel may be uniformly filled with activity, even though the source has a volume much lower than the volume of 1 voxel. In other words, the reconstructed number of counts in one voxel does not always reflect the true concentration of activity per volume [384]. Additionally, spillover into surrounding tissue may also occur [346, 385], which will lead to an underestimation of the signal amplitude in order to conserve the total activity.

One way to decrease the PVE is by improving the system spatial resolution. We already do this by using resolution recovery with pinhole diameter subsampling and detector pixel subsampling (see earlier). Although resolution recovery increases the image spatial resolution and thus reduces the PVE, it will lead to Gibbs ringing and overshoots for small objects. These image degrading effects can be minimized by smoothing the affected image. However, smoothing will also cause spill-over of activity into functionally unrelated surrounding tissue. It would be better to use adaptive smoothing, taking into account the edges of the different functional regions in the patient's body.

We use a correction technique which incorporates known anatomical information in the reconstruction with a Bayesian prior [135]. This is accomplished by first thresholding the gradient of the CT image [386], after which the voxels neighboring to edges are located [135]. Those neighbors are the areas wherein spillover may occur with conventional smoothing. After normalization, this image is a probability map, with each voxel value $\gamma_k \in [0, 1]$ representing the probability that voxel k

contains a significant CT boundary.

The weights γ_k are used in a Bayesian prior, to allow for quadratic smoothing in edge-less (uniform) areas, while areas with danger of spillover are left unsmoothed. The penalty has the form:

$$V(x_j) = \sum_{k \in N(j)} (1 - \gamma_k)(x_j - x_k)^2, \tag{6.11}$$

with $N(j)$ the set of 26 3D neighbors of voxel j. This penalty is used in the OSL-OSEM update equation (Eq. 2.72). The regularization factor β determines the magnitude of smoothing applied and was set empirically.

6.2.2.8 Quantitative calibration

After reconstructing all SPECT data, one last calibration is needed to relate the reconstructed count density to the actual radioactivity concentration (MBq/ml). This was accomplished by scanning a small amount of known activity A with the exact same protocol used during the other scans. The scaling factor SF can then be calculated by dividing the known activity of the calibration point by the volume V per voxel times the total number of reconstructed counts [357, 359]:

$$SF = \frac{A}{V \times \sum_{j=1}^{J} x_j}. \tag{6.12}$$

By multiplying a reconstructed image with this scaling factor, an image with unit MBq/ml per voxel is obtained.

The calibration point source was reconstructed without corrections, as attenuation and scatter are assumed to be negligible due to the small volume size of the point source. The PVE will have no effect here, because PVE does not influence the total number of counts, but only the measured activity counted in a limited volume.

For radioisotopes that emit photons in multiple photopeaks (e.g. ^{111}In), each photopeak is first reconstructed separately with all possible correction factors enabled. After summing the final reconstructed images into one single image, it is multiplied by the scaling factor determined from the summed reconstructions of the calibration vial. As the scaling factor is determined from the total number of reconstructed counts the isotope branching fraction is implicitly accounted for.

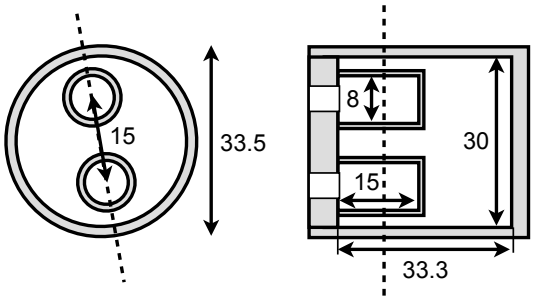

Figure 6.9: Technical specifications for the micro-SPECT quantification phantom (units mm).

6.2.3 Validation

The phantom design for the validation study is based on the image quality phantom described in the National Electrical Manufacturers Association (NEMA) NU 4-2008 specifications [387]. The phantom dimensions are illustrated on Fig. 6.9. This phantom was 3D printed at Shapeways (Shapeways NL, Eindhoven, The Netherlands) in the 'transparent detail plastic' material at a printing resolution of ± 0.1 mm.

Two experiments were conducted to evaluate the quantitative accuracy for the isotopes ^{99m}Tc and ^{111}In. The largest compartment was filled with a low background activity (ratio 1:1); the two smaller compartments with an 8:1 and 2:1 ratio. To allow delineation of all three compartments for the Bayesian prior, 0.375 ml iodine-based contrast agent (Visipaque 320 mg I/ml, GE Healthcare) was added to the 8:1 compartment, the 2:1 compartment received 0.750 ml contrast agent, and no contrast was added to the 1:1 background compartment.

The radioisotope was diluted with distilled water (dH_2O) in a separate vial while weighing on a calibrated scale (accuracy 0.1 mg) to obtain the correct concentrations. After measuring the activity in the vial with the gamma counter, iodine contrast was added to this vial by pipetting the correct volume. If done beforehand, the iodine would attenuate the ground-truth gamma counter measurements. Part of the contained volume was then used to fill the corresponding phantom compartment. The final activity concentrations can be found in Table 6.4.

The technical specifications of the 3 compartments were used to select volumes of interest (VOIs). These VOIs were shortened axially to exclude air bubbles. This resulted in 2 cylindrical volumes of diameter 8 mm

Isotope	1:1 (MBq/ml)	2:1 (MBq/ml)	8:1 (MBq/ml)	Point source (MBq)
^{99m}Tc	2.84	6.03	21.05	10.61
^{111}In	2.95	4.51	18.38	4.31

Table 6.4: Activity concentrations as determined from the dose calibrator, for the NEMA phantom compartments and for the quantitative calibration vial.

and height 5 mm for the 8:1 and 2:1 compartments, and one cylindrical volume of diameter 30 mm and height 10 mm for the 1:1 compartment. The quantitative analysis consists of measuring the mean activity in each compartment and comparing this to the known value from Table 6.4.

Our software will also be compared to the software provided by the vendor. Their software is based on an OSEM implementation. The data are pre-corrected for radioactive decay. The photopeak window width was always set to 10% of the photopeak energy. The OSEM reconstruction algorithm was used, and was set to 10 iterations and 8 subsets, with a voxel size of 0.5 mm.

6.3 Results

In order to make the use of different techniques more clear, we refer to uncorrected data as the data only corrected for decay, geometrical sensitivity, and quantitative calibration. All data are always corrected for decay, geometrical sensitivity, resolution, PVE, and quantitative calibration, with additionally attenuation correction and/or scatter correction. The vendor-reconstructed data is only corrected for decay and geometrical sensitivity.

Figure 6.10 shows a transaxial and coronal slice through the reconstructed SPECT image obtained after applying all corrections for both isotopes. The inner chambers are delineated more clearly with ^{99m}Tc compared to ^{111}In, although both images have the same outer edge quality. This could be due to the penetration, which will be significantly higher for ^{111}In because of the higher photon energy. Furthermore, ^{111}In is known to stick to plastic, and is sometimes even absorbed into the plastic walls of phantoms [388]. This could be a cause of the reduced uniformity for ^{111}In in the 2:1 vial, compared to ^{99m}Tc.

Figure 6.11 correlates the activity concentrations measured on the re-

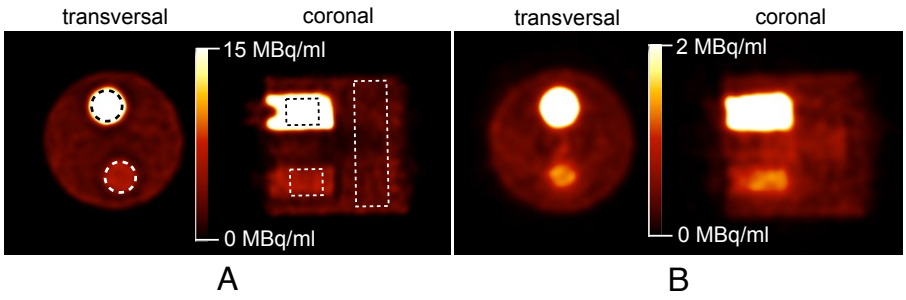

Figure 6.10: Reconstructed images of the NEMA phantom for (A) ^{99m}Tc and (B) ^{111}In. The cylindrical VOIs used in the evaluation are depicted by a dashed white line.

constructed images to the activity concentrations measured in the dose calibrator. The uncorrected data and the fully corrected data were fit with a full and a dashed trend line respectively. A full grey-colored trend line is fitted to the data from the images reconstructed with the vendor software.

As can be seen from Figure 6.11, attenuation correction has the largest influence on the quantitative accuracy. When all corrections were applied, except for scatter correction, the errors[1] decrease on average from -2.78±2.62 MBq/ml to -0.30±0.25 MBq/ml for ^{99m}Tc, from -1.91±1.23 MBq/ml to 0.80±1.66 MBq/ml for the low-energy peak of ^{111}In, and from -1.48±1.58 MBq/ml to 0.53±0.58 MBq/ml for the high-energy peak of ^{111}In. Combining both peaks leads to a decrease from -1.77±1.34 MBq/ml to 0.72±1.30 MBq/ml for ^{111}In, a small overcorrection. When all corrections are applied, including scatter correction, the quantification errors decrease from -2.78±2.62 MBq/ml to -0.88±0.85 MBq/ml for ^{99m}Tc, from -1.91±1.23 MBq/ml to 0.02±1.04 MBq/ml for the low-energy peak of ^{111}In and from -1.48±1.58 MBq/ml to -0.08±0.51 MBq/ml for the high-energy peak of ^{111}In. Combining both peaks decreases the error from -1.77±1.34 MBq/ml to only -0.01±0.79 MBq/ml.

Although these errors are low on average, a one-sample t-test of each vial to the known reference value shows that each reconstructed vial value is significantly different ($p < 0.01$) from the reference data. The quantification errors for the separate vials are included in the summarized results in Table 6.5. Generally a small under-correction is found for ^{99m}Tc, while the data for ^{111}In show a small overcorrection. For ^{111}In,

[1] mean ± standard deviation per VOI

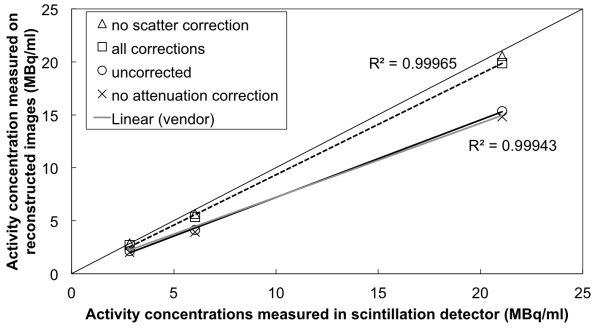

(a) ^{99m}Tc

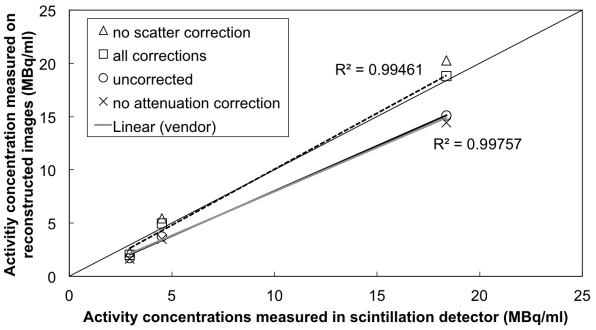

(b) ^{111}In - 171 keV + 245 keV

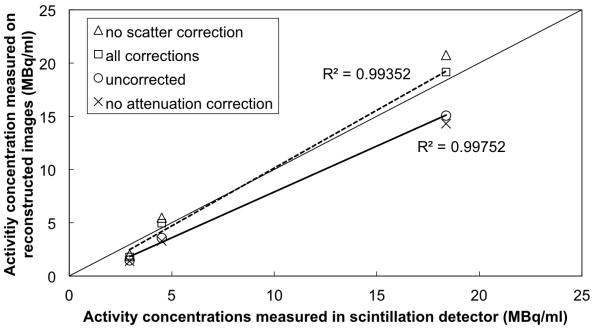

(c) ^{111}In - 171 keV

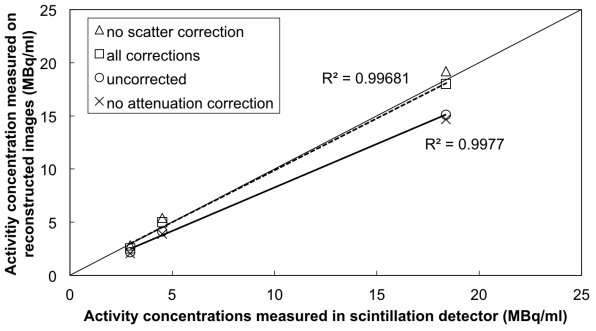

(d) ^{111}In - 245 keV

Figure 6.11: Correlation between reconstructed and the ground-truth values.

the largest error can always be found in the 1:1 background region.

6.4 Discussion

Our study shows that a quantification error of ±10% is achievable with ^{99m}Tc for activity concentrations between 2.84 and 21.05 MBq/ml, by using model-based iterative reconstruction. The same error is achieved for ^{111}In between 4.51 and 18.38 MBq/ml. However, the lowest activity vial (2.95 MBq/ml) still remains with an undercorrection of 31±11% or 0.92±0.33 MBq/ml. The low-energy peak undercorrected by 39±13%, whereas the high-energy peak undercorrected by 13±15%. According to these measurements, it would be better to use only the data of the high-energy window for ^{111}In instead of a combination of both energy windows.

These low quantification errors were achieved by correcting for the image degrading effects. When our model-based iterative reconstruction was used without any correction mechanisms, the same quantification error was achieved as with the vendor-provided reconstruction software. The noise was higher in the uncorrected vendor-provided reconstructions than obtained with our own software.

The results indicate that a decrease in quantification error is primarily influenced by attenuation correction. The influence of scatter correction is much smaller. Because we use a pixelated CZT detector, little scattered photons will be included in the photopeak window (due to the CZT-tail), at the expense of a lower amount of primary photons. The statistical noise will thus increase. This agrees with the findings of Chen et al. [389], who concluded that narrowing the energy windows is an effective way to correct for scatter in ^{99m}Tc and ^{111}In studies, provided sufficient energy resolution is available. It should be stressed that the influence of scatter correction will increase in importance when other detectors are used (e.g. NaI with a worse energy resolution), but will remain less important than attenuation correction in small animal SPECT [351]. This is also in agreement with the findings of Lee et al. [361], who determined that attenuation is the prime factor to consider for this CZT-based system.

	1:1		2:1		8:1	
	MBq/ml	Relative	MBq/ml	Relative	MBq/ml	Relative
^{99m}Tc						
Vendor	-0.41±0.70	-14±25%	-1.81±1.29	-30±21%	-6.06±3.53	-29±17%
Uncorrected	-0.71±0.53	-25±19%	-1.90±1.05	-32±17%	-5.73±3.67	-27±17%
Corrected	-0.15±0.66	-5±23%	-0.68±1.29	-11±21%	-1.81±4.36	-9±21%
^{111}In						
Vendor	-1.16±0.43	-39±15%	-0.70±0.75	-16±17%	-3.52±2.11	-19±11%
Uncorrected	-1.24±0.37	-42±12%	-0.77±0.49	-17±11%	-3.29±1.64	-18±9%
Corrected	-0.92±0.33	-31±11%	0.47±0.67	10±15%	0.42±1.94	2±11%
^{111}In - Low						
Uncorrected	-1.47±0.32	-50±11%	-0.95±0.47	-21±10%	-3.30±1.64	-18±9%
Corrected	-1.16±0.39	-39±13%	0.46±0.76	10±17%	0.83±2.03	5±11%
^{111}In - High						
Uncorrected	-0.76±0.31	-26±11%	-0.38±0.50	-8±11%	-3.28±1.79	-18±10%
Corrected	-0.39±0.44	-13±15%	0.51±0.68	11±15%	-0.36±1.90	-2±10%

Table 6.5: Quantitative errors obtained from the NEMA phantom with the vendor-provided software and with our own software, before and after all corrections were applied. Negative errors are undercorrections; positive errors are overcorrections.

6.5 Conclusion

In this chapter, we demonstrated how absolute quantitative micro-SPECT can be achieved with ray-based iterative reconstruction. The most important image degrading effects—attenuation, scatter and the PVE—were corrected with specific solutions in an OSL-OSEM algorithm. The implementation was validated using a NEMA phantom, by comparing image-based absolute quantification values to the known activity concentrations. A good agreement was found, leading to an error around $\pm 10\%$ for ^{99m}Tc and ^{111}In-High.

Even though we have shown that absolute quantification in phantoms can be achieved in micro-SPECT using these correction techniques, the question remains whether this will also work for *in vivo* data. Such validation is the subject of the next Chapter.

Chapter 7

Validation of quantitative micro-SPECT/CT reconstruction in vivo

In the previous chapter, we validated our ray-based micro-SPECT reconstruction software that includes correction factors for the different image degrading effects. In this chapter, the *in vivo* quantification accuracy is determined for the same isotopes, in two different tracers: ^{99m}Tc-dimercaptosuccinic acid ([^{99m}Tc]DMSA) and [^{111}In]Octreotide.

[^{99m}Tc]DMSA is used to assess the renal function [158, 159] and, preclinically, mostly used as an indicator of tubular functioning after ^{90}Y therapy [160]. A system spatial resolution better than 1 mm is needed to delineate the functional renal cortex in mice [390], necessitating PVE correction and CT contrast agent to accurately delineate the kidneys.

The second tracer, [^{111}In]Octreotide, is a radioactively labeled octapeptide that pharmacologically mimics natural somatostatin. It is internalized in neuroendocrine tumors expressing somatostatin receptor type 2 (SSTR2) (and to a lesser extent SSTR3 and SSTR5) [391].

7.1 Blood-pool activity correction

Apart from the correction factors already included in the iterative reconstruction software (see the previous chapter), an extra correction factor is needed when working with live animals. At early time points, the tracer will still reside in the blood circulation [346]. This means that

some activity will be measured in a VOI that may not be fully representative of the activity taken up by the tissue of interest. This is especially true for tracers with slow pharmacokinetics.

It is therefore important to correct for the blood pool activity. This can generally be done in two steps. The first step is measuring the activity in the blood pool itself, through a cardiac puncture (ex vivo), with a gamma-counting blood sampler (in vivo), or estimated from the images themselves [392]. Once the activity is known, the reconstructed image data are corrected by subtracting the absolute organ activity by the blood concentration (MBq/ml) times the vascular volume fraction (VVF, unit ml/g) times the organ weight (g). The VVF represents the blood volume per gram of organ tissue, and can be gathered from literature.

7.2 In vivo small animal imaging

The absolute quantification error in realistic pre-clinical experiments is determined with two in vivo studies. The Ghent University ethical committee approved all animal experiments (ECD 12/53).

All in vivo measurements are acquired on the same micro-SPECT/CT scanner as in Chapter 6. The geometrical sensitivity will be very low because only 1 camera head is installed instead of the possible 4 cameras. Combined with low biological uptake in typical preclinical studies (typically only 1 to 10% ID/g), it is necessary to increase the number of detected counts. In this study we double the acquisition time per view as well as doubling the injected dose. This lead to a 4-fold increase in collected data, as if the system would have 4 heads. This results in a SPECT acquisition protocol using 64 views over a 360 degrees total rotational angle, with an exposure of 2 minutes per projection view. All data are acquired for one bed position.

7.2.1 [^{99m}Tc]DMSA

BALB/c mice were selected with weight 26±1 g and age 11±1 wk (n=6). Anesthesia was induced using 4% isoflurane, for maintenance of the anesthesia the concentration was set at 1.7%. All mice were injected in the lateral tail vein with 78±3 MBq [^{99m}Tc]DMSA (TechneScan DMSA®, Mallinckrodt Medical BV, Petten, The Netherlands). We aimed for a synchronous start of the SPECT scan 4.5 hours post-injection to maximize the uptake of the DMSA in the kidneys [390].

To visualize the kidneys on the CT images, 1 hour before the SPECT scan an iodine-based contrast agent (Visicover^{TM}ExiTron^{TM}V, Miltenyi Biotec, Bergisch-Gladbach, Germany) was injected into the lateral tail vein (4 μl/g). A pilot test had shown that such a protocol results in a maximal contrast increase in the kidneys between 30 and 60 minutes post-injection. Therefore, the micro-CT scan was started 30 minutes after administering the contrast agent. The 128-minute SPECT acquisition was started after the micro-CT scan finished.

Immediately following the SPECT scan, the animals were euthanized by cervical dislocation and a blood sample was taken by cardiac puncture. Both kidneys were dissected, rinsed with physiological saline, dried, and weighed. Kidney weight was converted into volume by assuming a 1.05 g/ml density [393]. All samples were measured in a NaI(Tl) well-type gamma counter, calibrated with activity measured in the same dose calibrator as used for the in vivo experiment. The kidney VOIs were determined by thresholding the kidneys on the reconstructed CT images. The blood-pool activity correction was applied with a VVF chosen at 0.27 ml/g kidney weight [393], with the kidney weight determined from the VOI volume.

7.2.2 [^{111}In]Octreotide

A human non-small cell lung carcinoma (NCI-H727) was chosen as a neuroendocrine tumor model. CD-1 nude mice (n=10) (Charles River, France) were injected subcutaneously with 5×10^6 cells in the right hind leg. The animals without a palpable tumor were euthanized 3 weeks after inoculation. All remaining mice (n=6, age 13±1 wk, weight 27±2 g) were shortly anesthetized for injection of 31±1 MBq [^{111}In]Octreotide (Octreoscan^{TM}, Covidien Belgium, Mechelen, Belgium) via the lateral tail vein. The micro-CT scan was started 23 hours post-injection, after which the 128-minute micro-SPECT scan was started [394]. The anesthesia was induced with 4% isoflurane, and maintained with the concentration set at 1.7%.

Immediately following the SPECT scan, the animals were euthanized by cervical dislocation, and a blood sample was taken by cardiac puncture. The tumor was excised from the thigh and rinsed in physiological saline, dried, and weighed. Tumor weight was converted into volume assuming a 1 g/ml density [395]. All samples were measured in a calibrated NaI(Tl) well-type gamma counter.

The CT image was used to delineate the boundaries of each tumor. The total activity and volume inside the VOI were measured. Because the VVF is unknown for these tumors, we used a value of 5.2% ml/g tumor tissue as determined by Bremer et al. [396] for fibrosarcoma implanted in the gluteal region in mice.

7.3 Data Analysis

As in the previous chapter, all data are analyzed by comparing fully corrected data to the vendor's software and to our uncorrected data. Uncorrected data refers to data only corrected for decay, geometrical sensitivity and quantitative calibration. The corrected data is corrected for (1) decay, (2) geometrical sensitivity, (3) resolution, (4) PVE, (5) quantitative calibration, (6) blood-pool activity, (7) photon attenuation and (8) photon scatter, unless stated otherwise.

All VOIs were analyzed using the open-source AMIDE software package (version 1.0.4). Quantification errors were calculated per VOI, and then averaged. The paired t-test is used to quantify significant differences between the quantification from reconstructed data and the known ground-truth values. Furthermore, a Bland-Altman analysis is conducted to further evaluate the agreement between reconstructed values and ground-truth values.

7.4 Results

Figures 7.1 shows example reconstructions of the reconstructed in vivo data. Because of the difference in injected dose and tracer specificity, the background activity is much more of a confounding factor for [^{111}In]Octreotide (Fig. 7.1b) than with [^{99m}Tc]DMSA (Fig. 7.1a).

Table 7.1 shows the average absolute errors and average relative errors for both studies. For [^{111}In]Octreotide, the separate quantification of each photopeak (low = 171 keV, high = 245 keV) is also included. Only 10 data points are available for [^{99m}Tc]DMSA (instead of 12 kidneys harvested from 6 mice), as one acquisition failed due to the animal waking up during the SPECT scan.

The average activity reduction due to the VVF is 0.068±0.026 MBq for the [^{99m}Tc]DMSA kidneys, and 0.004±0.003 MBq for the [^{111}In]Octreotide tumors. A paired t-test indicates that there is no

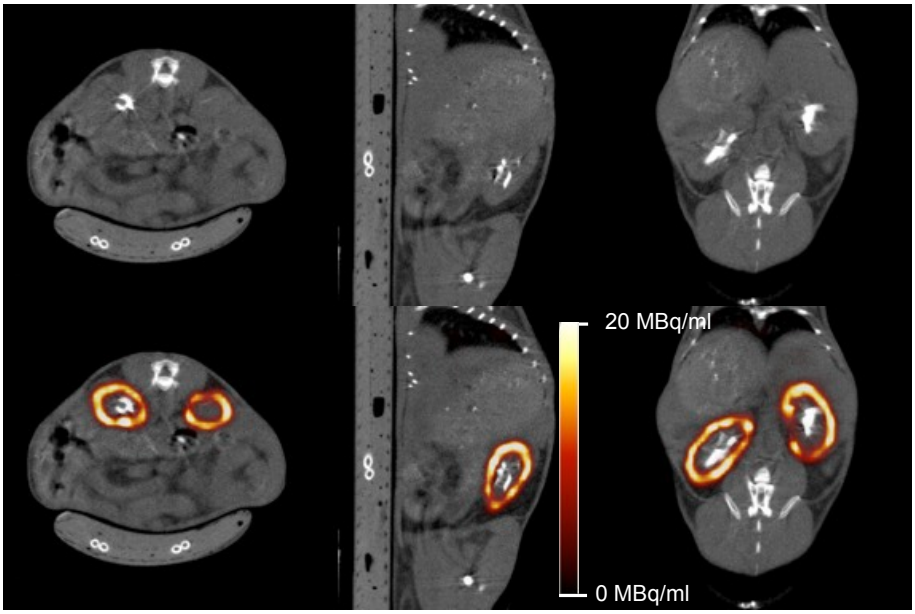

(a) For [^{99m}Tc]DMSA. The kidneys can be delineated on the micro-CT image thanks to the contrast agent.

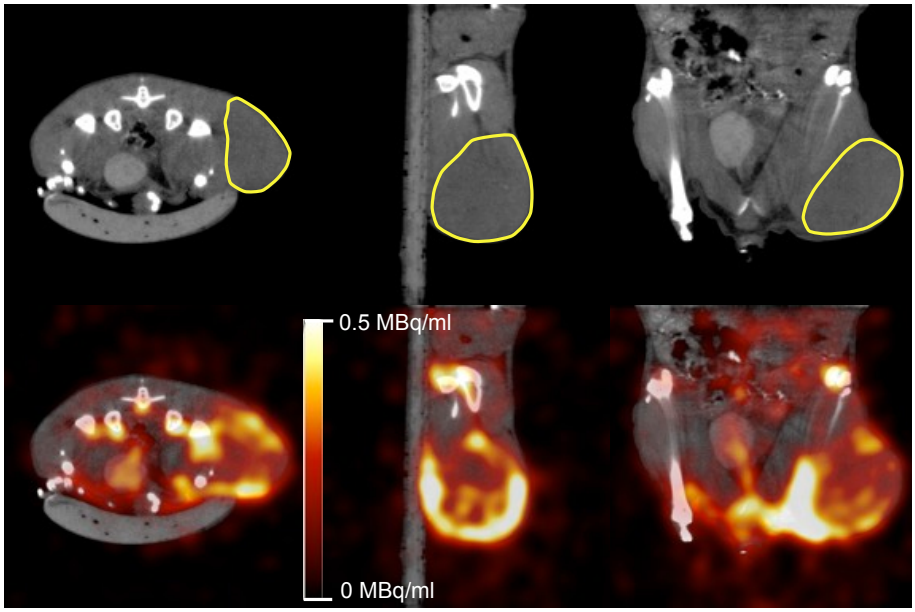

(b) For [^{111}In]Octreotide. The tumor VOI is shown with a yellow line on the micro-CT image.

Figure 7.1: Images of reconstructed *in vivo* micro-SPECT/CT data.

	Reference	Vendor Error		Uncorrected Error		Corrected Error	
Tracer	MBq/ml	MBq/ml	Relative	MBq/ml	Relative	MBq/ml	Relative
[^{99m}Tc]DMSA	8.42±2.77	-1.12±0.37	-13.6±3.1%	-1.31±0.33	-16.2±2.8%	0.03±0.20	0.3±2.1%
[^{111}In]Octreotide	0.35±0.09	-0.09±0.13	-22.4±29.0%	-0.06±0.01	-16.7±10.1%	-0.01±0.04	-2.2±10.6%
Low	-	-	-	-0.08±0.05	-22.7±11.4%	-0.03±0.05	-8.1±11.8%
High	-	-	-	0.01±0.02	3.8±8.6%	0.06±0.01	18.8±8.5%

Table 7.1: Summary of quantitative errors obtained from in vivo studies with the vendor-provided software, with our own software before corrections, and after applying all corrections ([^{99m}Tc]DMSA: n=10; [^{111}In]Octreotide: n=6).

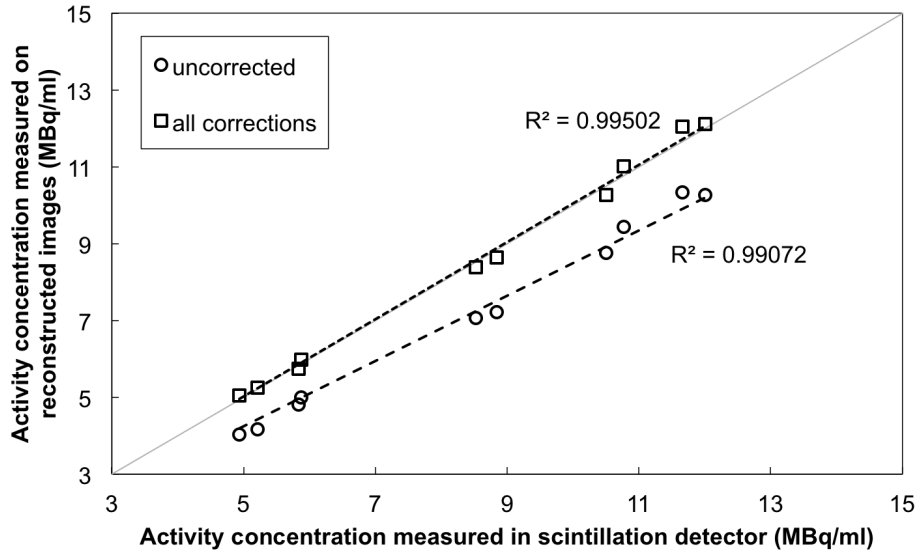

(a) [^{99m}Tc]DMSA

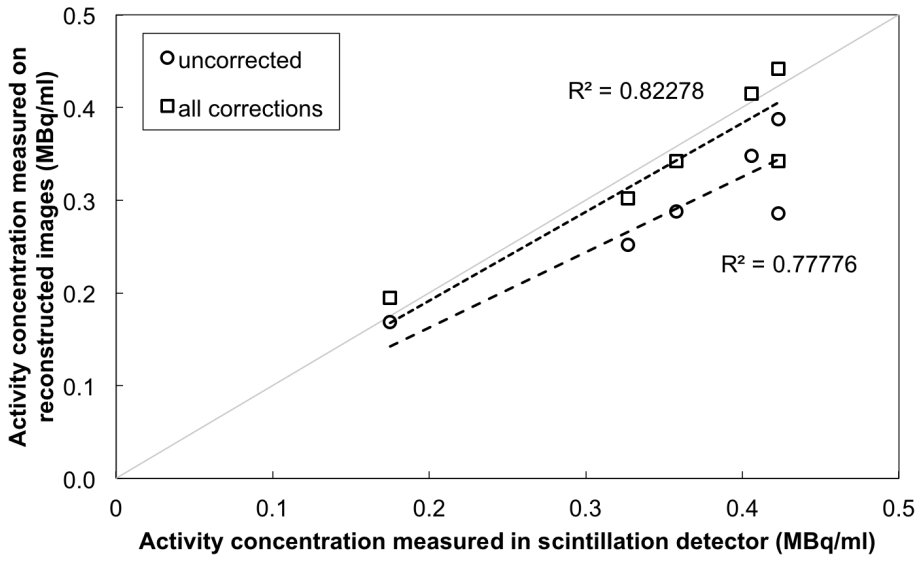

(b) [^{111}In]Octreotide

Figure 7.2: Quantification error for in vivo studies. Diagonal is the ground truth.

significant difference between the reference data and the fully corrected data, whether the VVF is used or not. However, applying the VVF significantly ($p < 0.01$) decreases the quantification error for [^{99m}Tc]DMSA from -0.038±0.198 MBq/ml to 0.030±0.201 MBq/ml. For [^{111}In]Octreotide, a significant ($p < 0.05$) increase of -0.008±0.040 MBq/ml to -0.012±0.038 MBq/ml was found.

Figure 7.2 correlates the measured activity concentration to the reference ex vivo activity concentration. For [^{99m}Tc]DMSA (Fig. 7.2a), there is a significant difference (paired t-test, $p < 0.01$) comparing uncorrected data to the reference data, while the difference between fully corrected data and the same reference data is not significant ($p = 0.64$). Also for [^{111}In]Octreotide (Fig. 7.2b), a paired t-test on the summed two-peak reconstruction shows a significant difference ($p < 0.05$) between the uncorrected and reference data, while there is no significant difference ($p = 0.113$) between the fully corrected and the reference data.

In both studies the goodness of fit improves by applying all corrections, but is still worse for ^{111}In ($R^2 = 0.778$ and 0.823) than for ^{99m}Tc data ($R^2 = 0.991$ and 0.995).

A Bland-Altman analysis is presented in Fig. 7.3. A one-sample t-test to zero mean difference indicates a significant absolute systematic error for the difference between the uncorrected data and the reference data, and this for both isotopes (^{99m}Tc: $p < 0.01$; ^{111}In: $p < 0.05$). The systematic error is relatively lower for ^{99m}Tc than with ^{111}In. No significant absolute systematic bias is found for fully corrected data. These results indicate a better agreement between the reference and the fully corrected data than between the reference and the uncorrected data.

7.5 Influence of low-dose CT

The influence of low-dose CT on quantitative SPECT was also analyzed. The full-dose CT acquisitions (512-view) are reconstructed with MLTR, while 64-view (1/8th dose) and 32-view (1/16th) data is reconstructed with ISRA-TV. The same implementation of ISRA-TV is used as first implemented for Chapter 4.

Figure 7.4 shows the reconstructed CT dataset for one mouse with the full dose, a dose reduction of factor 8, and a dose reduction of factor 16. Comparing these attenuation maps with a $5 \times 5 \times 5$ mm^3 VOI in the soft-tissue shows no significant difference between the three methods. The 1/8th dose differs 0.4% from the full-dose reconstruction, while

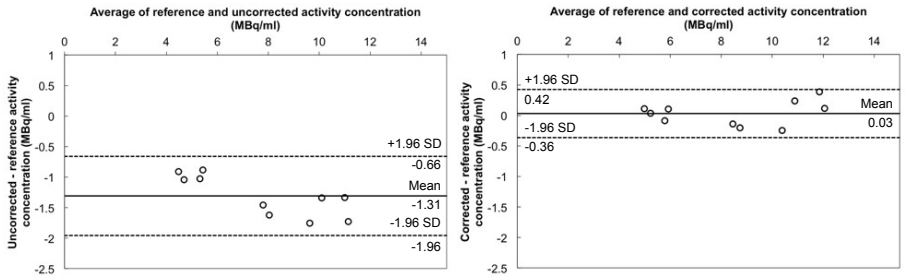

(a) [^{99m}Tc]DMSA

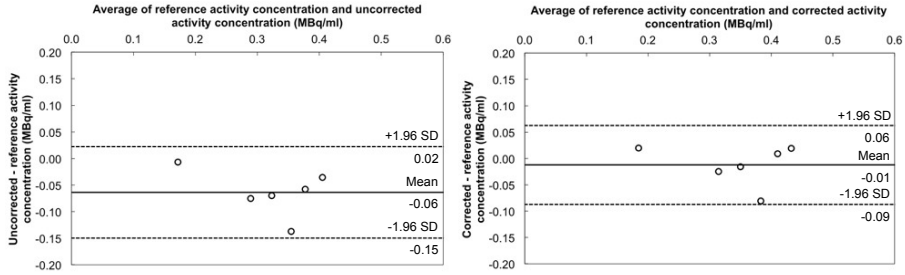

(b) [^{111}In]Octreotide

Figure 7.3: Bland-Altman plots comparing (left) reference activity concentration to uncorrected reconstructed data and (right) reference activity concentration to corrected reconstructed data. Both uncorrected datasets show a significant absolute systematic error, the corrected datasets do not.

the 1/16th dose differs 0.5%. When these low-dose attenuation maps are used in the SPECT reconstruction, the quantification error changes by 0.16±0.28% for the 1/8th dose, while for the 1/16th dose the error changes by 0.64±0.92%. The spatial distribution of the quantification error change is depicted on Figure 7.5. The largest relative changes are located in the areas of lowest activity (e.g. the 2.5% change just above and below the kidneys), while the lowest changes are located in the kidneys (e.g. less than 0.2% change).

This shows that attenuation maps obtained from low-dose CT can successfully be used for absolute SPECT quantification. Unfortunately, the acquired CT data are not only used to determine the attenuation factors. The reconstructed image is also used as a starting point for the PVE correction, where the organ edges are determined before penalizing the quadratic smoothing step (see Section 6.2.2.7). This will not be possible on data acquired at 1/16th of the original dose, due to the decreased image quality.

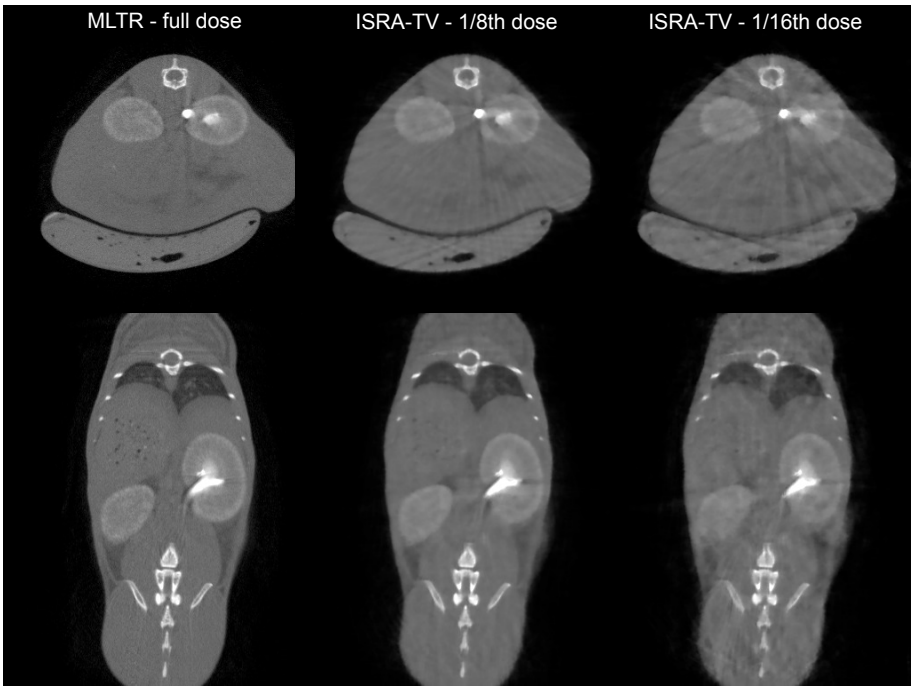

Figure 7.4: Comparison of different low-dose CT attenuation maps to the full-dose map, reconstructed from 512 projection views.

7.6 Discussion

The *in vivo* results indicate that an *in vivo* quantification error of less than 5% is achievable with ^{99m}Tc and ^{111}In. This was achieved with model-based iterative SPECT reconstruction on a standard commercially available multi-pinhole micro-SPECT scanner. When ISRA-TV is used to reconstruct the CT data, an acquisition of only 64 projection views will suffice for attenuation correction and for PVE correction.

The in vivo quantification error is smaller than the quantification obtained with the phantoms in Chapter 6, which is counter-intuitive. Comparing the average in vivo error to the error in the vial of the phantom with similar activity concentration indicates a significant difference for ^{111}In ($p < 0.01$). The large error in the phantom was caused by an undercorrection in the lowest activity vial for the low-energy photopeak of ^{111}In.

Although the presented results are promising for routine usage of absolute quantification in *in vivo* micro-SPECT imaging, some issues were

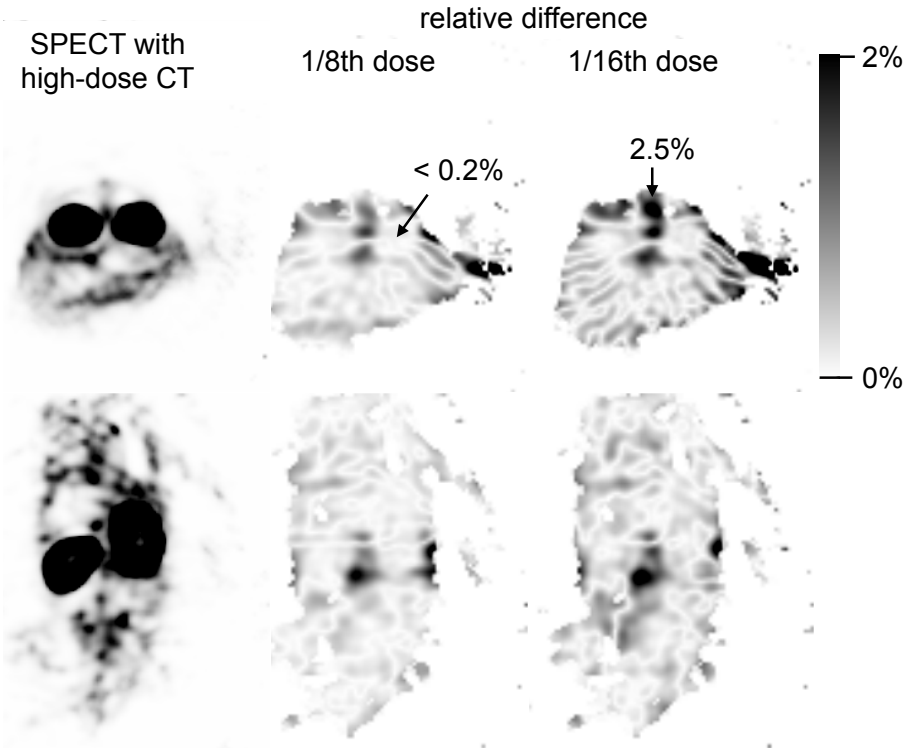

Figure 7.5: Comparison between the SPECT activity after attenuation correction from a high-dose CT acquisition, and the activity after correcting for attenuation measured from lower-dose CT acquisitions.

noticed during the experimental work. First, the importance of blood volume correction is not as clear as reported in [346]. Applying blood volume correction significantly changes the absolute quantification values. For [^{99m}Tc]DMSA, this leads to a lower quantification error, while for [^{111}In]Octreotide, the quantification error increases. This could be due to a misestimated blood volume for the H727 tumors. Although we measured the blood activity concentration by a heart puncture, a gamma-counting blood sampler can also be used. This was unavailable to us at the time. Little data of the VVF of different tissues are available, which makes this correction difficult in practice. One possible solution would be to directly measure the VVF using e.g. in vivo MRI [396, 397]. Using in vivo VVF measurements would also allow us to account for intraspecies differences.

An important limitation of the DMSA study is the delineation of the

renal cortex. The complete kidney was delineated and compared to the dissected complete kidney, instead of quantifying only the renal cortex. This was done because the renal cortex is still difficult to delineate on contrast-enhanced CT, and because the cortex is also difficult to separate from the medulla during dissection. However, edge-preserving smoothing is still necessary to limit the overspill of activity in non-renal tissue. These high-resolution details form the limiting factor for using low-dose CT as a prior image. Whereas attenuation correction will perform identical in the case of only 32 views, it will be difficult to reconstruct the renal cortex accurately on those images.

A second issue is the low system sensitivity in pinhole SPECT, which is combined with low biological uptake in typical preclinical studies. The H727 cell line used in the [^{111}In]Octreotide study showed an uptake of only 1.4±0.5% ID/g, resulting in an activity of only 151±40 kBq per tumor during the SPECT acquisition. Our results indicate that in vivo quantification is still possible at such a low activity, which is more than an order of magnitude lower than the activity reported by Finucane et al. [360], when normalized to the low sensitivity of our system [141]. This could be alleviated by injecting a higher dose. Unfortunately, increasing the activity is not always possible due to specific tracer kinetics in some tracers. In cases of irreversible binding, increasing the dose would not increase the uptake ratio due to receptor saturation. Furthermore, the irradiation dose should also be taken into account. Hoppin et al. [398] estimate that ^{111}In and ^{99m}Tc will deliver a dose of 76.76 mGy/MBq and 4.59 mGy/MBq respectively, assuming a 72 h biological half-life. For the current study, this results in an average total dose of 2.38 Gy due to [^{111}In]Octreotide, while [^{99m}Tc]DMSA will result in a 358 mGy dose. [^{111}In]Octreotide will also irradiate nearby tissue (0.02 to 500 μm) with Auger and internal conversion electrons [399, 400]. Therefore, the injected dose should be kept as low as possible, not only for micro-CT but also for micro-SPECT.

Some system design ideas allow for pinhole systems with increased sensitivity. One of the options is the use of multiplexing pinhole collimators, as is already used in the X-SPECT system used in this and the previous Chapters. Several research groups have shown that multiplexing leads to image artifacts such as image non-uniformities and ghost activity, due to the ambiguity of the projected data in overlapping regions [139–141, 401–403]. A uniform phantom scanned with the X-SPECT system has already been shown to exhibit some non-uniformities (Fig. 8 in Ref. [141]) when a multi-pinhole collimator is used. However, the extent of multiplexing

artefacts is dependent on the activity distribution and the geometrical system design [140]. A similar non-uniformity was noticed in the uniform part of the phantom study (Fig. 6.10). This may influence the quantification error when only a small VOI is analyzed.

7.7 Conclusion

We have shown that absolute in vivo quantification is possible in micro-SPECT using direct modeling in iterative reconstruction, without the need for explicit measurements of the system matrix. An absolute in vivo quantification error smaller than 5% was achieved for two typical tracers.

Chapter 8

Concluding remarks

In this final chapter, a general overview is given about the work presented in the preceding chapters. The results from each individual chapter will be concisely summarized together with the limitations, novelties and future work, and the respective conclusions that can be drawn. Finally, an overall conclusion will be presented to conclude this dissertation.

8.1 Summary

The purpose of this dissertation was to investigate the use of improved iterative reconstruction in CT and micro-SPECT/CT imaging to address two challenges: (i) the X-ray radiation dose and (ii) absolute quantification in micro-SPECT/CT. To achieve a dose reduction in CT, our approach consisted of reducing the number of projection views per acquisition. Although this linearly decreases the dose and acquisition time, such angular undersampling will introduce aliasing artifacts into the reconstructed images. The aliasing artifacts were minimized by applying regularized reconstruction techniques. This approach was first applied to in vivo vascular imaging in mice using the ISRA-TV algorithm. However, due to the image model imposed by the TV regularizer, some new image artifacts were introduced. Therefore, a general framework for regularized CT reconstruction was implemented, where a general regularizer could be included. A method, novel for CT, was developed using shearlet-based regularization. For the second challenge, we investigated if model-based iterative reconstruction enables truly quantitative SPECT reconstruction, and we determined the accuracy and precision of this method both on phantoms and on in vivo animal studies.

This dissertation started in Chapter 2 with a historical overview of medical and molecular imaging. A thorough introduction was given into the CT and SPECT modalities, with special attention to the challenges in CT and SPECT, mainly concerning the X-ray dose and absolute quantification in SPECT. These challenges were further discussed in the specific case of small-animal CT and SPECT, as those miniaturized systems significantly differ from their clinical counterparts.

Chapters 3, 4 and 5 address the radiation-dose challenge of CT. First, in Chapter 3 we determined if and how in vivo preclinical imaging can replace ex vivo measurements, allowing for longitudinal research. The golden standard involves vascular corrosion casting followed by *ex vivo* micro-CT scans to generate a 3D model of the cast. We investigated if this can be replaced by *in vivo* micro-CT scanning. We showed that enough contrast can be obtained in the vascular system to enable accurate segmentation with an iodine-based contrast-agent. The in vivo models were significantly larger than the in vitro models, but did not lead to significantly different wall shear stress values. Unfortunately, when retrospective respiratory gating was applied to remove motion artifacts, the delineation quality did not increase. There was a substantial increase in image noise, caused by the limited angular sampling.

Even though the data presented shows that *in vivo* imaging is possible, longitudinal scans remain challenging. First of all, the contrast agent possibly attributed to the high mortality in the mice, due to the contrast agent toxicity and the relatively high injected volume. We currently use a different contrast agent for these studies, which does not show these effects. A second problem is the radiation dose, calculated at 196 mGy per scan. This is for instance higher than the total dose of 180 mGy proven to lead to tumor growth inhibition, and thus needs to be lowered to enable longitudinal imaging studies.

In Chapter 4, we determined how iterative reconstruction can be used to reduce the imaging dose. The dose was lowered by decreasing the number of projection views acquired during the CT acquisition. Whereas this introduces substantial image noise and image artifacts when traditional reconstruction techniques are used (analytical or simple iterative), using regularized reconstruction leads to images that can be segmented. We found that TV-based regularization was very useful here, as images reconstructed with TV minimization showed good image quality with much less streaking artifacts than when no regularization is applied (i.e. with FBP). This allowed us to achieve an 8-fold reduction in dose and

8-times acquisition speed-up, if the images were to be used only for segmentation and not for diagnostics. The same type of analysis can also be done for other tasks (e.g. for trabecular bone analysis), in order to determine the minimal dose when advanced reconstruction techniques are used.

Unfortunately, the image quality is insufficient for diagnostic tasks, because of small block-like artifacts (staircasing). These are caused by the underlying image model imposed by TV regularization, of which its use can certainly be questioned in medical imaging: medical images are not approximately piecewise constant, but exhibit texture. With TV regularization, some image features important to diagnostics might be removed.

Realizing TV-based regularization is not ideal; in Chapter 5 a different regularizer was proposed for CT. This chapter was started by working on a very general framework for CT regularized reconstruction based on the split-Bregman technique, in order to embed any possible regularizer into iterative CT reconstruction. This framework was later applied to the shearlet-transformation, a multiscale and multidirectional transformation shown to be optimal for 2D piecewise smooth surfaces with discontinuities along C^2 edges.

The shearlet-based reconstruction was validated on three different phantoms: a smooth-gradient phantom to determine the influence of staircasing, a contrast phantom to determine the effect of contrast magnitude on the noise-resolution tradeoff, and an *ex vivo* acquired ultra-high-dose dataset of a plastinated mouse to determine its influence on texture. These three phantoms allowed us to evaluate the regularization without using a phantom biased for the TV model.

Based on the noise-resolution tradeoff study, TV minimization outperformed shearlet-based reconstruction. However, on acquired data with realistic image texture, shearlets reconstructed the textures more similar to the reference texture of the ultra-high-dose dataset. We found some important limitations of using shearlets in CT reconstruction. Although the shearlet-transform was suited for structures representing sharp and elongated structures (edges), it was unsuited for spherical-like sources. This is a limitation similar to those found with other multi-resolution techniques: when they represent isotropic features well, they are far from optimal for analyzing anisotropic objects. We therefore suggest that the shearlet-based approach should be combined with an isotropic wavelet transform. The sensitivity of each transform to a particular shape in the

multiresolutional analysis would possibly make it a very strong discriminating tool. Future work could thus include the combination of both transforms in one algorithm, and the application of these developed techniques to different datasets with numerical observer studies.

In micro-SPECT/CT, Chapter 2 indicated that one of the major challenges is quantitative SPECT. With absolute quantification, the activity concentration can be directly derived from the reconstructed images. This is needed e.g. to enable dose calculations in targeted therapy treatment planning, to follow the treatment of tumors longitudinally, to measure the dose-response for an experimental drug. Physical effects will be detrimental to the quantitative accuracy.

Chapter 6 was used to determine the absolute quantification accuracy in micro-SPECT imaging. Several methods were proposed in the past to correct for each individual image degrading effect, but were never used together and tested for accuracy and precision in an *in vivo* ^{111}In application. After describing the necessary system calibrations, we show how an efficient model-based iterative reconstruction algorithm can be implemented on the GPU for micro-SPECT reconstruction. Detector uniformity, geometric sensitivity, resolution recovery, photon scatter, photon attenuation and PVE correction were included into an OSL-OSEM algorithm, which was calibrated to absolute activity values using a calibration vial.

The implementation was validated on a multi-modal micro-SPECT/CT system, using a CZT detector with energy resolution 4.22±0.23%, on 3D-printed NEMA phantoms for ^{99m}Tc and ^{111}In. Using phantoms in this step allowed us to optimize and validate the reconstruction software, because the ground-truth values were known. In order to be able to define the 3 phantom compartments on the CT for the PVE correction, 2 compartments were filled with iodine-based contrast agent. Comparing the measured activity to the known activity, the accuracy error decreased to a quantification error of ±10% for ^{99m}Tc and ^{111}In. Only the lowest activity vial was undercorrected for ^{111}In, due to the contribution of the 39±13% undercorrection for the low-energy photopeak. The quantification errors indicate that a decrease in error is primarily caused by the attenuation correction. The influence of photon scatter was effectively minimized by photopeak windowing, made possible by the excellent energy resolution of the CZT detector.

Finally in Chapter 7 the absolute quantification error was measured *in vivo* using the improved reconstruction from chapter 6. Additional

blood-pool activity correction was therefore implemented. The first mouse model used is one of tubular functioning after PRRT therapy with ^{90}Y, measured by [^{99m}Tc]DMSA. An iodine-based contrast agent was additionally used to enable the delineation of the renal cortex on the micro-CT images. The second mouse model is one of human non-small cell lung carcinoma (cell line H727). As imaging agent the radioactively labeled [^{111}In]Octreotide was used, an octapeptide that pharmacologically mimics natural somatostatin. Because the H727 tumor expresses somatostatin receptor type 2, 3 and 5, [^{111}In]Octreotide is a good match for H727 studies.

For each model, a strict imaging protocol was followed, after which the relevant organs were prelevated and measured in a gamma-counter. The value obtained from the reconstructed images was then compared to this ground-truth value. Our *in vivo* results indicate that a quantification error of less than 5% can be achieved with both ^{99m}Tc and ^{111}In on this micro-SPECT system, by using a model-based iterative reconstruction algorithm. This in vivo error is lower than the errors determined for the phantoms, which is counter intuitive. However, only a significant difference was found when comparing to the lowest activity vial for ^{111}In, where the error was caused by an undercorrection for the low-energy photopeak. A proof of concept study was done to determine if low-dose CT measurements can be used as an attenuation map for the SPECT reconstruction. This was possible at 1/16th the original dose. However, at least 64 views are needed to enable the delineation of organs for PVE correction.

Some issues were encountered, which will be solved in future work. Firstly, applying blood-pool activity correction significantly changes the absolute quantification error. Because little VVF data of different tissues is available in literature, it is difficult to use this correction in practice. A possible solution may be to directly measure the VVF with e.g. in vivo MRI, which would also allow us to account for intraspecies differences. However, an MRI is currently still a very expensive alternative to CT and will therefore not be available for every research lab. Secondly, there is the low system sensitivity with pinhole SPECT, combined with the typically low biological uptake for preclinical studies. We had to increase the injected dose and total acquisition time to achieve an activity measurable on our micro-SPECT system. This will however not be possible for all tracers due to specific tracer kinetics and due to the irradiation dose delivered by the tracer. Therefore, the system should be adapted to increase the geometrical sensitivity (e.g. with more pinholes), and/or

by using a more advanced reconstruction algorithm than OSL-OSEM.

8.2 Final conclusion

Model-based iterative reconstruction techniques can help to solve some challenges still faced currently in micro-CT and in micro-SPECT/CT imaging.

Regularized iterative CT reconstruction was shown to reduce the minimum X-ray dose necessary and increases the imaging throughput considerably, as long as an appropriate regularizer is found for medical images. A possible choice is the shearlet transform, which shows an improvement for textured tissue, but results in different artifacts than when TV is used. TV regularization still has its merit when texture should not remain intact, e.g. for segmentation tasks.

Model-based iterative reconstruction also enables in vivo absolute quantitative micro-SPECT/CT imaging, thus removing the need for explicit measurements of the system matrix. An absolute in vivo quantification error smaller than 5% was achieved for two typical tracers in mouse models.

"I may not have gone where I intended to go, but I think I have ended up where I needed to be."
Douglas Adams

Appendix

Appendix A

Split-Bregman pseudocode

The following algorithm shows the pseudocode of the split-Bregman algorithm for regularized CT reconstruction.

Require: $\mathbf{d} \leftarrow \mathbf{0}, \mathbf{b} \leftarrow \mathbf{0}$, $\mathbf{C} \leftarrow \text{diag}(e^{-y_i})$, μ, λ.
Ensure: image $\mathbf{x}$.

if $\mathbf{\Phi}$ = Shearlet-transform **then**
    $\mathbf{u} = \mathbf{\Phi}(\mathbf{1})$
    for $s = 0 \rightarrow scales(\mathbf{u})$ **do**
        for $i = 0 \rightarrow size(\mathbf{u}[s])$ **do**
            $\mathbf{E}[s][i] = \sqrt{\sum_{j=0}^{size(\mathbf{u}[s])} \mathbf{u}[s][j]^2}$
        end for
    end for
else
    $\mathbf{E} = \mathbf{1}$
end if
for $0 \rightarrow iterations$ **do**
    $\mathbf{r} \leftarrow \mathbf{W}^{\dagger}(\mathbf{C}^{-1}\mathbf{y}) + (\mu/\lambda)\mathbf{\Phi}^{\dagger}(\mathbf{d} - \mathbf{b})$
    $\mathbf{p} \leftarrow \mathbf{r}$
    $new\_err \leftarrow \mathbf{r}' * \mathbf{r}$
    for $0 \rightarrow cg\_iterations$ **do**
        $err \leftarrow new\_err$
        $\mathbf{M} \leftarrow \mathbf{W}^{\dagger}(\mathbf{C}^{-1}\mathbf{W}(\mathbf{p})) + (\mu/\lambda)\mathbf{\Phi}^{\dagger}(\mathbf{\Phi}(\mathbf{p}))$
        $\alpha \leftarrow err/(\mathbf{p}' * \mathbf{M})$
        $\mathbf{x} \leftarrow \mathbf{x} + \alpha\mathbf{p}$
        $\mathbf{r} \leftarrow \mathbf{r} - \alpha\mathbf{M}$
        $new\_err \leftarrow \mathbf{r}' * \mathbf{r}$
        $\beta \leftarrow new\_err/err$

$\mathbf{p} \leftarrow \mathbf{r} + \beta\mathbf{p}$
end for
$\mathbf{S} = \mathbf{\Phi}(\mathbf{x})$
$\mathbf{k} = \mathbf{S} + \mathbf{b}$
for $i = 0 \rightarrow size(\mathbf{k})$ **do**
$\mathbf{d}[i] \leftarrow \text{sign}\,(\mathbf{k}[i]) * \max(|\mathbf{k}[i]| - \mathbf{E}[i]/\mu, 0)$
end for
$\mathbf{b} \leftarrow \mathbf{b} + (\mathbf{S} - \mathbf{d})$
end for
return $\mathbf{x}$

References

[1] European Commission. Seventh Report on the Statistics on the Number of Animals used for Experimental and other Scientific Purposes in the Member States of the European Union. *Tech. rep.* 2013.

[2] De Man B, Nuyts J, Dupont P, Marchal G, Suetens P. An iterative maximum-likelihood polychromatic algorithm for CT. *IEEE Transactions on Medical Imaging.* 2001;20(10):999–1008.

[3] Hsieh J. *Computed Tomography: Principles, Design, Artifacts, and Recent Advances.* SPIE, 2nd ed. 2009.

[4] Spiegel PK. The first clinical X-ray made in America–100 years. *AJR American journal of roentgenology.* 1995;164(1):241–243.

[5] Hrabak M, Padovan RS, Kralik M, Ozretic D, Potocki K. Scenes from the Past: Nikola Tesla and the Discovery of X-rays1. *Radiographics.* 2008;28(4):1189–1192.

[6] Elliott JC, Dover SD. X-ray microtomography. *Journal of Microscopy.* 1982;126(Pt 2):211–213.

[7] Elliott JC, Dover SD. Three-dimensional distribution of mineral in bone at a resolution of 15 micron determined by x-ray microtomography. *Metab Bone Dis Relat Res.* 1984;5(5):219–221.

[8] Cao G, Lee YZ, Peng R, Liu Z, Rajaram R, Calderon-Colon X, An L, Wang P, Phan T, Sultana S, Lalush DS, Lu JP, Zhou O. A dynamic micro-CT scanner based on a carbon nanotube field emission x-ray source. *Physics in Medicine and Biology.* 2009;54(8):2323–2340.

[9] Duclos SJ, Greskovich CD, Lyons RJ, Vartuli JS, Hoffman DM, Riedner RJ, Lynch MJ. Development of the HiLightTM scintillator for computed tomography medical imaging. *Nuclear Instruments and Methods in Physics Research Section A: Accelerators, Spectrometers, Detectors and Associated Equipment*. 2003;505(1-2):68–71.

[10] Chandra N, Langan DA. Gemstone Detector: Dual Energy Imaging via Fast kVp Switching. In: *Dual Energy CT in Clinical Practice*, edited by Johnson TRC, Fink C, Schönberg SO, Reiser MF, pp. 35–41. Berlin, Heidelberg: Springer Berlin Heidelberg. 2010;.

[11] Karellas A, Harris LJ, Liu H, Davis MA, D'Orsi CJ. Charge-coupled device detector: performance considerations and potential for small-field mammographic imaging applications. *Medical Physics*. 1992;19(4):1015–1023.

[12] Goertzen AL. Development of a Combined microPET and microCT System for Mouse Imaging. Ph.D. thesis, University of Los Angeles. 2003.

[13] Goertzen AL, Nagarkar V, Street R, Paulus M, Boone JM, Cherry SR. A comparison of x-ray detectors for mouse CT imaging. *Physics in Medicine and Biology*. 2004;49:5251–5265.

[14] Koch A, Raven C, Spanne P, Snigirev A. X-ray imaging with submicrometer resolution employing transparent luminescent screens. *JOSA A*. 1998;15(7):1940–1951.

[15] Fuchs T, Kachelrieß M, Kalender WA. Direct comparison of a xenon and a solid-state CT detector system: measurements under working conditions. *IEEE Transactions on Medical Imaging*. 2000; 19(9):941–948.

[16] Barrett JF, Keat N. Artifacts in CT: Recognition and Avoidance. *Radiographics*. 2004;24(6):1679–1691.

[17] Meganck JA, Kozloff K, Thornton MM, Broski SM, Goldstein SA. Beam hardening artifacts in micro-computed tomography scanning can be reduced by X-ray beam filtration and the resulting images can be used to accurately measure BMD. *Bone*. 2009;45(6):1104–1116.

[18] Klein O, Nishina Y. Über die Streuung von Strahlung durch freie Elektronen nach der neuen relativistischen Quantendynamik von Dirac. *Zeitschrift für Physik*. 1929;52(11-12):853–868.

[19] Kyriakou Y, Kalender WA. Efficiency of antiscatter grids for flat-detector CT. *Physics in Medicine and Biology*. 2007;52(20):6275–6294.

[20] Chow PL, Vu N, Chatziioannou AF. Estimating the magnitude of scatter in small animal cone-beam CT. *IEEE Nuclear Science Symposium Conference Record*. 2004;.

[21] Gutierrez D, Zaidi H. Assessment of scatter for the micro-CT subsystem of the trimodality FLEX Triumph^{TM} preclinical scanner. *Medical Physics*. 2011;38(7):4154–4165.

[22] Siewerdsen JH, Moseley DJ, Bakhtiar B, Richard S, Jaffray DA. The influence of antiscatter grids on soft-tissue detectability in cone-beam computed tomography with flat-panel detectors. *Medical Physics*. 2004;31(12):3506.

[23] Siewerdsen JH, Daly MJ, Bakhtiar B, Moseley DJ, Richard S, Keller H, Jaffray DA. A simple, direct method for x-ray scatter estimation and correction in digital radiography and cone-beam CT. *Medical Physics*. 2006;33(1):187.

[24] Ning R, Tang X, Conover D. X-ray scatter correction algorithm for cone beam CT imaging. *Medical Physics*. 2004;31(5):1195.

[25] Zbijewski W, Beekman FJ. Efficient Monte Carlo based scatter artifact reduction in cone-beam micro-CT. *IEEE Transactions on Medical Imaging*. 2006;25(7):817–827.

[26] Baek J, Pineda AR, Pelc NJ. To bin or not to bin? The effect of CT system limiting resolution on noise and detectability. *Physics in Medicine and Biology*. 2013;58(5):1433–1446.

[27] Hsieh J, Gard MA, Gravelle S. Reconstruction technique for focal spot wobbling. In: *SPIE Proceedings*, edited by Loew MH. SPIE. 1992; pp. 175–182.

[28] Kachelrieß M, Knaup M, Penßel C, Kalender WA. Flying focal spot (FFS) in cone-beam CT. *IEEE Transactions on Nuclear Science*. 2006;53(3):1238–1247.

[29] Joseph PM, Schulz RA. View sampling requirements in fan beam computed tomography. *Medical Physics*. 1980;7(6):692–702.

[30] Radon J. Über die Bestimmung von Funktionen durch ihre Integralwerte läng bestimmter Mannigfaltigkeiten. *Ber Verb Sächs Akad Wiss Leipzig, Math-Nat Kl*. 1917;69:262–277.

[31] Van Laere K, Koole M, Lemahieu I, Dierckx R. Image filtering in single-photon emission computed tomography: principles and applications. *Computerized Medical Imaging and Graphics*. 2001; 25(2):127–133.

[32] Feldkamp LA, Davis LC, Kress JW. Practical cone-beam algorithm. *Journal of the Optical Society of America A, Optics, image science, and vision*. 1984;1(6):612–619.

[33] Defrise M, Clack R. A cone-beam reconstruction algorithm using shift-variant filtering and cone-beam backprojection. *IEEE Transactions on Medical Imaging*. 1994;13(1):186–195.

[34] Katsevich A. Theoretically exact filtered backprojection-type inversion algorithm for spiral CT. *SIAM Journal on Applied Mathematics*. 2002;62(6):2012–2026.

[35] Gordon R, Bender R, Herman GT. Algebraic reconstruction techniques (ART) for three-dimensional electron microscopy and X-ray photography. *Journal of Theoretical Biology*. 1970;29(3):471–481.

[36] Czaja W, Tanis JH. Kaczmarz Algorithm and Frames. *International Journal of Wavelets Multiresolution and Information Processing*. 2013;11(5).

[37] Cegielski A. Bibliography on the Kaczmarz method. 2010. URL `http://www.uz.zgora.pl/~acegiels/Publikacje-Kaczmarz.pdf`

[38] Hudson HM, Larkin RS. Accelerated image reconstruction using ordered subsets of projection data. *IEEE Transactions on Medical Imaging*. 1994;13(4):601–609.

[39] Badea CT, Gordon R. Experiments with the nonlinear and chaotic behaviour of the multiplicative algebraic reconstruction technique (MART) algorithm for computed tomography. *Physics in Medicine and Biology*. 2004;49(8):1455–1474.

[40] Daube-Witherspoon ME, Muehllehner G. An Iterative Image Space Reconstruction Algorthm Suitable for Volume ECT. *IEEE Transactions on Medical Imaging*. 1986;5(2):61–66.

[41] De Pierro AR. On the relation between the ISRA and the EM algorithm for positron emission tomography. *IEEE Transactions on Medical Imaging*. 1993;12(2):328–333.

[42] Fessler JA. Iterative methods for image reconstruction. In: *ISBI Tutorial on Statistical Image Reconstruction Methods*. Arlington, Virginia. 2006; p. 130.

[43] Archer GEB, Titterington DM. The iterative image space reconstruction algorithm (ISRA) as an alternative to the EM algorithm for solving positive linear inverse problems. *Statistica Sinica*. 1995; 5:77–96.

[44] Reader AJ, Létourneau E, Verhaege J. Generalization of the image space reconstruction algorithm. *IEEE Nuclear Science Symposium Conference Record*. 2011;pp. 4233–4238.

[45] Nuyts J, De Man B, Dupont P, Defrise M. Iterative reconstruction for helical CT: a simulation study. *Physics in Medicine and Biology*. 1998;43:729–737.

[46] Barrett HH, Myers KJ. *Foundations of Image Science*. Wiley Series in Pure and Applied Optics. 2004.

[47] Lange K, Fessler JA. Globally Convergent Algorithms for Maximum a-Posteriori Transmission Tomography. *IEEE Transactions on Image Processing*. 1995;4(10):1430–1438.

[48] Fessler JA, Ficaro EP, Clinthorne NH, Lange K. Grouped-coordinate ascent algorithms for penalized-likelihood transmission image reconstruction. *IEEE Transactions on Medical Imaging*. 1997;16(2):166–175.

[49] Jakab G, Huszár T, Csébfalvi B. Iterative CT Reconstruction on the GPU. In: *Sixt Hungarian Conference on Computer Graphics and Geometry*. Budapest. 2012; .

[50] Vanhove C, Vandeghinste B, Van Holen R, Vandenberghe S. Performance evaluation of GPU implementations of four different iterative reconstruction algorithms for micro-computed tomography. *Society of Nuclear Medicine Annual Meeting Abstracts*. 2013;.

[51] Erdogan H, Fessler JA. Ordered subsets algorithms for transmission tomography. *Physics in Medicine and Biology*. 1999;44:2835–2851.

[52] Sidky EY, Yu L, Pan X, Zou Y, Vannier MW. A robust method of x-ray source spectrum estimation from transmission measurements: Demonstrated on computer simulated, scatter-free transmission data. *Journal of Applied Physics*. 2005;97:124701.

[53] Thibault JB, Sauer KD, Bouman CA, Hsieh J. A three-dimensional statistical approach to improved image quality for multislice helical CT. *Medical Physics*. 2007;34(11):4526.

[54] Bolus NE. Basic review of radiation biology and terminology. *Journal of Nuclear Medicine Technology*. 2001;29(2):67–73– test 76–7.

[55] Parkin DM, Boyd L, Walker LC. The fraction of cancer attributable to lifestyle and environmental factors in the UK in 2010. *British Journal of Cancer*. 2011;105(S2):S77–S81.

[56] Ozasa K, Shimizu Y, Suyama A, Kasagi F, Soda M, Grant EJ, Sakata R, Sugiyama H, Kodama K. Studies of the Mortality of Atomic Bomb Survivors, Report 14, 1950–2003: An Overview of Cancer and Noncancer Diseases. *Radiation Research*. 2012; 177(3):229–243.

[57] Doss M, Egleston BL, Litwin S. Comments on "Studies of the Mortality of Atomic Bomb Survivors, Report 14, 1950-2003: An Overview of Cancer and Noncancer Diseases" (Radiat Res 2012; 177:229-43). *Radiation Research*. 2012;178(3):244–245.

[58] Doss M. Evidence Supporting Radiation Hormesis in Atomic Bomb Survivor Cancer Mortality Data. *Dose-Response*. 2012;10(4):584–592.

[59] Mathews JD, Forsythe AV, Brady Z, Butler MW, Goergen SK, Byrnes GB, Giles GG, Wallace AB, Anderson PR, Guiver TA, McGale P, Cain TM, Dowty JG, Bickerstaffe AC, Darby SC. Cancer risk in 680 000 people exposed to computed tomography scans in childhood or adolescence: data linkage study of 11 million Australians. *BMJ*. 2013;346:f2360.

[60] Cardis E, Vrijheid M, Blettner M, Gilbert E, Hakama M, Hill C, Howe G, Kaldor J, Muirhead CR, M SB, Yoshimura T, Bermann

F, Cowper G, Fix J, Hacker C, Heinmiller B, Marshall M, Thierry-Chef I, Utterback D, Ahn YO, Amoros E, Ashmore P, Auvinen A, Bae JM, Bernar Solano J, Biau A, Combalot E, Deboodt P, Diez Sacristan A, Eklof M, Engels H, Engholm G, Gulis G, Habib R, Holan K, Hyvonen H, Kerekes A, Kurtinaitis J, Malker H, Martuzzi M, Mastauskas A, Monnet A, Moser M, Pearce MS, Richardson DB, Rodríguez-Artalejo F, Rogel A, Tardy H, Telle-Lamberton M, Turai I, Usel M, Veress K. Risk of cancer after low doses of ionising radiation: retrospective cohort study in 15 countries. *BMJ*. 2005;331(7508):77–0.

[61] Xia T, Alessio AM, De Man B, Manjeshwar R, Asma E, Kinahan PE. Ultra-low dose CT attenuation correction for PET/CT. *Physics in Medicine and Biology*. 2011;57(2):309–328.

[62] Sato F, Sasaki S, Kawashima N, Chino F. Late Effects of Whole or Partial Body X-irradiation on Mice: Life Shortening. *Int J Radiat Biol Relat Stud Phys Chem Med*. 1981;39(6):607–615.

[63] Mole RH. Quantitative observations on recovery from whole body irradiation in mice. II. Recovery during and after daily irradiation. *Br J Radiol*. 1956;29(349):40–46.

[64] McCollough CM, Bruesewitz MR, Kofler JM. CT Dose Reduction and Dose Management Tools: Overview of Available Options. *Radiographics*. 2006;26(2):503–512.

[65] McCollough CM, Primak AN, Braun N, Kofler JM, Yu L, Christner J. Strategies for Reducing Radiation Dose in CT. *Radiologic Clinics of North America*. 2009;47(1):27–40.

[66] Wilting JE, Zwartkruis A, van Leeuwen MS, Timmer J, Kamphuis AGA, Feldberg M. A rational approach to dose reduction in CT: individualized scan protocols. *European Radiology*. 2001; 11(12):2627–2632.

[67] Bian J, Siewerdsen JH, Han X, Sidky EY, Prince JL, Pelizzari CA, Pan X. Evaluation of sparse-view reconstruction from flat-panel-detector cone-beam CT. *Physics in Medicine and Biology*. 2010; 55:6575–6599.

[68] Zoltowski P. Techniques to lower CT dose. *Nepalese Journal of Radiology*. 2013;.

[69] GE Healthcare. Introducing Veo on Discovery CT750 HD. 2011; pp. 1–40.

[70] Fletcher JG, Takahashi N, Hartman R, Guimaraes L, Huprich JE, Hough DM, Yu L, McCollough CM. Dual-Energy and Dual-Source CT: Is There a Role in the Abdomen and Pelvis? *Radiologic Clinics of North America*. 2009;47(1):41–57.

[71] Granton PV, Pollmann SI, Ford NL, Drangova M, Holdsworth DW. Implementation of dual- and triple-energy cone-beam micro-CT for postreconstruction material decomposition. *Medical Physics*. 2008; 35(11):5030.

[72] Moding EJ, Clark DP, Qi Y, Li Y, Ma Y, Ghaghada K, Johnson A, Kirsch DG, Badea CT. Dual-Energy Micro-Computed Tomography Imaging of Radiation-Induced Vascular Changes in Primary Mouse Sarcomas. *Radiation Oncology Biology*. 2012;pp. 1–7.

[73] Flohr T, McCollough CM, Bruder H, Petersilka M, Gruber K, Süβ C, Grasruck M, Stierstorfer K, Krauss B, Raupach R. First performance evaluation of a dual-source CT (DSCT) system. *European Radiology*. 2006;16(2):256–268.

[74] Shikhaliev PM, Xu T, Molloi S. Photon counting computed tomography: Concept and initial results. *Medical Physics*. 2005;32:427.

[75] Shikhaliev PM. Tilted angle CZT detector for photon counting/energy weighting x-ray and CT imaging. *Physics in Medicine and Biology*. 2006;51(17):4267–4288.

[76] Bennett JR, Opie AMT, Xu Q, Yu H, Walsh M, Butler APH, Butler PH, Cao G, Mohs A, Wang G. Hybrid Spectral Micro-CT: System Design, Implementation & Preliminary Results. *IEEE*. 2013;.

[77] Burghardt AJ, Link TM, Majumdar S. High-resolution Computed Tomography for Clinical Imaging of Bone Microarchitecture. *Clinical Orthopaedics and Related Research®*. 2011;469(8):2179–2193.

[78] Ritman EL. Micro-computed tomography—current status and developments. *Annu Rev Biomed Eng*. 2004;6:185–208.

[79] Calder WA. *Size, function and life history*. Harvard University Press. 1984.

[80] Zbijewski W, De Jean P, Prakash P, Ding Y, Stayman JW, Packard N, Senn R, Yang D, Yorkston J, Machado A, Carrino JA, Siewerdsen JH. Design and optimization of a dedicated cone-beam CT system for musculoskeletal extremities imaging. *SPIE Medical Imaging*. 2011;7961:796104–796104–8.

[81] Kalender WA, Beister M, Boone JM, Kolditz D, Vollmar SV, Weigel MCC. High-resolution spiral CT of the breast at very low dose: concept and feasibility considerations. *European Radiology*. 2011;22(1):1–8.

[82] Holdsworth DW, Thornton MM. Micro-CT in small animal and specimen imaging. *Trends in Biotechnology*. 2002;20(8):S34–S39.

[83] Parnham KB, Chowdhury S, Li J, Wagenaar DJ, Patt BE. Second-generation, tri-modality pre-clinical imaging system. *IEEE Nuclear Science Symposium Conference Record*. 2006;.

[84] Verhaegen F, Granton P, Tryggestad E. Small animal radiotherapy research platforms. *Physics in Medicine and Biology*. 2011; 56(12):R55–R83.

[85] Flynn MJ, Hames SM, Reimann DA, Wilderman SJ. Microfocus x-ray sources for 3D microtomography. *Nuclear Inst and Methods in Physics Research, A*. 1994;353(1):312–315.

[86] Grodzins L. Optimum energies for x-ray transmission tomography of small samples: Applications of synchrotron radiation to computerized tomography I. *Nuclear Instruments and Methods in Physics Research*. 1983;206(3):541–545.

[87] Mukundan S, Ghaghada KB, Badea CT, Kao CY, Hedlund LW, Provenzale JM, Johnson GA, Chen E, Bellamkonda RV, Annapragada A. A Liposomal Nanoscale Contrast Agent for Preclinical CT in Mice. *American Journal of Roentgenology*. 2006;186(2):300–307.

[88] Boll H, Nittka S, Doyon F, Neumaier M, Marx A, Kramer M, Groden C, Brockmann MA. Micro-CT Based Experimental Liver Imaging Using a Nanoparticulate Contrast Agent: A Longitudinal Study in Mice. *PLoS ONE*. 2011;6(9):e25692.

[89] Li X, Anton N, Zuber G, Zhao M, Messaddeq N, Hallouard F, Fessi H, Vandamme TF. Iodinated alpha-tocopherol nano-emulsions as

non-toxic contrast agents for preclinical X-ray imaging. *Biomaterials*. 2013;34(2):481–491.

[90] Thomsen HS, Morcos SK. Contrast media and the kidney: European Society of Urogenital Radiology (ESUR) Guidelines. *British Journal of Radiology*. 2003;76(908):513–518.

[91] Namati E, Chon D, Thiesse J, Hoffman EA, Ryk Jd, Ross A, McLennan G. In vivo micro-CT lung imaging via a computer-controlled intermittent iso-pressure breath hold (IIBH) technique. *Physics in Medicine and Biology*. 2006;51(23):6061–6075.

[92] Cavanaugh D, Johnson E, Price RE, Kurie J, Travis EL, Cody DD. In vivo respiratory-gated micro-CT imaging in small-animal oncology models. *Molecular Imaging*. 2004;3(1):55–62.

[93] Ritschl L, Sawall S, Knaup M, Hess A, Kachelrieß M. Iterative 4D cardiac micro-CT image reconstruction using an adaptive spatio-temporal sparsity prior. *Physics in Medicine and Biology*. 2012; 57(6):1517–1525.

[94] Badea CT, Fubara B, Hedlund LW, Johnson GA. 4-D micro-CT of the mouse heart. *Molecular Imaging*. 2005;4(2):110–116.

[95] Hansen J, Jurik AG. Analysis of Current Practice of CT examinations. *Acta Oncologica*. 2009;48(2):295–301.

[96] Mettler FA Jr, Bhargavan M, Faulkner K, Gilley DB, Gray JE, Ibbott GS, Lipoti JA, Mahesh M, McCrohan JL, Stabin MG, Thomadsen BR, Yoshizumi TT. Radiologic and Nuclear Medicine Studies in the United States and Worldwide: Frequency, Radiation Dose, and Comparison with Other Radiation Sources—1950–2007 1. *Radiology*. 2009;253(2):520–531.

[97] Kaste M. Reborn Workhorse, CT, Pulls the Wagon Toward Thrombolysis Beyond 3 Hours. *Stroke*. 2004;35(2):357–359.

[98] Feldkamp LA, Goldstein SA, Parfitt MA, Jesion G, Kleerekoper M. The direct examination of three-dimensional bone architecture in vitro by computed tomography. *Journal of Bone and Mineral Research*. 2009;4(1):3–11.

[99] Campbell GM, Tiwari S, Grundmann F, Purcz N, Schem C, Glüer CC. Three-dimensional Image Registration Improves the Long-term Precision of In Vivo Micro-Computed Tomographic Measurements in Anabolic and Catabolic Mouse Models. *Calcified Tissue International*. 2013;.

[100] Hashimoto M, Hotokezaka H, Sirisoontorn I, Nakano T, Arita K, Tanaka M, Yoshida N. The effect of bone morphometric changes on orthodontic tooth movement in an osteoporotic animal model. *The Angle Orthodontist*. 2013;83(5):766–773.

[101] Kiessling F, Greschus S, Lichy MP, Bock M, Fink C, Vosseler S, Moll J, Mueller MM, Fusenig NE, Traupe H, Semmler W. Volumetric computed tomography (VCT): a new technology for noninvasive, high-resolution monitoring of tumor angiogenesis. *Nature Medicine*. 2004;10(10):1133–1138.

[102] Bolland BJRF, Kanczler JM, Dunlop DG, Oreffo ROC. Development of in vivo μCT evaluation of neovascularisation in tissue engineered bone constructs. *Bone*. 2008;43(1):195–202.

[103] Landazuri N, Joseph G, Guldberg RE, Taylor WR. Growth and regression of vasculature in healthy and diabetic mice after hindlimb ischemia. *AJP: Regulatory, Integrative and Comparative Physiology*. 2012;303(1):R48–R56.

[104] Savai R, Langheinrich AC, Schermuly RT, Pullamsetti SS, Dumitrascu R, Traupe H, Rau WS, Seeger W, Grimminger F, Banat GA. Evaluation of Angiogenesis Using Micro-Computed Tomography in a Xenograft Mouse Model of Lung Cancer. *Neoplasia (New York, NY)*. 2009;11(1):48–56.

[105] Masschaele B, Dierick M, Loo DV, Boone MN, Brabant L, Pauwels E, Cnudde V, Hoorebeke LV. HECTOR: A 240kV micro-CT setup optimized for research. *Journal of Physics: Conference Series*. 2013;463:012012.

[106] Morgan EF, Mason ZD, Chien KB, Pfeiffer AJ, Barnes GL, Einhorn TA, Gerstenfeld LC. Micro-computed tomography assessment of fracture healing: relationships among callus structure, composition, and mechanical function. *Bone*. 2009;44(2):335–344.

[107] Freeman TA, Patel P, Parvizi J, Antoci V Jr, Shapiro IM. Micro-CT analysis with multiple thresholds allows detection of bone formation and resorption during ultrasound-treated fracture healing. *Journal of Orthopaedic Research*. 2009;27(5):673–679.

[108] Tremoleda JL, Khalil M, Gompels LL, Wylezinska-Arridge M, Vincent T, Gsell W. Imaging technologies for preclinical models of bone and joint disorders. *EJNMMI Research*. 2011;1(1):11.

[109] Sharir A, Ramniceanu G, Brumfeld V. High Resolution 3D Imaging of Ex-Vivo Biological Samples by Micro CT. *Journal of Visualized Experiments*. 2011;52:e2688.

[110] Saito S, Murase K. Ex vivo imaging of mouse brain using micro-CT with non-ionic iodinated contrast agent: a comparison with myelin staining. *British Journal of Radiology*. 2012;85(1019):e973–e978.

[111] Heindryckx F, Mertens K, Charette N, Vandeghinste B, Casteleyn C, van Steenkiste C, Slaets D, Libbrecht L, Staelens SG, Starkel P, Geerts A, Colle I, van Vlierberghe H. Kinetics of angiogenic changes in a new mouse model for hepatocellular carcinoma. *Molecular cancer*. 2010;9:219.

[112] Trachet B, Swillens A, Van Loo D, Casteleyn C, De Paepe A, Loeys BL, Segers P. The influence of aortic dimensions on calculated wall shear stress in the mouse aortic arch. *Computer Methods in Biomechanics and Biomedical Engineering*. 2009;12(5):491–499.

[113] Suo J, Ferrera DE, Sorescu D, Guldberg RE, Taylor WR, Giddens DP. Hemodynamic shear stresses in mouse aortas: implications for atherogenesis. *Arterioscler Thromb Vasc Biol*. 2007;27:346–351.

[114] Feintuch A, Ruengsakulrach P, Lin A, Zhang J, Zhou YQ, Bishop J, Davidson L, Courtman D, Foster FS, Steinman DA, Henkelman RM, Ethier CR. Hemodynamics in the mouse aortic arch as assessed by MRI, ultrasound and numerical modeling. *Am J Physiol Heart Circ Physiol*. 2007;292(2):H884–92.

[115] Cnudde V, Boone MN. High-resolution X-ray computed tomography in geosciences: a review of the current technology and applications. *Earth Science Reviews*. 2013;pp. 1–48.

[116] Kastner J, Harrer B, Kickinger R, Requena G. Microstructure characterization of high-strength Al-alloys by high resolution X-ray

computed tomography. In: *3DMM - 3D Microstructure Meeting*. Saarbrücken, Germany. 2011; .

[117] Mallard JR, Myers MJ. Performance of a Gamma Camera for Visualization of Radioactive Isotopes in Vivo. *Physics in Medicine and Biology*. 1963;8:165–182.

[118] Gullberg GT, Huesman RH, Malko J, Pelc NJ, Budinger TF. An attenuated projector-backprojector for iterative SPECT reconstruction. *Physics in Medicine and Biology*. 1985;30:799–816.

[119] Chang LT. A method for attenuation correction in radionuclide computed tomography. *IEEE Transactions on Nuclear Science*. 1978;25(1):638–643.

[120] Keereman V, Fierens Y, Vanhove C, Lahoutte T, Vandenberghe S. Magnetic Resonance-Based Attenuation Correction for Micro-Single-Photon Emission Computed Tomography. *Molecular Imaging*. 2011;.

[121] Jaszczak RJ, Greer KL, Floyd CE, Harris CC, Coleman RE. Improved SPECT quantification using compensation for scattered photons. *Journal of Nuclear Medicine*. 1984;25(8):893–900.

[122] Ogawa K, Harata Y, Ichihara T, Kubo A, Hashimoto S. A practical method for position-dependent Compton-scatter correction in single photon emission CT. *IEEE Transactions on Medical Imaging*. 1991;10(3):408–412.

[123] Bowsher JE, Floyd CE. Treatment of Compton scattering in maximum-likelihood, expectation-maximization reconstructions of SPECT images. *Journal of Nuclear Medicine*. 1991;32(6):1285–1291.

[124] King MA, deVries DJ, Pan TS, Pretorius PH, Case JA. An investigation of the filtering of TEW scatter estimates used to compensate for scatter with ordered subset reconstructions. *IEEE Transactions on Nuclear Science*. 1997;44(3):1140–1145.

[125] Smith MF, Jaszczak RJ. The effect of gamma ray penetration on angle-dependent sensitivity for pinhole collimation in nuclear medicine. *Medical Physics*. 1997;24(11):1701–1709.

[126] Shepp LA, Vardi Y. Maximum Likelihood Reconstruction for Emission Tomography. *IEEE Transactions on Medical Imaging*. 1982;1(2):113–122.

[127] Lange K, Carson R. EM reconstruction algorithms for emission and transmission tomography. *Journal of Computer Assisted Tomography*. 1984;8(2):306–316.

[128] Zeng GL, Gullberg GT. A study of reconstruction artifacts in cone beam tomography using filtered backprojection and iterative EM algorithms. *IEEE Transactions on Nuclear Science*. 1990; 37(2):759–767.

[129] Jaszczak RJ, Li J, Wang H, Coleman RE. Three-dimensional SPECT reconstruction of combined cone beam and parallel beam data. *Physics in Medicine and Biology*. 1992;37(3):535–548.

[130] Byrne CL. Block-iterative methods for image reconstruction from projections. *IEEE Transactions on Image Processing*. 1996; 5(5):792–794.

[131] Defrise M. Possible Criteria for Choosing the Number of Iterations in Some Iterative Reconstruction Methods. *Mathematics and Computer Science in Medical Imaging NATO ASI Series*. 1988; 39:293–303.

[132] Green PJ. Bayesian reconstructions from emission tomography data using a modified EM algorithm. *IEEE Transactions on Medical Imaging*. 1990;9(1):84–93.

[133] Geman S, McClure DE. Bayesian image analysis: an application to single photon emission tomography. *Amer Statist Assoc*. 1985; pp. 12–18.

[134] Green PJ. On use of the EM for penalized likelihood estimation. *Journal of the Royal Statistical Society Series B (Methodological)*. 1990;pp. 443–452.

[135] Vanhove C, Defrise M, Bossuyt A, Lahoutte T. Improved quantification in multiple-pinhole SPECT by anatomy-based reconstruction using microCT information. *European Journal of Nuclear Medicine and Molecular Imaging*. 2010;pp. 1–13.

[136] McElroy DP, MacDonald LR, Beekman FJ, Wang Y, Patt BE, Iwanczyk JS, Tsui BMW, Hoffman EJ. Performance evaluation of A-SPECT: a high resolution desktop pinhole SPECT system for imaging small animals. *IEEE Transactions on Nuclear Science*. 2002;49(5):2139–2147.

[137] Liu Z, Kastis GA, Stevenson GD, Barrett HH, Furenlid LR, Kupinski MA, Patton DD, Wilson DW. Quantitative analysis of acute myocardial infarct in rat hearts with ischemia-reperfusion using a high-resolution stationary SPECT system. *Journal of Nuclear Medicine*. 2002;43(7):933–939.

[138] Beekman FJ, van der Have F, Vastenhouw B, van der Linden AJA, van Rijk PP, Burbach JPH, Smidt MP. U-SPECT-I: a novel system for submillimeter-resolution tomography with radiolabeled molecules in mice. *Journal of Nuclear Medicine*. 2005;46(7):1194–1200.

[139] Vunckx K, Suetens P, Nuyts J. Effect of overlapping projections on reconstruction image quality in multipinhole SPECT. *IEEE Transactions on Medical Imaging*. 2008;27(7):972–983.

[140] Mok GSP, Wang Y, Tsui BMW. Quantification of the multiplexing effects in multi-pinhole small animal SPECT: a simulation study. *IEEE Transactions on Nuclear Science*. 2009;56(5):2636–2643.

[141] Deleye S, Holen R, Verhaeghe J, Vandenberghe S, Stroobants S, Staelens SG. Performance evaluation of small-animal multipinhole μSPECT scanners for mouse imaging. *European Journal of Nuclear Medicine and Molecular Imaging*. 2013;40(5):744–758.

[142] Meng LJ, Tan JW, Spartiotis K, Schulman T. Preliminary evaluation of a novel energy-resolved photon-counting gamma ray detector. *Nuclear Instruments and Methods in Physics Research Section A: Accelerators, Spectrometers, Detectors and Associated Equipment*. 2009;604(3):548–554.

[143] Madsen MT. Recent Advances in SPECT Imaging. *Journal of Nuclear Medicine*. 2007;48(4):661–673.

[144] Rahmim A, Zaidi H. PET versus SPECT: strengths, limitations and challenges. *Nuclear medicine communications*. 2008;29(3):193–207.

[145] Frey EC, Humm JL, Ljungberg M. Accuracy and precision of radioactivity quantification in nuclear medicine images. *Seminars in nuclear medicine*. 2012;42(3):208–218.

[146] King MA, Glick SJ, Pretorius PH, Wells RG, Gifford HC, Narayanan MV, Farncombe T. Attenuation, scatter, and spatial resolution compensation in SPECT. In: *Emission Tomography*, edited by Wernick MN, Aarsvold JN. San Diego: Academic Press. 2004;.

[147] Franc BL, Acton PD, Mari C, Hasegawa BH. Small-Animal SPECT and SPECT/CT: Important Tools for Preclinical Investigation. *Journal of Nuclear Medicine*. 2008;49(10):1651–1663.

[148] Hwang AB, Hasegawa BH. Attenuation correction for small animal SPECT imaging using x-ray CT data. *Medical Physics*. 2005; 32:2799.

[149] van der Have F, Vastenhouw B, Ramakers RM, Branderhorst W, Krah JO, Ji C, Staelens SG, Beekman FJ. U-SPECT-II: An Ultra-High-Resolution Device for Molecular Small-Animal Imaging. *Journal of Nuclear Medicine*. 2009;50(4):599–605.

[150] Stevens A. Nuclear Medicine Europe 2012. *Tech. rep.*, Aunt Minnie Europe, London. 2012.

[151] Uematsu T, Yuen S, Yukisawa S, Aramaki T, Morimoto N, Endo M, Furukawa H, Uchida Y, Watanabe J. Comparison of FDG PET and SPECT for detection of bone metastases in breast cancer. *AJR American journal of roentgenology*. 2005;184(4):1266–1273.

[152] Andersson P, Forssell-Aronsson E, Johanson V, Wängberg B, Nilsson O, Fjälling M, Ahlman H. Internalization of Indium-111 into Human Neuroendocrine Tumor Cells after Incubation with Indium-111-DTPA-D-Phe1-Octreotide. *Journal of Nuclear Medicine*. 1996; 37(12):2002–2006.

[153] Arslan N, Ilgan S, Yuksel D, Serdengecti M, Bulakbasi N, Ugur O, Ozguven MA. Comparison of In-111 octreotide and Tc-99m (V) DMSA scintigraphy in the detection of medullary thyroid tumor foci in patients with elevated levels of tumor markers after surgery. *Clin Nucl Med*. 2001;26(8):683–688.

[154] Small GR, Wells RG, Schindler T, Chow BJW, Ruddy TD. Advances in Cardiac SPECT and PET Imaging: Overcoming the Challenges to Reduce Radiation Exposure and Improve Accuracy. *Canadian Journal of Cardiology*. 2013;29(3):275–284.

[155] Petix NR, Sestini S, Coppola A, Marcucci G, Nassi F, Taiti A, Guarnaccia V, Mennuti A, Mazzoni V, Zipoli A. Prognostic Value of Combined Perfusion and Function by Stress Technetium-99m Sestamibi Gated SPECT Myocardial Perfusion Imaging in Patients With Suspected or Known Coronary Artery Disease. *The American Journal of Cardiology*. 2005;95(11):1351–1357.

[156] Vrachimis A, Hermann S, Máthé D, Schober O, Schäfers M. Systematic evaluation of 99mTc-tetrofosmin versus 99mTc-sestamibi to study murine myocardial perfusion in small animal SPECT/CT. *EJNMMI Research*. 2012;2(1):21.

[157] Taillefer R, DePuey EG, Udelson JE, Beller GA, Latour Y, Reeves F. Comparative diagnostic accuracy of Tl-201 and Tc-99m sestamibi SPECT imaging (perfusion and ECG-gated SPECT) in detecting coronary artery disease in women. *Journal of the American College of Cardiology*. 1997;29(1):69–77.

[158] Daly MJ, Jones W, Rudd TG, Tremann J. Differential renal function using technetium-99m dimercaptosuccinic acid (DMSA): in vitro correlation. *Journal of Nuclear Medicine*. 1979;20(1):63–66.

[159] Yen TC, Chen WP, Chang SL, Liu RS, Yeh SH, Lin CY. Technetium-99m-DMSA renal SPECT in diagnosing and monitoring pediatric acute pyelonephritis. *Journal of Nuclear Medicine*. 1996;37(8):1349–1353.

[160] Forrer F, Rolleman E, Bijster M, Melis M, Bernard BF, Krenning EP, de Jong M. From Outside to Inside? Dose-Dependent Renal Tubular Damage After High-Dose Peptide Receptor Radionuclide Therapy in Rats Measured with In Vivo99mTc-DMSA-SPECT and Molecular Imaging. *Cancer Biotherapy & Radiopharmaceuticals*. 2007;22(1):40–49.

[161] Cohen EP, Moulder JE, Robbins ME. Radiation nephropathy caused by yttrium 90. *The Lancet*. 2001;358(9287):1102–1103.

[162] Prandini N, Lazzeri E, Rossi B, Erba P, Parisella MG, Signore A. Nuclear medicine imaging of bone infections. *Nuclear medicine communications*. 2006;27(8):633.

[163] Catafau AM. Brain SPECT in clinical practice. Part I: perfusion. *Journal of Nuclear Medicine*. 2001;42(2):259–271.

[164] Ebmeier KP. Is there still a place for perfusion SPECT in the diagnosis of dementia. *The Open Nuclear Medicine Journal*. 2010; 2:40–45.

[165] Amen DG, Trujillo M, Newberg A, Willeumier K, Tarzwell R, Wu JC, Chaitin B. Brain SPECT Imaging in Complex Psychiatric Cases: An Evidence-Based, Underutilized Tool. *The open neuroimaging journal*. 2011;5:40–48.

[166] Bailey DL, Willowson KP. An Evidence-Based Review of Quantitative SPECT Imaging and Potential Clinical Applications. *Journal of Nuclear Medicine*. 2013;54(1):83–89.

[167] Mariani G, Bruselli L, Kuwert T, Kim EE, Flotats A, Israel O, Dondi M, Watanabe N. A review on the clinical uses of SPECT/CT. *European Journal of Nuclear Medicine and Molecular Imaging*. 2010;37(10):1959–1985.

[168] Tharp K, Israel O, Hausmann J, Bettman L, Martin WH, Daitzchman M, Sandler MP, Delbeke D. Impact of 131I-SPECT/CT images obtained with an integrated system in the follow-up of patients with thyroid carcinoma. *European Journal of Nuclear Medicine and Molecular Imaging*. 2004;31(10).

[169] Da Silva AJ, Tang HR, Wong KH, Wu MC, Dae MW, Hasegawa BH. Absolute quantification of regional myocardial uptake of 99mTc-sestamibi with SPECT: experimental validation in a porcine model. *Journal of Nuclear Medicine*. 2001;42(5):772–779.

[170] Israel O, Front D, Hardoff R, Ish-Shalom S, Jerushalmi J, Kolodny GM. In vivo SPECT quantitation of bone metabolism in hyperparathyroidism and thyrotoxicosis. *Journal of Nuclear Medicine*. 1991;32(6):1157–1161.

[171] Khalil MM, Tremoleda JL, Bayomy TB, Gsell W. Molecular SPECT Imaging: An Overview. *International Journal of Molecular Imaging*. 2011;2011:1–15.

[172] Vanhove C, Lahoutte T, Defrise M, Bossuyt A, Franken PR. Reproducibility of left ventricular volume and ejection fraction measurements in rat using pinhole gated SPECT. *European Journal of Nuclear Medicine and Molecular Imaging*. 2004;32(2):211–220.

[173] Constantinesco A, Choquet P, Monassier L, Israel-Jost V, Mertz L. Assessment of left ventricular perfusion, volumes, and motion in mice using pinhole gated SPECT. *Journal of Nuclear Medicine*. 2005;46(6):1005–1011.

[174] Kolodgie FD, Petrov A, Virmani R, Narula N, Verjans JW, Weber DK, Hartung D, Steinmetz N, Vanderheyden JL, Vannan MA, Gold HK, Reutelingsperger CPM, Hofstra L, Narula J. Targeting of Apoptotic Macrophages and Experimental Atheroma With Radiolabeled Annexin V: A Technique With Potential for Noninvasive Imaging of Vulnerable Plaque. *Circulation*. 2003;108(25):3134–3139.

[175] Zhou R, Thomas DH, Qiao H, Bal HS, Choi SR, Alavi A, Ferrari VA, Kung HF, Acton PD. In vivo detection of stem cells grafted in infarcted rat myocardium. *Journal of Nuclear Medicine*. 2005; 46(5):816–822.

[176] Ponsky LE, Cherullo EE, Starkey R, Nelson D, Neumann D, Zippe CD. Evaluation of preoperative ProstaScint^{TM} scans in the prediction of nodal disease. *Prostate Cancer Prostatic Diseases*. 2002; 5(2):132–135.

[177] Nikolaus S, Antke C, Kley K, Beu M, Wirrwar A, Muller HW. Pretreatment with Haloperidol Reduces 123I-FP-CIT Binding to the Dopamine Transporter in the Rat Striatum: An In Vivo Imaging Study with a Dedicated Small-Animal SPECT Camera. *Journal of Nuclear Medicine*. 2009;50(7):1147–1152.

[178] Acton PD, Hou C, Kung MP, Plössl K, Keeney CL, Kung HF. Occupancy of dopamine D 2 receptors in the mouse brain measured using ultra-high-resolution single-photon emission tomography and [123 I]IBF. *European Journal of Nuclear Medicine and Molecular Imaging*. 2002;29(11):1507–1515.

[179] Garea-Rodríguez E, Schlumbohm C, Czéh B, König J, Helms G, Heckmann C, Meller B, Meller J, Fuchs E. Visualizing dopamine

transporter integrity with iodine-123-FP-CIT SPECT in combination with high resolution MRI in the brain of the common marmoset monkey. *Journal of Neuroscience Methods*. 2012;pp. 1–25.

[180] Vanderheyden JL. The use of imaging in preclinical drug development. *The Quarterly journal of nuclear medicine and molecular imaging*. 2009;53(4):374–381.

[181] Schimmel K, Bennink R, de Bruin K, Leen R, Sand K, van den Hoff M, van Kuilenburg A, Vanderheyden JL, Steinmetz N, Pfaffendorf M, Verschuur A, Guchelaar HJ. Absence of cardiotoxicity of the experimental cytotoxic drug cyclopentenyl cytosine (CPEC) in rats. *Archives of Toxicology*. 2005;79(5):268–276.

[182] van Montfrans C, Bennink RJ, de Bruin K, de Jonge W, Verberne HJ, Ten Kate FJW, van Deventer SJH, Te Velde AA. In vivo evaluation of 111In-labeled T-lymphocyte homing in experimental colitis. *Journal of Nuclear Medicine*. 2004;45(10):1759–1765.

[183] Hricak H, Choi BI, Scott AM, Sugimura K, Muellner A, von Schulthess GK, Reiser MF, Graham MM, Dunnick NR, Larson SM. Global trends in hybrid imaging. *Radiology*. 2010;257(2):498–506.

[184] Bocher M, Balan A, Krausz Y, Shrem Y, Lonn A, Wilk M, Chisin R. Gamma camera-mounted anatomical X-ray tomography: technology, system characteristics and first images. *European Journal of Nuclear Medicine*. 2000;27(6):619–627.

[185] Kinahan PE, Townsend DW, Beyer T, Sashin D. Attenuation correction for a combined 3D PET/CT scanner. *Medical Physics*. 1998;25(10):2046–2053.

[186] Judenhofer MS, Catana C, Swann BK, Siegel SB, Jung WI, Nutt RE, Cherry SR, Claussen CD, Pichler BJ. PET/MR Images Acquired with a Compact MR-compatible PET Detector in a 7-T Magnet. *Radiology*. 2007;244(3):807–814.

[187] Schulz V, Weissler B, Gebhardt P, Solf T, Lerche CW, Fischer P, Ritzert M, Mlotok V, Piemonte C, Goldschmidt B, Vandenberghe S, Salomon A, Schaeffter T, Marsden PK. SiPM based preclinical PET/MR insert for a human 3T MR: first imaging experiments. *IEEE Nuclear Science Symposium Conference Record*. 2011;pp. 4467–4469.

[188] Tsui BMW, Xu J, Rittenbach A, Chen S, El-Sharkaway AM, Edelstein WA, Guo X, Liu A, Hugg JW. High performance SPECT system for simultaneous SPECT-MR imaging of small animals. *IEEE Nuclear Science Symposium Conference Record*. 2011;pp. 3178–3182.

[189] O'Connor MK, Kemp BJ. Single-Photon Emission Computed Tomography/Computed Tomography: Basic Instrumentation and Innovations. *Seminars in nuclear medicine*. 2006;36(4):258–266.

[190] Visvikis D, Ell PJ. Impact of technology on the utilisation of positron emission tomography in lymphoma: current and future perspectives. *European Journal of Nuclear Medicine and Molecular Imaging*. 2003;30(S1):S106–S116.

[191] Pérault C, Schvartz C, Wampach H, Liehn JC, Delisle MJ. Thoracic and abdominal SPECT-CT image fusion without external markers in endocrine carcinomas. *Journal of Nuclear Medicine*. 1997;38(8):1234–1242.

[192] Hutton BF, Braun M. Software for image registration: Algorithms, accuracy, efficacy. *Seminars in nuclear medicine*. 2003;33(3):180–192.

[193] Blankespoor SC, Wu X, Kalki K, Brown JK, Cann CE, Hasegawa BH. Attenuation correction of SPECT using X-ray CT on an emission-transmission CT system: Myocardial perfusion assessment. In: *Nuclear Science Symposium and Medical Imaging Conference Record, 1995., 1995 IEEE*. 1995; pp. 1126–1130.

[194] Hasegawa BH, Reilly SM, Gingold EL, Cann CE. Design considerations for a simultaneous emission-transmission CT scanner. *Radiology*. 1989;173(P):414.

[195] Hasegawa BH, Gingold EL, Reilly SM, Liew SC, Cann CE. Description of a simultaneous emission-transmission CT system. In: *SPIE Proceedings*. 1990; pp. 50–60.

[196] Hasegawa BH, Zaidi H. Dual-modality imaging: more than the sum of its components. In: *Quantitative analysis in nuclear medicine imaging*, edited by Zaidi H, pp. 35–81. Springer. 2006; .

[197] Buck AK, Nekolla S, Ziegler S, Beer A, Krause BJ, Herrmann K, Scheidhauer K, Wester HJ, Rummeny EJ, Schwaiger M, Drzezga A. SPECT/CT. *Journal of Nuclear Medicine*. 2008;49(8):1305–1319.

[198] Brown S, Bailey DL, Willowson KP, Baldock C. Investigation of the relationship between linear attenuation coefficients and CT Hounsfield units using radionuclides for SPECT. *Applied Radiation and Isotopes*. 2008;66(9):1206–1212.

[199] Wang H, Fu HL, Li JN, Zou RJ, Gu ZH, Wu JC. The role of single-photon emission computed tomography/computed tomography for precise localization of metastases in patients with differentiated thyroid cancer. *Journal of Clinical Imaging*. 2009;33(1):49–54.

[200] Wong KK, Zarzhevsky N, Cahill JM, Frey KA, Avram AM. Incremental Value of Diagnostic 131I SPECT/CT Fusion Imaging in the Evaluation of Differentiated Thyroid Carcinoma. *American Journal of Roentgenology*. 2008;191(6):1785–1794.

[201] Chowdhury FU, Scarsbrook AF. The role of hybrid SPECT-CT in oncology: current and emerging clinical applications. *Clinical Radiology*. 2008;63(3):241–251.

[202] Even-Sapir E, Keidar Z, Sachs J, Engel A, Bettman L, Gaitini D, Guralnik L, Werbin N, Iosilevsky G, Israel O. The new technology of combined transmission and emission tomography in evaluation of endocrine neoplasms. *Journal of Nuclear Medicine*. 2001; 42(7):998–1004.

[203] Özer S, Dobrozemsky G, Kienast O, Beheshti M, Becherer A, Niederle B, Kainberger F, Dudczak R, Kurtaran A. Value of combined XCT/SPECT technology for avoiding false positive planar 123I-MIBG scintigraphy. *Nuklearmedizin*. 2004;43(5):164–170.

[204] Clouse WD, Hallett JW Jr, Schaff HV, Gayari MM, Ilstrup DM, Melton LJ III. Improved prognosis of thoracic aortic aneurysms. *JAMA: the journal of the American Medical Association*. 1998; 280(22):1926–1929.

[205] Sawchuk AP, Unthank JL, Davis TE, Dalsing MC. A prospective, in vivo study of the relationship between blood flow hemodynamics and atherosclerosis in a hyperlipidemic swine model. *Journal of Vascular Surgery*. 1994;19(1):58–63– discussion 63–4.

[206] Nerem RM. Vascular fluid mechanics, the arterial wall, and atherosclerosis. *Journal of Biomechanical Engineering*. 1992; 114:274–282.

[207] Boussel L, Rayz V, McCulloch C, Martin A, Acevedo-Bolton G, Lawton M, Higashida R, Smith WS, Young WL, Saloner D. Aneurysm Growth Occurs at Region of Low Wall Shear Stress: Patient-Specific Correlation of Hemodynamics and Growth in a Longitudinal Study. *Stroke*. 2008;39(11):2997–3002.

[208] Trachet B, Renard M, Santis G, Staelens SG, Backer J, Antiga L, Loeys BL, Segers P. An Integrated Framework to Quantitatively Link Mouse-Specific Hemodynamics to Aneurysm Formation in Angiotensin II-infused ApoE -/- mice. *Annals of Biomedical Engineering*. 2011;39(9):2430–2444.

[209] Daugherty A, Manning MW, Cassis LA. Angiotensin II promotes atherosclerotic lesions and aneurysms in apolipoprotein E-deficient mice. *The Journal of clinical investigation*. 2000;105(11):1605–1612.

[210] Morimoto M, Miyamoto S, Mizoguchi A, Kume N, Kita T, Hashimoto N. Mouse Model of Cerebral Aneurysm: Experimental Induction by Renal Hypertension and Local Hemodynamic Changes. *Stroke*. 2002;33(7):1911–1915.

[211] Daugherty A. Mouse models of atherosclerosis. *The American journal of the medical sciences*. 2002;323(1):3–10.

[212] Reardon CA, Getz GS. Mouse models of atherosclerosis. *Current opinion in lipidology*. 2001;12(2):167–173.

[213] Choudhury RP, Aguinaldo JG, Rong JX, Kulak JL, Kulak AR, Reis ED, Fallon JT, Fuster V, Fisher EA, Fayad ZA. Atherosclerotic lesions in genetically modified mice quantified in vivo by non-invasive high-resolution magnetic resonance microscopy. *Atherosclerosis*. 2002;162(2):315–321.

[214] Korshunov VA, Berk BC. Flow-Induced Vascular Remodeling in the Mouse: A Model for Carotid Intima-Media Thickening. *Arteriosclerosis, Thrombosis, and Vascular Biology*. 2003;23(12):2185–2191.

[215] Couffinhal T, Silver M, Zheng LP, Kearney M, Witzenbichler B, Isner JM. Mouse model of angiogenesis. *The American Journal of Pathology*. 1998;152(6):1667.

[216] Lindsay ME, Schepers D, Bolar NA, Doyle JJ, Gallo E, Fert-Bober J, Kempers MJE, Fishman EK, Chen Y, Myers L, Bjeda D, Oswald G, Elias AF, Levy HP, Anderlid BM, Yang MH, Bongers EMHF, Timmermans J, Braverman AC, Canham N, Mortier GR, Brunner HG, Byers PH, Van Eyk J, Van Laer L, Dietz HC, Loeys BL. Loss-of-function mutations in TGFB2 cause a syndromic presentation of thoracic aortic aneurysm. *Nature Publishing Group*. 2012; 44(8):922–927.

[217] Lima BL, Santos EJC, Fernandes GR, Merkel C, Mello MRB, Gomes JPA, Soukoyan M, Kerkis A, Massironi SMG, Visintin JA, Pereira LV. A New Mouse Model for Marfan Syndrome Presents Phenotypic Variability Associated with the Genetic Background and Overall Levels of Fbn1 Expression. *PLoS ONE*. 2010; 5(11):e14136.

[218] Loeys BL, Schwarze U, Holm T, Callewaert BL, Thomas GH, Pannu H, De Backer JF, Oswald GL, Symoens S, Manouvrier S, Roberts AE, Faravelli F, Greco MA, Pyeritz RE, Milewicz DM, Coucke PJ, Cameron DE, Braverman AC, Byers PH, De Paepe AM, Dietz HC. Aneurysm syndromes caused by mutations in the TGF-beta receptor. *The New England journal of medicine*. 2006; 355(8):788–798.

[219] Habashi JP, Judge DP, Holm TM, Cohn RD, Loeys BL, Cooper TK, Myers L, Klein EC, Liu G, Calvi C, Podowski M, Neptune ER, Halushka MK, Bedja D, Gabrielson K, Rifkin DB, Carta L, Ramirez F, Huso DL, Dietz HC. Losartan, an AT1 antagonist, prevents aortic aneurysm in a mouse model of Marfan syndrome. *Science (New York, NY)*. 2006;312(5770):117–121.

[220] Dietz HC, Loeys BL, Carta L, Ramirez F. Recent progress towards a molecular understanding of Marfan syndrome. *American Journal of Medical Genetics Part C: Seminars in Medical Genetics*. 2005; 139C(1):4–9.

[221] Gannon BJ. Vascular Casting. In: *Principles and techniques of scanning electron microscopy: Biological applications*, edited by Hayat MA, pp. 170–193. Cambridge University Press. 1978;.

[222] Willmann JK, van Bruggen N, Dinkelborg LM, Gambhir SS. Molecular imaging in drug development. *Nature Reviews Drug Discovery*. 2008;7(7):591–607.

[223] Willekens I, Lahoutte T, Buls N, Vanhove C, Deklerck R, Bossuyt A, de Mey J. Time-Course of Contrast Enhancement in Spleen and Liver with Exia 160, Fenestra LC, and VC. *Molecular Imaging and Biology*. 2008;11(2):128–135.

[224] Marchant S. Fenestra VC User Guide with MicroCat II Imaging Hardware. *Tech. rep.* 2008.

[225] Rose A. The sensitivity performance of the human eye on an absolute scale. *Journal of the Optical Society of America*. 1948; 38(2):196–208.

[226] Burgess AE. The Rose model, revisited. *Journal of the Optical Society of America A, Optics, image science, and vision*. 1999; 16(3):633–646.

[227] Badea CT, Hedlund LW, Johnson GA. Micro-CT with respiratory and cardiac gating. *Medical Physics*. 2004;.

[228] Ford NL, Wheatley AR, Holdsworth DW, Drangova M. Optimization of a retrospective technique for respiratory-gated high speed micro-CT of free-breathing rodents. *Physics in Medicine and Biology*. 2007;52(19):5749–5769.

[229] Drangova M, Ford NL, Detombe SA, Wheatley AR, Holdsworth DW. Fast retrospectively gated quantitative four-dimensional (4D) cardiac micro computed tomography imaging of free-breathing mice. *Investigative radiology*. 2007;42(2):85–94.

[230] Sawall S, Bergner F, Lapp R, Mronz M, Karolczak M, Hess A, Kachelrieß M. Low-dose cardio-respiratory phase-correlated cone-beam micro-CT of small animals. *Medical Physics*. 2011; 38(3):1416–1424.

[231] Ford NL, Nikolov HN, Norley CJD, Thornton MM, Foster PJ, Drangova M, Holdsworth DW. Prospective respiratory-gated micro-CT of free breathing rodents. *Medical Physics*. 2005;32:2888–2898.

[232] Horn BKP. Density reconstruction using arbitrary ray-sampling schemes. *Proceedings of the IEEE*. 1978;66(5):551–562.

[233] Horn BKP. Fan-beam reconstruction methods. *Proceedings of the IEEE*. 1979;67(12):1616–1623.

[234] Batson OV. Corrosion specimens prepared with a new material. *Anat Rec*. 1955;p. 425.

[235] Hodde KC, Miodonski A, Bakker C, Veltman WAM. Scanning electron microsopy of microcorrosion casts with special attention on the arterio-venous differences and application to the rat's cochlea. *Scan Electron Microsc*. 1977;2:477–484.

[236] Schambach SJ, Bag S, Groden C, Schilling L, Brockmann MA. Vascular imaging in small rodents using micro-CT. *Methods*. 2010; 50(1):26–35.

[237] Kratky RG, Roach MR. Shrinkage of Batson's and its relevance to vascular casting. *Atherosclerosis*. 1984;51:339–341.

[238] Casteleyn C, Trachet B, Van Loo D, Devos DGH, Van Den Broeck W, Simoens P, Cornillie P. Validation of the murine aortic arch as a model to study human vascular diseases. *Journal of Vascular Research*. 2009;.

[239] Moore JA, Rutt BK, Karlik SJ, Yin K, Ethier CR. Computational blood flow modelling based on in vivo measurements. *Annals of Biomedical Engineering*. 1999;27:627–640.

[240] Carlson SK, Classic KL, Hadac EM, Bender CE, Kemp BJ, Lowe VJ, Hoskin TL, Russell SJ. In Vivo Quantitation of Intratumoral Radioisotope Uptake Using Micro-Single Photon Emission Computed Tomography/Computed Tomography. *Molecular Imaging and Biology*. 2006;8(6):324–332.

[241] Grudzenski S, Kuefner MA, Heckmann MB, Uder M, Löbrich M. Contrast Medium–enhanced Radiation Damage Caused by CT Examinations 1. *Radiology*. 2009;253(3):706–714.

[242] Laforest R, Waterson C, Broski SM, Lewis J. Radiation Dose Considerations in Tumor Growth Monitoring with CT. In: *3rd Annual Society of Molecular Imaging Conference Record*. 2004; p. 434.

[243] Hodde KC. Cephalic vascular patterns in the rat: A scanning electron microsopy (SEM) study of casts. Ph.D. thesis, Rodopi, Amsterdam. 1981.

[244] Klinck RJ, Campbell GM, Boyd SK. Radiation effects on bone architecture in mice and rats resulting from in vivo micro-computed tomography scanning. *Medical Engineering & Physics*. 2008; 30(7):888–895.

[245] Adams AJ, Cowey SL, Kappes JC, Hardy RW, Zinn KR. bioluminescence imaging confirms that weekly computed tomography studies do not change tumor growth in an animal model of breast cancer metastasis. In: *Scientific Abstracts of the 2006 Annual Conference of the AMI*. 2006; p. 124.

[246] Carlson SK, Classic KL, Bender CE, Russell SJ. Small Animal Absorbed Radiation Dose from Serial Micro-Computed Tomography Imaging. *Molecular Imaging and Biology*. 2007;9(2):78–82.

[247] Badea CT, Drangova M, Holdsworth DW, Johnson GA. In vivo small-animal imaging using micro-CT and digital subtraction angiography. *Physics in Medicine and Biology*. 2008;53(19):R319–R350.

[248] Sidky EY, Kao CM, Pan X. Accurate image reconstruction from few-views and limited-angle data in divergent-beam CT. *Journal of X-Ray Science and Technology*. 2006;14(2):119–139.

[249] Candès EJ, Romberg JK, Tao T. Robust uncertainty principles: Exact signal reconstruction from highly incomplete frequency information. *IEEE Transactions on Information Theory*. 2006; 52(2):489–509.

[250] Candès EJ, Wakin M. People hearing without listening: An introduction to compressive sampling. *IEEE Signal Processing Magazine*. 2008;25(2):21–30.

[251] Candès EJ, Romberg JK, Tao T. Stable signal recovery from incomplete and inaccurate measurements. *Communications on Pure and Applied Mathematics*. 2006;59(8):1207–1223.

[252] Herman GT, Davidi R. On Image Reconstruction from a Small Number of Projections. *Inverse Problems*. 2008;24(4):45011–45028.

[253] Chen GH, Tang J, Leng S. Prior image constrained compressed sensing (PICCS): a method to accurately reconstruct dynamic CT images from highly undersampled projection data sets. *Medical Physics*. 2008;35(2):660–663.

[254] Sidky EY, Pan X. Image reconstruction in circular cone-beam computed tomography by constrained, total-variation minimization. *Physics in Medicine and Biology*. 2008;53(17):4777–4807.

[255] Sidky EY, Pan X, Reiser IS, Nishikawa RM, Moore RH, Kopans DB. Enhanced imaging of microcalcifications in digital breast tomosynthesis through improved image-reconstruction algorithms. *Medical Physics*. 2009;36:4920.

[256] Han X, Bian J, Ritman EL, Sidky EY, Pan X. Optimization-based reconstruction of sparse images from few-view projections. *Physics in Medicine and Biology*. 2012;57(16):5245–5273.

[257] Sidky EY, Jørgensen JH, Pan X. Convex optimization problem prototyping for image reconstruction in computed tomography with the Chambolle–Pock algorithm. *Physics in Medicine and Biology*. 2012;57(10):3065–3091.

[258] Pan X, Sidky EY, Vannier MW. Why do commercial CT scanners still employ traditional, filtered back-projection for image reconstruction? *Inverse Problems*. 2009;25(12):123009.

[259] Han X, Bian J, Eaker DR, Kline TL, Sidky EY, Ritman EL, Pan X. Algorithm-Enabled Low-Dose Micro-CT Imaging. *IEEE Transactions on Medical Imaging*. 2011;30(3):606–620.

[260] Oliveira JP, Bioucas-Dias JM, Figueiredo MAT. Adaptative Total Variation Image Deblurring: A Majorization-Minimization Approach. *Signal Process*. 2009;89:1683–1693.

[261] Beck A, Teboulle M. Fast gradient-based algorithms for constrained total variation image denoising and deblurring problems. *IEEE Transactions on Image Processing*. 2009;18(11):2419–2434.

[262] Herman GT, Levkowitz H, Tuy HK, McCormick S. Multilevel Image Reconstruction. In: *Multiresoluion Image Processing and Analysis*, edited by Rosenfeld A, pp. 121–135. Berlin, Heidelberg: Springer Berlin Heidelberg. 1984;.

[263] Lange K. Convergence of EM image reconstruction algorithms with Gibbs smoothing. *IEEE Transactions on Medical Imaging*. 1990; 9(4):439–446.

[264] Defrise M, Vanhove C, Liu X. Iterative reconstruction in micro-CT. *International CT meeting*. 2010;pp. 1–4.

[265] Persson M, Bone D, Elmqvist H. Three-dimensional total variation norm for SPECT reconstruction. *Nuclear Inst and Methods in Physics Research, A*. 2001;471(1):98–102.

[266] Vanhove C, Andreyev A, Defrise M, Nuyts J, Bossuyt A. Resolution recovery in pinhole SPECT based on multi-ray projections: a phantom study. *European Journal of Nuclear Medicine and Molecular Imaging*. 2007;34(2):170–180.

[267] Kontaxakis G, Strauss LG, Van Kaick G. Optimized image reconstruction for emission tomography using ordered subsets, median root prior and a Web-based interface. In: *Nuclear Science Symposium, 1998. Conference Record. 1998 IEEE*. 1998; pp. 1347–1352.

[268] Johnson LC, Johnson RW, Munoz SA, Mundy GR, Peterson TE, Sterling JA. Longitudinal live animal micro-CT allows for quantitative analysis of tumor-induced bone destruction. *Bone*. 2011; 48(1):141–151.

[269] Campbell GM, Ominsky MS, Boyd SK. Bone quality is partially recovered after the discontinuation of RANKL administration in rats by increased bone mass on existing trabeculae: an in vivo micro-CT study. *Osteoporosis International*. 2010;22(3):931–942.

[270] Rudin LI, Osher S, Fatemi E. Nonlinear total variation based noise removal algorithms. *Physica D*. 1992;60(1-4):259–268.

[271] Chambolle A, Lions P. Image recovery via total variation minimization and related problems. *Numerische Mathematik*. 1997; 76(2):167–188.

[272] Caselles V. Total variation based image denoising and restoration. In: *Proceedings of the International Congress of Mathematicians*. Madrid, Spain. 2006; pp. 1453–1472.

[273] Chambolle A. An algorithm for total variation minimization and applications. *Journal of Mathematical Imaging and Vision*. 2004; 20(1):89–97.

[274] Burger M, Osher S. A guide to the TV zoo. *Level Set and PDE Based Reconstruction Methods in ....* 2013;.

[275] Almansa A, Caselles V, Haro G, Rougé B. Restoration and zoom of irregularly sampled, blurred, and noisy images by accurate total variation minimization with local constraints. *Multiscale Modeling and Simulation.* 2006;5(1):235–272.

[276] Blomgren P, Chan TF. Color TV: total variation methods for restoration of vector-valued images. *IEEE Transactions on Image Processing.* 1998;7(3):304–309.

[277] Ballester C, Caselles V, Igual L, Verdera J, Rougé B. A Variational Model for P+XS Image Fusion. *International Journal of Computer Vision.* 2006;69(1):43–58.

[278] Weickert J, Schnörr C. A theoretical framework for convex regularizers in PDE-based computation of image motion. *International Journal of Computer Vision.* 2001;45(3):245–264.

[279] Chan TF, Shen J. Mathematical models for local nontexture inpaintings. *SIAM Journal on Applied Mathematics.* 2002; 62(3):1019–1043.

[280] Yin W, Goldfarb D, Osher S. Total variation based image cartoon-texture decomposition. *SIAM Journal on Multiscale Modeling and Simulation.* 2005;.

[281] Meyer Y. *Oscillating patterns in image processing and nonlinear evolution equations.* Univ. Lecture Ser. 22. American Mathematical Soc. 2001.

[282] Shepp LA, Logan BF. Reconstructing Interior Head Tissue from X-Ray Transmissions. *IEEE Transactions on Nuclear Science.* 1974; 21(1):228–236.

[283] Garduño E, Herman GT, Davidi R. Reconstruction from a Few Projections by L1-Minimization of the Haar Transform. *Inverse Problems.* 2011;27(5):055006.

[284] Bond J, Frush D, Samei E, Segars WP. Simulation of anatomical texture in voxelized XCAT phantoms. *SPIE Medical Imaging Symposium.* 2013;.

[285] Tang J, Nett BE, Chen GH. Performance comparison between total variation (TV)-based compressed sensing and statistical iterative reconstruction algorithms. *Physics in Medicine and Biology*. 2009; 54(19):5781–5804.

[286] Song J, Liu QH, Johnson GA, Badea CT. Sparseness prior based iterative image reconstruction for retrospectively gated cardiac micro-CT. *Medical Physics*. 2007;34(11):4476–4483.

[287] Lustig M, Donoho DL, Pauly JM. Sparse MRI: The application of compressed sensing for rapid MR imaging. *Magnetic Resonance in Medicine*. 2007;58(6):1182–1195.

[288] Jung H, Sung K, Nayak KS, Kim EY, Ye JC. k-t FOCUSS: A general compressed sensing framework for high resolution dynamic MRI. *Magnetic Resonance in Medicine*. 2009;61(1):103–116.

[289] Segars WP, Sturgeon G, Mendonca S, Grimes J, Tsui BMW. 4D XCAT phantom for multimodality imaging research. *Medical Physics*. 2010;37(9):4902.

[290] Carasso AS. Singular integrals, image smoothness, and the recovery of texture in image deblurring. *SIAM Journal on Applied Mathematics*. 2004;pp. 1749–1774.

[291] Gousseau Y, Morel JM. Are natural images of bounded variation? *Siam Journal on Mathematical Analysis*. 2001;33(3):634–648.

[292] Buades A, Coll B, Morel JM. The staircasing effect in neighborhood filters and its solution. *IEEE Transactions on Image Processing*. 2006;15(6):1499–1505.

[293] Andreu F, Ballester C, Caselles V, Mazon JM. Minimizing total variation flow. *Differential and Integral Equations*. 2001;14(3):321–360.

[294] Andreu F, Caselles V, Diaz JI, Mazon JM. Some qualitative properties for the total variation flow. *Journal of Functional Analysis*. 2002;188(2):516–547.

[295] Steidl G, Weickert J, Brox T, Mrázek P, Welk M. On the equivalence of soft wavelet shrinkage, total variation diffusion, total variation regularization, and SIDEs. *SIAM Journal on Numerical Analysis*. 2005;42(2):686–713.

[296] Selesnick IW, Baraniuk RG, Kingsbury NG. The dual-tree complex wavelet transform. *IEEE Signal Processing Magazine*. 2005; 22(6):123–151.

[297] Candès EJ. Ridgelets: theory and applications. Ph.D. thesis, Stanford University. 1998.

[298] Do MN, Vetterli M. The finite ridgelet transform for image representation. *IEEE Transactions on Image Processing*. 2003;12(1):16–28.

[299] Candès EJ, Demanet L, Donoho DL, Ying L. Fast discrete curvelet transforms. *Multiscale Modeling and Simulation*. 2006;5(3):861–899.

[300] Starck JL, Candès EJ, Donoho DL. The curvelet transform for image denoising. *IEEE Transactions on Image Processing*. 2002; 11(6):670–684.

[301] Guo K, Labate D. Optimally sparse multidimensional representation using shearlets. *Siam Journal on Mathematical Analysis*. 2007;39(1):298–318.

[302] Guo K, Labate D, Lim WQ. Edge analysis and identification using the continuous shearlet transform. *Applied and Computational Harmonic Analysis*. 2009;27(1):24–46.

[303] Bochud F, Abbey CK, Eckstein M. Statistical texture synthesis of mammographic images with clustered lumpy backgrounds. *Optics Express*. 1999;4(1):33–43.

[304] Goossens B. Multiresolution image models and estimation techniques. Ph.D. thesis, Ghent University, Ghent. 2010.

[305] Easley GR, Labate D, Lim WQ. Sparse directional image representations using the discrete shearlet transform. *Applied and Computational Harmonic Analysis*. 2008;25(1):25–46.

[306] Kingsbury N. Complex wavelets for shift invariant analysis and filtering of signals. *Journal of Applied and Computational Harmonic Analysis*. 2001;10(3):234–253.

[307] Easley GR, Labate D, Colonna F. Shearlet-Based Total Variation Diffusion for Denoising. *IEEE Transactions on Image Processing*. 2009;18(2):260–268.

[308] Tadmor E, Nezzar S, Vese L. A Multiscale Image Representation Using Hierarchical (BV, L2) Decompositions. *Multiscale Modeling and Simulation*. 2004;2(4):554–579.

[309] Candès EJ, Donoho DL. Recovering edges in ill-posed inverse problems: Optimality of curvelet frames. *Annals of statistics*. 2002;pp. 784–842.

[310] Feng B, Kunis S, Potts D. On the computation of the polar FFT. *Applied and Computational Harmonic Analysis*. 2007;22(2):257–263.

[311] Aelterman J, Luong HQ, Goossens B, Pizurica A, Philips W. Augmented Lagrangian based reconstruction of non-uniformly sub-Nyquist sampled MRI data. *Signal Processing*. 2011;91(12):2731–2742.

[312] Vandeghinste B, Goossens B, Van Holen R, Vanhove C, Pizurica A, Vandenberghe S, Staelens SG. Iterative CT reconstruction using shearlet-based regularization. In: *Proc. of SPIE*. San Diego, CA. 2012; pp. 1–7.

[313] Colonna F, Easley GR, Guo K, Labate D. Radon transform inversion using the shearlet representation. *Applied and Computational Harmonic Analysis*. 2010;29(2):232–250.

[314] Tai XC, Wu C. Augmented Lagrangian method, dual methods and split Bregman iteration for ROF model. *Scale Space and Variational Methods in Computer Vision*. 2009;pp. 502–513.

[315] Goldstein T, Osher S. The split Bregman method for L1 regularized problems. *SIAM Journal on Imaging Sciences*. 2009;2(2):323–343.

[316] Gilbert P. Iterative methods for the three-dimensional reconstruction of an object from projections. *Journal of Theoretical Biology*. 1972;36(1):105–117.

[317] Herman GT, Lent A. Iterative reconstruction algorithms. *Computers in Biology and Medicine*. 1976;6(4):273–294.

[318] Wunderlich A, Noo F. Image covariance and lesion detectability in direct fan-beam x-ray computed tomography. *Physics in Medicine and Biology*. 2008;53(10):2471–2493.

[319] Sauer KD, Bouman CA. A local update strategy for iterative reconstruction from projections. *IEEE Transactions on Signal Processing*. 1993;41(2):534–548.

[320] Wang J, Chai A, Xing L. Noise correlation in CBCT projection data and its application for noise reduction in low-dose CBCT. *Proceedings of the SPIE*. 2009;7258:72582D1–8.

[321] Yu H, Wang G. A soft-threshold filtering approach for reconstruction from a limited number of projections. *Physics in Medicine and Biology*. 2010;55:3905–3916.

[322] Yu H, Wang G. Compressed sensing based interior tomography. *Physics in Medicine and Biology*. 2009;54(9):2791–2805.

[323] Nowak RD, Figueiredo MAT. Fast wavelet-based image deconvolution using the EM algorithm. In: *Proceedings of the 35th Asilomar Conference on Signals, Systems, and Computers*. Monterey, CA: IEEE. 2001; pp. 371–375.

[324] Daubechies I, Defrise M, De Mol C. An iterative thresholding algorithm for linear inverse problems with a sparsity constraint. *Communications on Pure and Applied Mathematics*. 2004;57(11):1413–1457.

[325] Pizurica A, Aelterman J, Bai F, Vanloocke S, Quang Luong H, Goossens B, Philips W. On structured sparsity and selected applications in tomographic imaging. *Proc of SPIE Conference Wavelets and Sparsity XIV*. 2011;p. 81381D.

[326] Wang Y, Yin W, Zhang Y. A fast algorithm for image deblurring with total variation regularization. *CAAM Technical Reports*. 2007; .

[327] Labate D, Lim WQ, Kutyniok G, Weiss G. Sparse multidimensional representation using shearlets. *Proceedings of the SPIE*. 2005;.

[328] Kutyniok G, Labate D. Resolution of the Wavefront Set Using Continuous Shearlets. *Transactions of the American Mathematical Society*. 2009;361(5):2719–2754.

[329] Yi S, Labate D, Easley GR, Krim H. A Shearlet Approach to Edge Analysis and Detection. *IEEE Transactions on Image Processing*. 2009;18(5):929–941.

[330] Goossens B, Aelterman J, Luong HQ, Pizurica A, Philips W. Efficient design of a low redundant discrete shearlet transform. *Proc of the 2009 Int Workshop on Local and Non-Local approximation in Image Processing*. 2009;pp. 112–124.

[331] Goossens B, Aelterman J, Luong HQ, Pizurica A, Philips W. Design of a Tight Frame of 2D Shearlets Based on a Fast Non-iterative Analysis and Synthesis Algorithm. In: *IEEE Optics & Photonics 2011, Wavelets and Sparsity XIV*. San Diego, CA, USA. 2011; p. 81381Q.

[332] Goossens B, Aelterman J, Luong HQ, Pizurica A, Philips W. An Efficient Design of a Discrete Shearlet Transform with Bandlimited Basis Functions. *in preparation*;.

[333] Daubechies I. *Ten lectures on wavelets* . SIAM. 1992.

[334] Hestenes MR, Stiefel E. Methods of conjugate gradients for solving linear systems. *Journal of Research of the National Bureau of Standards*. 1952;49(6):409–436.

[335] Evans JD, Politte DG, Whiting BR, O'Sullivan JA, Williamson JF. Noise-resolution tradeoffs in x-ray CT imaging: A comparison of penalized alternating minimization and filtered backprojection algorithms. *Medical Physics*. 2011;38(3):1444.

[336] von Hagens G, Tiedemann K, Kriz W. The current potential of plastination. *Anat Embryol (Berl)*. 1987;175(4):411–421.

[337] De Man B, Basu SK. Distance-driven projection and backprojection in three dimensions. *Physics in Medicine and Biology*. 2004; 49(11):2463–2475.

[338] Boone JM, Seibert JA. An analytical edge spread function model for computer fitting and subsequent calculation of the LSF and MTF. *Medical Physics*. 1994;21(10):1541–1545.

[339] Haralick RM, Shanmugam K, Dinstein I. Textural Features for Image Classification. *IEEE Transactions on Systems, Man and Cybernetics*. 1973;SMC-3(6):610–621.

[340] Starck JL, Bobin J. Astronomical Data Analysis and Sparsity: From Wavelets to Compressed Sensing. *Proceedings of the IEEE*. 2009;98(6):1021–1030.

[341] Candès EJ, Donoho DL. Ridgelets: A key to higher-dimensional intermittency? *Philosophical Transactions of the Royal Society of London Series A: Mathematical, Physical and Engineering Sciences*. 1999;357(1760):2495–2509.

[342] Goossens B, Luong HQ, Aelterman J, Pizurica A, Philips W. Efficient multiscale and multidirectional representation of 3D data using the 3D discrete shearlet transform. In: *SPIE Optics & Photonics*. International Society for Optics and Photonics. 2011; pp. 81381Z–13.

[343] Fessler JA, Booth SD. Conjugate-gradient preconditioning methods for shift-variant PET image reconstruction. *IEEE Transactions on Image Processing*. 1999;8(5):688–699.

[344] Myers KJ, Barrett HH. Addition of a channel mechanism to the ideal-observer model. *Journal of the Optical Society of America A, Optics and image science*. 1987;4(12):2447–2457.

[345] Platiša L, Goossens B, Vansteenkiste E, Park S, Gallas BD, Badano A, Philips W. Channelized Hotelling observers for the assessment of volumetric imaging data sets. *Journal of the Optical Society of America A, Optics, image science, and vision*. 2011;28(6):1145–1163.

[346] Cheng D, Rusckowski M, Pretorius PH, Chen L, Xiao N, Liu Y, Liu G, Liang M, Liu X, Dou S, Hnatowich DJ. Improving the quantitation accuracy in noninvasive small animal single photon emission computed tomography imaging. *Nuclear Medicine and Biology*. 2011;pp. 1–6.

[347] Tsui BMW, Zhao X, Frey EC, McCartney W. Quantitative single-photon emission computed tomography: basics and clinical considerations. *Seminars in nuclear medicine*. 1994;24(1):38–65.

[348] Almeida P, Ribeiro MJ, Bottlaender M, Loc'h C, Langer O, Strul D, Hugonnard P, Grangeat P, Mazière B, Bendriem B. Absolute quantitation of iodine-123 epidepride kinetics using single-photon emission tomography: comparison with carbon-11 epidepride and positron emission tomography. *European Journal of Nuclear Medicine*. 1999;26(12):1580–1588.

[349] Seo Y. Quantification of SPECT and PET for Drug Development. *Current Radiopharmaceuticals*. 2008;1:17–21.

[350] He B, Du Y, Song X, Segars WP, Frey EC. A Monte Carlo and physical phantom evaluation of quantitative In-111 SPECT. *Physics in Medicine and Biology*. 2005;50(17):4169–4185.

[351] Meikle SR, Kench PL, Kassiou M, Banati RB. Small animal SPECT and its place in the matrix of molecular imaging technologies. *Physics in Medicine and Biology*. 2005;50(22):R45–61.

[352] van der Have F, Vastenhouw B, Rentmeester M, Beekman FJ. System Calibration and Statistical Image Reconstruction for Ultra-High Resolution Stationary Pinhole SPECT. *IEEE Transactions on Medical Imaging*. 2008;27(7):960–971.

[353] Nuyts J, Vunckx K, Defrise M, Vanhove C. Small animal imaging with multi-pinhole SPECT. *Methods*. 2009;pp. 1–10.

[354] Metzler SD, Jaszczak RJ, Patil NH, Vemulapalli S, Akabani G, Chin BB. Molecular imaging of small animals with a triple-head SPECT system using pinhole collimation. *IEEE Transactions on Medical Imaging*. 2005;24(7):853–862.

[355] Accorsi R, Metzler SD. Analytic determination of the resolution-equivalent effective diameter of a pinhole collimator. *IEEE Transactions on Medical Imaging*. 2004;23(6):750–763.

[356] Smith MF, Jaszczak RJ. An analytic model of pinhole aperture penetration for 3D pinhole SPECT image reconstruction. *Physics in Medicine and Biology*. 1998;43:761.

[357] Vanhove C, Defrise M, Bossuyt A, Lahoutte T. Improved quantification in single-pinhole and multiple-pinhole SPECT using micro-CT information. *European Journal of Nuclear Medicine and Molecular Imaging*. 2009;36(7):1049–1063.

[358] Wu C, van der Have F, Vastenhouw B, Dierckx RAJO, Paans AMJ, Beekman FJ. Absolute quantitative total-body small-animal SPECT with focusing pinholes. *European Journal of Nuclear Medicine and Molecular Imaging*. 2010;37(11):2127–2135.

[359] Wu C, de Jong JR, Gratama van Andel HA, van der Have F, Vastenhouw B, Laverman P, Boerman OC, Dierckx RAJO, Beekman FJ. Quantitative multi-pinhole small-animal SPECT: uniform versus non-uniform Chang attenuation correction. *Physics in Medicine and Biology*. 2011;56(18):N183–N193.

[360] Finucane CM, Murray I, Sosabowski JK, Foster JM, Mather SJ. Quantitative Accuracy of Low-Count SPECT Imaging in Phantom and In Vivo Mouse Studies. *International Journal of Molecular Imaging*. 2011;2011:1–8.

[361] Lee HH, Chen JC. Investigation of Attenuation Correction for Small-Animal Single Photon Emission Computed Tomography. *Computational and Mathematical Methods in Medicine*. 2013; 2013(10):1–13.

[362] Kim JC, Anderson SE, Kaye W, Zhang F, Zhu Y, Kaye SJ, He Z. Charge sharing in common-grid pixelated CdZnTe detectors. *Nuclear Instruments and Methods in Physics Research Section A: Accelerators, Spectrometers, Detectors and Associated Equipment*. 2011;654(1):233–243.

[363] Wagenaar DJ, Zhang J, Kazules T, Vandehei T, Bolle E, Chowdhury S, Parnham KB, Patt BE. In vivo dual-isotope SPECT imaging with improved energy resolution. *IEEE Nuclear Science Symposium Conference Record*. 2006;.

[364] Bequé D, Nuyts J, Bormans G, Suetens P, Dupont P. Characterization of acquisition geometry of pinhole SPECT. *IEEE Transactions on Medical Imaging*. 2003;22(5):599–612.

[365] Bequé D, Nuyts J, Suetens P, Bormans G. Optimization of geometrical calibration in pinhole SPECT. *IEEE Transactions on Medical Imaging*. 2005;24(2):180–190.

[366] Vunckx K, Defrise M, Bequé D, Vanhove C, Andreyev A, Nuyts J. Geometrical calibration and aperture configuration design in multi-pinhole SPECT. *Biomedical Imaging: From Nano to Macro, 2008 ISBI 2008 5th IEEE International Symposium on*. 2008;pp. 1403–1406.

[367] Defrise M, Vanhove C, Nuyts J. Perturbative refinement of the geometric calibration in pinhole SPECT. *IEEE Transactions on Medical Imaging*. 2008;27(2):204–214.

[368] Guan H, Gordon R. A projection access order for speedy convergence of ART (algebraic reconstruction technique): a multilevel scheme for computed tomography. *Physics in Medicine and Biology*. 1994;39(11):2005–2022.

[369] Seret A, Vanhove C, Defrise M. Resolution improvement and noise reduction in human pinhole SPECT using a multi-ray approach and the SHINE method. *Nuklearmedizin Nuclear medicine*. 2009; 48(4):159–165.

[370] Verger L, Boitel M, Gentet M, Hamelin R, Mestais C, Mongellaz F, Rustique J, Sanchez G. Characterization of CdTe and CdZnTe detectors for gamma-ray imaging applications. *Nuclear Instruments and Methods in Physics Research*. 2001;458(1-2):297–309.

[371] Szeles C, Cameron SE, Ndap JO, Chalmers WC. Advances in the crystal growth of semi-insulating CdZnTe for radiation detector applications. In: *Nuclear Science Symposium Conference Record, 2001 IEEE*. 2001; pp. 2424–2428.

[372] Ogawa K, Chugo A, Ichihara T, Kubo A, Hashimoto S. Quantitative image reconstruction using position-dependent scatter correction in single photon emission CT. *IEEE Nuclear Science Symposium Conference Record*. 1992;pp. 1011–1013 vol. 2.

[373] Kint E, Staelens SG, Vandenberghe S. Five energy window scatter correction for 111In microSPECT. *Society of Nuclear Medicine Annual Meeting Abstracts*. 2009;50(Supplement 2):1469.

[374] Beekman FJ, de Jong H, van Geloven S. Efficient fully 3-D iterative SPECT reconstruction with Monte Carlo-based scatter compensation. *IEEE Transactions on Medical Imaging*. 2002;21(8).

[375] Bippus R, Goedicke A, Botterweck H. Monte-Carlo-Based Scatter Correction for Quantitative SPECT Reconstruction. *Bildverarbeitung für die Medizin*. 2010;574.

[376] Hutton BF, Buvat I, Beekman FJ. Review and current status of SPECT scatter correction. *Physics in Medicine and Biology*. 2011; 56(14):R85–R112.

[377] Wagenaar DJ. CdTe and CdZnTe Semiconductor Detectors for Nuclear Medicine Imaging. In: *Emission Tomography: The Fundamentals of PET and SPECT*, edited by Wernick MN, Aarsvold JN. Elsevier Academic Press. 2004;.

[378] Volokh L, Hugg J, Blevis I, Asma E, Jansen F, Manjeshwar R. Effect of detector energy response on image quality of myocardial

perfusion SPECT. In: *IEEE Nuclear Science Symposium Conference Record*. 2008; pp. 4043–4046.

[379] Xiao J, de Wit TC, Staelens SG, Beekman FJ. Evaluation of 3D Monte Carlo-based scatter correction for 99mTc cardiac perfusion SPECT. *Journal of Nuclear Medicine*. 2006;47(10):1662–1669.

[380] Anger HO. Radioisotope cameras. In: *Instrumentation in Nuclear Medicine*, edited by Hine GJ, pp. 485–552. New York: Academic. 1967;.

[381] Dimmock MR, Nikulin DA, Gillam JE, Nguyen CV. An OpenCL Implementation of Pinhole Image Reconstruction. *IEEE Transactions on Nuclear Science*. 2012;59(4):1738–1749.

[382] Harris CC, Greer KL, Jaszczak RJ, Floyd CE Jr, Fearnow EC, Coleman RE. Tc99m attenuation coefficients in water-filled phantoms determined with gamma cameras. *Medical Physics*. 1984; 11(5):681.

[383] Rousset OG, Ma Y, Evans AC. Correction for partial volume effects in PET: principle and validation. *Journal of Nuclear Medicine*. 1998;39(5):904–911.

[384] Hoffman EJ, Huang SC, Phelps ME. Quantitation in positron emission computed tomography: 1. Effect of object size. *J Comput Assist Tomogr*. 1979;3(3):229–308.

[385] Lehnert W, Gregoire MC, Hu X, Meikle SR. An investigation of partial volume effect and partial volume correction in small animal positron emission tomography (PET) of the rat brain. *IEEE Nuclear Science Symposium Conference Record*. 2008;pp. 5219–5224.

[386] Mortelmans L, Nuyts J, Pamel G, Maegdenbergh V, Roo M, Suetens P. A new thresholding method for volume determination by SPECT. *European Journal of Nuclear Medicine and Molecular Imaging*. 1986;12(5-6):284–290.

[387] *NEMA NU 04-2008: Performance Measurements of Small Animal Positron Emission Tomographs*. *Tech. rep.*, Rosslyn, VA. 2008.

[388] Park MA, Mahmood A, Zimmerman RE, Limpa-Amara N, Makrigiorgos GM, Moore SC. Adsorption of metallic radionuclides on plastic phantom walls. *Medical Physics*. 2008;35(4):1606.

[389] Chen CL, Wang Y, Lee JJS, Tsui BMW. Toward Quantitative Small Animal Pinhole SPECT: Assessment of Quantitation Accuracy Prior to Image Compensations. *Molecular Imaging and Biology*. 2008;11(3):195–203.

[390] Jouret F, Walrand S, Parreira KS, Courtoy PJ, Pauwels S, Devuyst O, Jamar F. Single photon emission-computed tomography (SPECT) for functional investigation of the proximal tubule in conscious mice. *AJP: Renal Physiology*. 2010;298(2):F454–F460.

[391] Reubi JC, Schär JC, Waser B, Wenger S, Heppeler A, Schmitt JS, Mäcke HR. Affinity profiles for human somatostatin receptor subtypes SST1-SST5 of somatostatin radiotracers selected for scintigraphic and radiotherapeutic use. *European Journal of Nuclear Medicine*. 2000;27(3):273–282.

[392] Laforest R, Sharp TL, Engelbach JA, Fettig NM, Herrero P, Kim J, Lewis JS, Rowland DJ, Tai YC, Welch MJ. Measurement of input functions in rodents: challenges and solutions. *Nuclear Medicine and Biology*. 2005;32(7):679–685.

[393] Sebas, Brabec V, Jelínek J, Hlavatá O. Red cell, plasma and whole blood volumes in organs of normal and hypersplenic rats. *Blut Zeitschrift für die Gesamte Blutforschung*. 1974;29(3):203–209.

[394] Bernhardt P, Kölby L, Johanson V, Nilsson O, Ahlman H, Forssell-Aronsson E. Biodistribution of 111in-DTPA-D-Phe1-octreotide in tumor-bearing nude mice: influence of amount injected and route of administration. *Nuclear Medicine and Biology*. 2003;30(3):253–260.

[395] Montelius M, Ljungberg M, Horn M, Forssell-Aronsson E. Tumour size measurement in a mouse model using high resolution MRI. *BMC medical imaging*. 2012;12:12.

[396] Bremer C, Mustafa M, Bogdanov A, Ntziachristos V, Petrovsky A, Weissleder R. Steady-State Blood Volume Measurements in Experimental Tumors with Different Angiogenic Burdens–A Study in Mice. *Radiology*. 2003;226(1):214–220.

[397] Persigehl T, Wall A, Kellert J, Ring J, Remmele S, Heindel W, Dahnke H, Bremer C. Tumor Blood Volume Determination by Using Susceptibility-corrected R2* Multiecho MR. *Radiology*. 2010; 255(3):781–789.

[398] Hoppin J, Orcutt KD, Hesterman JY, Silva MD, Cheng D, Lackas C, Rusckowski M. Assessing Antibody Pharmacokinetics in Mice with In Vivo Imaging. *Journal of Pharmacology and Experimental Therapeutics*. 2011;337(2):350–358.

[399] Melis M, Vegt E, Konijnenberg MW, de Visser M, Bijster M, Vermeij M, Krenning EP, Boerman OC, de Jong M. Nephrotoxicity in Mice After Repeated Imaging Using 111In-Labeled Peptides. *Journal of Nuclear Medicine*. 2010;51(6):973–977.

[400] Capello A, Krenning EP, Breeman WAP, Bernard BF, de Jong M. Peptide receptor radionuclide therapy in vitro using [111In-DTPA0]octreotide. *Journal of Nuclear Medicine*. 2003;44(1):98–104.

[401] Mok GSP, Tsui BMW, Beekman FJ. The effects of object activity distribution on multiplexing multi-pinhole SPECT. *Physics in Medicine and Biology*. 2011;56:2635–2650.

[402] Lin J. On Artifact-Free Projection Overlaps in Multi-Pinhole Tomographic Imaging. *IEEE Transactions on Medical Imaging*. 2013; 32(12):2215–2229.

[403] Kench PL, Lin J, Gregoire MC, Meikle SR. An investigation of inconsistent projections and artefacts in multi-pinhole SPECT with axially aligned pinholes. *Physics in Medicine and Biology*. 2011; 56(23):7487–7503.

List of Publications

Journal papers

[1] Pato L R V, **Vandeghinste B**, Vandenberghe S, Van Holen R. Evaluation of Fisher Information Matrix Approximation Methods for Assessment of Image Quality in Pinhole SPECT *IEEE Transactions on Medical Imaging* under review.

[2] **Vandeghinste B**, Van Holen R, Vanhove C, De Vos F, Vandenberghe S, Staelens S. Use of a ray-based reconstruction algorithm to accurately quantify preclinical micro-SPECT images *Molecular Imaging* 2014; accepted.

[3] Renard M, Trachet B, Casteleyn C, Campens L, Cornillie P, Callewaert B, Deleye S, **Vandeghinste B**, Dietz H, Devos F, Staelens S, Segers P, Loeys B, Coucke P, De Paepe A, De Backer J. Absence of cardiovascular manifestations in a haploinsufficient Tgfbr1 mouse model *PLOS One* 2014; accepted.

[4] Van Holen R, **Vandeghinste B**, Deprez K, Vandenberghe S. Design and performance of a compact and stationary microSPECT system *Medical Physics* 2013;40(11):112501.

[5] **Vandeghinste B**, Goossens B, Van Holen R, Vanhove C, Pižurica A, Vandenberghe S, Staelens S. Iterative CT reconstruction using shearlet-based regularization *IEEE Transactions on Nuclear Science* 2013;60(5):3305-3317.

[6] Van Audenhaeghe K, Vandenberghe S, Deprez K, **Vandeghinste B**, Van Holen R. Design and simulation of a full-ring multi-lofthole collimator for brain SPECT *Physics in Medicine and Biology* 2013;58:6317-6336.

[7] **Vandeghinste B**, Vandenberghe S, Vanhove C, Staelens S, Van Holen R. Low-dose micro-CT imaging for vascular segmentation and analysis using sparse-view acquisitions *PLOS One* 2013;8(7):e68449.

[8] Deprez K, Vandenberghe S, **Vandeghinste B**, Van Holen R. FlexiSPECT: A SPECT system consisting of a compact high-resolution scintillation detector (SPECTatress) and a lofthole collimator *IEEE Transactions on Nuclear Science* 2013;60(1):53-64.

[9] **Vandeghinste B**, Trachet B, Renard M, Casteleyn C, Staelens S, Loeys B, Segers P, Vandenberge S. Replacing vascular corrosion casting by in vivo μCT imaging for building 3D cardiovascular models in mice *Molecular Imaging and Biology* 2011;13(1):78-86.

[10] Heindryckx F, Mertens K, Charette N, **Vandeghinste B**, Casteleyn C, Van Steenkiste C, Slaets D, Libbrecht L, Staelens S, Stärkel P, Geerts A, Colle I, Van Vlierberghe H. Kinetics of angiogenic changes in a new mouse model for hepatocellular carcinoma *Molecular Cancer* 2010;9:219.

Conference proceedings

[1] Deleye S, Verhaeghe J, Van Holen R, **Vandeghinste B**, Vanhove C, Vandenberghe S, Stroobants S, Staelens S. An image quality phantom to assess the performance of small animal SPECT systems *Proc. of the 2013 Medical Imaging Conference* 2013.

[2] Pato L R V, **Vandeghinste B**, Van Holen R. Evaluation of the Local Shift-Invariance Approximation in the Fisher Information-Based Variance Calculation for Pinhole SPECT *Proc. of the 2013 Medical Imaging Conference* 2013.

[3] Van Audenhaege K, **Vandeghinste B**, Vandenberghe S, Van Holen R. Time Multiplexing using a Static Full-Ring Multi-Pinhole Collimator for Brain SPECT *Proc. of the 2012 Medical Imaging Conference* 2012.

[4] Bouckaert C, **Vandeghinste B**, Vandenberghe S, Vanhove C. Dual-Energy micro-CT for small animal bone-iodine decomposition *Proc. of the 2012 Medical Imaging Conference* 2012.

[5] **Vandeghinste B**, Goossens B, Van Holen R, Vanhove C, Pižurica A, Vandenberghe S, Staelens S. Iterative CT reconstruction using shearlet-based regularization *Proc. of SPIE Medical Imaging* 2012.

[6] **Vandeghinste B**, Vanhove C, De Beenhouwer J, Van Holen R, Vandenberghe S, Staelens S. Absolute quantification in multi-pinhole micro-SPECT for different isotopes *Proc. of the 2011 Medical Imaging Conference* 2011;3720-3724.

[7] **Vandeghinste B**, De Beenhouwer J, Van Holen R, Vandenberghe S, Staelens S. Characterizing the parallax error in multi-pinhole micro-SPECT reconstruction *Proc. of the 2011 Medical Imaging Conference* 2011;2738-2742.

[8] **Vandeghinste B**, Goossens B, De Beenhouwer J, Pižurica A, Philips W, Vandenberghe S, Staelens S. Split-Bregman-based sparse-view CT reconstruction *Proc. International Conference on Fully 3D Reconstruction* 2011;431-434.

Conference abstracts

[1] **Vandeghinste B**, De Wilde D, Van der Donckt C, De Meyer G, Segers P, Van Holen R, Vandenberghe S, Vanhove C. Improved cerebral vasculature visualization in mice with model-based iterative micro-CT reconstruction. *Proceedings of the 13th FirW PhD Symposium* 2013.

[2] Van Den Berge N, Keereman V, Vanhove C, van Mierlo P, Van Niewenhuyse B, **Vandeghinste B**, Raedt R, Boon P, Vandenberghe S, Van Holen R. PET functional imaging of deep brain stimulation in the healthy rat brain. *International Congress of Clinical Neurophysiology and Functional Imaging (ICCN/DGKN), 30th/58th* 2014.

[3] De Wilde D, **Vandeghinste B**, Trachet B, Van der Donckt C, Descamps B, Van Holen R, Vanhove C, De Meyer G, Segers P. In vivo 3D visualization of the mouse cerebral vasculature using contrast enhanced micro-CT. *Belgian Day on Biomedical Engineering, 12th, Abstracts* 2013.

[4] De Wilde D, **Vandeghinste B**, Van Holen R, Vanhove C, Descamps B, Trachet B, Segers P. In vivo visualization and re-

construction of the mouse cerebral vasculature using contrast enhanced micro-CT *Artery* 2013.

[5] **Vandeghinste B**, De Wilde D, Van der Donckt C, De Meyer G, Segers P, Van Holen R, Vandenberghe S, Vanhove C. In Vivo Cerebral Plaque Visualisation in Mice with Polychromatic Iterative microCT Reconstruction *2013 World Molecular Imaging Congress, Abstracts* 2013.

[6] Gutiérrez S, Keereman V, **Vandeghinste B**, Vandenberghe S, Van Holen R. Reproducible, Realistic and Stable Lung Phantom for CT and MR *ESMRMB* 2013.

[7] Van Holen R, **Vandeghinste B**. A compact stationary microSPECT system based on high-resolution detectors and collimator additive manufacturing *Proc. of SNM* 2013.

[8] Vanhove C, **Vandeghinste B**, Van Holen R, Vandenberghe S. Performance evaluation of GPU implementations of four different iterative reconstruction algorithms for micro-computed tomography *Proc. of SNM* 2013.

[9] **Vandeghinste B**, Goossens B, Van Holen R, Vanhove C, Pižurica A, Vandenberghe S, Staelens S. Combined shearlet and TV regularization in sparse-view CT reconstruction *International Conference on Image Formation in X-Ray Computed Tomography* 2012.

[10] Van Holen R, Deprez K, **Vandeghinste B**, Vandenberghe S. Design and simulations of a multi-lofthole MicroSPECT imager using minifying projections *JNM* 2012;53(Supplement 1):2393-2393.

[11] Deprez K, Van Holen R, **Vandeghinste B**, Vandenberghe S. FlexiSPECT: A compact SPECT system with a lofthole collimator and a high-resolution scintillation detector *Proc. of SNM* 2012.

[12] **Vandeghinste B**, Goossens B, Vanhove C, De Beenhouwer J, Van Holen R, Vandenberghe S, Staelens S. Micro-CT contrast increase using regularized CT reconstruction *Belgian Day on Biomedical Engineering, 10th, Abstracts* 2011.

[13] **Vandeghinste B**, Goossens B, Trachet B, De Beenhouwer J, Staelens S, Vandenberghe S. Innovative in vivo preclinical micro-CT *X-ray tomography as a multidisciplinary research tool: exploring new frontiers* 2010.

[14] **Vandeghinste B**, De Beenhouwer J, Vandenberghe S, Staelens S. Development of reconstruction software to investigate influence of μCT on μSPECT *Proceedings of the 11th FirW PhD Symposium* 2010.

[15] **Vandeghinste B**, De Beenhouwer J, Vandenberghe S, Staelens S. Development of reconstruction software to investigate influence of μCT on μSPECT *National Day of Biomedical Engineering* 2010.

[16] Heindryckx F, **Vandeghinste B**, Casteleyn C, Charette N, Slaets D, Libbrecht L, Staelens S, Stärkel P, Geerts A, Colle I, Van Vlierberghe H. Angiogenic changes in a new mouse model for hepatocellular carcinoma assessed with state-of-the-art imaging technology *Journal of Hepatology* 2010;52(1):S340-S340.

[17] Heindryckx F, **Vandeghinste B**, Slaets D, Mertens K, Libbrecht L, Casteleyn C, Staelens S, Geerts A, Colle I, Van Vlierberghe H. Angiogenic changes in a new mouse model for hepatocellular carcinoma assessed with state-of-the-art imaging technology *Knowledge for Growth, Abstracts* 2010.

[18] Heindryckx F, **Vandeghinste B**, Libbrecht L, Casteleyn C, Staelens S, Colle I, Van Vlierberghe H, Geerts A. Angiogenic changes in a new mouse model for hepatocellular carcinoma *Signaling in the liver* 2010.

[19] Trachet B, **Vandeghinste B**, Renard M, Casteleyn C, Staelens S, Loeys B, Segers P, Vandenberghe S. Comparison between vascular corrosion casting and in vivo micro-CT imaging for wall shear stress calculations in the mouse aorta *Abstract book: the 5th international symposium on Biomechanics in Vascular Biology and Cardiovascular Disease* 2010.

[20] Trachet B, **Vandeghinste B**, Renard M, Casteleyn C, Staelens S, Loeys B, Vandenberghe S, Segers P. Vascular corrosion casting vs in vivo micro-CT casting : what is the effect on wall shear stress calculations in the mouse aorta? *Abstracts: 6th World Congress of Biomechanics, International Federation for Medical and Biological Engineering (IFMBE)* 2010;274.

[21] **Vandeghinste B**, Trachet B, Renard M, Casteleyn C, Deleye S, Joye P, Vandenberghe S, Staelens S, Segers P, Loeys B. Replacing vascular corrosion casting by in-vivo μCT imaging for building

3D cardiovascular models in mice *2009 World Molecular Imaging Congress, Abstracts* 2009.